

https://dspace.org/

Corrosion initiation of reinforcing steel induced by combined penetration of chlorides and carbon dioxide in concrete with construction cold joints

Teggin, James William

2022
https://hdl.handle.net/10539/34937

Downloaded from a DSpace repository. https://dspace.org/

Corrosion of Reinforcing Steel induced by Combined Penetration of Chlorides and Carbon Dioxide in Concrete with Construction Cold Joints

A Dissertation submitted to the Faculty of Engineering and the Built Environment, University of the Witwatersrand, in fulfilment of the requirements for the degree of Master of Science in Engineering.

Author

Mr. James William Teggin

Student number: 1840583

Supervisor

Associate Professor

Sunday Onyebuchi Nwaubani

Course Details

Master of Science in Engineering by Research

Course code: CIVN8001A



Johannesburg, 2022

Declaration

I, James William (JW) Teggin, hereby declare that I am the author of this Dissertation which is my own, unaided work except where specifically referenced in text. I know the meaning of plagiarism and declare that all of the work contained herein, save for that which is properly acknowledged, is my own. It is being submitted for the degree of Master of Science in Engineering, MSc (Eng) at the University of the Witwatersrand. It has not been submitted before it in its entirety or in part for any degree or examination to any other University.

J.W. Teggin (James William)

7th day of October 2022

Abstract

Corrosion of reinforcing steel in concrete is regarded as the greatest threat to the durability and integrity of concrete structures in many regions worldwide. The safety and performance of structures is at risk due to a reduction of the carrying capacity of the steel and bond strength to concrete. The most important causes of corrosion are the ingress of chlorides or carbon dioxide, which is reflected in the exposure classes of standards. Most of the corrosion research has involved the isolated exposure to each, however, in many structures, corrosion occurs due to the combined exposure. When carbonation occurs in concrete with chloride, or when chloride penetrates into carbonated concrete, these mechanisms interact to increase the corrosion rate. The corrosion rate is increased under this condition due to an increase in the chloride content beyond the carbonation depth.

The corrosion rate may also increase when the transport of gasses, moisture and ions occurs at defects such as cracks and cold joints. Many types of defects can increase the chloride content at the concrete surface, which can be diffused faster to the steel level if the carbonation depth is sufficient. An increase in the chloride content at defects may thus be considered as a severe case for corrosion and has not been addressed yet in the literature. A cold joint was selected for this study as it is formed over the entire cross-section of concrete elements, unlike defects that form at the concrete surface. This corrosion case may result in a reduction of the corrosion initiation time and occurrence of cracking during the propagation phase. It is practical to consider such cases of corrosion as these may be present more frequently due to urbanisation and population growth in marine environments. The aim of this study was to determine if the corrosion rate could be increased due to an increase in the chloride content at a cold joint in carbonating concrete.

The experimental programme was set out to determine the corrosion state of reinforcing steel, chloride penetration and carbonation depths, transport of gasses, moisture and ions, and corrosion damages to the steel and concrete. It is useful to investigate any corrosion cases by supplementing the corrosion rate with other

parameters such as chloride penetration, carbonation depth, etc. The concretes that were used to cast the test specimens included either fly ash or metakaolin, for the comparisons to ordinary concrete. The exposure period of this study lasted 294 days, which was intended to achieve a carbonation depth that was influential to the chloride penetration and corrosion rate. A cold joint was included in selected specimens for comparison to the monolithically-cast specimens, with a time delay of 24 hours between the casting. The exposure conditions were either combined exposure to chloride and carbon dioxide, or chloride exposure in isolation.

The results found an agreement from the comparisons between the experimental parameters which validated the hypothesis of this study. The chloride content was increased beyond the carbonation depth at a cold joint in all concretes within the timeframe of the exposure. The corrosion rate of the steel was increased due to the increase in the chloride content beyond the carbonation depth in the vicinity of a cold joint. The benefit of fly ash and metakaolin was limited to the test specimens with a larger cover depth where the corrosion rate was lower than the ordinary concrete. The oxygen permeability was lower than the ordinary concrete, which is the main factor to the corrosion rate in saturated or partially-saturated concrete. The concrete resistivity was higher than the ordinary concrete, in that there was a lower conductivity to allow for a passage of current in the corrosion reactions.

Contents

1. INTRODUCTION 1

1.1. Study background and justification 1

1.2. Aim of the study 5

1.3. Objectives of the study 5

1.4. Scope and limitations of the study 6

1.5. Hypothesis of the study 7

1.6. Report outline 7

2. LITERATURE REVIEW 9

2.1. Overview 9

2.2. Reinforcing steel corrosion in concrete 9

2.2.1. The stages of corrosion 9

2.2.2. Corrosion initiation 11

2.2.3. Corrosion propagation 12

2.2.4. Moisture and oxygen availability 13

2.2.5. Concrete cover depth 14

2.2.6. Concrete resistivity 15

2.2.7. Concrete quality and defects 17

2.2.8. Manifestation of corrosion 18

2.2.9. Types of corrosion 20

2.3. Chloride-induced corrosion 21

2.3.1. Exposure to chlorides 21

2.3.2. Chloride penetration in concrete 22

2.3.3. Chloride transport mechanisms 23

2.3.4. Chloride binding 27

2.3.5. Chloride threshold 29

2.4. Cement extenders and their influence on corrosion 31
2.4.1. Overview 31
2.4.2. Fly ash 32
2.4.3. Metakaolin 33
2.4.4. Ground granulated blast-furnace slag 34
2.4.5. Condensed silica fume 35

2.5. Carbonation-induced corrosion 36
2.5.1. Exposure to carbon dioxide 36
2.5.2. Carbonation of concrete 37
2.5.3. Carbonation of concrete 38
2.5.4. Carbonation-induced corrosion 41

2.6. Influence of carbonation on chloride penetration 43
2.6.1. Overview 43
2.6.2. Chloride penetration in carbonated concrete 44
2.6.3. Carbonation in concrete with chloride 47
2.6.4. Corrosion risk due to combine exposure 48

2.7. Corrosion assessment 49
2.7.1. Visual inspection 50
2.7.2. Corrosion monitoring 51

3. EXPERIMENTAL PROGRAMME 61

3.1. Overview 61

3.2. Materials used 61
3.2.1. Cementing binders and aggregates 61
3.2.2. Aggregates 71
3.2.3. Mixing water and plasticiser 73

3.3. Concrete mixture design 74

3.3.1. C & CI procedure 74
3.3.2. Proposed concrete mixtures 78

3.4. Concrete mixing and sampling 79
3.4.1. Concrete mixing 79
3.4.2. Concrete sampling 79

3.5. Test specimen fabrication 80
3.5.1. Reinforced beam specimen details 80
3.5.2. Cube specimen details 82
3.5.3. Circular disc specimen details 82
3.5.4. Cold joints in test specimens 83
3.5.5. Concrete handling 85

3.6. Preliminary testing 87
3.6.1. Overview 87
3.6.2. Cover depth testing 88

3.7. Exposure conditions 89
3.7.1. Overview 89
3.7.2. Ponding on beam specimens 89
3.7.3. Exposure to carbon dioxide 91
3.7.4. Application and monitoring of the exposure 93

3.8. Compressive strength testing 94

3.9. Durability testing 95
3.9.1. Durability index testing 95
3.9.2. Penetration state testing 101
3.9.3. Corrosion monitoring 106
3.9.4. Corrosion damage testing 115

3.10. Experimental summary 117

4. EXPERIMENTAL RESULTS AND DISCUSSION 121

4.1. Overview 121

4.2. Fresh-state properties 121

4.2.1. Mixture proportions 121

4.2.2. Slump measurement 123

4.2.3. Cohesion level 126

4.2.4. Stone content 127

4.2.5. Plastic density 128

4.3. Mechanical properties 128

4.3.1. Overview 128

4.3.2. Early-age compressive strength 129

4.3.3. Long-term compressive strength 131

4.4. Exposure conditions 132

4.4.1 Overview 132

4.4.2. Timeline of exposure conditions 133

4.4.3. Temperature behaviour 133

4.4.4. Relative humidity behaviour 134

4.5. Durability 136

4.5.1. Overview 136

4.5.2. Transport properties 137

4.5.3. Penetration state 145

4.5.4. Corrosion behaviour 160

4.5.5. Corrosion damages 192

4.6. Final discussion 201

5. CONCLUSIONS AND RECOMMENDATIONS 206

5.1. Summary 206

5.2. Conclusions 207

5.3. Recommendations 208

REFERENCES 210

APPENDIX A: COVER DEPTH TESTING I

APPENDIX B: COMPRESSIVE STRENGTH TESTING II

APPENDIX C: DURABILITY INDICES III

APPENDIX D: PENETRATION STATE VI

Appendix D 1: Chloride profiles in reinforced beams VI

Appendix D 2: Carbonation depth testing details VIII

APPENDIX E: CORROSION BEHAVIOUR IX

Appendix E 1: Coulostat apparatus potential behaviour IX

Appendix E 2: Coulostat apparatus resistivity behaviour XII

List of figures

Figure		Page
2.1	3-stage corrosion damage model (Heckroodt, 2002)	10
2.2	Relative volume of iron and its oxides (Mansfield, 1981)	20
2.3	Chloride profiles in a bridge deck and car park (Broomfield, 2007)	22
2.4	Influence of the diffusion coefficient and cover depth on chloride penetration (Bertolini et al., 2013)	25
2.5	Convection zone in concrete (LIFE-365, 2005)	26
2.6	pH reduction due to carbonation (Alexander et al., 2009)	39
2.7	pH reduction across a carbonation front (Broomfield, 2007)	42
3.1	Binder density measurement apparatus	64
3.2	Binder surface area measurement apparatus	65
3.3	Binder particle size distribution apparatus	66
3.4	Cement particle size distributions	67
3.5	Binder particle size distributions	67
3.6	SEM images of the cement and fly ash particles	69
3.7	SEM image of the metakaolin particles	68
3.8	Aggregate grading curves	72
3.9	Reinforced beam moulding details	81
3.10	Circular disc geometric details	83
3.11	Typical cold joint reinforced beam mould	84
3.12	Cover depth testing	89
3.13	Chloride solution ponding details	90
3.14	Carbonation chamber operation details	91
3.15	Carbonation chamber control unit and gas inlet	92
3.16	Application of exposure regimes	93
3.17	Oxygen permeability testing	96
3.18	Water sorptivity testing	98
3.19	Chloride conductivity testing	100
3.20	Reinforced beam sampling location and drilling set-up	102

3.21	Total chloride testing	104
3.22	Cube fracturing set-up	105
3.23	Elcometer half-cell locations	108
3.24	Coulostat half-cell location	108
3.25	Coulostat corrosion potential transients	111
3.26	Wenner probe array test locations and probe bases	113
3.27	Coulostat resistivity test potential transients	114
3.28	Preparatory work	117
3.29	Curing, exposure and testing details	119
4.1	Compressive strength from 2 to 28 days	129
4.2	Compressive strength gained in intervals up to 28 days	130
4.3	Compressive strength from 2 to 90 days	131
4.4	Temperature behaviour records	134
4.5	Relative humidity behaviour records	135
4.6	Oxygen permeability indices from 28 to 90 days	138
4.7	Water sorptivity indices from 28 to 90 days	140
4.8	Chloride conductivity indices from 28 to 90 days	142
4.9	Total porosities from 28 to 90 days	144
4.10	Chloride profiles in the ordinary concrete 20 mm cover beams	147
4.11	Chloride profiles in the ordinary concrete 10 mm cover beams	149
4.12	Chloride profiles in the fly ash concrete 20 mm cover beams	150
4.13	Chloride profiles in the fly ash concrete 10 mm cover beams	151
4.14	Chloride profiles in the metakaolin concrete 20 mm cover beams	152
4.15	Chloride profiles in the metakaolin concrete 10 mm cover beams	153
4.16	Carbonation depths after 10 and 21 cycles	154
4.17	Baseline of the carbonation depths	155
4.18	Carbonation depths after 10 cycles	156
4.19	Carbonation depths after 21 cycles	157
4.20	Corrosion potential in the ordinary concrete 20 mm cover beams	161
4.21	Corrosion potential in the ordinary concrete 10 mm cover beams	163
4.22	Corrosion potential in the fly ash concrete 20 mm cover beams	164
4.23	Corrosion potential in the fly ash concrete 10 mm cover beams	165

4.24	Corrosion potential in the metakaolin concrete 20 mm cover beams	167
4.25	Corrosion potential in the metakaolin concrete 10 mm cover beams	168
4.26	Corrosion rate in the ordinary concrete 20 mm cover beams	170
4.27	Corrosion rate in the ordinary concrete 10 mm cover beams	171
4.28	Corrosion rate in the fly ash concrete 20 mm cover beams	172
4.29	Corrosion rate in the fly ash concrete 10 mm cover beams	173
4.30	Corrosion rate in the metakaolin concrete 20 mm cover beams	175
4.31	Corrosion rate in the metakaolin concrete 10 mm cover beams	176
4.32	Potential-corrosion rate relationship	181
4.33	Concrete resistivity in the ordinary concrete 20 mm cover beams	183
4.34	Concrete resistivity in the fly ash concrete 20 mm cover beams	184
4.35	Concrete resistivity in the metakaolin concrete 20 mm cover beams	185
4.36	Corrosion rate-temperature relationship	188
4.37	Corrosion rate-relative humidity relationship	189
4.38	Measured cover depths	189
4.39	Corrosion in the 20 mm cover monolithic beams	193
4.40	Corrosion in the 20 mm cover cold joint beams	194
4.41	Corrosion in the 10 mm cover cold joint beams	196
4.42	Cracking in the 10 mm cover monolithic beams	198
4.43	Cracking in the 10 mm cover cold joint beams	198
E.1	Corrosion potential in the ordinary concrete 20 mm cover beams	ix
E.2	Corrosion potential in the ordinary concrete 10 mm cover beams	ix
E.3	Corrosion potential in the fly ash concrete 20 mm cover beams	x
E.4	Corrosion potential in the fly ash concrete 10 mm cover beams	x
E.5	Corrosion potential in the metakaolin concrete 20 mm cover beams	xi
E.6	Corrosion potential in the metakaolin concrete 10 mm cover beams	xi
E.7	Concrete resistivity in the ordinary concrete 20 mm cover beams	xii
E.8	Concrete resistivity in the fly ash concrete 20 mm cover beams	xii
E.9	Concrete resistivity in the metakaolin concrete 20 mm cover beams	xiii

List of tables

Table		Page
2.1	Relation between the corrosion rate and concrete resistivity (Langford & Broomfield, 1987)	16
3.1	Typical cement oxide composition	62
3.2	Cement impurity requirements	63
3.3	Cement strength and setting time requirements	63
3.4	Typical fly ash oxide composition	68
3.5	Fly ash impurity requirements	68
3.6	Typical metakaolin oxide composition	70
3.7	Concretes use to cast specimens	83
3.8	Corrosion probability ranges (ASTM, 1999)	109
3.9	Corrosion level ranges (RILEM, 2004)	112
3.10	Concrete resistivity ranges (RILEM, 2004)	115
4.1	Trial mixture proportions	122
4.2	Trial assessment and modifications	123
4.3	Trial assessment and modifications	125
4.4	Concrete quality grading (Alexander et al., 1999)	137
4.5	Corrosion resistance summary	177
4.6	Corroded lengths in the 20 mm cover monolithic beams	193
4.7	Corroded lengths in the 20 mm cover cold joint beams	194
4.8	Corroded lengths in the 10 mm cover monolithic beams	196
4.9	Corroded lengths in the 10 mm cover cold joint beams	197
4.10	Crack formation in the 10 mm cover monolithic beams	199
4.11	Crack formation in the 10 mm cover monolithic beams	200
A.1	Cover depth in the ordinary concrete beams	i
A.2	Cover depth in the cement extender concrete beams	i
B.1	Details of the compressive strength testing	ii
C.1	Details of the oxygen permeability testing	iii
C.2	Darcy coefficients of permeability	iii

C.3	Details of the water sorptivity testing	iv
C.4	Details of the total porosity testing	iv
C.5	Details of the chloride conductivity testing	v
C.6	Details of the chloride solution porosity testing	v
D.1	Chloride profiles in the ordinary concrete 20 mm cover beams	vi
D.2	Chloride profiles in the fly ash concrete 20 mm cover beams	vi
D.3	Chloride profiles in the metakaolin concrete 20 mm cover beams	vi
D.4	Chloride profiles in the ordinary concrete 10 mm cover beams	vii
D.5	Chloride profiles in the fly ash concrete 10 mm cover beams	vii
D.6	Chloride profiles in the metakaolin concrete 10 mm cover beams	vii
D.7	Carbonation depths under isolated carbon dioxide exposure	viii
D.8	Carbonation depths under combined exposure	viii

List of equations

Equation		Page
2.1	Anodic reaction of a corrosion cell (Broomfield, 2007)	12
2.2	Cathodic reaction of a corrosion cell (Broomfield, 2007)	12
2.3	Reaction to form ferrous hydroxide (Broomfield, 2007)	19
2.4	Reaction to form ferric hydroxide (Broomfield, 2007)	19
2.5	Reaction to form hydrated ferric hydroxide (rust) (Broomfield, 2007)	19
2.6	Fick's 2nd law of diffusion (Bertolini et al., 2013)	23
2.7	Solution of Fick's 2nd law of diffusion (Bertolini et al., 2013)	24
2.8	Crank's error function (Bertolini et al., 2013)	24
2.9	Pozzolanic reaction of cement extenders in concrete (Domone & Illston, 2001)	32
2.10	Reaction to form carbonic acid (Bertolini, et al., 2013)	37
2.11	Reaction to form calcium carbonate (Bertolini, et al., 2013)	37
2.12	Fick's 2nd law of diffusion for carbonation (Broomfield, 2007)	38
2.13	Solution of Fick's 2nd law of diffusion for carbonation (Broomfield, 2007)	38
2.14	Carbonation depth with boundary conditions (Broomfield, 2007)	38
2.15	Polarisation resistance (Stern & Geary, 1957)	55
2.16	Corrosion current density (Andrade et al., 2004)	55
2.17	Randles circuit description of potential decay (Song & Saraswathy, 2007)	57
2.18	Total potential charge in the steel (Song & Saraswathy, 2007)	57
2.19	Polarisation resistance (Coulostatic polarisation) (Song & Saraswathy, 2007)	57
2.20	Interfacial capacitance (Song & Saraswathy, 2007)	57
2.21	Charge delivered in the polarisation (Song & Saraswathy, 2007)	58

2.22	Concrete resistivity of a Wenner Probe (Song & Saraswathy, 2007)	59
3.1	Brunauer-Emmet-Teller (BET) model equation (Lowell, 2004)	65
3.2	Surface area equation (Lowell, 2004)	66
3.3	Stone content equation (Alexander et al., 2009)	77
3.4	Compressive strength equation at failure (SANS, 2006)	95
3.5	Darcy permeability coefficient equation (SANS, 2015)	97
3.6	Sorptivity equation (Alexander, 2017)	99
3.7	Porosity equation (Alexander, 2017)	99
3.8	Chloride conductivity equation (SANS, 2017)	100

List of symbols

Symbol	Description
µm	Micrometre or micron ($1x10^{-6}$ m).
mm	Millimetre ($1x10^{-3}$ m).
mm^2	Square millimetres.
kg/m^3	Kilograms per cubic meter.
m^2/g	Metres squared coverage per gram.
SA	Surface area (m^2/g).
m^2/l	Meters squared coverage per litre.
mm/√hr	Millimetres per square root of time.
S	Sorptivity (mm/√hr).
l/m^3	Litres per cubic meter.
g/cc	Grams per cubic metre.
g/ml	Grams per millilitre.
fc	Compressive strength.
Ac	Load-bearing area.
kPa	Kilo Pascal (10^3 Pascal).
MPa	Mega Pascal (10^6 Pascal).
kN	Kilo Newton.
kN/s	Kilo Newton per second.
MPa/s	Mega Pascal per second.
psi	Pounds per square inch.
k	Darcy coefficient of permeability in m/s.
°C	Degrees Celsius.
t	Exposure duration, concrete age or test duration.
P	Pressure (kPa or psi).
S	Sorptivity (mm/√hr).
n	Porosity or void percentage.
A	Ampere.
mA	Milliampere (10^{-3} Amperes).

Cl^-	Chloride concentration at any depth in concrete.
D	Chloride or carbonation diffusion coefficient.
d	Carbonation depth.
M	Molarity.
mol	Mole
S	Siemens, indicator of conductance, the reciprocal of electrical conductance.
mS/cm	Milli-Siemen per centimetre.
C	Chloride conductivity (mS/cm).
V	Volt.
mV	Millivolt (10^{-3} Volt).
$\mu A/cm^2$	Microampere per square centimetre.
µm/Y	Micrometre per year.
icorr	Corrosion current density ($\mu A/cm^2$)
kΩ·cm	Kilo Ohms per square centimetre.
B	Stern-Geary constant.
ρ	Concrete resistivity (kΩ·cm).
R_P	Polarisation resistance.
i.e.	For example.
etc.	Et cetera.
viz.	As follows.

List of abbreviations

Abbreviation	Description
AASHTO	American Association of State Highway and Transportation Officials.
ACI	American Concrete Institute.
aka	Also known as.
AR	Analytical Reagent.
ASTM	American Society for Testing and Materials.
CCI	Chloride Conductivity Index.
C & CI	Cement and Concrete Institute
CEM	Cement type (I-V) based on strength class and composition.
DC	Direct Current.
EN	European Standards.
FM	Fineness Modulus (of sand).
GGBS	Ground-Granulated Blast-Furnace Slag.
IG	Instrument Grade.
MIP	Mercury Intrusion Porosimetry.
N	Normal (cement strength gain class).
OPI	Oxygen Permeability Index.
pH	(or apparent pH) “Power of Hydrogen” or negative log of the hydrogen ion concentration.
psi	Pound Per Square Inch.
R	Rapid (strength gain cement class).
SANAS	South African National Accredited System.
SANS	South African National Standards.
SEM	Scanning Electron Microscopy.
TMH	Testing Methods for Highways.
USDOTD	United States Department of Transportation and Development.
WSI	Water Sorptivity Index.
W: B	Water: Binder ratio.

1. Introduction

1.1. Study background and justification

Corrosion of reinforcing steel in concrete is the "greatest threat to the durability and integrity of concrete structures in many regions" (Domone & Illston, 2010). When the design, concrete quality and construction processes are adequate, the concrete may provide protection to the steel throughout the service life (Bertolini et al., 2013). The steel may, however, corrode sooner than anticipated when the durability requirements of an environment are not correct, requiring rehabilitation within the service life. The safety and performance of structures may be at risk due to a reduction of the carrying capacity of steel and bond strength to concrete (Neville, 2011). The widespread occurrence of corrosion rehabilitation costs "billions of dollars annually" to maintain the performance of structures (Quraishi et al., 2017). Corrosion prevention costs in the design and construction stages are "minimal" compared to the costs during the service life (Bertolini et al., 2013).

The "most important" causes of corrosion of reinforcing steel in concrete are "the ingress of chloride ions or carbon dioxide" (Song & Saraswathy, 2007). Structures that are located in marine zones may be exposed to airborne chlorides in the salt spray, further inland, or by direct contact at the sea. Chloride penetration from the environment is characterised by the reduction of the chloride content from the concrete surface to greater depths (Bertolini et al., 2013). Carbonation progresses as a front and is the result of the interaction between the carbon dioxide in the atmosphere and pore solution of concrete (Broomfield, 2007). There are numerous studies that involve corrosion due to chloride or carbon dioxide in isolation, which is reflected in the exposure classes of standards, such as BS EN 206-1 (BS-EN, 2000). These corrosion studies involve the isolated exposure to each, however, for many structures, corrosion occurs due to the combined exposure (Yoon, 2007).

When carbonation occurs in concrete with chloride, or when chloride penetrates into carbonated concrete, these mechanisms interact to "accelerate" the corrosion

(Alexander et al., 2009). A proportion of the chloride in concrete is chemically-bound to the compounds of the cementing binders thus it built-up at the surface, instead of penetrating to greater depths. However, the alkalinity (pH) reduction due to carbonation causes a "break down" of the bound chloride, which increases the amount of soluble (free) beyond the carbonation front (Broomfield, 2007). The corrosion rate of reinforcing steel may thus be increased due to an increase in the chloride content beyond the carbonation depth. The trend of an increase in the chloride content beyond the carbonation depth has been reported in studies such as Pakawat & Uomoto (2005), Yoon (2007), Malheiro et al., (2016) and Wang et al., (2016). Though the chloride content was lower at the concrete surface than the chloride exposure in isolation, it was increased beyond the carbonation depth.

Factors of the concrete quality and exposure conditions are determined by monitoring the corrosion state over a period of exposure. Corrosion monitoring is an approach of determining the changes in corrosion activity before the signs of corrosion require rehabilitation (Bertolini et al., 2013). Corrosion behaviour over time may be more representative of the corrosion state as it reflects the changes in concrete quality and exposure conditions. The progress of carbonation in concrete with chloride has been found in a laboratory setting by monitoring the corrosion state over a period of exposure. Corrosion activity as the potential and corrosion rate was increased under combined exposure when the carbonation depth was sufficient in studies such as Moreno & Sagues (1998) and Pakawat & Uomoto (2005). The carbonation rate is important to influence the chloride penetration and corrosion rate thus it is accelerated to equate to a larger time of natural exposure.

Corrosion is "especially worse" when the transport of gasses, moisture and ions takes place at defects such as cracking and cold joints (Miyazato & Otsuki, 2010). Concrete quality factors such as the water: binder ratio may be less-influential to the transport properties where defects are present. Cold joints are present from the start of exposure and are used at successive placements of concrete to limit the extent of cracking (Alexander et al., 2009). There are other defects that originate in the construction process, however, their degree of influence may be reduced by

suitable concrete quality, handling and curing. Defects are particularly influential to the chloride content as the absorption of moisture (with chloride) takes place nearer the concrete surface. Whatever the type defect, its presence may influence the chloride penetration or carbonation depth thus increase the corrosion rate.

A cold joint in the direction of exposure resulted in an increase in the chloride diffusion coefficient in Sung-Won & Seung-Jun (2016). The diffusion coefficient was increased in the cold joint specimens compared to the monolithically-cast (plain) specimens. Some of the specimens were cracked, which further increased the chloride diffusion coefficient, on top of that caused by the cold joint only. The cold joint in the direction of exposure in Farzad et al., (2019) resulted in deeper chloride penetration beyond the surface region of the concrete specimens. The cracks that were fabricated prior to the exposure in Paul (2015) resulted in higher chloride contents at the concrete surface and deeper chloride penetration. The chloride content at the surface was increased by the crack width and spacing of multiple cracks, which is more likely than single cracks developing in isolation.

The corrosion rate has also been found to increase at the location of cold joints and cracks in corrosion monitoring schemes. A cold joint increased the corrosion rate in ordinary and fly ash concretes that were exposed to fresh and sea water in Roxas & Lejano (2018). The cold joint was fabricated in separate specimens for comparing the corrosion rate to the monolithically-cast (or plain) specimens. The cold joint in Miyazato & Otsuki (2010) increased corrosion rate under isolated exposure to chloride or carbon dioxide. The cold joint was fabricated in the same specimen, in that the corrosion rate was decreased away from the location of this defect. The corrosion rate was increased with an increase in the width of cracks that were present at the start of the exposure in studies such as Scott & Alexander (2007), Otieno (2014) and Paul (2015). An increase in the amount of cracks in Paul (2015) also resulted in an increase in the corrosion rate during the exposure.

In the engineering field, the severe cases of any degradation process may be seen as more practical to base an understanding on. The influence of carbonation on

chloride penetration is an initial step to such severe cases as it is has been found to increase the corrosion rate. However, in concrete structures there are an array of defects that form in the construction process and service life, which may increase the chloride content at the concrete surface and carbonation depth. The influence of carbonation on chloride penetration may thus be considered as a severe case of corrosion at defect locations. The increased chloride content at these locations may penetrate to the steel at any point in the service life, when there is a sufficient carbonation depth. A cold joint is of interest to this study as the continuity of the concrete properties is influenced over the entire section of concrete elements, not only the cover region. The effectiveness of this defect may cause cracking in its vicinity, which would accelerate corrosion rate and damages to the cover concrete.

The corrosion case due to a cold joint and carbonation has not been addressed yet and incorporates a number of important aspects of corrosion research. The first of which is encapsulating the influence of climate change, population growth and urbanisation trends. The carbon dioxide content in the atmosphere has increased continuously since the industrialisation period of the 19th century (Kunowsky et al., 2013). This trend raises a need to consider the presence of carbonation in concrete with chloride penetration as it has been found to be synergistic in nature. Carbonation in the concrete structures of marine zones would present a risk to the service life, especially where defects are located. The second aspect is a larger understanding of corrosion monitoring over a short period in a laboratory setting compared to the service life of structures. Corrosion monitoring may determine the coupled effect of a cold joint and progress of carbonation in concrete with chloride. The relationship between the chloride penetration and corrosion rate would be of importance to represent the influence of a cold joint and carbonation.

The last aspect of research to this corrosion case was to explore the performance of cement extenders to improve the concrete durability. In recent years the cement industry has come under scrutiny as a “significant contributor of carbon dioxide” to the atmosphere (Alexander et al., 2009). “Over the last 60 years or so” there has been increasing use of materials to replace some of the Portland cement to yield a

wider range of concrete properties (Domone & Illston, 2010). A lower production of cement is promoted within the framework of sustainability, by using industrial wastes and more recently, agricultural and general wastes (Neville, 2011). Cement extenders such as fly ash, slag and silica fume have been found to decrease the corrosion rate at a given cover depth in studies such as Scott & Alexander (2007), Otieno (2014) and Paul (2015). This is due to their ability to decrease the pore sizes and connectivity of pores the paste in concrete, along with their composition.

1.2. Aim of the study

Against the background, the aim was to determine if an increase in the chloride content at a cold joint and accelerated carbonation causes an increase in the corrosion rate of reinforcing steel, considering the use of cement extenders.

1.3. Objectives of the study

The objectives that were set out to achieve the stated aim of the study were:

- to conduct a ***literature study*** into the fundamentals and critical studies that were relevant of the scope of this study, broadly under the concrete properties, corrosion fundamentals, chloride penetration and carbonation and the presence of defects in the cover concrete.

  Specific aspects were (1) the characteristics of Portland cement and cement extenders and their properties in concrete, (2) the phases and factors of the corrosion mechanism, (3) chloride penetration and carbonation in isolation and in combination and (4) the visual inspection and monitoring of corrosion.

- carry out an ***experimental programme*** where specimens were cast and tested with parameters reflecting (1) the corrosion state of embedded steel, (2) chloride penetration and carbonation depths (3) transport properties of gasses, moisture and ions and (4) corrosion damages to the steel and concrete.

It is useful to investigate corrosion cases by supplementing the corrosion rate with other parameters such as chloride penetration, carbonation depth, etc. The corrosion rate is important to the service life as it relates to parameters such as the crack width and loss of the cross-section of reinforcing steel.

- *collate* and *critically analyse* the experimental results and
- make necessary *conclusions* and *recommendations*.

1.4. Scope and limitations of the study

The overarching scope of the study involved comparisons based on isolated chloride exposure in monolithically-cast (plain) concrete to combined exposure to chloride and carbon dioxide in concrete with a cold joint. Cement replacement with pozzolanic cement extenders was the basis of these comparisons due to the differences in their compositions and physical characteristics. Of the common cement extenders in concrete practice, fly ash and metakaolin were used, together with Portland cement, for comparisons to ordinary concrete. Corrosion due to carbonation in isolation was not part of the scope as the carbonation rate is slower than chloride penetration in partially-saturated or saturated concrete, i.e. the tidal zone. The carbonation was accelerated to achieve a depth that was influential to the chloride penetration and corrosion rate within the timeframe of exposure.

The corrosion behaviour was monitoring for a period of exposure in terms of the corrosion potential, corrosion rate and concrete resistivity. The corrosion initiation time and maximum corrosion rate were used to assess the corrosion resistance of concrete specimens, of a given concrete type and cover depth. The corrosion damage was assessed in terms of the locality and extent of concrete cracking and steel corrosion. The corrosion damage assessment was simplified, in that it was based more on the locality of the damages, not to determine any relationships with the corrosion rate. Cracking due to corrosion is random, based on the fracture of concrete, instead of cracks with a specific width that are formed in the process of

casting at a position of interest. Corrosion protection is not included as the focus was on the concrete quality by cement replacement to improving the durability.

1.5. Hypothesis of the study

This study was set up based on the hypothesis so that:

- the chloride penetration at a cold joint and on-going carbonation would decrease the corrosion initiation time and increase the corrosion rate in the propagation phase.
- an increase in the chloride content beyond the carbonation depth would be more significant at a cold joint thus increase the corrosion rate of reinforcing steel.
- the remaining experimental parameters would validate the corrosion rate of the reinforcing steel that was reached in the exposure period. These included the chloride penetration, carbonation depth, transport properties of gasses, moisture and ions and corrosion damages to the concrete and steel surface.

1.6. Report outline

The chapters contained in the body of this report are as follows:

- **Chapter 1** is an introduction to this study in the form of the background and justification, aim and objectives that were set out and scope and hypothesis.
- **Chapter 2** is a review of fundamentals and studies in line with the study scope with an emphasis on the direction of the stated aim.
- **Chapter 3** details the preparatory work of the test specimens, set-up of exposure conditions and test principles and methodologies.
- **Chapter 4** presents the results of the testing in the experimental programme in an analysis of the raw data for the comparisons.

- **Chapter 5** contains the conclusions of the study, which pertain to the findings of the experimental tests, and recommendations are that were made based on the test methodologies and their limitations.
- **Appendices A-E** contains the statistical parameters and plots of recorded data which are sub-divided in the same manner as Chapters 3 and 4.

2. Literature review

2.1. Overview

The fundamentals on the corrosion of reinforcing steel in concrete that were applicable to the scope of this study are presented and discussed in this chapter. The starting point of the literature review in **Section 2.2** is on the fundamentals of corrosion and factors that are influential throughout the service life of concrete structures. The damages due to corrosion are also discussed in terms of their type and occurrence, which is based on the exposure conditions and concrete quality. **Sections 2.3** and **2.5** discuss the mechanisms that either hinder or promote the penetration of chlorides and carbonation into concrete, respectively. **Section 2.4** discusses the properties of concretes with cement extenders, which improve the durability to corrosion in marine environments with chloride. Combined exposure to chloride and carbon dioxide is discussed in **Section 2.6**, which is based on the fundamentals of chloride and carbon dioxide exposure in isolation. The remaining section of the literature review (**Section 2.7**) discusses a number of methods to assess the causes of corrosion and monitor the corrosion state of reinforcing steel.

2.2. Reinforcing steel corrosion in concrete

2.2.1. The stages of corrosion

The occurrence of the corrosion of reinforcing steel and its economic influence were discussed in the background of this study in **Section 1.1**. The stages of corrosion in the service life of concrete structures and their influential factors are discussed in this section. There have been a number of conceptual models that estimate the residual service life of concrete structures based on their present condition. The corrosion degradation model was introduced in Tuutti (1982) to represent the service life of concrete structures in 2 sequential stages; initiation and propagation. The corrosion rate is negligible in the former where after it is

characterised by active conditions, based on the moisture and oxygen availability. The corrosion rate increases steadily until a predefined limit of corrosion damage in the 2-stage corrosion model, which does not include the "acceleration" stage.

The 3-stage corrosion degradation model in Heckroodt (2002) also includes the acceleration stage of corrosion, as shown in **Figure 2.1**. This model is a means of discerning the corrosion rate when it is influenced by the concrete quality until a time when there are damages in the concrete. The corrosion rate is negligible in the initiation stage (A) until agents such as chloride reach the steel in a sufficient quantity. Once this occurs, the corrosion rate is more rapid during the propagation stage (B), however, concrete quality is still influential to the transport of gasses, moisture and ions. The corrosion rate reaches the acceleration stage (C) when micro-cracks begin to form, which may increase the transport rates into concrete.

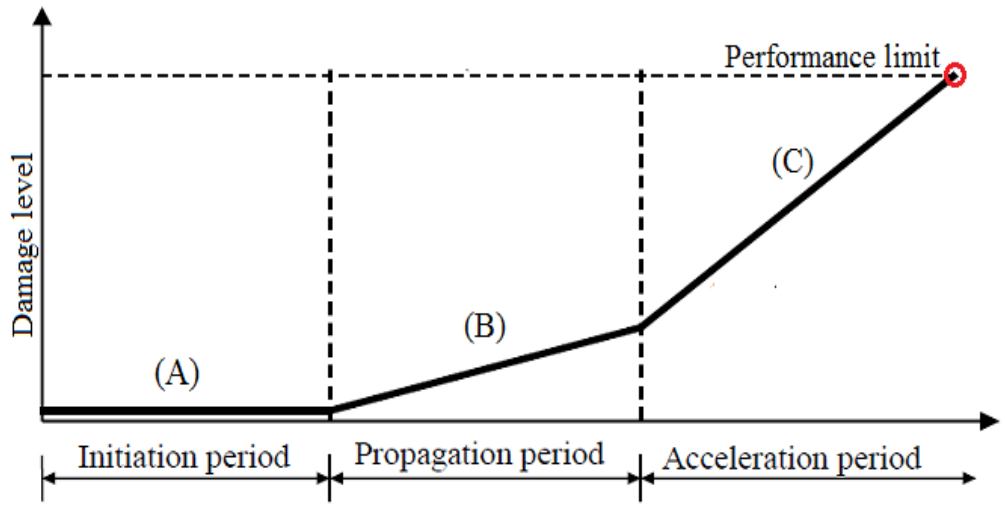

Figure 2.1: 3-stage corrosion damage model (Heckroodt, 2002)

Corrosion degradation is sub-divided based on the sequence of cracking where micro-cracks in turn develop into spalling and delamination. Crack characteristics such as crack width, orientation and connectivity are factors to the transport of gasses, moisture and ions (Alexander et al., 2009). The corrosion rate is important to the service life of structures as it relates to the loss of the steel cross-section, time to cracking in the cover concrete and bond strength to concrete (Andrade & Alonso, 1996). Cracking to any extent may thus be a degradation limit during the

service life of structures as the corrosion rate can freely accelerate into higher ranges. The Duracrete (1999) model makes use of limit states where the corrosion initiation and start of cracking relate to the serviceability, and spalling or collapse relate to safety. The corrosion initiation and propagation periods are discussed in further detail together with their influential factors in the following sections.

2.2.2. Corrosion initiation

When reinforcing steel is embedded in sound concrete, there is natural protection due to a high alkalinity and barrier effect of the cover layer. The soluble calcium, potassium and sodium oxides in the paste pores form alkaline hydroxides in the pore solution when water is present, with a high pH range of 12-13 (Broomfield, 2007). The high alkaline conditions at the steel level promote the formation of a layer of gamma ferric oxide over the steel surface (Alexander et al., 2009). Once the "passive layer" breaks down on certain areas of the steel surface, "rust" may start to appear (Broomfield, 2007). The breakdown of the passive layer is thus the initiation period, which is based on the resistance of concrete to the transport of gasses, moisture and ions. The main causes of corrosion in urban settlements are chloride penetration and carbonation, which are discussed in **Sections 2.3** and **2.5**, respectively. The combined exposure to chloride and carbon dioxide extends the principles of chloride penetration and carbonation, as discussed in **Section 2.6**.

Corrosion of reinforcing steel in concrete is an electrochemical process that is "mediated" by the formation of cathodic and anodic areas over the steel surface (Alexander et al., 2009). This takes place due to the inherent instability of metals, in their metallic form, to revert to more stable forms, i.e. oxides, hydroxides, etc. (Heckroodt, 2002). When there is a difference in the electrical potential over the steel surface, a corrosion cell may be set-up, with anodic and cathodic areas that are connected by an electrolyte, in the form of the pore solution (Neville, 2011). Any differences in the potential are due to the electrons at the anodic area, which need to be consumed elsewhere on the steel to preserve the electrical neutrality (Broomfield, 2007). The basic reactions between the anodic and cathodic areas of

a corrosion cell in concrete are expressed in **Equations 2.1** and **2.2**, respectively. These reactions are the first steps in the process of creating rust, however, this pair is "widely-quoted" for corrosion and corrosion prevention (Broomfield, 2007).

$$Fe \rightarrow Fe^{2+} + 2e^{-} \qquad \text{Eqn. 2.1}$$

$$1/2O_2 + H_2O + 2e^{-} \rightarrow 2OH^{-} \qquad \text{Eqn. 2.2}$$

The corrosion process is discussed in a number of sources such as Broomfield (2007), Neville (2011), Alexander et al., (2009), etc. When reinforcing steel in concrete corrodes, it dissolves in the pore water and gives up electrons ($2e^{-}$) at the anode in **Equation 2.1**. The electrons are required to be consumed elsewhere on the steel surface or else there is a build-up of electrons at the anode, which is the role of the cathodic reaction in **Equation 2.2**. The positively charged ferrous ions at the anode (Fe^{2+}) pass into solution while the negatively charged free electrons ($2e^{-}$) pass through the steel to the cathode. At the cathode, the negative electrons become absorbed by the electrolyte and combine with water (H_2O) and oxygen (O_2) to form hydroxyl ions ($2OH^{-}$). The remaining steps (reactions) to forming rust in the cathode reaction with oxygen and water are discussed in **Section 2.2.8**.

2.2.3. Corrosion propagation

The propagation stage of corrosion is dependent on the availability of corrosion agents at the anodes and cathodes of the corrosion cell. The corrosion rate may accelerate due to the start of cracking or instead be restricted to small magnitudes, which do not result in cracking. Some influential factors to the propagation stage of corrosion that were relevant to the scope of this study are discussed in **Sections 2.2.4** to **2.2.7**. The oxygen availability, concrete resistivity and moisture content are discussed interchangeably with reference to sustaining the corrosion rate in **Sections 2.2.4** and **2.2.6**. Of these, the moisture content is based on the exposure conditions, i.e. tidal zone, which is reflected in the exposure classes of standards. The cover depth and presence of defects, i.e. cracks or cold joints, are discussed in

Sections 2.2.5 and **Section 2.2.7**, respectively. These factors are not based on the concrete quality, however, are influential to the corrosion rate that is sustained.

Corrosion is influenced by the environmental temperature as electrochemical reactions possess the kinetic energies of reactant molecules. The corrosion rate was increased by a magnitude of 100 in Tuutti (1982) over a temperature range of -25 °C to 20 °C under carbon dioxide exposure in isolation. There are a number of studies after this that considered factors such as the moisture content of the pore solution and reported a varying influence on the corrosion rate. A recent study, Zivica (2002), reported an increase in the corrosion rate until a temperature of 40 °C, which progressed at a relatively constant magnitude thereafter. This restriction of the corrosion rate at temperatures of above 40 °C was due to the limited oxygen availability in the pore solution, which is necessary for the cathodic reaction.

2.2.4. Moisture and oxygen availability

Once the passive layer of reinforcing steel in concrete is "destroyed", corrosion will occur only if water and oxygen are present at the steel level (Bertolini et al., 2013). The concrete resistivity is a function of the moisture content of concrete, in that drying would "halt" the corrosion rate, which, however, can "re-start" upon wetting (Neville, 2011). Without dissolved oxygen in the pore solution, corrosion cannot progress to "completion" and becomes "stifled" (Alexander et al., 2009). The corrosion rate decreases in dry or saturated concrete whereas at intermediate moisture contents, there is sufficient oxygen and an electrolyte (DuraCrete, 1998). Concrete that is constantly submerged is less susceptible to corrosion compared to wetting and drying, due to the lower oxygen availability (Alexander et al., 2009).

The influence of relative humidity on the corrosion rate was determined in Tuutti (1982) in concretes that were carbonated or contained admixed chloride. There was a reduction of the corrosion rate when the relative humidity decreased below 85 % as there was less moisture in the concretes. The corrosion rates were highest when the relative humidity fell within a range of 90-95 % and then decreased at a

relative humidity of 100 %. The oxygen diffusion coefficient of the concretes in Bentur et al., (1997) was decreased abruptly when the relative humidity was close to the saturation value, of 100 %. Without the presence of moisture, the concrete quality and cover depth are influential to the oxygen availability at the steel level. The dispersion of moisture in the elements of concrete structures thus results in different types of corrosion of reinforcing steel, as discussed in **Section 2.2.9**.

2.2.5. Concrete cover depth

The overall resistance of cover concrete to the transport of gasses, moisture and ions is based on the concrete quality and cover depth. A balance between these is determined during the design phase of concrete structures using economic and practical considerations (Alexander et al., 2008). The cover region of concrete is regarded as a "transition zone", with properties being inferior to those in the bulk, particularly at the exposed surface (Alexander & Mindess, 2005). Larger cover depths impose a larger path for the transport of gasses, moisture and ions, thus are specified to decrease the corrosion rate. An increase in the concrete quality for a given cover depth may be necessary if there are restrictions on the cover depth.

The influence of the cover depth on the oxygen permeability of concrete in Bentur et al., (1997) was increased due to the relative humidity. The oxygen diffusion coefficient of the concretes was decreased at a faster rate due to an increase in the relative humidity from 60 % to 80 %. With a cover depth of 60 mm and relative humidity of 60 %, the oxygen diffusion coefficient of the concretes was decreased to nothing (0). With an increase in the relative humidity from 60 % to 80 %, the oxygen diffusion coefficient was decreased to nothing (0) at cover depths of 30-40 mm. The corrosion rate has been influenced by the cover depth regardless of the moisture content and presence of defects in cover concrete. The corrosion rate was decreased with an increase in the cover depth in un-cracked and cracked concretes in studies such as Paul (2015), Scott & Alexander (2007), Otieno (2014), etc.

2.2.6. Concrete resistivity

Corrosion is an electrochemical process thus the electrical resistivity is influential to the corrosion rate, since the ionic current must pass for the corrosion to occur (Alexander et al., 2009). Concrete may also be exposed to impressed electrical activity at cables, however, it generally provides a resistance to corrosion current to or from reinforcing steel (Neville, 2011). The concrete resistivity is measured to determine the degree of saturation and more recently, the resistance to chloride penetration, as discussed in **Section 2.7.2.5**. The factors that are influential to the resistivity include the moisture content of concrete, connectivity of the paste pores and amount of ions in the pore solution (Alexander et al., 2009). Concrete quality factors such as the binder type, water: binder (W: B) ratio, etc. are thus important to the resistivity. The temperature is an influential factor to the resistivity due to the mobility of ions and rates of other chemical reactions (Polder et al., 2000).

The moisture content has been found to be more influential to the resistivity, instead of the temperature, particularly with more ions in concrete. The resistivity was increased by several orders of magnitude in Tuutti (1982) due to an increase in the relative humidity, however, the corrosion rate was not proportional to the resistivity. This trend was similar in the concretes in Hope et al., (1985) when the resistivity was measured together with the electric potential of reinforcing steel. An inverse proportional relationship was, however, reported in Alonso et al., (1988) between the corrosion rate and resistivity in a linear trend of a log of both parameters. This trend between the corrosion rate and resistivity has been reported since in a number of studies with a variation due to differences in the binder type.

Cement replacement is an influential factor to the corrosion rate due to an increase in the concrete resistivity at a given cover depth. The cover depth is influential to the corrosion rate as the oxygen availability at reinforcing steel decreases with the cover depth. Cement extenders may increase the concrete resistivity at a given cover depth thus decrease the corrosion rate compared to ordinary concrete. The corrosion rate was decreased in un-cracked and cracked concretes due to the use

of fly ash, slag or silica fume in studies such as Scott & Alexander (2007) and Otieno (2014). The corrosion rate was decreased at a given cover depth in un-cracked and cracked concretes with these materials due to an increase in their resistivity. The corrosion rate was decreased in concretes with metakaolin due to an increase in resistivity compared to ordinary concrete in Ferreira et al., (2015).

There are number of relationships between the concrete resistivity and corrosion rate, which indicate the conductivity of the pore solution to carry electrons and ions. Concrete resistivity in Kilo Ohms per centimetre (kΩ·cm) was related to the corrosion rate in Langford & Broomfield (1987). These ranges of the corrosion severity are listed with the corrosion rate in µm/year units of the cross-section of reinforcing steel in **Table 2.1**. There are other resistivity ranges in the literature with a similarity in their magnitude, which were established based on the moisture content of concrete. The relationship between the corrosion rate and resistivity in Alonso et al., (1988) was used to establish the resistivity ranges in RILEM TC 154-EMC (RILEM, 2004). This corrosion severity relationship is listed together with the resistivity testing in **Section 3.9** of the experimental programme.

Table 2.1: Relationship between the corrosion rate and concrete resistivity (Langford & Broomfield, 1987)

Corrosion severity	Concrete resistivity (kΩ·cm)	Corrosion rate (µm/Y)
Low	> 20	≤ 2
Low to moderate	10-20	2-6
Moderate to high	5-10	6-12
Very high	< 5	> 12

Whereas there is an agreement regarding the concrete resistivity ranges in the literature, the corrosion rate differs by a larger margin between the corrosion stages. The corrosion rates fall within respective ranges of up to 49 µm/Y and 99 µm/Y under a moderate-to-high and very-high corrosion severity, respectively, in Bertollini et al., (2004). The corrosion rate ranges in RILEM TC 154-EMC are based on multiple sources, such as Andrade & González (1978) and González & Andrade (1982). These ranges are generally used for concrete structures where the

cover depth and concrete quality are specified for un-cracked concrete. In cracked concrete, the corrosion rate reaches above these ranges as there is an acceleration of the corrosion process. Corrosion rates higher than 1 $\mu A/cm^2$ are seldom and values higher than 10 $\mu A/cm^2$ have almost never been measured (RILEM, 2004).

2.2.7. Concrete quality and defects

Concrete quality is the other factor to the corrosion resistance to reach a desired service life under given exposure conditions (Alexander et al., 2009). In South Africa, the "Durability Index" approach was developed to improve the quality of reinforced concrete construction (Alexander et al., 2008). This is based on the measurement of suitable transport properties of laboratory and in-situ concrete, which reflects the dual factors of the concrete quality and construction processes. The durability indices were compared to the internationally-accepted tests of the oxygen permeability, water sorptivity and chloride diffusion in Beushausen & Alexander (2008). The oxygen permeability and chloride conductivity indices were reported to have a similar merit in establishing the concrete properties to the internationally-accepted tests. The durability indices were used herein to assess the influence of cement replacement on the transport of gasses, moisture and ions.

Corrosion monitoring is an approach to determine the changes in concrete quality as a continuous response to the exposure conditions. Factors of concrete quality and exposure conditions were related to the corrosion rate and other corrosion parameters such as the corrosion potential and concrete resistivity in studies such as Scott & Alexander (2007), Otieno (2014), Paul (2015), etc. Concrete quality factors such as the W: B ratio and binder type may be determined over the course of exposure. The monitoring of corrosion potential found that an increase in the W: B ratio resulted in an earlier drop into the range of active corrosion in Islam & Sugiyama (2010). The corrosion rate was thus increased due to a shorter initiation time and the specimens with a larger cover depth did not corrode within a period of 1 year. A change in the W: B ratio was more influential to the corrosion rate that could be reached instead of the binder content in Mangat et al., (1994).

If defects are present in concrete, the resistance to gasses, moisture and ions is not influenced only by the concrete quality. The defect of interest to this study was a cold joint as it spans the entire section of concrete elements whereas other defects from the construction process form at the surface only. A cold joint resulted in an increase in the corrosion rate under isolated exposure to either chloride or carbon dioxide in Miyazato & Otsuki (2010). The corrosion rate was increased by several orders of magnitude at the cold joint compared to the surrounding concrete, away from the cold joint. A cold joint also resulted in an increase in the corrosion rate in Roxas & Lejano (2018) in ordinary and fly ash concretes that were exposed to either fresh or sea water. The corrosion rate was increased in the specimens with a cold joint compared to separate specimens that were monolithically-cast (plain).

Cracks that are formed in the process of construction or induced by corrosion may increase the corrosion rate that is sustained for a given concrete quality. Studies such as Scott & Alexander (2007) and Otieno (2014) found an increase in the corrosion rate due to an increase in the width of cracks that were present from the introduction of the exposure period. An increase in the crack width and spacing of multiple cracks in Paul (2015) also resulted in an increase in the corrosion rate throughout the exposure period. The cracking herein was corrosion-induced, thus not created before the exposure, which is a result of a reduction of the corrosion initiation time and acceleration of the corrosion rate thereafter in the propagation stage. The occurrence of cracking is a thus means of assessing the influence of corrosion factors on the extent of cracking, not only the corrosion initiation time.

2.2.8. Manifestation of corrosion

Corrosion manifests in 2 primary forms; (1) a reduction of the cross-section of steel at the anode, reducing its load-carrying capacity, and (2) cracking, spalling and delamination of cover concrete due to the expanding corrosion products at the cathode (Neville, 2011). Corrosion damages involve a number of factors that are connected with the condition of a concrete structure, such as “esthetic appearance, serviceability, safety and structural performance” (Bertolini et al., 2013). The rust

stains that are initially visible on a concrete surface are "often the first signs" of corrosion at greater depths (Alexander et al., 2009). There are several stages that take place for the parent steel to be converted into rust, which are expressed in the sequential reactions in **Equations 2.3** to **2.5**. These extend the basic reactions in **Section 2.2.2** in the sources that describe the rust formation from the parent steel.

$$Fe^{2+} + 2OH^{-} \rightarrow Fe(OH)_2 \qquad \text{Eqn. 2.3}$$

$$Fe(OH)_2 + O_2 + 2H_20 \rightarrow 4Fe(OH)_3 \qquad \text{Eqn. 2.4}$$

$$2Fe(OH)_3 \rightarrow Fe_2O_3 \cdot H_2O + 2H_2O\ (\text{Rust}) \qquad \text{Eqn. 2.5}$$

There would be no cracking due to the expansive corrosion products if the soluble ferrous ions (or Fe^{2+}) were only to dissolve in the pore solution. The ferrous ions combine with the hydroxyl ions to form ferrous hydroxide ($Fe(OH)_2$) in **Equation 2.3**, then ferric hydroxide ($4Fe(OH)_3$) in **Equation 2.4** and finally, hydrated ferric oxide (rust) in **Equation 2.5**. The relative volumes of iron and its oxides in the corrosion reactions from Mansfield (1981) are presented in a scaled plot in **Figure 2.2**. The plot scale is based on the magnitudes of the volumes of these ions in the cathode reaction, from 1, the parent steel (Fe), until 7, the expansive rust product. Un-hydrated ferric oxide (Fe_2O_3) has a volume of about twice that of the parent steel when it is "fully dense" and it swells even more and becomes porous when hydrated, such that the volume of rust over 6 times the parent steel (Broomfield, 2007). In general, the volume of rust is a mixture of the various oxides and can be considered to be 3-4 times the volume of the parent steel (Bertolini et al., 2013).

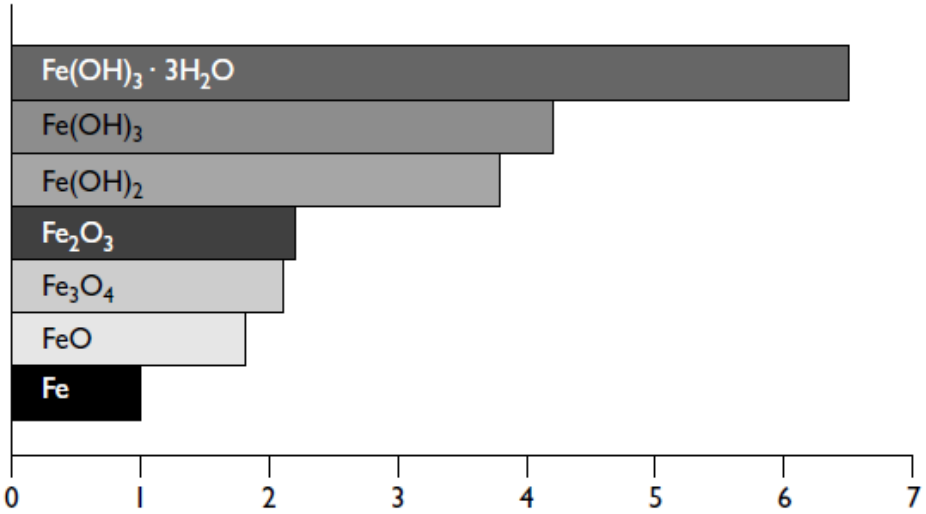

Figure 2.2: Relative volume of iron and its oxides (Mansfield, 1981)

2.2.9. Types of corrosion

The corrosion type is based on the manner in which the steel is degraded and this varies due to the concrete quality and exposure conditions. Concrete structures may be exposed to various conditions, i.e. submerged, tidal or atmospheric, which is influential to the corrosion type and its distribution. The anodic and cathodic areas of corrosion cells are separated in the pore solution by an adequate drop of the alkalinity (pH) and oxygen availability at the steel surface. Chloride penetrates in a localised manner where small areas of steel may be subjected to a significant reduction of pH (Bertolini et al., 2013). This may be more prominent at defects and where there is an increase in the moisture content, i.e. pooling, to distribute the chlorides in concrete. Carbonation generally progresses in all exposed areas thus the pH reduction may be "expected over a relatively large area" (Paul, 2015).

Concrete is generally dryer for carbonation to take place thus the corrosion tends to be on a "microcell" level with "apparently continuous corrosion" of reinforcing steel (Broomfield, 2007). With this type of corrosion, the anodic and cathodic areas on the surface of reinforcing steel are adjacent to each other (Otieno, 2014). It is impossible for the conditions of uniform corrosion to form over the entire surface of reinforcement due to the heterogeneity of concrete (Paul, 2015). The cathodic reaction in areas is stronger than the anodic reaction while at other areas,

the anodic reaction may be faster (Broomfield, 2007). A particularly destructive form of "pitting" corrosion may occur the geometric relationship is favourable between the anodic and cathodic areas (Alexander et al., 2009). The corrosion cells are formed with anodic dissolution in a pit while the remaining areas may be cathodes where the rust is deposited. This occurs in concrete with chloride as an increase in the ion content poses a risk to corrosion in terms of the low electrical resistivity (Bertolini, et al., 2013). The steel is corroded at a faster rate than due to carbonation thus factors are used to increase the corrosion rate (RILEM, 2004).

2.3. Chloride-induced corrosion

2.3.1. Exposure to chlorides

Chloride becomes present in concrete either in the casting stage or due to the subsequent ingress of chloride from the environment. The contribution to chloride in the casting stage is deliberate or by impurities whereas external chlorides are found in marine zones or in de-icing salts, etc. (Broomfield, 2007). The exposure conditions herein were based on the ingress of chloride from an external source, which was at the sea level, where there is cyclic wetting. Structures in marine zones are exposed to airborne chlorides, further inland, or by direct contact at the sea level. The fundamentals of isolated exposure to chloride and carbon dioxide are discussed in this section and the next as a background to combined exposure.

The exposure classes in standards reflect the severity of corrosion in the marine zone in terms of a structure's locality and fluctuation of moisture. The exposure conditions in Britain were classified in BS EN 206-1 (BS-EN, 2000) and modified for the South African standards (Alexander, et al., 2009). Direct contact with the sea increases the moisture content in concrete, which is a high risk to corrosion as there is a reduction of the concrete resistivity. Cyclic wetting and drying creates a continuous movement of chloride in the concrete pores which accelerates their penetration (Hong & Hooton, 1999). The saline atmosphere of marine zones may also lead to chloride penetration as there is still a cyclic action of the moisture.

2.3.2. Chloride penetration in concrete

Chloride penetration from the environment creates a chloride profile which is characterised by a reduction of the chloride content from the concrete surface to the greater depths (Bertolini et al., 2013). The factors that are influential to the distribution of chloride in concrete are determined such as the exposure conditions and presence of cracks or a cold joint. The influence of the exposure conditions on chloride penetration for different structures is illustrated in the chloride profiles up to cover depths of 45 mm and 250 mm in **Figure 2.3**. The resistance to chloride penetration is shown in (a) where the chloride content decreased from the surface to the end of the profile range, at a depth of 45 mm. The influence of the exposure conditions is shown in (b) where the chloride content increased at the opposite side of the specimen, at a depth of 250 mm. The erratic distribution of chlorides in the 250 mm-thick concrete slab (b) was due to the exposure at the opposite side.

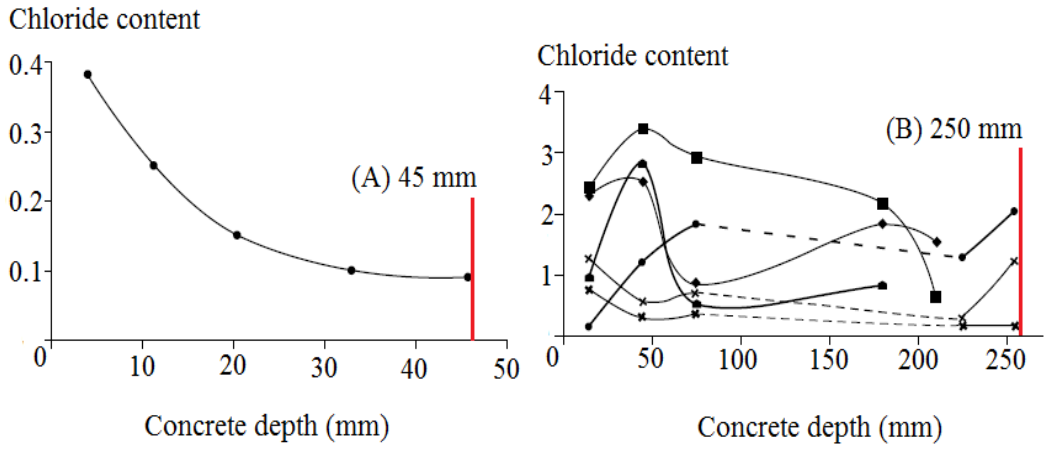

Figure 2.3: Chloride profiles in a bridge deck and car park (Broomfield, 2007)

Defects influence a chloride profile by increasing the chloride content to be resisted over the same depth of cover concrete. The chloride penetration depth was increased at a cold joint between existing concrete and high-performance concrete in Farzad et al., (2019). The cracks that were created before the exposure in Paul (2015) increased the chloride content at the concrete surface compared to un-cracked concrete. There was also an increase in the chloride content at the surface on the other side of the specimens as the exposure was performed on both

sides. The chloride diffusion rate of the specimens in Sung-Won & Seung-Jun, (2016) was increased by a maximum of 20 % due a cold joint in the direction of exposure. The presence of loading-induced cracks in these specimens further increased the chloride diffusion rate, on top of that caused by the cold joint only.

2.3.3. Chloride transport mechanisms

Pure diffusion of chloride only occurs in saturated concrete thus in most cases there are other mechanisms that are influential to chloride transport (Bertolini, et al., 2013). These mechanisms have been found to influence the conditions of pure diffusion, particularly within the surface region of concrete, where there is a fluctuation of moisture. Moisture is absorbed in dry concrete by capillary suction and then carried to greater depths by capillary movement, to where pure diffusion occurs (Broomfield, 2007). The equations of pure diffusion are discussed in a number of sources such as Bertolini et al., (2013), Broomfield (2007) and Neville (2011). These are discussed first in this section to aid the interpretation of chloride diffusion, as a background to other mechanisms that influence chloride transport.

Chloride diffusion is not stationary thus approximated using Fick's 2nd law which describes the kinetics of non-stationary behaviour. The general form in **Equation 2.6** is a starting point in predictions even though a continuous medium of moisture is not strictly correct. This is a first-type boundary problem where the differential is integrated under 2 boundary conditions to determine the diffusion coefficient. The solution in **Equation 2.7** is based on the conditions of no chloride prior to the exposure and the same chloride content in the concrete volume after some time. Gauss' error-function in **Equation 2.8** (denoted as erf) was used in the differential solution of the previous equation where the function argument is regarded as real.

$$\frac{dC}{dt} = D\frac{d^2C}{dx^2} \qquad \text{Eqn. 2.6}$$

where:

- D (m^2/S) denotes the apparent diffusion coefficient,
- dC/dt denotes the change in the chloride content with time and

- dC/dx denotes the change in the chloride content with depth.

$$C_{x,t} = C_S[1 - \mathrm{erf}\left(\frac{x}{2\sqrt{Dt}}\right)] \quad \text{Eqn. 2.7}$$

where:

- $C_{x,t}$ denotes the chloride content at the depth x after an exposure duration t,
- Cs denotes the surface chloride content,
- D denotes the diffusion coefficient,
- x denotes the sampling depth and
- t denotes the duration of exposure.

$$\mathrm{erf}() = \frac{2}{\sqrt{\pi}}\int_0^x e^{-t^2}\,dt \quad \text{Eqn. 2.8}$$

The existing models in the literature on chloride penetration to initiate corrosion are mostly based on Fick's 2nd law of diffusion. The chloride diffusion coefficient is tested to characterise the concrete resistance using the internally-accepted test methods such as AASHTO T277, NT BUILD 492 and ASTM C 1202. The short-term tests on steady-state diffusion are not relevant in practice due to the different transport mechanisms that occur in an environment (Bertolini et al., 2013). The evolution of a chloride profile into concrete may be determined using **Equation 2.7**, which is a function of the diffusion coefficient and surface chloride content. The chloride content at any depth within the profile range may be determined at any time during the service life, i.e. at the steel level when corrosion has initiated.

The corrosion initiation time has been predicted using a threshold chloride content at the steel level using the differential solution in **Equation 2.7**. The corrosion initiation times of various concretes were calculated from the differential solution for cover depths of up to 100 mm in **Figure 2.4**. The chloride profiles in part (a) were calculated from the diffusion coefficients, which fell within a range of 10^{-11} to 10^{-13} m^2/S. The concrete in (b), with the smallest diffusion coefficient of 10^{-13}, (in red) had an initiation time of ten times larger as there was no chloride after a

depth of 20 mm. There was also a similar trend between the diffusion coefficients and chloride profiles in the concretes in Safehiana & Ramezanianpour (2015).

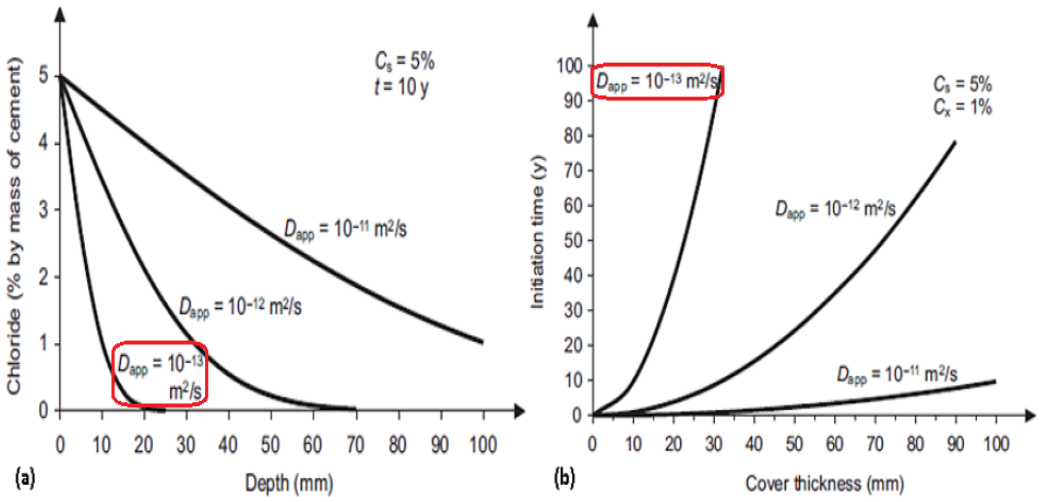

Figure 2.4: Influence of the diffusion coefficient and cover depth on chloride penetration (Bertolini et al., 2013)

The assumptions to solving Fick's 2nd law do not consider the conditions of the surface region, where there is a fluctuation of moisture under cyclic exposure. These equations are ideal, in that they are based on a constant chloride content with time, which is not a reality, due to the fluctuation of moisture. Any deviation from these conditions is due to the intermittent contact of chloride when moisture enters and leaves an exposed surface. The moisture that transports the dissolved chloride into and out of the surface under cyclic exposure prevents the conditions of pure diffusion (Hunkeler, 2005). This occurs in the "convection zone", which is shown in A of **Figure 2.5**, where after diffusion is the primary mechanism, in B.

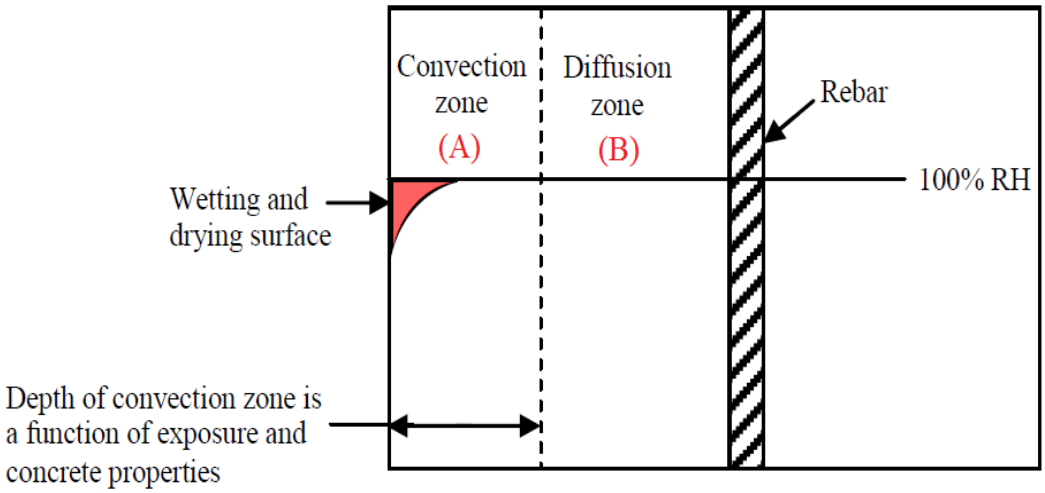

Figure 2.5: Convection zone in concrete (LIFE-365, 2005)

The chloride contents in the convection zone of concrete may be neglected to not influence the conditions of pure diffusion. An alternative solution to Fick's 2nd law of diffusion was introduced in Gehlen (2000), which excludes the chloride contents of the convection zone. A starting point to solve the differential equation is after the convection zone, with the assumption of a constant chloride content in the bulk concrete. A chloride profile is altered by excluding the convection zone, which obtains the trend of a decrease in the chloride content from the surface to greater depths. Defects such as cracking or cold joints would further influence the conditions of diffusion as these are highly-influential to absorption of moisture.

Another factor that influences the assumptions of Fick's 2nd law is the on-going mechanisms that decrease the pore sizes of paste (Alexander et al., 2009). A chloride diffusion coefficient that is time-dependent considers a decreased rate of diffusion due to hydration and contamination of the paste pores. The apparent diffusion coefficient is used to calculate the chloride contents in a chloride profile that is time-dependent. The diffusion coefficient after any duration of exposure may be related to a reference value, i.e. after 28 days of curing, using an "aging factor". This factor is specific to the concrete quality and has not been established although some values have been reported, such as in Mangat & Molloy (1994).

2.3.4. Chloride binding

Chloride in concrete comprises of the free (soluble) chloride, which is dissolved in the pore solution and that chemically-bound to paste (Bertolini et al., 2013). Either the total or free chloride fraction is used to establish a chloride profile thus the ability to bind chlorides may be determined. Chloride binding is important to retain the free chlorides within the surface region of concrete so that they may not diffuse to the steel in the pore solution. Concrete may bind to chloride physically by adsorption onto the pore surfaces of paste and chemically with the hydrates, which forms chloro-aluminates (Broomfield, 2007). The tri-calcium aluminate (C_3A) and tetra-calcium alumina ferrite (C_4AF) hydrates can chemically bind to free chloride (Montemor et al., 2003). The mechanism of chloride binding also influences the assumptions of Fick's 2nd law, by retarding the chloride diffusion.

It was previously believed that only the free chloride fraction may diffuse to the steel level while that adsorbed to the CSH or bound as tri-calcium aluminate does not (Bertolini et al., 2013). This initial understanding of chloride binding was challenged in Glass & Buenfeld (1997) where the bound chloride was found to be released thus be able to diffuse to greater depths. The release of bound chloride into the pore solution occurred when the pH of the pore solution decreased to a value of below 12. The chloride binding mechanism in Glass & Buenfeld (2000) was investigated using different cements, with C_3A proportions of 14 %, 8 % and 2 %. The chloride content was decreased at greater depths in the concretes with a higher C_3A content, even i there was a higher chloride content at the surface.

The influence of cement extenders on chloride binding is based on their reactivity to decrease the pore sizes of paste and alumina content. There are a number of studies on the chloride resistance of common cement extenders in the literature that are based on chloride profiling. There was a difference in the binding capacity of concretes with cement extenders from measuring the free and total chloride contents in Glass et al., (1997). The free chloride content in the slag concrete was 50 % lower than the ordinary concrete as the slag contained the highest alumina

content of the binders. The free chloride content in the fly ash concrete was 9 % lower than the ordinary concrete as the alumina content in the fly ash was lower than the slag. The fly ashes in the literature have yielded an indifferent resistance to chloride due to a variation of their composition and physical characteristics.

Fly ash was found to decrease the resistance to chloride in binary blends with replacement levels of 15 % and 30 % in Liu et al., (2014). There were higher chloride contents in the fly ash concretes in a sampling depth of 3 mm compared to ordinary concrete. This increase in the chloride content at the surface of the fly ash concretes was due to starting the exposure on completion of the de-moulding. The chloride exposure in Liu et al., (2020) was started after 90 days of curing, which resulted in lower free chloride contents in the fly ash concretes than the ordinary concrete. The free chloride content was lower in the fly ash concretes up to a sampling depth of 15 mm with both replacement levels of 15 % and 30 %.

Metakaolin has been found to generally to yield a higher resistance to chloride penetration than ordinary concrete due to its high reactivity and composition. Chloride profiles up to a depth of 40 mm were used for estimating the diffusion coefficients after 90 days of exposure in Ferreira et al., (2015). The diffusion coefficient was decreased by up to 75 % in the concretes with binary blends of metakaolin and ternary blends with metakaolin and fly ash. The chloride contents of the profiles in Bai et al., (2003) were decreased in the concretes with ternary blends of fly ash and metakaolin after 180 days exposure. There was a similar trend of a reduction of the chloride content in the profiles in Bakera & Alexander (2019) in concretes with binary blends of metakaolin after 90 days of exposure.

The corrosion initiation time of concretes with cement extenders has thus been found to be greater in studies based on chloride penetration. The initiation time in Tarek et al., (2002) was respectively 3 and 6.8 times larger in the fly ash and slag concretes at a cover depth of 70 mm. The fly ash and slag increased the corrosion initiation time in Mackechnie (1996) by a similar margin of 7-8 times at a cover depth of 60 mm. The prediction model that was established in Mackechnie (2001)

was based on these findings and pertains to marine environments in South Africa. Other service life prediction models for marine environments such as DuraCrete and LIFE 365 are used in Europe and North American countries, respectively.

2.3.5. Chloride threshold

The chloride content at the steel surface that is required to induce corrosion is important to the durability, due to the rapid degradation that follows. The chloride threshold is based on a number of interrelated factors such as the properties at the steel surface and pore solution of concrete (Bertolini et al., 2013). The chloride threshold has been found over a broad range with an increase in the magnitude, depending on exposure conditions and concrete quality (Domone & Illston, 2010). Chlorides that are contributed during the mixing stage may pose an earlier risk to corrosion as these are already at the steel surface. The impurity levels of binders are thus limited in a number of standards, i.e. 0.1 % chloride by mass in SANS 50197-1. In the Middle East, the use of sea water for mixing water until the 1970s was found to be an "expensive error for the next 20 years" (Broomfield, 2007).

There are several means to express the chloride threshold; the total, bound or free chloride contents and chloride: hydroxyl ion ($[CL^-]/ [OH^-]$) ratio. The chloride threshold was initially investigated in Hausmann (1967) as the [CL-]/ [OH-] ratio where the corrosion initiation was regarded to occur at a theoretical value of 0.6. A $[CL^-]/ [OH^-]$ ratio of 0.6 was found to equate to a chloride content of 0.4 % by mass in the concrete, when the chloride was added in the mixing, and 0.2 % by mass from external diffusion. The chloride threshold in the British Standard (BS EN 206) is limited to 0.2 % and 0.1 % in ordinary and pre-stressed concretes, respectively. There was no intention to determine a chloride threshold at the time of corrosion initiation herein as the sampling was performed after the exposure.

Voids in concrete are influential to the durability as chemical compounds may be retained, which causes a reduction of the pore solution alkalinity. A cold joint may present a plane of weakness to the steel level with an increase in pore sizes

and total porosity compared to the surrounding concrete. The total porosity was influential to the chloride threshold in concretes with fly ash and slag in Glass & Buenfeld (2000). The chloride thresholds followed the same trend over a range of porosities, in that the higher thresholds corresponded to the lower total porosities. The fly ash and slag yielded higher porosities than the ordinary concrete whereas plasticiser in the ordinary concrete yielded the largest reduction of the porosity.

Corrosion monitoring is an approach of determining a chloride threshold instead of using the chloride content at an exposed surface or diffusion coefficient. This indicates an exact point in time when to sample concrete until the steel surface, where the chlorides present are that which induce corrosion. The reliability of the threshold in this approach is based on the accuracy of the corrosion monitoring to detect the corrosion initiation. Corrosion monitoring has been used to obtain a threshold value in studies such as Islam & Sugiyama (2010) and Horiguch et al., (2020). The corrosion potential entered the range of active corrosion when the thresholds were determined by obtaining the chloride content at the steel surface.

The exposure conditions are also influential to the chloride threshold due to the requirement of moisture and oxygen in the corrosion reactions. The influence of the exposure conditions on the chloride threshold was investigated in DuraCrete (2000) under constant submergence or cyclic wetting. The chloride thresholds under cyclic wetting fell within a range of 31-39 % of that under the submergence as there was more oxygen for the corrosion. The Committee Euro-International du Beton established a relationship in CEB (1989) between the chloride threshold and relative humidity. The thresholds were higher in the concretes under constant dry or saturated conditions and then reduced under a moderate relative humidity.

The compositions of cement extenders tend to decrease the threshold due to a lower calcium oxide content compared to Portland cement. These materials are based on silica and alumina thus yield a lower alkalinity even through the chloride binding is enhanced. The thresholds of concretes with binary and ternary blends of slag, fly ash and silica fume in Scott (2004) reflects the composition differences

in simulated pore solutions. The concretes that were ideal comprised of 25 % slag and 30 % fly ash where after higher replacement levels had less calcium oxide and lower thresholds. The thresholds in Ann & Song (2007) were reduced in concretes that contained 35 % fly ash or 65 % slag in terms of the $[Cl^-]$: $[OH^-]$ ion ratio.

2.4. Cement extenders and their influence on corrosion

2.4.1. Overview

The influence of cement extenders on corrosion, chloride penetration and carbonation is discussed throughout the literature review. Cement extenders have been found to primary increase the durability of reinforced concrete with respect to chloride-induced corrosion. This section follows chloride-induced corrosion section to discuss the characteristics of cement extenders and their influence on the pore sizes and total porosity of the paste in concrete. BS-EN 206 (BS-EN, 2000) specifies 2 broad divisions of cement extenders; almost inert, which acts as a "filler", and pozzolanic cement extenders. Pozzolanic materials do not possess "binding properties" in themselves, but obtain them in the presence of calcium hydroxide, which forms hydration products similar to Portland cement (Bertolini et al., 2013). The pozzolanic reaction is secondary to cement hydration, which has led to the name of "latent hydraulic" materials (Domone & Illston, 2010).

The natural pozzolanic materials "most commonly met with" are volcanic ash (pumicite), opaline, shales and cherts, calcined diatomaceous earth and burnt clay (Neville, 2011). The artificial pozzolanic materials "in use worldwide" are fly ash, ground granulated blast-furnace slag, condensed silica fume, calcined clay or shale and rice husk ash (Domone & Illston, 2010). The characteristics of common artificial pozzolanic cement extenders are discussed in this section to highlight their influence on the paste's microstructure. When a pozzolanic material is used with Portland cement in concrete, calcium silicate hydrate (CSH) is produced from the calcium hydroxide (CH) of the cement hydration, silica (S) and water (H), as expressed in **Equation 2.6**. Cement extenders contain greater quantities of

silica than Portland cement, “but crucially”, most of this is in an active amorphous form that is necessary for the “pozzolanic action” (Domone & Illston, 2010).

$$S+CH+H \rightarrow CSH \qquad \text{Eqn. 2.9}$$

2.4.2. Fly ash

Fly ash, aka “pulverised fuel ash”, is the ash from the pulverised coal in power stations, collected from the exhaust gasses before being discharged to atmosphere (Domone & Illston, 2010). Fly ash particles are spherical and have a “very high fineness”; the vast majority of the particles have a diameter between less than 1 μm and 100 μm (Neville, 2011). The composition of fly ash depends on the coal it is derived from; the most common type of pulverised fuel ash is mainly siliceous (Bertolini et al., 2013). Two types of fly ash are typically used, high- and low-lime, the latter being the most commonly available in many countries (Domone & Illston, 2010). The composition of fly ash in South Africa is based on silica and alumina, and includes a fraction of calcium oxide of below 10 % (Alexander et al., 2009). The alumina in fly ash, slag and metakaolin is also in an active form, and becomes involved in the pozzolanic reactions (Domone & Illston, 2010).

There are a number of studies on the influence of fly ash on the microstructure of concrete due to the contribution from the pozzolanic reaction. There were larger proportions of the smaller pores in the pore size distributions (PSD) in Meddah & Tagnit-Hamou (2009) in the concretes with fly ash or silica fume. The pore sizes were decreased at faster rates in curing periods of 1-3 and 3-7 days than thereafter as cement hydration is faster in the initial stages. The influence of fly ash on the pore sizes in Liu et al., (2014) was determined using the PSDs over curing ages of greater than 90 days. The proportions of smaller pore sizes in the fly ash concretes were larger than the ordinary concrete between the curing periods of 90 and 180 days. There was a similar trend of larger proportions of the smaller pore sizes in the concretes with fly ash in Liu et al., (2020) beyond a curing period of 90 days.

The influence of porosity on the transport of gasses, moisture and ions "cannot be explained simply" by the porosity alone, the connectivity of pores also has to be taken into account (Bertolini et al., 2013). The pore sizes of concretes with cement extenders may be decreased, as the particle sizes of these materials are smaller, although with an increase in the total porosity. The connectivity of pores in these concretes may thus be decreased, which would decrease the transport of gasses, moisture and ions. The concretes with fly ash in Zeng et al., (2012) were reported to have larger proportions of the smaller pore sizes although with an increase in the total porosity. The total porosity was higher at curing ages of up to 28 days in the fly ash concretes although with an increase in the proportions of the smaller pore sizes. After 90 days of curing, however, the fly ash yielded a reduction of the porosity together with an increase in the proportions of the smaller pore sizes.

2.4.3. Metakaolin

Metakaolin is a pozzolanic material that has a faster rate of pozzolanic reaction compared to fly ash and slag (Domone & Illston, 2010). The manufacturing process of metakaolin is discussed in a number of sources such as Neville (2011) and Siddique (2008) where kaolin clay is the raw material. Metakaolin is obtained by calcination of pure or refined kaolinitic clay within a temperature range of 650-850 °C (Neville, 2011). The change that takes place is de-hydroxylation, which is brought on by the application of heat over a defined period of time (Siddique, 2008). Clay minerals loose most of their adsorbed water at "just above 100 °C" while kaolinite loses its water due to de-hydroxylation within a temperature range of 500-800 °C. Beyond the temperature of de-hydroxylation, kaolinite retains two-dimensional order in the crystal structure and the product is termed "metakaolin". Metakaolin characteristics are specified in ASTM C 618 and EN 197-1 although not with cement extenders such as fly ash, slag and silica fume in South Africa.

A number of studies have found enhancements to the microstructure of concrete with metakaolin due to the high reactivity and composition. A reduction of the pore sizes and total porosity in concretes with metakaolin was not always found in

these studies, however, there was an overall trend of an increase in resistance to chloride penetration. This was due to 2 reasons, the alumina content of metakaolin and its high reactivity compared to fly ash and slag, which have a slower rate of pozzolanic reaction. The proportions of the smaller pore sizes in the metakaolin concretes were larger than the ordinary concrete after 3 days of curing in Khatib & Wild (1996). The total porosities of the metakaolin concretes were, however, larger throughout the majority of the curing periods, from 3 until 90 days. There was also an increase in the proportions of the smaller pore sizes in concretes with metakaolin in Ferreira et al., (2015) together with an increase in total porosity.

Of the earlier research on metakaolin, Cabrera & Nwaubani (1998) reported a reduction of the chloride diffusion rate in paste with metakaolin after 60 days of curing. The pore sizes and total porosity of the metakaolin pastes were smaller than the fly ash pastes, however, these changes were less than the reduction of the chloride diffusion rate. Metakaolin has also been found to decrease the chloride diffusion rate in concretes that were based on ternary blends with other pozzolanic materials that are less reactive. The metakaolin in Nwaubani et al., (2003) resulted in a reduction of the chloride diffusion rate in concretes with silica fume or arc furnace slag. The concretes with ternary blends of fly ash and metakaolin resulted in lower chloride diffusion rates than binary blends of metakaolin in Ferreira et al., (2015). Ternary blends were not included in the scope herein as the focus was placed on the corrosion resistance based on the characteristics of each material. Metakaolin has also shown to be a suitable cement extender in South Africa in Bakera & Alexander (2017) due to a reduction of the chloride conductivity index.

2.4.4. Ground granulated blast-furnace slag

Ground granulated blast-furnace slag (GGBS) is the “scum” formed in the process of iron smelting in a blast furnace, which is rapidly cooled in water and ground to a “similar fineness” to Portland cement (Domone & Illston, 2010). If this scum is cooled gradually it takes on a crystalline form which is not sufficiently reactive in concrete and assumes a reactive, glassy state if the cooling is rapid (Alexander et

al., 2009). Unlike pozzolanic materials, which hydrate only in the presence of calcium hydroxide, GGBS has latent hydraulic characteristics thus might be used as a hydraulic binder (Bertolini et al., 2013). The composition of GGBS in South Africa includes up to 37 % of calcium oxide and a similar proportion of silica dioxide to fly ash, of up to 40 % (Alexander et al., 2009). The hydration process of GGBS is slower than Portland cement, however, it "refines" the pore structure of paste when it replaces certain proportion of the cement (Bertolini et al., 2013).

The properties of the paste's microstructure, i.e. pore sizes and total porosity, with GGBS and silica fume are not elaborated on using various studies as the focus is placed on fly ash and metakaolin. The composition and physical characteristics of GGBS and silica fume are discussed as these materials are commonly used in a number of standards. The inclusion of GGBS and silica fume has also increased the concrete durability to chloride-induced corrosion due to their composition and physical characteristics. Fly ash and metakaolin were used herein to compare the concrete durability in terms of chloride penetration, carbonation and corrosion.

2.4.5. Condensed silica fume

Condensed silica fume is the "extremely fine particles" of silica condensed from waste gasses of the manufacturing process of silicon metal (Domone & Illston, 2010). The oxide composition of silica fume in South Africa is based mainly on silica dioxide, up to 96 %, together with trace compounds, such as calcium and aluminium oxides (Alexander et al., 2009). The largest use of this material is producing concrete with enhanced properties, such as low permeability, due the fineness of the particles (Neville, 2011). The average particle diameter is "about 100 times" smaller than Portland cement thus may yield a very low porosity in paste (Bertolini et al., 2013). The fine particles have the ability to be located in a close proximity to aggregates, a "known source of weakness" (Neville, 2011).

2.5. Carbonation-induced corrosion

2.5.1. Exposure to carbon dioxide

Carbonation of concrete is the interaction between gaseous carbon dioxide and alkaline hydroxides in the pore solution, in the presence of moisture (Broomfield, 2007). Even minor carbon dioxide contents in the atmosphere of rural regions can cause carbonation whereas that of highly-urbanised areas averages 0.3 %, and can reach 1 % (Neville, 2011). The exposure conditions of interest to this study were urbanised, at the tidal level of a marine zone, i.e. harbours, which creates a cyclic exposure of moisture. Carbonation is facilitated by the air-filled pores and may be up to 4 orders of magnitude slower in pores that are filled by moisture (Bertolini et al., 2013). An increase in the carbonation depth imposes a larger corrosion risk to reinforcing steel when there is also chloride built-up at the exposed surface.

Carbonation occurs progressively into concrete at a decreasing rate with its depth as the carbon dioxide diffuses through the carbonated pores (Neville, 2011). As with chloride penetration under cyclic exposure to moisture, the wetting time and frequency are factors to the carbonation rate. Frequent periods of wetting are thus likely to increase the carbonation rate as there is continuous drying of the pores and moisture for the reaction. Under equilibrium conditions with the environment the carbonation rate was found to be highest if the relative humidity falls within a range of 40-60 % (Alexander et al., 2009). There are a number of studies on the influence of relative humidity on the carbonation rate, which found similar ranges.

The carbon dioxide content is important to the carbonation rate thus accelerated methods of carbonation have been used in a laboratory setting. These methods can achieve many years of natural exposure due to an increase in the carbon dioxide content and a suitable relative humidity. An increase in the carbon dioxide content from 5 % to 20 % over a period of 120 days caused an increase in the carbonation depth by 39-143 % in Zhiguon & Ri, (2013). Though the carbonation depth was increased at a carbon dioxide content of 20 %, the trends did not obey Fick's law

of diffusion. The carbonation rate was increased significantly in Chi et al., (2002) in a period of 28 days using carbon dioxide contents of 50 %, 75 % and 100 %.

2.5.2. Carbonation of concrete

Carbonation occurs when carbon dioxide (CO_2) reacts with calcium hydroxide ($Ca(OH)_2$) in the pore solution of concrete in a sequence of reactions. The gaseous carbon dioxide enters the pores and dissolves in water (H_20) to form carbonic acid (H_2CO_3), as expressed in **Equation 2.10**. The carbonic acid may then react with calcium hydroxide in the pore solution to finally precipitate as calcium carbonate ($Ca(CO)_3$). This secondary reaction is expressed in **Equation 2.11** where calcium carbonate lines the pores, which may decrease the pore sizes and transport rates thereafter. The pore solution is neutralised as a result of carbonation where the pH decreases from that of sound concrete, of 12.5, to 8.5 at full carbonation. (Neville, 2011). Other acid gasses neutralise the alkalinity of the pore solution, however, to a depth that is not significant compared to carbonation (Bertolini et al., 2013).

$$CO_2 + H_2O \rightarrow H_2CO_3 \qquad \text{Eqn. 2.10}$$

$$H_2CO_3 + Ca(OH)_2 \rightarrow CaCO_3 + 2H_2O \qquad \text{Eqn. 2.11}$$

When the $Ca(OH)_2$ is depleted due to carbonation in the pozzolanic reaction, the carbonation of calcium silicate hydrate also occurs (Neville, 2011). The $Ca(OH)_3$ product is larger than the $Ca(OH)_2$ thus decreases the porosity of paste whereas carbonation of CSH causes shrinkage (Bertolini et al., 2013). Carbonation of the CSH is crucial in cement extender concretes as the pore sizes increase when there is a larger amount of CSH from the pozzolanic reaction. The expansion pressures from the $Ca(OH)_3$ may cause cracking thus increase the transport rates of gasses, moisture and ions. Chloride penetration into carbonated concrete may thus be less hindered due to cracking even through the pore sizes are reduced at the surface.

2.5.3. Carbonation of concrete

Carbonation proceeds roughly according to the laws of diffusion as expressed in **Equation 2.12** where the rate is proportional to the depth (Broomfield, 2007). The differential is integrated over the carbonation depth (x) and exposure duration (t), to yield the parabolic expression in **Equation 2.13**. The proportionality constant of the carbonation depth (D = 1/k) is based on an ideal condition of homogenous concrete throughout the entire volume. If there is no carbonation initially (t = 0) the integration constant, $K_O = 0$, in the parabolic expression yields the square root trend in **Equation 2.14**. Under a steady-state condition of moisture at the surface, the carbonation rate is based on $\sqrt{t}$, characteristic of sorptivity (Neville, 2011).

$$\frac{dx}{dt} = \frac{D}{x} \qquad \text{Eqn. 2.12}$$

where:

- x denotes the carbonation depth,
- D denotes the diffusion coefficient and
- dx/dt denotes the change in the carbonation depth with time.

$$t = kx^2 + K_0 \qquad \text{Eqn. 2.13}$$

where:

- t denotes the duration of exposure and
- k denotes the integration constant.

$$x = D\sqrt{t} \qquad \text{Eqn. 2.14}$$

The progress of a carbonation front is illustrated in a plot of the pH of the pore solution against the cover depth in **Figure 2.6**. At the concrete surface all of the calcium hydroxide in the pore solution is regarded to be depleted, as shown by the lowest pH value at point A. With further exposure the pH of the pore solution is decreased as the carbonation had reached greater depths, from the solid line to the

dashed line. There are a number of relationships on carbonation progress in the literature which are mostly based on the square root of time (Broomfield, 2007). **Equation 2.14** is rather correct although tends to overestimate the carbonation depth in ordinary concrete with a lower total porosity (Bertolini et al., 2013).

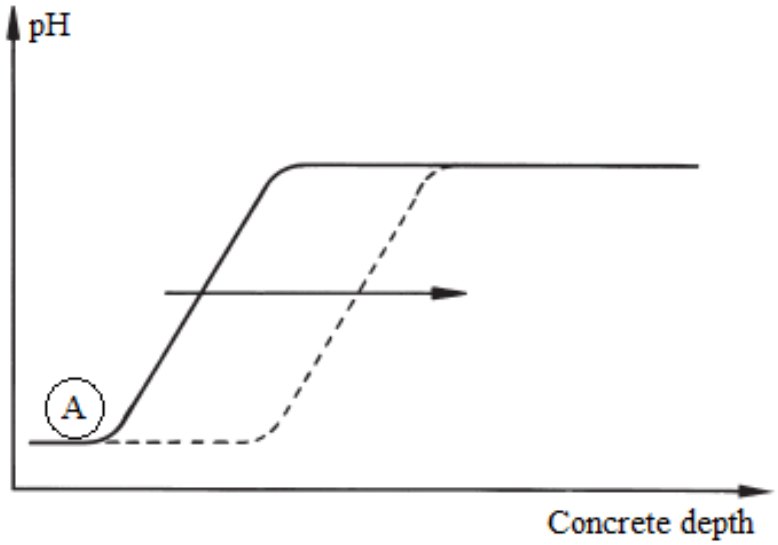

Figure 2.6: pH reduction due to carbonation (Alexander et al., 2009)

An influential factor to the carbonation rate is the diffusivity of the paste's pores in the period wherein the carbon dioxide ingress occurs. The characteristics of cementing binders are important to decrease the pore sizes and their connectivity so that there are fewer transport paths for the carbon dioxide gas. Neither the strength nor water: binder (W: B) ratio are indicative of the carbonation resistance while the carbon dioxide ingress occurs, as curing is also a major factor (Neville, 2011). A reduction in the ingress of carbon dioxide in concrete is achieved at a sufficient stage of curing as the gas transport may occur even through the smallest pores in paste. The oxygen permeability test is used to characterise the resistance of concrete to carbonation, which is based on the measurement of flow through a sample under an externally-applied pressure gradient (Alexander et al., 2009).

Carbonation resistance is also influenced largely by the alkalinity (or pH) of the pore solution thus the calcium oxide content of the cementing binders. Cement extenders contain lower calcium oxide contents compared to Portland cement thus

may be more susceptible to carbonation. Calcium hydroxide is consumed in the pozzolanic reactions of cement extenders thus less carbon dioxide is required to increase the carbonation depth compared to ordinary concrete (Neville, 2011). An increase in the carbonation depth in concrete with cement extenders has thus been found in a number of studies, even though these materials may decrease the gas permeability. A decrease in the gas permeability thus was not controlling of the carbonation depth in such concretes due to the lower calcium oxide contents.

The carbonation depth of concretes with common cement extenders in Ikotun et al., (2017) was increased due to their low calcium oxide contents. The oxygen permeability index of the concretes with fly ash, slag and silica fume was lower than the ordinary concrete after 28 days of curing. The carbonation depths after 2 years of atmospheric exposure were, however, larger due to the lower calcium oxide contents in these cement extenders. The concretes with fly ash in Moreno & Sagues (1998) had larger carbonation depths after accelerated exposure to carbon dioxide contents of 0.5 % and 4 % for up to 545 days and 84 days respectively. The carbonation depths were larger with an increase in the replacement level of the fly ash from 20 % to 50 % as there was less calcium oxide in the binder blend.

Metakaolin has also been found to result in an increase in the carbonation depth due to a lower calcium oxide content than Portland cement. The concretes with metakaolin in Bucher et al., (2015) contained larger carbonation depths than the ordinary concrete after either 70 days of accelerated carbonation or 2 years of atmospheric exposure. The carbonation depths were larger due to an increase in the replacement level of the metakaolin, from 15 % to 25 %, as there was a lower calcium oxide content in these binder blends. There was also an increase in the carbonation depth in concretes with binary blends of metakaolin in Kim et al., (2007) under accelerated carbonation. The carbonation depth was increased by a similar magnitude after 56 and 90 days in concretes with up to 20 % metakaolin.

Cement with limestone filler has been used in a number of studies to decrease the carbonation depth in concrete with metakaolin. This was found in Bucher et al.,

(2015) in the concrete with a replacement level of 15 % metakaolin and cement based on limestone filler. The carbonation depths in this concrete were lower than the concrete with limestone cement only after 70 days of accelerated carbonation and 2 years of atmospheric exposure. This reduction of the carbonation depth in concrete with metakaolin and limestone cement was attributed to a formation of hemi-carbo-aluminate in Antoni et al., (2012) which decreases the pore sizes of paste. The carbonation depth in Bakera & Alexander, (2019) was decreased in the concretes with a metakaolin replacement level up to 20 % and limestone cement.

2.5.4. Carbonation-induced corrosion

The progress of carbonation in concrete has been determined by several methods in the literature in terms the alkalinity (or pH) of the pore solution. A decrease in the pH over a carbonation front causes corrosion at some point between the fully-carbonated surface and alkaline portion at the greater depths. Corrosion may even initiate when the carbonation depth is not yet at the steel surface in that there is partial carbonation in the cover region (Neville, 2011). A decrease in the pH over a carbonation front is illustrated as the curved line in the plot against the cover depth in **Figure 2.7**. The pH is constant at the greater depths, closer to 30 mm and beyond, until the limit of fully-alkaline concrete, within a pH range of 11-11.5 (at A). The pH decreases from this alkaline part to a pH range of 9.5-11 (at B) near the surface, such that corrosion may initiate if steel is placed at these cover depths.

The pH reduction due to carbonation causes de-passivation over a larger area of steel with no distinct anodes and cathodes. The concrete resistivity is the main factor to the corrosion rate in carbonated concrete when there is a lower moisture content (Bertolini et al., 2013). As the moisture content decreases, the resistivity becomes controlling of the corrosion rate until there is limited oxygen availability at the steel surface. The corrosion initiation time, i.e. for the carbonation front to reach the steel, is determined using the solution of the differential in **Equation 2.14**. The corrosion rate in carbonated concrete has been found to be lower than chloride exposure in studies such as Tuutti (1982) and Miyazato & Otsuki (2010).

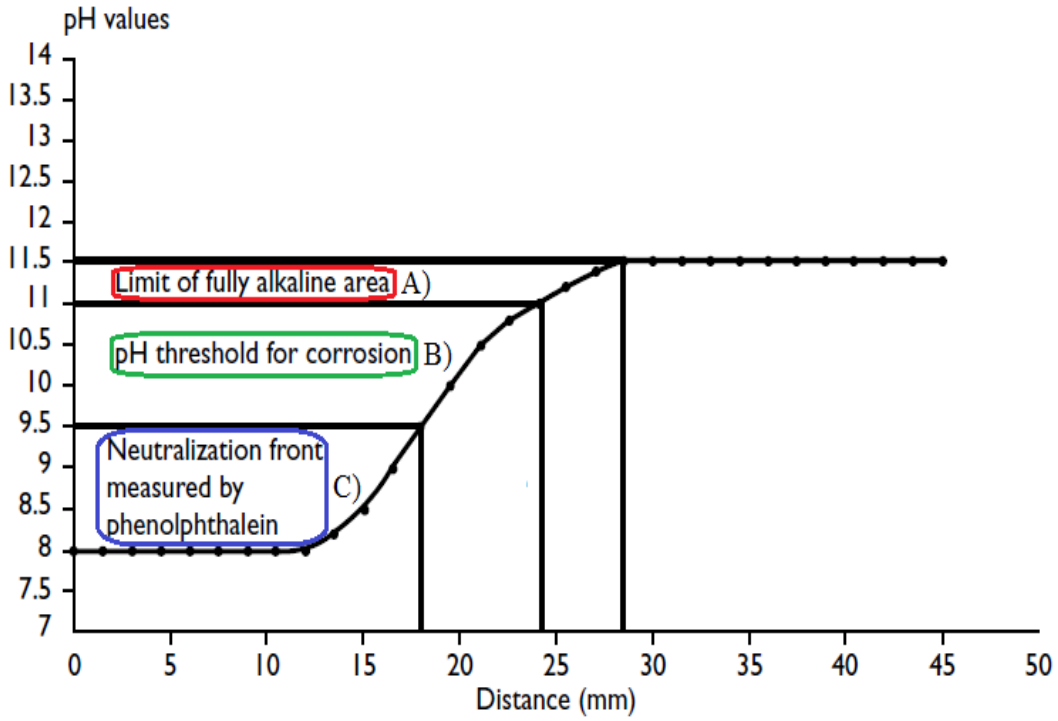

Figure 2.7: pH reduction across a carbonation front (Broomfield, 2007)

The phenolphthalein test is commonly used for the carbonation depth although it only measures the depth of fully-carbonated concrete (Neville, 2011). This test discerns the fully-carbonated concrete which has a pH of within a pH range of 8-9.5, as shown at C in **Figure 2.7**. There are a number of studies that have found carbonated products in the cover depths beyond this using the phenolphthalein test. These carbonated products thus did not decrease the pH to the range of fully-carbonated concrete although the pH was below that of fully-alkaline concrete. Other methods such as X-ray diffraction (XRD), infrared spectroscopy (IR) and thermal gravimetric analysis (TGA) can discern the partially-carbonated concrete.

The cover region of concrete has been subdivided so the amount of carbonated products can be related to parameters such as the pore solution pH, pore sizes, etc. The carbonation depths of the concretes in Chang & Chen (2004) were compared between the phenolphthalein test and other methods such as XRD, TGA and IR. The carbonation depths of the phenolphthalein test were approximately half that of the other methods due to the presence of carbonated products after the fully-carbonated concrete. The partially-carbonated concrete thus is underestimated in

the phenolphthalein test which may also result in corrosion of the embedded steel. The phenolphthalein test however used as all chloride in carbonated concrete is regarded as soluble with certainty thus diffuses to the steel (Broomfield, 2007).

2.6. Influence of carbonation on chloride penetration

2.6.1. Overview

When carbonation occurs in concrete with chloride, or when chloride penetrates into carbonated concrete, these mechanisms interact to "accelerate" the corrosion (Alexander et al., 2009). There are numerous studies that involve corrosion due to chloride or carbon dioxide in isolation, which is reflected in the exposure classes of standards, such as BS EN 206-1 (BS-EN, 2000). These studies involve the isolated exposure to each, however, for many structures, corrosion occurs due to the combined exposure (Yoon, 2007). Under conditions of combined exposure, the carbon dioxide and chloride reacts with hydration products together with the products of the previous carbon dioxide and chloride ingress (Wang et al., 2016). The corrosion rate may be increased with 2 mechanisms; carbonation progress and loss of the bound chloride in carbonated concrete (Alexander et al., 2009).

The interactions of chloride penetration and carbonation are discussed in this section from a number of studies under different exposure conditions. There is no general consensus in the literature as the interaction is more complex than each mechanism in isolation (Malheiro et al., 2016). The exposure conditions that are favourable to chloride penetration may decrease the carbonation rate, and vice versa, thus cyclic exposure has been followed. Accelerated carbonation has been used in a laboratory setting for a suitable degree of influence of the carbonation on chloride penetration. Several aspects to the interaction of combined exposure to chloride and carbon dioxide are discussed in this section, which are as follows:

- The influence of carbonation on chloride penetration and vice versa.
- The application of exposure, i.e. cyclic wetting vs maintained submergence.

- The influence of carbonation on the corrosion behaviour in concrete with chloride compared to that of chloride-induced corrosion.

2.6.2. Chloride penetration in carbonated concrete

Chloride penetration has been found to be more severe in carbonated concrete regardless of the exposure regime in a laboratory setting. This is the result of an increase in the chloride content from the surface region to beyond the carbonation depth, due to the loss of free (diffusible) chloride. The ordinary concrete in Yoon (2007) contained the largest chloride contents at the greater depths of chloride profiles in carbonated concrete after 1 year of exposure. The total chloride content was increased beyond the carbonation depth under combined exposure compared to isolated exposure to chloride or in concrete with admixed chloride. This trend of an increase in the chloride content beyond the carbonation depth within 1 year of exposure was regarded to not obey Fick's 2nd law of chloride diffusion.

The free chloride content was also tested which was found to contribute the majority of the total chloride content in carbonated concrete. This was due to the lack of chloride binding ability in carbonated concrete as the alkalinity (pH) was lower than sound concrete. Beyond the carbonation depth, there was, however, a proportion of bound chloride present as the partially-carbonated concrete can bind to the free chloride. The total chloride content in a sampling increment of 1 mm (at the surface) was also lower in the carbonated concrete compared to the isolated chloride exposure. This decrease in chloride content at the surface was attributed to a decrease in the pore sizes and shift of bound chloride to the greater depths.

The ordinary concrete was pre-carbonated for a period of 1 month and then exposed to chloride for 4 months in Malheiro et al., (2016). The chloride content beyond the carbonation depth was higher than the chloride exposure in isolation over the same duration. There were the same trends of lower chloride contents within the surface region of the carbonated concrete and higher chloride contents beyond the carbonation depth. The latter was relatively minor within the entire

exposure duration of 5 months thus further exposure was required for there to be a larger increase in the chloride content beyond the carbonation depth. The pore size distribution found that the proportions of larger pore sizes were decreased under combined exposure and proportions of smaller pore sizes due to chloride only.

The trend of an increase in the chloride content beyond the carbonated depth has been found to be in larger in concrete with cement extenders. The carbonation depth in these types of concretes is generally larger than in ordinary concrete thus more bound chloride at the surface may reach greater depths. This was found in Wang et al., (2016) when pre-contaminating the concretes with chloride and then exposure to carbon dioxide, both for 3-month periods. The chloride profiles were established in terms of the hydroxide ion (OH^-) content after each month of the carbon dioxide exposure. The OH^- consumption occurred at the surface within 1 month of carbon dioxide exposure and then at the greater depths, until 3 months.

The OH^- content in the concretes with fly ash and silica fume was lower than the ordinary concrete throughout the OH^- profile range. This reduction of OH^- ions was due to low calcium oxide contents in these pozzolanic materials compared to Portland cement. There was a decrease in the OH^- content beyond the carbonation depth which was attributed to a shift of chloride from the surface to greater depths of the profile range. The OH^- consumption beyond the carbonation depth was also larger in the cement extender concretes thus more of the chloride had shifted from the surface region. This is an indirect measure of the influence of carbonation on chloride penetration as either chloride fraction, bound or free, is generally used.

An increase in the chloride content beyond the carbonated depth in Pakawat & Uomoto (2005) was larger with an increase in replacement level of slag. The chloride contents beyond the carbonation depth after 182 days of exposure were larger than the same depths under isolated exposure to chloride. The carbonation depths under the combined exposure were up to 12 mm larger due to an increase in replacement level of slag, to 45 % and then 70 %. There were, however, lower chloride contents at greater depths in the concretes with slag under the isolated

chloride exposure due to their binding ability. The lower carbonation resistance in concretes with cement extenders thus increases the complexity of the binder type under combined exposure. Combined exposure poses a risk if any chlorides are present, even in such quantities that do not cause corrosion (Bertolini et al., 2013).

The carbon dioxide content is important to accelerated carbonation to not significantly decrease the pore sizes and their connectivity, and be influential to the chloride penetration. There is thus a small range of carbon dioxide contents in the studies on combined exposure to carbon dioxide and chloride whatever the exposure regime. The cyclic exposure in Yoon (2007) and Pakawat & Uomoto (2005) increased the chloride content beyond the carbonation depth with a carbon dioxide content of 5 %. A carbon dioxide content of 4 % was used in Malheiro et al., (2016) and Wang et al., (2016) for a single period which resulted in the same trend. This suggests that a carbon dioxide content of around 5 % is more suitable to not significantly decrease the pore sizes of paste under combined exposure.

A low carbon dioxide content of 7550 ppm (or 0.75 %) was used for the cyclic exposure in Ghahari et al., (2016) with a chloride solution. This did not increase the chloride content beyond the carbonation depth compared to that at the same depths under the isolated exposure to chloride. The sampling was performed after 28 and 90 days thus further exposure may have increased the chloride contents beyond the carbonation depth. A carbon dioxide content of over 5 % has also been used in a laboratory setting which resulted in an increase in the chloride content beyond the carbonation depth. The pastes in Liu et al., (2016) contained admixed chloride in a form of dredged marine sands that were exposed to a carbon dioxide content of 20 %. The free chloride contents beyond the carbonation depth in the carbonated pastes were lower than the pastes with the ad-mixed chloride only.

The physical changes to paste pores due to the reactions of chloride penetration and carbonation have been investigated in a number of studies. The carbonation in Ramezanianpour et al., (2014) was assessed as a presence of crystalline-shaped particles and forms of calcium carbonate. The amount of carbonation products in

the pores was decreased under the combined exposure due to a slower carbonation rate in the concrete. The concretes in Ghahari et al., (2016) also were found to have less of these crystalline particles and calcium carbonate under the combined exposure. The influence of carbonation on chloride binding in Liu et al., (2016) was determined using XRD diagrams after 28 days in pastes with and without admixed chlorides. The amount of bound chlorides was decreased in the paste due to carbonation while there was an increase in the amount of calcium carbonate.

2.6.3. Carbonation in concrete with chloride

The carbonation rate under combined exposure is important to the degree of influence of the carbonation on chloride penetration. Moisture from an external source with chloride absorbs into the concrete surface which blocks the transport paths of carbon dioxide gas. A reduction of the carbonation rate due to admixed chloride has also been found in a number of studies thus not due to external moisture. The admixed chloride in the dredged marine sands in Liu et al., (2016) resulted in a decrease of the carbonation depth by several millimetres after 1 year of exposure. The carbonation depths were decreased by a similar magnitude due to admixed chloride in Moreno & Sagues (1998) after up to 545 days of exposure.

The carbonation depth has been found to be decreased by larger magnitudes in studies that are based on external sources of chloride. The carbonation depth in Ghahari et al., (2016) was up to 1/3rd lower under combined exposure compared to carbon dioxide exposure in isolation after 28 and 90 days. The wetting cycles were performed every 6 hours which still decreased the carbonation depth with relatively short drying periods. There was a similar trend of a reduction of the carbonation depth in Pakawat & Uomoto (2005) using wetting periods of 3 days under combined exposure. The carbonation depth was up to 1/3rd lower under the combined exposure compared to carbon dioxide exposure in isolation after 186 days of exposure. A wetting duration of 3 days under the combined exposure in Yoon (2007) decreased the carbonation depth by up to ¼ after 1 year of exposure.

2.6.4. Corrosion risk due to combine exposure

The progress of carbonation in chloride-contaminated concrete has also been found in a number of studies involving corrosion monitoring. The focus of this study was on the corrosion behaviour in a laboratory setting which has been used to determine influence of carbonation on chloride-induced corrosion. This study was based on if there would be an increase in the corrosion rate at a cold joint in concrete with chloride due to carbonation. The carbonation depth at a cold joint would be required to be sufficiently influential to chloride penetration within the timeframe of exposure. Corrosion severity due to combined exposure has been found to increase compared to isolated chloride exposure in terms of the corrosion potential and corrosion rate. The progress of carbonation is important as it may influence the chloride penetration to reinforcing steel, even with a shallow depth.

The monitoring of corrosion potential in Pakawat & Uomoto (2005) found an increase in the corrosion activity due to combined exposure. The potentials were lower than the chloride exposure in isolation which represents a higher corrosion activity of reinforcing steel. The differences in the potential between the exposure regimes were apparent after 70 days of exposure, when the carbonation depth was sufficient to increase the chloride penetration. The potentials were lower under the combined exposure for the remainder of a 182-day period thus the carbonation depth was sufficient to increase the corrosion activity over the majority of the exposure period. The concretes with slag had larger carbonation depths which resulted in an increase in the corrosion activity compared to the ordinary concrete.

The corrosion severity has been better represented in studies where the electric potential was monitored in conjunction with the corrosion rate. The potential of the carbonated specimens with admixed chloride in Moreno & Sagues (1998) was the first to drop into the range of active corrosion followed by that exposed to carbon dioxide chloride only. Once the potentials of these specimens under both exposure regimes had decreased from the range of passive corrosion to active corrosion, there was an increase in the corrosion rate. The corrosion rate was thus

higher in the carbonating specimens with admixed chloride over the majority of the exposure period of 545 days. This increase in corrosion rate was mainly due to the admixed chloride, before the carbonation depth had reached the steel level.

The electric potential and corrosion rate were monitored together in Chaparro et al., (2012) which found the same trend between these parameters. The concrete with slag was carbonated to the steel within 45 days which caused a rapid drop of the potential into the range of active corrosion. The corrosion rate was thus the largest in the slag concrete for the remainder of the exposure period, from 45 days until 1 year, during the chloride exposure. The potential of the ordinary concrete dropped into the range of active corrosion after 265 days once the carbonation depth reached the steel. The corrosion rate of the ordinary concrete was thus lower than the slag concrete during the chloride exposure, from 265 days until 600 days. An increase in the carbonation depth of the slag concrete during the period of pre-carbonation was thus the main factor to the corrosion rate that could be reached.

2.7. Corrosion assessment

Concrete structures with signs of corrosion damage to any extent are required to be repaired in order to reach the desired service life. For an "effective" repair to be performed, the origin and extent of the damage must be fully understood or the cost will unnecessarily be increased (Broomfield, 2007). A full assessment is generally a 2-stage process; a preliminary assessment to identify the nature of the corrosion and detailed assessment, to quantify its extent (Bertolini et al., 2013). This section discusses a number of common methods in such assessments in terms of their ability to determine the corrosion risk in structures. The corrosion rate is important to any assessment as it relates to the carrying capacity of steel and bond strength to concrete (Neville, 2011). The specification of repair methods also must consider the causes of corrosion and extent of damage (Alexander et al., 2009).

2.7.1. Visual inspection

The preliminary survey generally involves a visual inspection, probing of any cracks and spalls and measurement of the cover depth (Broomfield, 2007). Special attention is given to where cracking or spalling is present and areas with moisture or rust stains on the concrete surface (Bertolini et al., 2013). The condition of concrete structures may be assessed visually and repair methods are resorted to only when it is serious, by way of rust stains, cracking, etc. (Song & Saraswathy, 2007). It is thus important to understand the nature of all defects in concrete as these may be a starting point to the determining the source and extent of corrosion damage and its repair. Defects that may be naturally found in concrete structures throughout the duration of their service life are as follows (Heckroodt, 2002):

- Cracking due to corrosion, temperature gradient, shrinkage or fatigue.
- Joint deficiencies: joint spalls, upward or lateral movement and seal damage.
- Cold joints due to delays in the sequence of construction.
- Surface damage: abrasion, rust stains, delamination, pop-outs and spalls.
- Changes in element shape: curling, deflection, settlement and deformation.
- Textural features: blow holes, honeycombing, sand pockets and segregation from the processes of construction..

The visual inspection of reinforcing steel and cover concrete can provide useful information when it is done in a rational, systematic manner (Alexander et al., 2009). The corrosion damages to the reinforcing steel and cover concrete herein were assessed in terms of their locality and extent in the results in **Section 4**. The cold joint of the specimens herein was a known factor that was present from the start of the exposure thus a possible source for cracks to develop. Defects that originate during the casting stage, i.e. honeycombing, may also be a starting point for cracking, depending on the concrete quality. The development of cracks at any other type of defect is an issue as the corrosion rate can accelerate freely to result in spalling and delamination, where reinforcement is exposed to the atmosphere. When there are significant damages to cover concrete, other causes of cracking,

i.e. alkali-silica reaction between the aggregates and paste, freeze-thaw etc. “must not be overlooked” in the corrosion damage assessment (Broomfield, 2007).

2.7.2. Corrosion monitoring

2.7.2.1. Overview

The detailed survey is the second part of the corrosion assessment which involves using a number of methods to quantifying the extent of the corrosion. Corrosion monitoring is an approach of determining the changes in corrosion activity before the signs of damage require rehabilitation (Bertolini et al., 2013). Early detection of corrosion in concrete structures is important as it only manifests after there is build-up of the corrosion products (Alexander et al., 2009). There are a multitude of factors to relate to corrosion parameters in a monitoring scheme, i.e. oxygen permeability, etc. so that there is more certainty to the corrosion state. Corrosion behaviour over time may be more representative of the corrosion state as it reflects the changes in concrete quality and exposure conditions. It is “desirable” to monitor the corrosion state right from the construction stage by carrying out periodic testing and maintaining a record of the data (Song & Saraswathy, 2007).

2.7.2.2. Half-cell potential

The tendency of metals to corrode in an electrolyte such as the pore solution of concrete is measured using the electric potential (Song & Saraswathy, 2007). The potential comes about from the mutual polarisation of the corrosion reactions in an overall reaction (Roberge, 2008). The potential of reinforcing steel is measured against a reference (or half-cell), with a stable potential, which is placed on the concrete surface. Half-cell testing is a non-destructive way to detect the existence of corrosion activity, even with no signs of corrosion damage on the concrete surface (Nakamura et al., 2008). The lowest potential values of an arrangement of reinforcing steel correspond to a higher corrosion activity, relative to that in sound concrete, which has a higher alkalinity. The existence of active corrosion in a

laboratory setting has been determined using the measurement of half-cell potential in studies such as Islam & Sugiyama (2010) and Horiguch et al., (2020).

Half-cell testing may be performed over multiple locations in concrete structures in a grid-like manner where the corrosion potentials are expressed as gradients. This approach of measurement is more useful than an absolute value at a single point as it may identify any changes in the moisture content, presence of defects, etc. Chloride penetration is associated with distinct anodes and cathodes thus results in potential gradients to the passive areas of reinforcing steel (Alexander et al., 2009). Whereas the potential gradient is increased in concrete with chloride, the corrosion cells in carbonated concrete are closer, to form a mixed potential (Broomfield, 2007). The latter is dependent on the electrical resistivity thus any changes in the moisture content may also result in gradients of the potential.

Half-cells are constructed as a metal electrode in a saturated solution of its own ions, i.e. copper in copper-sulphate (Bertolini et al., 2013). Of the common half-cell types in practice the copper-copper sulphate (denoted Cu-$CuSO_4$) and silver-silver chloride (Ag-AgCl) were used herein. The former is recommended in ASTM C 876 and there are a number of methods to convert the potential value between the common half-cells. The Cu-$CuSO_4$ half-cell is robust and accurate in concrete structures although errors to the measurement may arise in a laboratory setting (Roberge, 2008). The Ag-AgCl half-cell is widely used in practice as it non-toxic and less reactive with the paste hydrates (Song & Saraswathy, 2007).

The potential value that is measured with the common half-cells is classified to determine the existence of active corrosion. These ranges of potential values are specified in ASTM C 876 against a Cu-$CuSO_4$ half-cell which is most common in practice. This standard interpretation of potential was derived empirically from the bridge decks of a marine zone thus not universally applicable (Bertolini et al., 2013). There is a conversion method for the potentials of the other common half-cell in ASTM C 876 which is found in the ASTM G3 (ASTM, 2014) standard and in Ives et al., (1961). There are other methods for converting the potential between

the common half-cell types, such as the graphical scheme in Robberge (2008). There was no intention to determine the correctness of such conversion schemes herein, however, the initiation times were compared between half-cell types.

There is a tendency to relate the potential to the corrosion rate however the influential factors of each parameter are different thus any correlation is fortuitous (Broomfield, 2007). Potential mapping however has been used to determine the areas of active corrosion which decreases the amount of corrosion rate values that are required. The potential typically falls within a range of +50 and -200 mV and may drop to -500 mV and -700 mV due to carbonation and chloride respectively (Bertolini et al., 2013).In saturated concrete, with no oxygen at the steel level, the potential may drop to less than -700 mV, even without significant corrosion (Broomfield, 2007). Corrosion testing may be performed after a drying period so that the lack of oxygen does not decrease the potential in the anodic (-) direction.

The suitability of potential measurement against the potential ranges in ASTM C 876 was assessed on an existing bridge deck in Nakamura et al., (2008). The potentials were monitored together the corrosion rate and other parameters such as the chloride penetration. The potential values were above -350 mV against a standard copper-copper sulphate half-cell which does not fall within the range of active corrosion in ASTM C 876. This was not found when inspecting the steel as rust was present, which is not consistent with the numerical criteria of ASTM C 876. There was however localised corrosion on the bridge where the lowest potentials were measured which corresponded to the highest chloride contents.

The gradients of potential maps were regarded as a better assessment method for existing bridges, which was also found prior to the aforementioned case study. The potential gradients were reliable to detect the existence of localised corrosion on the bridge where the lowest potentials were measured. The RILEM TC 153-EMC recommendation promulgated that numerical criterion, i.e. ASTM C 876, results in a misinterpretation due to the many factors that are influential to the potential. This recommendation was published after the ASTM C 876 standard

thus based on more experience in the potential mapping of different corrosion scenarios. The numerical magnitude was however used in this study to detect the existence of corrosion and compare the potential between the common half-cells.

2.8.2.3. Linear polarisation resistance

The potential of reinforcing steel may be shifted about its equilibrium for a time period, in that it is polarised in the negative or positive directions. This leads to a net current through the concrete between a half-cell on the exposed surface and reinforcing steel, when electrically connected. The polarisation methods in the literature are based either on the potential response to an applied current through the cover concrete, or vice versa. In both these subdivisions of polarisation, the concrete resistivity is taken into account in the calculation of the corrosion rate (Broomfield, 2007). Polarisation methods based on current application only are discussed in this section where the corrosion rate is determined from the potential response. These include the linear polarisation resistance and coulostatic methods which differ based on their current application to polarise the reinforcing steel.

The linear polarisation method requires reinforcing steel to be polarised with an electric current while measuring the potential response. This method of corrosion rate measurement is discussed in a number of sources such as RILEM TC 153-EMC, Broomfield (2007) and Bertollini et al., (2013). The change in potential about the equilibrium in linear polarisation methods is required to fall within a linear range in a relationship with the applied current. Outside of this range there is less certainty to the corrosion rate the potential response may be erratic after the current is applied. The range of linearity between the potential and applied current was found to be ± 20-30 mV in Stern & Geary (1957), which was then validated in Andrade & Gonzalez (1978). There are other ranges such as that in RILEM TC 153-EMC; ± 100 mV for high corrosion rates and ± 20 mV for passive corrosion.

The polarisation resistance is calculated as the ratio of the shift in potential as a response to an applied current using **Equation 2.15**. The corrosion current density

on the steel surface is calculated as the inverse of the polarisation resistance using **Equation 2.16**. The Stern-Geary constant (B) was determined using a relationship between the current density and mass loss of steel in Andrade & González (1978). This constant is recommended in RILEM TC 153-EMC to be 52 mV and 26 mV for passive and active corrosion respectively. The current density (corrosion rate) is expressed in micro-Amperes (μA) per cm^2 of the steel which is polarised due to the applied current. The unit of polarisation resistance (R_P) is either $\Omega.cm^2$ or Ω depending if the polarized area (in cm^2) is taken into account or not respectively.

$$R_P = \frac{\Delta E}{\Delta i} \qquad \text{Eqn. 2.15}$$

where:

- ΔE (V) denotes the magnitude of potential shifted,
- Δi (A) denotes the magnitude of applied current and
- R_P denotes the polarisation resistance of the steel in concrete.

$$i_{Corr}\left(\frac{\mu A}{cm^2}\right) = \frac{B}{R_P} \qquad \text{Eqn. 2.16}$$

where:

- i_{Corr} $(\mu A/cm^2)$ denotes the corrosion current density and
- B denotes the Stern-Geary constant.

The area of reinforcing steel that is measured is "far smaller" than an entire arrangement, however, it cannot be assumed that this area is directly below an electrode as the current may become dispersed (Broomfield, 2007). This may be an issue if the corrosion is localised as the anodic and cathodic areas are dispersed depending on the presence of moisture and oxygen. Current is applied through a counter electrode to polarise the underlying steel and may also spread laterally, or reach greater depths in concrete (Bertolini et al., 2013), The confining effect ensures that the steel area that is measured in terms of its potential response is equal to the length of contact of the reference electrode itself (Paul, 2015).

The applied current is confined using a guard ring which is another electrode located concentrically around the counter electrode (Montemor et al., 2003). The confinement of polarising current has been investigated in different configurations of the guard ring and counter electrode. The polarisation current in Clément et al., (2012) was simulated using a finite element method to estimate the error of the polarisation measurement. The assumption of a uniform distribution of the applied current in concrete was considered to be incorrect using rectangular- and annular-shaped probes. This error was attributed in RILEM TC 153-EMC to a presence of local maximums of the polarizing current which is not a general consideration.

2.8.2.4. Coulostatic method

The coulostatic method is based on an applied current and was used to determine the corrosion rates in this study using commercially-built apparatus. Coulostatic measurement is similar to the polarisation resistance, however, a small current is applied into the concrete and the transient potential is then recorded (Paul, 2015). This approach may be preferred for corrosion rate testing due the slow reactions of corrosion at the steel-to-concrete interface (Montemor et al., 2003). A current pulse is applied into concrete through a counter electrode for a brief time, of up to 10 ms, to measure the potential response until it has decreased close to or back to the equilibrium potential (Song & Saraswathy, 2007). The potential transient in the Coulostatic test is shown in plots of the potential shift about the equilibrium in the experimental programme (**Chapter 3**). These included the period before the current pulse, current pulse and the potential decay back to the equilibrium.

The coulostatic method is discussed in a number of sources such as Song & Saraswathy, (2007), Montemor et al., (2003), etc. The potential decay of the steel decays back to the equilibrium potential after the current pulse is applied which may be described using Randles' circuit model in **Equation 2.17**. For a given increment of the applied current (ΔI) the total potential charge in the coulostatic test consists of the concrete resistivity (ΔIR_{Ω}) and potential that polarised the steel (ΔIR_{P}). If the current pulse is switched off the total potential charge between the

counter electrode and steel is lost thus the potential decays back to the equilibrium potential. The potential decay of the steel back to the equilibrium potential is approximated in terms of an exponential function with time (t) in **Equation 2.18**.

$$\eta_T = \Delta IR_\Omega + \Delta IR_P(\exp\left(\frac{-t}{\tau_C}\right)) \quad \text{Eqn. 2.17}$$

where:

- η_T (mV) denotes the total potential charge,
- ΔIR_Ω denotes the concrete resistivity between the steel and half-cell on the concrete surface,
- ΔIR_P denotes the magnitude of charge due to the applied current,
- τ_C denotes the Coulostatic time constant describing the potential decay and
- t (mS) denotes the time during the potential decay.

$$\eta_T = \eta_O \exp\left(\frac{-t}{\tau_C}\right) \quad \text{Eqn. 2.18}$$

where:

- η_T (mV) denotes the potential shift at time = t,
- η_O (mV) denotes the initial potential shift and

The polarisation resistance of reinforcing steel in concrete (Rp) is calculated from a time constant of the potential decay (τ_C) using **Equation 2.19**. The potential charge that is imparted into concrete due to current pulsing (C) is required which is calculated using **Equation 2.20**. The parameters in this equation include the magnitude of charge due to the current pulse (q_S), steel area that is polarised and magnitude of the potential before the decay (η_O). The polarised area of steel (A) is typically calculated using the steel diameter and length that is influenced by the polarising current. The potential charge due to the applied current is calculated from the magnitude and duration of the current pulse using **Equation 2.21**.

$$R_P = \frac{\tau_C}{C} \qquad \text{Eqn. 2.19}$$

$$C = \frac{q_S}{A\eta_O} \qquad \text{Eqn. 2.20}$$

$$q_S = \Delta i \cdot \Delta t \qquad \text{Eqn. 2.21}$$

where:

- C denotes the total potential charge imparted through the counter electrode,
- Δi denotes the amount of current applied,
- Δt denotes the current pulse duration
- q_s denotes the charge due to the current pulse and
- η_O (mV) denotes the initial potential shift.

Earlier studies on Coulostatic measurement dealt with analysing the potential transient in a calculation of the polarisation resistance. The interfacial capacitance however had to be assumed to determine the polarisation resistance from a time constant of the potential decay. A different method was used in Sathiyanarayanan et al., (2006) without this assumption, by measuring the polarised potential with and without the concrete resistivity. The corrosion rates were compared to that of the galvano-dynamic polarisation test and the steel mass losses that were present after the exposure. The galvano-dynamic test was performed in a normal range of the polarised potential for active corrosion, of ± 20 mV about the equilibrium.

The potential shifted was greatest in the concrete without admixed chloride and this was decreased in concretes with up to 5 % chloride by mass of the cement. The passive potential in the concrete without admixed chloride was succeeded by the larger magnitude of shifted potential during the polarisation. The corrosion was more established in the concrete with chloride in that the magnitude of shifted potential was lower than that of the passive corrosion. The steel mass loss after the exposure agreed more with the corrosion rates of the Coulostatic method, thus regarded as more reliable. The corrosion rates of the galvano-dynamic method were lower due to an inclusion of the concrete resistivity in the cover concrete.

2.8.2.5. Concrete resistivity

The electrical resistivity (or conductivity) of concrete is measured using a number of methods, based on the current application, AC or DC. The test methods are different under these subdivisions and generally apply current into concrete while measuring the potential response. DC testing is based on applying a constant electric potential between 2 probes whereas AC testing is based on 2- and 4-probe configurations (Song & Saraswathy, 2007). The Wenner probe is an apparatus that is generally used in laboratories and structures, and consists of 4 equally-spaced probes. This apparatus was developed for soil (ASTM G 57) and modified for concrete in RILEM TC 154-EMC and the ACI Journal (Broomfield, 2007).

The resistivity of Wenner probes is measured by applying an alternating current through the outer probes and detecting the potential drop with the inner probes. This measurement method is expressed in terms of an array of 4 probes which have an equal spacing at a distance of a, using **Equation 2.22**. The resistivity is measured with good reproducibility using the various methods when the probes are well-bound to concrete and have an adequate spacing (Song & Saraswathy, 2007). The sources of error that arise in the resistivity measurement of Wenner probes were investigated with different probe configurations in Gowers & Millard (1999). For a given cover depth spacing between the probes in this array was an important factor to the resistivity due to the heterogenic nature of concrete.

$$\rho\ (k\Omega \cdot cm) = \frac{2\pi aV}{I} \qquad \text{Eqn. 2.22}$$

where:

- $\rho\ (k\Omega \cdot cm)$ denotes the concrete resistivity,
- V denotes the voltage measured by the inner probes,
- I denotes the current applied though the outer probes, and
- a denotes the spacing between the probes.

Resistivity testing is simplistic compared to the chloride diffusion rate thus has been evaluated as a replacement, to represent the concrete durability. This was

found in Kevern et al., (2015) with the same type of Wenner probe as herein, to replace the rapid chloride permeability (RCP) test. The RCP test is standardised in ASTM C 1202 and AASHTO T 277 and was requested to be replaced with the surface concrete resistivity, as it is less-rigorous. The Wenner probe conformed to AASHTO TP 95 -11 and the RCP was tested according to AASHTO T 277, to represent the chloride diffusion. The surface resistivity was intended to represent the electrolyte resistance of the surface region rather than that at greater depths.

The strength of the relationship between the chloride diffusion rate and surface resistivity was based on the correlation coefficient. The correlation coefficient was larger than 90 % between these parameters thus the resistivity was considered to be a good replacement for the RCP test. There was a similar correlation between the surface resistivity and chloride diffusion rate in Safehiana & Ramezanianpour (2015) in samples of the piles from a concrete jetty. The resistivity is thus also a suitable replacement parameter for representing the chloride penetration resistance of concrete. The influence of defects and carbonation would be required to be determined together with chloride profiles, electrical potential, corrosion rate, etc.

3. Experimental programme

3.1. Overview

The experimental programme was performed in line with the aim of the study, to assess the influence of a cold joint and carbonation on chloride-induced corrosion. Defects in concrete such as cold joints or cracks have been found to increase the chloride content in the surface region of concrete. This additional chloride to be resisted was hypothesised to increase the corrosion rate when carbonation was part of the exposure conditions. The carbonation depth that is reached within the timeframe of exposure was required to be influential to the chloride penetration to be consistent with this hypothesis. The experimental programme was focussed on this corrosion condition by testing a number of parameters which are grouped as:

1. Corrosion monitoring of the embedded steel,
2. Chloride penetration and carbonation depths in the concrete,
3. Transport properties of oxygen, moisture and chloride ions and,
4. Corrosion damage as the concrete cracking and steel corrosion.

The experimental programme details in this chapter are sub-divided broadly as the preparatory works, exposure conditions and specimen testing. The first of which involved characterising the concrete materials, concrete mixture design and test specimen fabrication. The corrosion monitoring of the embedded steel (group 1) formed the bulk of the specimen testing and was supplemented with the remaining parameters, grouped 2-4. There are diagrams to summarise the salient details of this chapter, at the end in **Section 3.10**, as the parameters tested and their curing and exposure durations. The temperature, relative humidity and cover depth were also part of the testing to identify any discrepancies against the other parameters.

3.2. Materials used

3.2.1. Cementing binders and aggregates

The details of the cementing binders and aggregate materials that were used in the concrete mixtures are discussed in this section. The details of the other items that were required in the experimental programme, i.e. reinforcing steel, plasticiser, epoxy coatings, etc. is discussed in the relevant sections. The characterisation of the binders and aggregates was performed in the mixture design and to interpret the results in **Chapter 4**. Rapid-hardening cement was the main cementing binder and cement extenders were used in binary blends, so that the comparisons were based on the binder type. A number of characteristics of the concrete materials are discussed in **Section 3.2** against the requirements of the South African standards.

3.2.1.1. Rapid-hardening Portland cement

The main binder, Afrisam's rapid-hardening Portland cement, is manufactured for high-performance concretes in terms of the strength development. The reactivity of this material is due to its small particle sizes, which increases the hydration rate after mixing. The compressive strength, setting time and impurity requirements of this cement are specified in SANS 50197-1 (SANS, 2011). Concrete durability tends to be improved by the inclusion of cement extenders that conform to SANS 50450-1 (SANS, 2014). The composition of the conformability testing at Afrisam according to SANS 50197-1 is listed as the percentage (%) mass in **Table 3.1**.

Table 3.1: Typical cement oxide composition

Compound	Formula	Percentage (%)
Calcium oxide	CaO	65.05
Silicon dioxide	S_iO_2	20.79
Aluminium oxide	Al_2O_3	4.64
Sulphur trioxide	SO_3	2.99
Iron(III) oxide	Fe_2O_3	2.69
Magnesium oxide	MgO	1.73
Potassium oxide	K_2O	0.47
Titanium dioxide	TiO_2	0.39
Sodium oxide	Na_2O	0.15
Manganese(II) oxide	Mn_2O_2	0.12
Phosphorus pentoxide	P_2O_5	0.07
Loss on ignition		2.98

The impurity levels of the cement according to SANS 50197-1 in terms of the sulphate and chloride contents are listed in **Table 3.2**. The requirements under the 52.5 R strength class in terms of the setting time and strength development after 2 and 28 days of curing are listed in **Table 3.3**. These requirements impose a limit on the concrete reactivity to fast-track construction, due to earlier stripping of the formwork or precast methods. The high strength of concrete with this cement is due to the C_3S content, sometimes up to 70 %, and fine grinding of the particles (Neville, 2011). The calcium oxide content is controlling to the alkalinity (or pH) of concrete, so that it may resist neutralisation due to chloride or carbonation.

Table 3.2: Cement impurity requirements

Compound	SANS 50197-1	Performance
Sulphate (SO_3) (%)	$\leq$ 3.5 %	2.99 %
Chloride (Cl^-) (%)	$\leq$ 0.1 %	0.04 %

Table 3.3: Cement strength and setting time requirements

Parameter	SANS 50197-1	Performance
2-day strength (MPa)	$\geq$ 30	33
28-day strength (MPa)	$\geq$ 52.5	59
Initial setting time (minutes)	$\geq$ 60	191

Particle characterisation apparatus at the Anton Paar laboratory in Midrand was used to measure the solid density, surface area and particle sizes of the binders. Anton Paar is an Austrian-based company that develops apparatus to measure the characteristics of gasses, liquids and solid materials. The reactivity of cementing materials to form a paste with pores of various sizes is dependent on the surface area, grading and composition. Scanning electron microscopy (SEM) images from the suppliers of the binders are included in this section to compare the differences in the surface characteristics. The shape and texture of such materials may be determined using SEM images and the differences in particle sizes using a particle size distribution. The surface characteristics are also measurable using the surface area alone thus the SEM images served as a means of validating this parameter.

The density was measured using the Quantachrome PentaPyc 5200e gas pycnometer, jointly based on Archimedes' principle of fluid displacement and Boyle's Law of gas expansion. Quantachrome was acquired by Anton Paar in 2018 and develops apparatus to measure the characteristics of porous materials and powders. The PentaPyc 5200e pycnometer comprises of chambers of various sizes, which may be pressurised, as shown with a typical sample in **Figure 3.1**. The binder volume was determined from the pressure decay once a target pressure was reached, with helium, as it is inert and penetrates the finest pores. The density of the cement and fly ash, 3630 kg/m^3 and 2310 kg/m^3 respectively, was up to 8 % higher than that of the conformability testing. These differences in the density may be attributed to factors such as the test method (or apparatus) and testing of various batches. The density of the metakaolin, 2470 kg/m^3, is similar to that of metakaolin in the literature, within a range of 2000-2600 kg/m^3 (Siddique, 2008).



Figure 3.1: Binder density measurement apparatus

The surface area was measured using the Quantachrome NOVA touch LX2 surface area and pore size analyser which is based on the Brunauer-Emmet-Teller (BET) theory of physical adsorption of gas molecules. This apparatus is shown in **Figure 3.2** where the samples were first heated to a constant temperature by an external bath and then pressurised. Small quantities of helium gas were applied in

increments to the sample cells to form a layer over the surface of the binder particles. The BET method is widely-used to determine the number of molecules of a known size that cover an adsorbent surface with a monolayer of molecules (Xm) (Thommes at al., 2015). A multi-point BET analysis was used, thus not a single-point BET, which takes into account the entire surface of the particles.

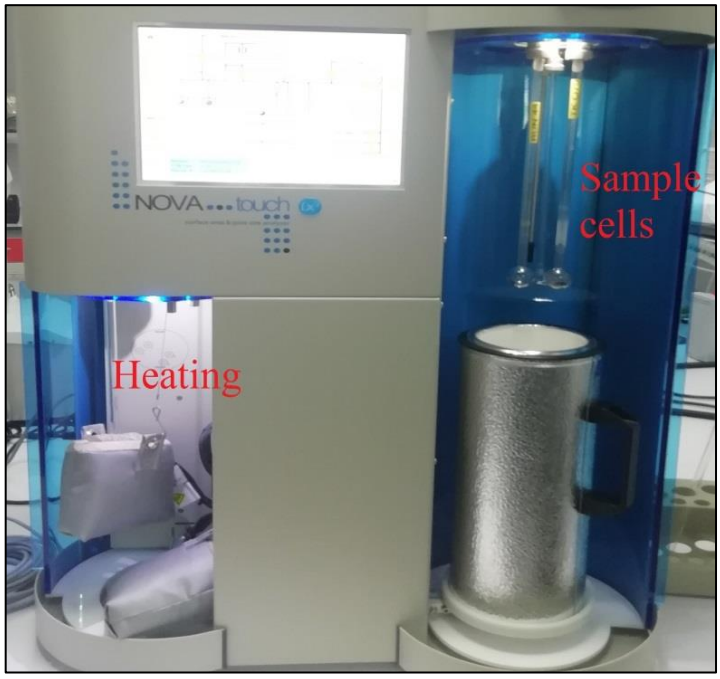

Figure 3.2: Binder surface area measurement apparatus

The relationship between the number of gas molecules that were adsorbed (X) and pressure relative to a reference (P/Po) is described using **Equation 3.1**. During this adsorption, heat is released due to the kinetic energy of the molecules, which is expressed as a constant, C. The surface area (SA) is then calculated from the intercept and slope on an isotherm using **Equation 3.2** where CSA is the cross-section area of the gas molecules (Lowell et al., 2004). Further application of gas to beyond the monolayer leads to stacking, until the pores are saturated, and their sizes can be determined. This determines the pore size distribution of a porous solid which was not included in the scope due to the high cost of the test method.

$$\frac{1}{X\left[\left(\frac{P_O}{P}\right)-1\right]} = \frac{1}{X_m C} + \frac{C-1}{X_m C}\left(\frac{P_O}{P}\right) \qquad \text{Eqn. 3.1}$$

$$SA = \frac{1}{\text{slope} + \text{intercept}} \text{x CSA} \qquad \text{Eqn. 3.2}$$

The particle sizes were measured using the Anton Paar PSA 1190 apparatus, which is based on the laser diffraction of particles, once in a dispersed state. The Anton Paar PSA 1190 covers the largest measurement range of the particle size analysers developed by Anton Paar, from 0.03 μm to 2500 μm. The apparatus is shown in **Figure 3.3** where the particles were transported from the sample cell to the dry-dispersion unit, to be energised. The lasers in the sonicator were projected onto the particles so that the diffracted pattern could be used to estimate their sizes. The Fraunhofer Diffraction and Mie Scattering Theories are jointly used to incorporate a larger range of light intensity distribution patterns in the analysis. The particle sizes were measured over the upper nm to mm ranges with the PSA 1190 apparatus which is larger than if either of these theories is used alone.

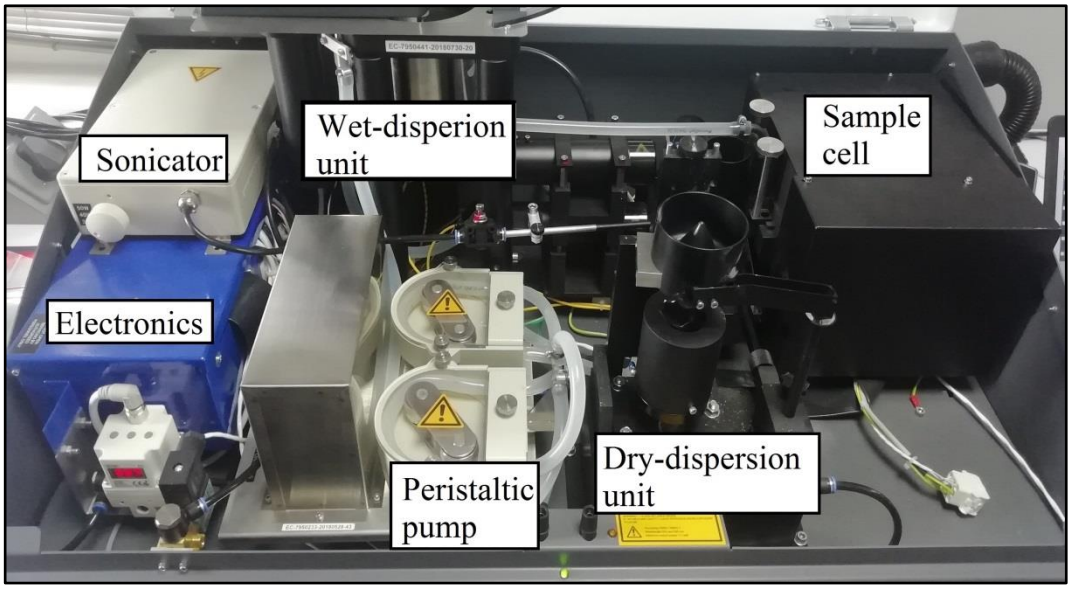

Figure 3.3: Binder particle size distribution apparatus

The density, surface area and particle size distribution (PSD) were calculated as the average between 3 tests, as the apparatus' calibrated in the first test. The PSDs of 3 samples of rapid-hardening cement were established on a volume-weighted basis, and plotted in **Figure 3.4**. The particle diameter (X) axis excludes 0 μm due to the log scale in place, and there is a larger difference between the first PSD (in

red) and subsequent PSDs, due to an agglomeration of particles. These differences between the first and subsequent PSDs of the cement extenders were of a similar magnitude to this plot. The average PSD of the 3 binders are plotted in **Figure 3.5** where the largest fractions were within the 1-10 µm and 10-100 µm size ranges.

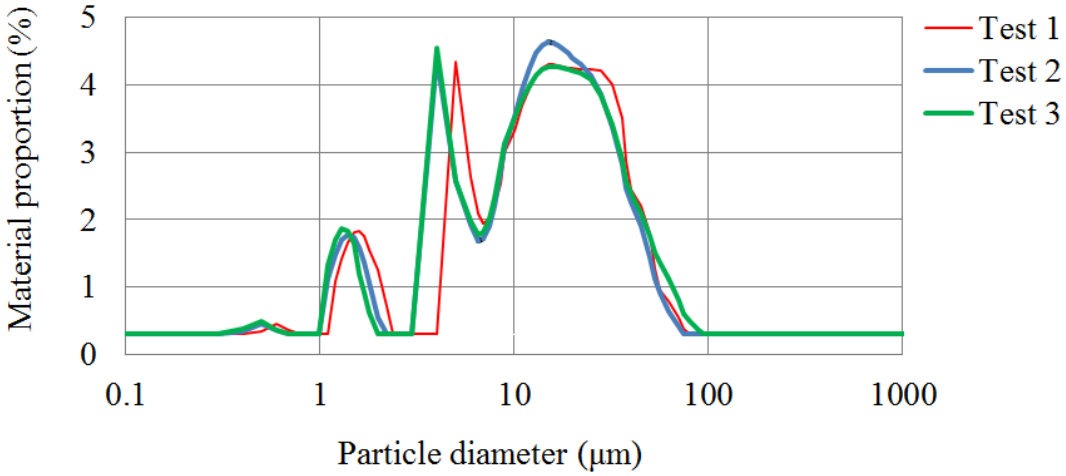

Figure 3.4: Cement particle size distributions

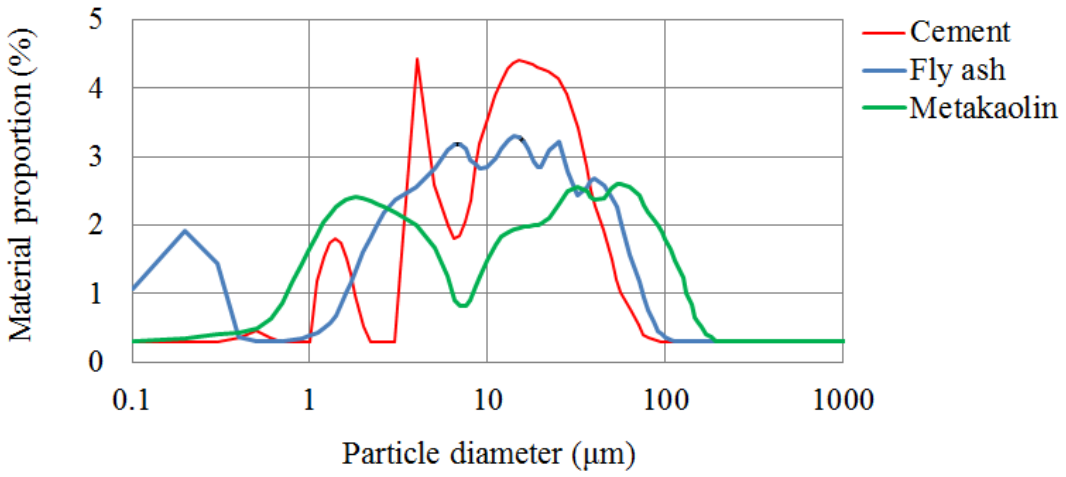

Figure 3.5: Binder particle size distributions

3.2.1.2. Fly ash

The first of the cement extenders was fly ash from the Ulula Ash plant in Pretoria, which is milled to a specific fineness from a coarser, raw material (or pulverised fuel ash). The raw material emanates from the Kriel power station in Mpumulanga where all of the burning coal is obtained from the surrounding colliery, ensuring a

high degree of consistency. The raw fly ash conforms to the un-classified (Class N) criteria after burning and is fed into a classifier, to achieve the required particle sizes and shape. The characteristics of the fly ash are tested at the Ulula Ash plant to conform to the requirements in the SANS 50450-1 (SANS, 2014) standard.

The oxide composition of the conformability testing is listed in the same manner as the rapid-hardening cement in **Table 3.4**. The composition was tested at PPC Group Laboratory in Johannesburg for the Ulula Ash plant over the period of February to October 2015. The fly ash was based mainly on silica and alumina oxides, which contributed 79-83 % of the mass, and a calcium oxide content of approximately 50 % less than the cement. Cement extenders invariably contain a higher alumina content, which enhances the capacity to chemically bind to the free chloride fraction. The impurity levels of the conformability testing to SANS 50450-1 in terms of the sulphate and chloride contents are listed in **Table 3.2**.

Table 3.4: Typical fly ash oxide composition

Compound	Formula	Proportion (%)
Silicon dioxide	S_iO_2	50-52.5
Aluminium oxide	Al_2O_3	28.5-30.5
Calcium oxide	CaO	6.0-9.5
Iron(III) oxide	Fe_2O_3	2.0-3.0
Magnesium oxide	MgO	2.0-2.5
Titanium dioxide	TiO_2	1.5-2.0
Sodium equivalent	Na	< 1.5
Potassium oxide	K_2O	< 1
Loss on ignition		0.8-1.6

Table 3.5: Fly ash impurity requirements

Compound	SANS 50450-1	Performance (%)
Sulphate (SO_3) (%)	≤ 3	0.8-1.2
Chloride (Chl^-) (%)	≤ 0.1	< 0.1

The particle size distributions (PSDs) of the 3 binders were presented in **Figure 3.5** where most particles fell within the 1-10 and 10-100 μm size ranges. The

PSDs of the cement were skewed towards the latter whereas that of both cement extenders was dispersed over a larger range. The cement contained proportions of 30 % and 70 % within the 1-10 μm and 10-100 μm size ranges respectively which was the majority of the material. The fly ash contained 7 % more particles within the 1-10 μm size range and 10 % less within the 10-100 μm size range, thus finer than the Portland cement. Cementing materials with a steadier PSD (or better packing) and finer particles tend to reduce the pore sizes and their connectivity.

Scanning Electron Microscopy (SEM) images of the rapid-hardening cement (a) and fly ash after the classification (b) are shown in **Figure 3.6**. The differences in the surface characteristics are compared using these images which have scale distances of 10 μm, as shown in red. The fly ash particles took on a spherical shape and smooth texture which reduces the water content that is required in fresh concrete. The rapid-hardening cement particles took on an angular shape which is consistent with the differences in the surface area between these binders. The surface area of the fly ash particles was 25 % less than that of the cement, of 1.93 m^2/g, due its surface characteristics. A SEM image of the coarse fractions of the fly ash is not included for the sake of brevity as this material was not used herein.

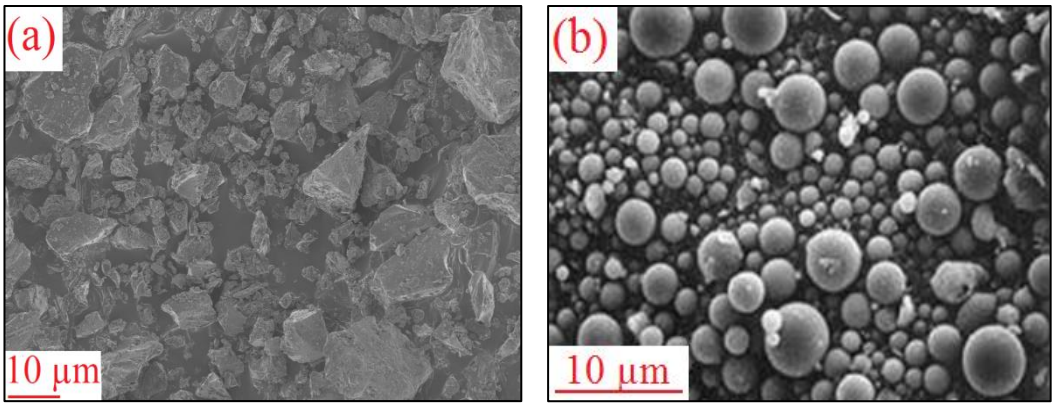

Figure 3.6: SEM images of the cement and fly ash particles

3.2.1.3. Metakaolin

The second cement extender was metakaolin K40 from the Serena trading plant in Cape Town which is processed at the Kaolin Group in Atlantis. The process of

flash-calcination is patented whereby a solid, in a finely divided form, is rapidly heated, held at temperature, briefly, and then cooled. Metakaolin is highly reactive in concrete thus increases the strength and durability when less-reactive materials such as fly ash are also used. The oxide composition is listed in **Table 3.6** where the silica content was similar to the fly ash however the alumina content was 13-15 % higher. The characteristics of calcined clay were not formalised in SANS 40450-1 during the study although are specified in standards such as ASTM 618.

Table 3.6: Typical metakaolin oxide composition

Compound	Formula	Proportion (%)
Silicon dioxide	S_iO_2	56.8
Dialuminum dioxide	Al_2O_3	43.5
Titanium dioxide	TiO_2	1.3
Iron(III) oxide	Fe_2O_3	0.5
Potassium oxide	K_2O	0.14

The particle size distributions (PSDs) found that 34 % and 55 % of the metakaolin particles fell within size ranges of 1-10 µm and 10-100 µm, respectively. The fly ash contained the largest proportion of particles up to 10 µm in size, with 40 %, then the metakaolin and cement with 38 % and 30 %, respectively. The particle sizes of the binders were thus similar in that coarse, low-grade cements may have accentuated the smaller particles of the cement extenders. The surface area of the metakaolin, of 7.74 m^2/ g, was 400 % and 426 % larger than that of the cement and fly ash respectively. A SEM image with a scale distance of 1 µm in **Figure 3.7** shows that the metakaolin took on a flaky shape for most of the particle sizes.

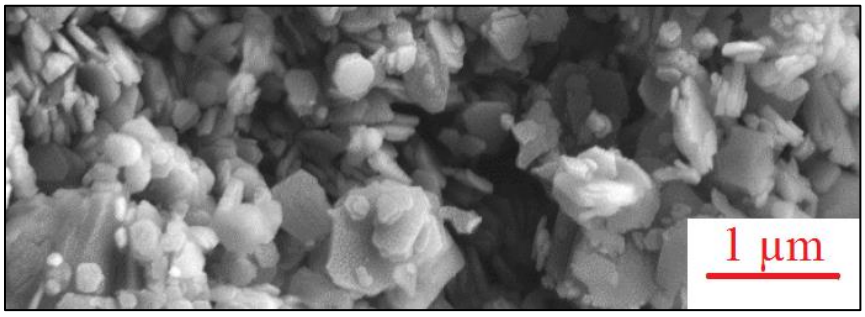

Figure 3.7: SEM image of the metakaolin particles

3.2.2. Aggregates

The coarse and fine aggregates were selected from the same parent rock type thus a difference in the aggregate characteristics was not investigated. The aggregates were sourced from the Afrisam plant in Eikenhoff, Johannesburg, which processes crushed sand and concrete stone from the in-situ andesite. Andesites in a form of Ventersdorp Eruptives cover parts of the Gauteng, North West and Northern Cape provinces, and are used for concrete (Alexander & Mindess, 2005). The 6.7 mm stone and crusher sand were used and comply with the requirements of crushed material in SANS 1083 (SANS, 2014). Fine aggregate for concrete in SANS 1083 (SANS, 2014) is required to contain at least 90 % of its particles below a sieve size of 5 mm. The crusher sand and stone contents were interchanged in a series of trials in the mixture design as it was a coarse sand, as discussed in **Section 3.3**.

The relative density and bulk densities, loose and compacted, of the aggregates were tested by the GeoStrada laboratory in Pretoria. The densities formed part of the yearly conformability testing for the aggregates of the Afrisam plant and were required in the mixture design. The relative density of the parent rock, andesite, was found to be 2.93 using the TMH1 A12 T test method of the Testing Materials for Highways recommendation (TMH). The natural aggregates such as that in rivers, dunes, etc. tend to take on relative densities of within a range of 2.6-2.95 (Alexander & Mindess, 2005). There was a potential for the aggregates to settle in the casting stage thus an adequate cohesion level was necessary, given a selected compaction method. The impurity levels were assumed to conform to SANS 1083 (SANS, 2014) in that there was no major influence on the concrete properties.

The loose and compacted bulk densities of the stone were found to be 1539 kg/m^3 and 1714 kg/m^3 respectfully using the TMH1 B9 methods. The bulk density of stone is increase with a better grading of the particles compared to aggregates that have a particle size distribution over a smaller size range. The andesite stones took on a flaky shape, which is synonymous of a higher bulk density, as they compact better into a closed volume, instead of circular stones. The flakiness index was found to be 11.1 as the average between 8 tests that were performed at Afrisam,

according to SANS 5847 (SANS, 2008). This is low compared to the maximum of 35 for crushed aggregate in SANS 1083 (SANS, 2014), even with a flaky shape.

3.2.2.1. Crusher sand

The particle size distributions (PSD) of the crusher sand were established using a series of sieve analyses from Afrisam according to SANS 1083 (SANS, 2014). The sand-size fractions, of less than 0.03 mm, that are in excess or defficient may be determined in a PSD against the required sieve sizes. The PSDs are plotted as the measured percentages of the crusher sand by mass against the required sieves sizes in **Figure 3.8**. The solid and dashed lines represent the PSDs of the sand and stone respectfully and the colour-scheme of the plots is randomised. The grading curves were based on the average between 5 tests that were performed in the week of 12-16 March 2018. There is no major variation in the particle sizes between these plots thus the characteristics were based on a good consistency of crushing.

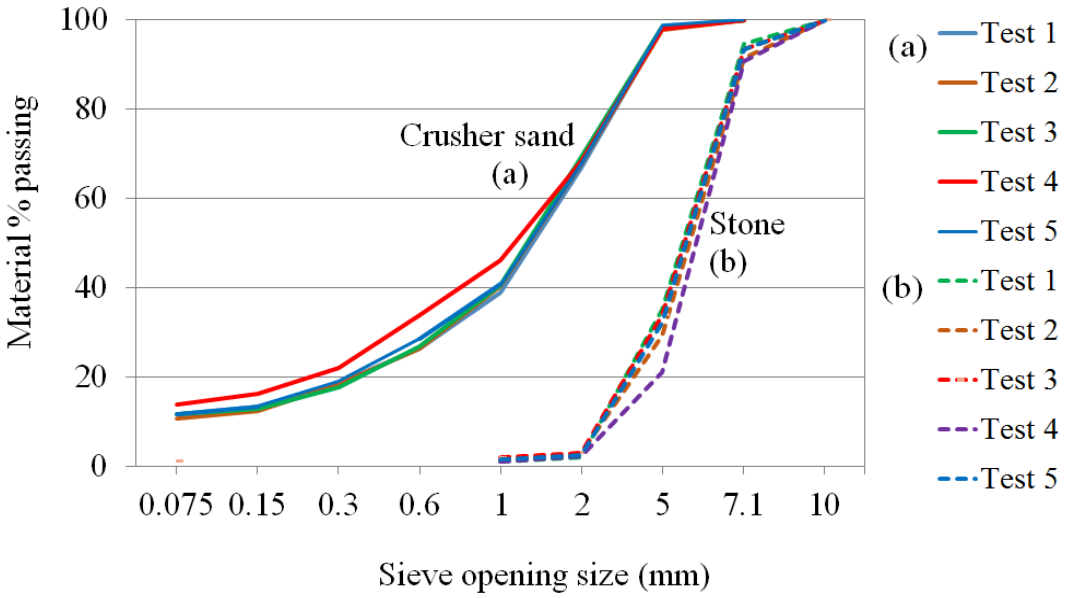

Figure 3.8: Aggregate grading curves

The slopes of the sand grading curves are steepest between a sieve size of 1 mm and 5 mm thus most of the particles fell within a size range of 1-5 mm. There was an average contribution of 58 % from within a size range of 1-5 mm, with 26 % and 32 % on the 2 mm and 5 mm sieves respectively. This caused a defficiency of

the sand-size fractions, of 0.075 mm, 0.15 mm and 0.3 mm, thus were required to be increased to adequate percentages. The fineness modulus (FM) was calculated to be 3.31 as the average between the 5 PSDs that were performed at Afrisam according to SANS 201 (SANS, 2014). This is near the limiting value of the FM in SANS 1083, of 3.5, thus the crusher sand may be regarded as coarse overall.

3.2.2.2. Concrete stone

The particle size distributions (PSD) of the concrete stone were established in the same manner as the crusher sand, over a larger range of particle sizes. The test period was the same as the sand, which was when most of the aggregates had been sourced for the concrete casting. The stone was graded according to Afrisam's own specification using sieve sizes of 10 mm, 7.1 mm, 5 mm, 2 mm, 1 mm and 0.075 mm sizes. The material masses that were retained on these sieves differed by within 1 % over the test period, with the exception of the 5 mm sieve, shown at point A. The slope of the grading curves is steepest between the sieve sizes of 2 mm and 10 mm thus most of the stone particles fell within a size range of 2-5 mm.

There was an average contribution of 90 % of the particles within a size range of 2 -7.1 mm, with 62 % and 28 % from the 2 mm and 5 mm sieves respectively. The bulk density of stone is increased with an improved grading however this was limited mostly to a particle size range of 2-7.1 mm. The nominal stone sizes that are used in practice fall within a range of 9.5-37.5 mm with a maximum of 20 mm in ordinary concrete (Alexander et al., 2009).The cover depths herein were small to reduce the time for chloride or carbonation to reach the steel thus a small stone was used to increase the concrete homogeneity. Aggregates of a similar size to that used for mortar, of a nominal size of 5 mm, could be worked into the moulds and were within the nominal maximum limit in SANS 10100-2 (SANS, 2014).

3.2.3. Mixing water and plasticiser

Impurities in mixing water for concrete may influence the fresh- and hardened-states thus appropriate levels are specified in standards to grade the water quality.

If the hydration reactions are influenced to any degree the pore sizes and their connectivity may not be sufficient after the selected curing age. The resistance to the transport of gasses, moisture and ions is thus insufficient when the concrete is introduced to the environment. Tap (or potable) water was used in the concretes under the assumption that the relevant impurities levels were suitable according to SANS 10100-2 (SANS, 2014). Tap water is accepted as mixing water for concrete in SANS 51008 (SANS, 2014) without any tests to determine the water quality.

A super-plasticiser, Sika ViscoCrete 3088, was used to reduce the water content in the metakaolin concrete, due to the high reactivity of metakaolin. The chemical base of this plasticiser is an aqueous solution of modified polycarboxylate, which is generally the organic group for plasticisers. This type of admixture is water-reducing due to the surface absorption and sterical effects that separate the binder particles. Decreasing the hydration rate in the setting stage improves the bond strength at a cold joint as concrete plasticity is important to the joint preparation (Alexander et al., 2009). The influence of plasticising on the fresh-state was based on the dosage which fell within a range of 0.2-2.0 % by mass of the total binder content. The performance of the plasticiser is required to conform to BS EN 934-2 (BS-EN, 2001) in terms of impurity levels, to be suitable for reinforced concrete.

3.3. Concrete mixture design

3.3.1. C & CI procedure

Concrete mixture design is a procedure of appropriately selecting, characterising and proportioning the dry materials and water, to yield the required properties. This procedure is customary worldwide where standardised methods are specified with the considerations of the concrete cost and quality. The calculations in the methods of such standards are based on the empirical relations of investigations that involve locally-sourced materials. The Cement and Concrete Institute (C & CI) procedure is used in South Africa and was derived from ACI 211.1-91 (ACI, 1991), which is used for normal, heavyweight and mass concrete in North

America. In this approach the concrete mixture proportions are calculated by mass in a series of trials, with a requirement that the mixture volume is kept constant.

The C&CI procedure involves specifying the concrete properties, characterising the dry materials, proportioning the mixture, preparing and assessing the mixture, and modifying if necessary. These stages of the C&CI procedure are discussed in this section, against the applicable requirements of the South African standard. The material proportions of each concrete that were accepted in the final trials had to yield specific fresh-state properties to be used to cast the test specimens. The concretes were required to have minimal segregation and bleeding in the specimen moulds, given a selected method for compaction, which is discussed in **Section 3.3.1.4**. The material proportioning and concrete handling are factors to reduce the extent of such casting imperfections thus these factors are specified in standards.

3.3.1.1. Concrete properties

The concrete properties that were specified include a slump range of 75-150 mm, water: binder (W: B) ratio of 0.55 and method of compaction. The slump of the cement extender concretes was selected to vary within a small range of 20 mm from that of the ordinary concrete. This was done so that there was a similarity in the properties between the concretes in the fresh state, using the same W: B ratio. A single W: B ratio of 0.55 was used in this study which falls within the W: B range of ordinary concrete and mortar in the South African standards, of 0.45-0.8. The compaction method of the mixture design may be found in **Section 3.3.1.4** and the compaction method of the test specimens is discussed in **Section 3.5.5.1**. The compressive strength of the ordinary concrete after 2 and 28 days was also compared to the strength under the 52.5 R class in SANS 50197-1 (SANS, 2011).

3.3.1.2. Material selection

The binder type was the main factor to compare the concrete properties in this study as the water: binder (W: B) ratio was constant. The reactivity of the cement extenders was increased by using rapid-hardening cement so that the curing was

sufficient at an earlier age. The fly ash was the least reactive of the binders as it had the lowest surface area, even though the material had the smallest of particle sizes. The metakaolin particles had the largest surface area thus were anticipated to react faster than the fly ash in concrete at earlier ages of curing. The 6.7 mm stone was appropriate to the dimensions of the test specimens against that required in SANS 10100-2 (SANS, 2014). The nominal stone size of 6.7 mm was smaller than 1/4 of the beam depth herein, of 100 mm, and lowest cover depth of 10 mm.

3.3.1.3. Material characteristics

The concrete materials were sourced over different times of the study although most of the batches were sourced before the mixture design. The characteristics of concrete materials and moisture contents of stockpiles inevitably vary with time, depending on the quality control and conditions of storage. The changes to these aspects, mainly in aggregate stockpiles, were expected to influence the fresh-state properties, even though sheltered. There are procedures for adjusting the water content, such as the ACI and BS standards, by satisfying that of the dry materials individually. The water content was not adjusted herein although the fresh-state properties were tested in the casting to report any differences from the final trials.

3.3.1.4. Material proportioning

The concretes were proportioned first by estimating the water and stone contents, then calculating the binder content using the water: binder ratio, and finally the sand content, based on a constant mixture volume. The water content of concrete is that required to yield a specific slump with minimal segregation or bleeding, when fully-compacted (Alexander et al., 2009). The binder content was limited to the maximum of 550 kg/m^3 in SANS 10100-2 (SANS, 2014) as it was increased with the water content. The cement extenders were both replaced at a percentage of 30 %, which is ideal for fly ash concrete in the marine settlements in SANS 50450-1 (SANS, 2014). The replacement percentage of metakaolin was not yet standardised in South Africa although up to 30 % has been used in the literature.

The stone content (St) was calculated using **Equation 3.3** which is dependent on the stone size, stone compacted bulk density (CBD), sand fineness modulus (FM), compaction method and slump. The andesite density of the conformability tests at the Afrisam plant (**Section 3.2.3**) was used to calculate the solid volumes of the aggregates. The constant K in the equation is based on the nominal maximum stone size and workability, in terms of the slump range and compaction method. A nominal maximum stone size of 9.5 mm was assumed to estimate this constant, which is the smallest of these sizes. The compaction method was selected to be by hand, and not moderate or heavy, to correspond to a slump range of 75-150 mm.

$$S_t = \text{CBD} \times (\text{K} - 0.1 \times \text{FM}) \qquad \text{Eqn.3.3}$$

3.3.1.5. Trial assessment and modifications

The trial mixtures were prepared in a 57-litre pan mixer using the same procedure as that for the test specimens, as discussed in **Section 5.3.4.1**. The consistency of the concretes was first quantified as the slump that was measured according to the method in SANS 5862-1 (SANS, 2006). The cohesion level was then assessed qualitatively as the collapsing behaviour of the slump mass when tapping the base plate below the slump mould. A uniform collapse occurs if the fresh concrete is held in place laterally while the base plate is tapped, without breaking, or being sheared off. Another test was performed to assess the cohesion level, which is not part of the C & CI method, although useful to validate the fresh-state cohesion.

The supplementary test of cohesion was based on the settlement of the largest stones in the mortar, after being stored to harden for 24 hours. This settlement test was performed using the mixture proportions of the final trials, wherein a suitable slump and cohesion level had yielded. The dispersion of stones in the mortar was a means of determining the resistance to settlement over the same depth as the test specimens, of 100 mm. In this test, cubes with 100 mm sides were sliced through the entire section using a circular saw with a diamond-tipped blade, to identify the largest of stones in the mortar. The stone settlement in each concrete was based on sets of 3 cubes which were prepared from the mixtures of the final trials only.

The stone content of the concretes was the last part of the mixture design and was also assessed in a qualitative manner, although in 3 parts. The first was based on the resistance that was given to the tamping rod when the concrete layers in the slump mould were compacted. The stones had to move easily away from the rod, without much resistance, or else the trial mixture was considered to be too harsh. The fresh concrete in the slump test was then smoothed with a steel trowel, where the void coverage on the surface was required to be minimal. Lastly, this concrete was transferred into a bucket and compacted using a vibrating table, briefly for up to 5 seconds. The largest stones are required to be located at a depth in the order of a few millimetres below the surface, not deeper, or protruding to any extent.

The trial modifications were based on that when only 1 type of sand is used, rather than substituting or replacing the sand with a finer aggregate. The stone content in the first trial was calculated using **Equation 3.3** and modified thereafter, once the behaviour and appearance in the 3 workability tests was assessed. A harsh mixture with voids on the surface when smoothed, and stones protruding after compaction, required that the stone content be decreased by 100 kg/m^3. The sand-size fractions (less than 0.3 mm in size) were deficient (in **Section 3.2.2**) thus the sand content was increased in the trial mixtures. Concretes with a low cohesion level require larger fractions of particle sizes below 0.03 mm to reduce the stone settlement.

3.3.2. Proposed concrete mixtures

The material proportions of the final trial mixtures yielded suitable fresh-state properties thus were proposed to cast the test specimens. These are listed in terms of the binder, stone, sand and mixing water contents in kg/m^3 units together with the slump values in **Table 3.7**. The approach was to obtain the required mixture proportions in the ordinary concrete to keep constant in the fly ash and metakaolin concretes, at a water: binder (W: B) ratio of 0.55. The binder content of 500 kg/m^3 comprised of the rapid-hardening cement, either in full proportion (100 %), or replaced at 30 %. The details of the trial mixtures are discussed in **Section 4.2** of the results in terms of the material proportions and their fresh-state properties.

Table 3.7: Concretes use to cast specimens

Material (kg/m^3)	Ordinary concrete	Fly ash concrete	Metakaolin concrete
	100 % CEM 1	70/30 CEM 1/FA	70/30 CEM 1/MK
CEM I 52, 5 R	500	350	350
Fly ash	0	150	0
Metakaolin	0	0	150
Concrete stone	477	477	477
Crusher sand	1179	1114	1144
Mixing water	275	275	275
Slump (mm)	120	140	100

3.4. Concrete mixing and sampling

3.4.1. Concrete mixing

The specimen casting was performed using a drum mixer with a 175-litre volume, according to the procedure in SANS 5861-1 (SANS, 2006). The mixer was wetted to remove any foreign materials and to reduce the amount of water that absorbed against its sides. The mixer was then loaded sequentially to combine the materials, with half the stone, all the cementing materials, all the sand and the remainder of the stone. Once loaded these materials were mixed together for a short duration of 30 seconds before the water was introduced. The majority of the water was added initially and mixed in for 2-3 minutes while the residues were re-worked, to obtain a uniform appearance. The remainder of the water was then added, where after the mixer was kept running until the specimen moulds were filled and compacted.

3.4.2. Concrete sampling

The fresh-state properties of the mixture design stage were tested again during the casting to report the differences from the final trials. The same tests as the mixture design were performed, excluding the settlement test in the cubes, along with the density of the fresh concrete. The density was measured during the casting only as the mass of concrete in cube moulds with 100 mm sides, after being floated flush.

The casting details may be found in **Section 4.2** of the results which includes the moulds that were provisioned for, fresh-state properties and density, all based on 3 tests. The mixture volumes that were used for the specimen casting were within a range of 20-149 litres, the lower bound of which was used for the trial mixtures.

3.5. Test specimen fabrication

3.5.1. Reinforced beam specimen details

Reinforced beams were used to monitor the corrosion behaviour of the embedded steel and sample the concrete for its chloride penetration. A single steel bar with electrical connectivity was placed in the moulds, to facilitate the non-destructive corrosion tests. The steel was made to comply with SANS 920 (SANS, 2014) to yield at 450 MPa and had a "ribbed surface" with a diameter of 12 mm over its length. The beams were cast to the standard dimensions of prismatic specimens in SANS 5860 (SANS, 2006), to have section sides of 100 mm and a length of 500 mm. The casting details are illustrated in the front, top (A-A) and section views, at the mid-span (B-B) and bar ends (C-C), in the Autocad drawing in **Figure 3.9**.

The beam moulds were constructed using 19 mm thick shutter-ply and screws, to cast the beams to the aforementioned dimensions. The beams were cast face-down so that the exposed surface was levelled against the mould bases, with the cover depths to the nearest steel level, denoted as C. This was done so that the exposed surface (against the mould bases) had fewer imperfections such as shrinkage cracks, after being de-moulded. The steel bar in each mould was fixed to stoppers at either end which were cut from the same ply-wood as the beam moulds, to the dimensions as shown. There were thus small indentations in the concrete at the beam ends which exposed the steel bar ends to atmosphere after the de-moulding.

The steel bars were cut to the same length of the beams (of 500 mm) and the ends then chamfered so that these could be placed in the stoppers. The surface of the steel bars was wire-brushed, to remove any mill scale, and then de-greased with

acetone, as specified in SANS 10100-2 (SANS, 2014). This preparation of the steel was necessary to bond to an epoxy paint, to prevent the paint from being removed due to abrasion forces. The steel bars were coated at both ends with the epoxy to a distance of 45 mm from the bar ends which translated to an un-coated length of 410 mm. The epoxy paint, abe.cote 352, was based on coal tar resin and was brushed onto the steel surface in 3 coats over a curing duration of 3 days.

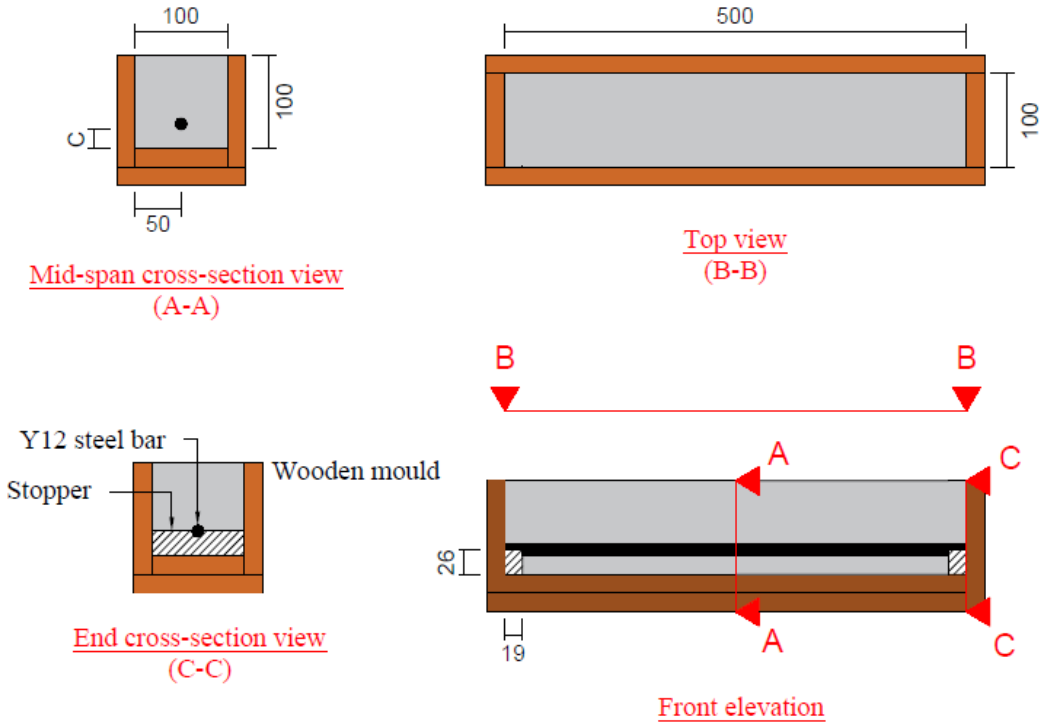

Figure 3.9: Reinforced beam moulding details

The cover depth to the steel surface was either 10 mm or 20 mm, so that the concrete resistance could be assessed at a varied cover depth. A minimum cover depth of 40 mm is specified for ordinary concrete that is exposed to a marine zone and falls under the 40 MPa strength class in SANS 10100:2 (SANS, 2014). The corrosion was accelerated in terms of the cover depth and exposure conditions, to decrease the initiation time and then increase the corrosion rate in propagation. Multiple steel bars were not used in the beams as there is an interference of the electric potential in concrete with a rebar spacing of less than 75 mm (Broomfield, 2007). A copper lead wire was connected to a hole that was drilled in each steel bar so that the concrete did not have to be broken to for the corrosion testing.

3.5.2. Cube specimen details

Cube specimens were used for compressive strength and carbonation depth testing according to the procedures in **Sections 3.8** and **3.9.3** respectively. The corrosion conditions herein were based on unidirectional exposure into a particular concrete surface of interest, as discussed in **Section 3.7**. The perpendicular surfaces of the beams and cubes, which were not exposed to chlorides and carbon dioxide, had to be coated with epoxy paint to promote this condition. The epoxy paint, under the trade name, abe.cote 337, was applied in the same manner as that on the steel, in 3 coats over 3 days. Plastic moulds were used for casting the cubes which complied with that required for cubes with 100 mm sides in SANS 5860 (SANS, 2006).

3.5.3. Circular disc specimen details

Circular disc specimens were used for testing the concrete resistance to the ingress of gasses, moisture and chloride ions. The preparation method of the discs from cubes with 100 mm sides was originally described in Alexander et al., (1999) and specified in SANS 3001-CO3-1 (SANS, 2015). The cubes were first cored using a coring drill that was orientated perpendicularly to the direction of casting, as is the case when extracting cores in structures. The cores had a diameter of 70 ± 2 mm, the internal diameter of the coring drill, and a length of 100 mm, the side lengths of the cubes. These were cut into circular discs of varying thicknesses using a circular saw with a diamond-saw blade. The cutting positions of the circular saw (left) and cross-section of the discs (right) are shown in a drawing in **Figure 3.10**.

The 30 mm thick parts in grey were tested while the remaining parts in black, all contributing a thickness of 30 mm, were discarded. A total cutting thickness of 10 mm between the 4 cuts is recommended, given that the thickness of diamond-saw blade is 2.5 mm. The discs represented the cover region of concrete between the exposed surface (denoted A) and steel level (B), at a depth of 30 mm. The extent of hydration decreases inwards when moisture is available at the concrete surface although the bulk contains more moisture when the surface is dried (Bertolini et

al., 2013). The cross-section of the discs (right) was subjected to a flux of oxygen gas, moisture and chlorides in accelerated tests, as discussed in **Section 3.9.2**.

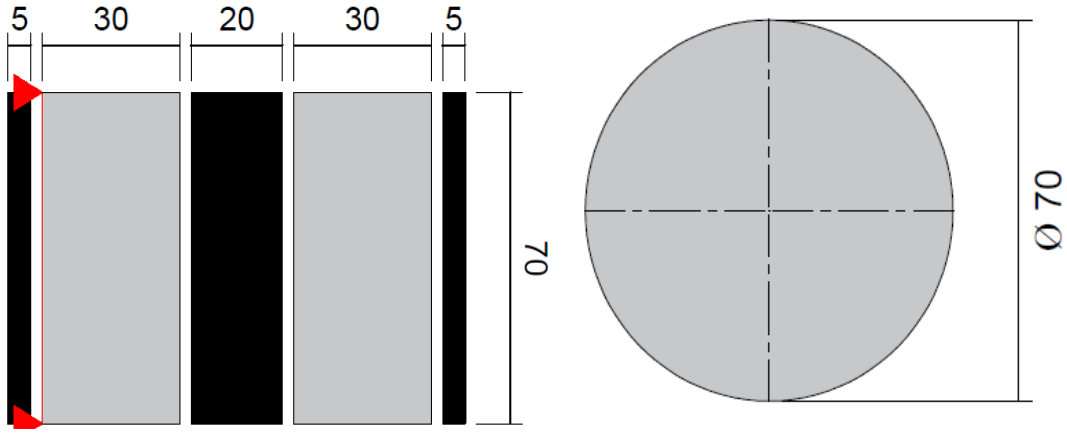

Figure 3.10: Circular disc geometric details

The circular discs were conditioned before testing so that the moisture content was uniform throughout their volume. After the discs were cured they were dried in an oven that was maintained at a temperature of 50 ± 2 ° C for 7 days. After the drying period the discs were cooled off in a desiccator with anhydrous silica for a period of 2-4 hours. The thickness and diameter of the discs were measured using a Vernier calliper at 4 points equally-spaced over the curved edge, to be averaged in the calculations. There is an allowable tolerance of 2 mm on the diameter of the discs, of 70 mm, due to due to the variation in inner diameters of core barrels.

3.5.4. Cold joints in test specimens

3.5.4.1. Cold joint details

Half the number of beam and circular disc specimens contained a cold joint defect to determine the influence on the concrete durability. The fabrication of the cold joint specimens varied to that cast monolithically, where there was a continuity of the concrete throughout the mould volume. A vertical cold joint was formed in the direction of exposure which is a plane with a high void content and connectivity of pores in the paste. The preparation of a cold joint requires a time delay between

the concrete casts which is taken from the time when the fresh concrete is initially poured into the moulds. The joints were roughened according to the procedure in SANS 10100-2 (SANS, 2014) for a delay of up to 24 hours, which is less-rigorous than that up 3 days. This included roughing the hardened concrete of the first cast, using a chisel, removing the unattached material and finally wetting the plane.

3.5.4.2. Cold joint reinforced beam specimens

The cold joint in the reinforced beams was located at the mid-span and orientated in the transverse plane, with the same dimensions as the cross-section. The steel bar ran perpendicularly to the joint, as specified in SANS 10100-2 (SANS, 2014), which is done to carry more of the bending stress. The mid-span of beams is ideal for a cold joint as there is no shear stress whereas these forces are more prominent closer to supports. Lateral forces may result in a relative displacement between the concrete either side of a joint, to increase the transport rates of gasses, moisture and ions. Photographs of a typical wooden beam mould (a) and de-moulded beam specimen (b), both with a cover depth of 20 mm, are shown in **Figure 3.11**.

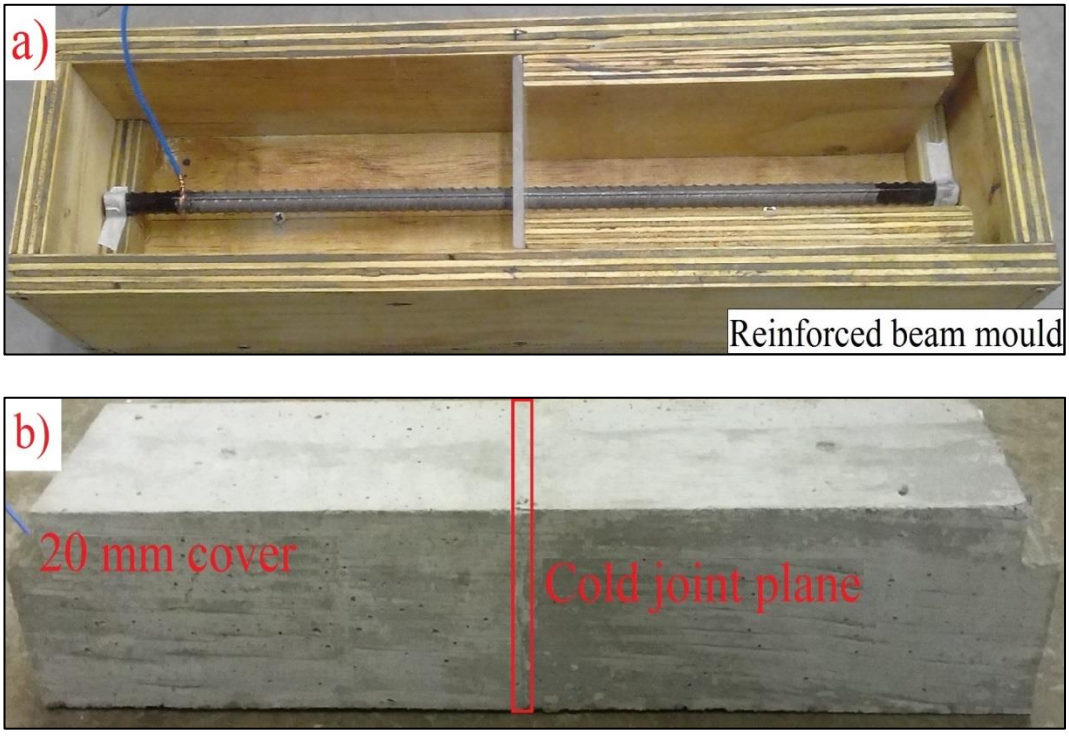

Figure 3.11: Typical cold joint reinforced beam mould

The concrete was first cast into the part of the mould where a blue lead wire was located in (a) and shuttered off using a stopper at the mid-span. The stoppers were cut from 5 mm thick sheets of Perspex to the same dimensions as the beam cross-section. Spacer blocks were used to keep the stoppers in place during the casting and were cut from the 19 mm thick shutter-ply that was used for the beam moulds. The edges of the stoppers (in the mould) were sealed using silicon and there was a spacing of approximately 100 mm between the spacer blocks to resist the pressure of the fresh concrete. The stoppers had a hole drilled with a diameter of 14 mm so that the steel bar could pass, which took into account the ribbed steel surface.

3.5.4.3. Cold joint circular disc specimens

Circular discs with a cold joint were tested to determine whether the transport rates of gasses, moisture and ions had been increased. The preparation of the discs removes any surface defects as the core ends are cut off, which is influential to the concrete sorptivity (Ballim, 1993). The transport properties of the concretes were thus used together the remaining durability parameters to determine the influence of a cold joint on corrosion resistance. The joint was orientated in the direction of exposure, which was done in studies such as Sung-Won & Seung-Jun (2016) and Farzad et al., (2019). The procedures of casting the cold joint specimens and roughening the joint plane in-between the casting were similar to such studies.

3.5.5. Concrete handling

3.5.5.1. Handling of fresh concrete

The fresh concretes were cast into the wooden beam and plastic cube moulds once the moulds had been coated with mould-release oil. The concrete mixer was left to run until all of the casting was performed to minimise the loss of plasticity in the setting stage. The setting time that is specified under the 52.5 R class in SANS 50197-1 (SANS, 2011), of less than 60 minutes, was used as a limitation for the casting. The setting and hardening rates during cement hydration are not the same,

in fact ordinary and rapid-hardening Portland cements have a similar setting time (Neville, 2011). The conditions wherein the casting was performed were assumed to conform to SANS 5861-1 (SANS, 2006), within a temperature of 22-25 °C.

The test specimens were cast by filling the moulds in 50 mm deep layers, each compacted by a vibrating table, as specified in SANS 5861-3 (SANS, 2006). The moulds of the monolithically-cast specimens were filled with the first portion of the specimen moulds that contained a cold joint. The remainder of the concrete on the other side of the joint was then poured into the moulds after a time delay of 24 hours and joint roughening in-between the casting. The mixture volumes of the test specimens were calculated from the volumes of all the beam and cube moulds without the wooden or Perspex stoppers and steel bar. A wastage volume of 10 % was taken into account in the calculation of the volumes of the trial mixtures and specimen casts. The concrete layers were each vibrated for 5-10 s to not cause an excessive movement of the stoppers and steel bar in the specimen moulds.

After the casting was completed the specimens were left to stand in laboratory conditions so the concrete could set and harden. The beam and cube moulds were covered with plastic sheets to minimise the evaporation rates, which may result in shrinkage cracks at a concrete surface. The initial set defines the time for concrete handling where after the final set is the start of strength development (Domone & Illston, 2001). The monolithically-cast specimens were stored for 24 hours, as specified in SANS 5861-3 (SANS, 2006), whereas the specimens with a cold joint included a time delay of 24 hours. The concrete in these moulds was thus stored for 48 hours which placed an importance on the extent of the roughening work.

3.5.5.2. Handling of hardened concrete

The specimens were de-moulded after the storage period wherein the concrete had set and begun to harden in the beam and cube moulds. A compressed air machine was used to de-mould the cubes while the beams were de-moulded after removing the wood screws, spacer blocks and stoppers. The beam moulds were constructed

to enable an easier removal of the concrete so that was less damage to the surfaces and corners. Mould-release oil was used to reduce the bond strength between the concrete and moulds and the specimens were scraped with a trowel to remove any excess concrete, once de-moulded. The specimens were stored to cure until the exposure or until selected ages for testing the strength and durability indices.

There are 2 broad divisions of curing; wet and membrane, recognising that actual procedures differ widely, based on factors such as construction practice, specimen dimensions, etc. (Neville, 2011). The curing was performed by submergence in a tank with tap (potable) water that was maintained within a temperature range of 22-25 ° C, as specified in SANS 5861-3 (SANS, 2006). The specimens that were exposed to the corrosive conditions were cured for 28 days which is the minimum curing duration for structural concrete in most of the design standards worldwide. The transport properties of the circular discs were initially tested after 28 days, to determine the concrete resistance to gasses, moisture and ions before exposure.

The testing period of the strength and transport properties was sub-divided as the early-age and long-term, of up to 28 and 90 days, respectively. The majority of the strength of concrete with rapid-hardening cement is yielded within 2 days under the 52.5 R strength class in SANS 50197-1 (SANS, 2011). The early-age strength was tested after 2, 7, 14 and 28 days of curing, which is when the rapid-hardening cement was most reactive. The strength after 2 and 28 days was also compared to the conformability tests at the Afrisam plant, against that required in SANS 50197 -1 standard. The strength and transport properties were then tested after 56 and 90 days to determine the contributions of the fly ash and metakaolin.

3.6. Preliminary testing

3.6.1. Overview

There was testing before the start of exposure as a baseline for comparison to that induced by the exposure to chloride and carbon dioxide. The corrosion behaviour,

chloride penetration and carbonation depths were a response to the exposure, for comparison to the baseline results after 28 days of curing. The cracks apparent on the surface of the reinforced beams at the same stage provided some certainty that the cracks after the exposure were corrosion-induced. The cover depth to the steel in the beams was also measured before the exposure as this parameter may vary from the planned cover depth. The measured cover depths of the beams are listed as the minimum, maximum and average in sets of 3 specimens in **Appendix C**.

3.6.2. Cover depth testing

The cover depths of the beams were measured using metal detection apparatus, as the closest level between the steel bar and exposed surface. The measurement was performed using the Elcometer 331 cover metre which is suitable for cover depths of less than 70 mm. Elcometer is a multinational company that develops apparatus for non-destructive testing, such as cover depth meters and corrosion monitoring apparatus. A typical measurement of the cover depth with the probe of the cover metre at the mid-span/ cold joint position in the beams is shown in **Figure 3.12**. The metal detection probe was placed on the exposed surface and orientated in the line of the steel bar, to measure the depth to the closest steel surface. A number of factors are influential to cover depth measurement, mostly the steel bar diameter in question and signal range of the metal detection probe (Barnes & Zheng, 2008). The standard probe was used, which was adequate as there was only a single steel bar, whereas narrow pitch probes are used when steel bars are closely placed.

The cover depth was measured at the mid-span and either end of the beams which translated to a spacing of 130 mm between these test locations. The cover depth at the bar ends was also included to determine if there were significant differences in the cover depth away from the mid-span. The actual cover depth was anticipated to vary from that planned due to factors such as the casting, steel bar preparation and alignment over the bar length. The epoxy coating at the bar ends was applied in 3 coats which increases the cover depth by up to 2 mm, as per the manufacturer specifications. The vibrating table was anticipated to cause some movement of the bar although this could be resisted to an extent by the mass of the fresh concrete.



Figure 3.12: Cover depth testing

3.7. Exposure conditions

3.7.1. Overview

The exposure to chloride and carbon dioxide was intended as unidirectional, into a surface of interest on the test specimens. The reactions of chloride penetration and carbonation occurred at the exposed surfaces while the perpendicular surfaces remained inert. Chloride penetration and carbonation in concrete is however multi -directional in reality and approximated using the laws of diffusion. The exposure was done in a cyclic manner using a chloride solution and accelerated carbonation to replicate the tidal zone of urbanised settlements. Carbonation is slower in wet concrete thus cyclic exposure was used to promote the simultaneous penetration of chloride and carbonation. Corrosion is also hindered in continuously dry or wet concrete due to a need for moisture as an electrolyte and oxygen at the steel level.

3.7.2. Ponding on beam specimens

The chloride exposure was performed using a sodium-chloride solution that could absorb into the un-coated surfaces of the beam and cube specimens. The solution

was ponded in dikes on the exposed surface of the beams which spanned the un-coated length of the steel bar, as shown in the drawing (a) and photograph (b) in **Figure 3.13**. The dikes were cut of 5 mm Perspex sheets and then were bonded at their corners using Magmabond C1, a suitable bonding product for cast-acrylic. The ponding method in ASTM C 1543 (ASTM, 1999) was followed in terms of the geometric requirements of the ponding area on the exposed surface of the beams. This method is applicable to concrete that has not been treated with any type of concrete coating which decreases the ingress of gasses, moisture and ions.

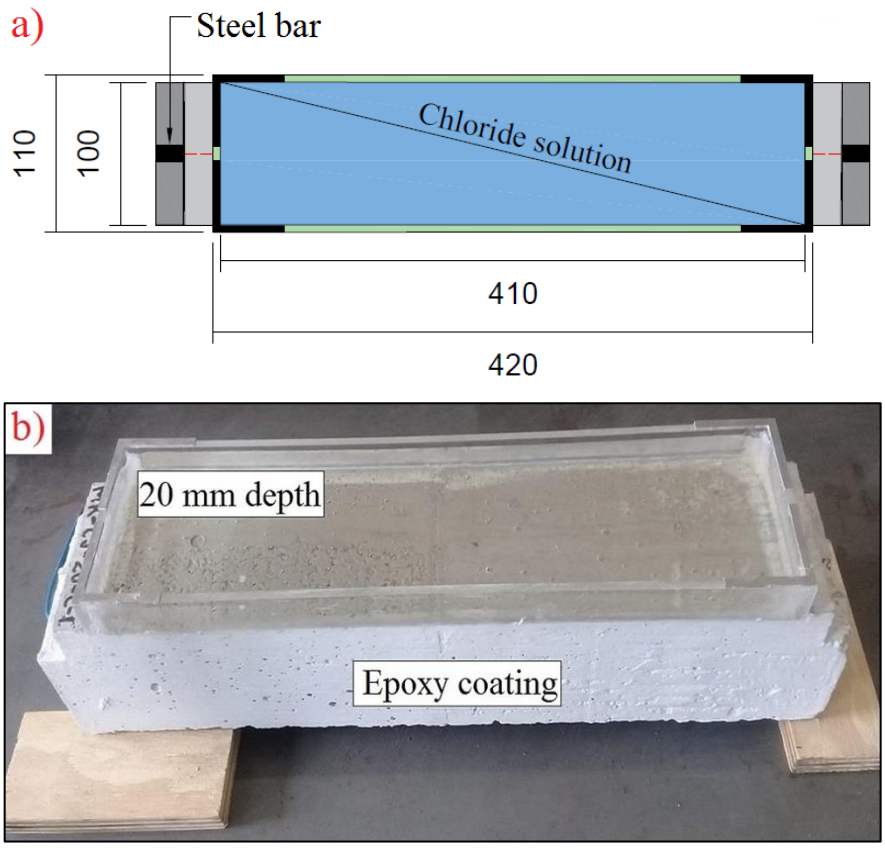

Figure 3.13: Chloride solution ponding details

The chloride solution was prepared by dissolving AR grade (Analytical Reagents) granules of sodium-chloride in distilled water. This was ponded on the exposed surface of the beams while the cubes were submerged in a tank with a similar volume to the curing tank. The sodium-chloride was dissolved in distilled water as a content of 5 % by mass, which is common for studies on combined exposure to chloride and carbon dioxide. The Perspex ponds were covered with plastic sheets

to reduce the evaporation rate, in the same manner as in the curing stage. The pond surface area of 0.041 m^2 falls within that the area that is required, larger than 0.03 m^2, and was calculated as the entire beam width (100 mm) over the un-coated length of steel. A solution depth of 20 mm is the maximum value in the ASTM C 1543 for ponding to increase the hydrostatic pressure onto the concrete.

3.7.3. Exposure to carbon dioxide

The carbonation chamber was set-up as a closed system with a significantly high carbon dioxide content compared to that in the atmosphere. A carbon dioxide content of 5 % was maintained in the chamber within a small tolerance of 0.5 % to achieve an accelerated rate of carbonation. This high carbon dioxide content is the same as in a number of studies on combined exposure, as discussed in **Section 2.7.2** of the literature review. An electronic control unit was used for maintaining the carbon dioxide content by continuously sampling and applying the carbon dioxide gas into the chamber. The chamber geometries, operation and connections to this control unit, gas supply and sampling tube are illustrated in **Figure 3.14**.

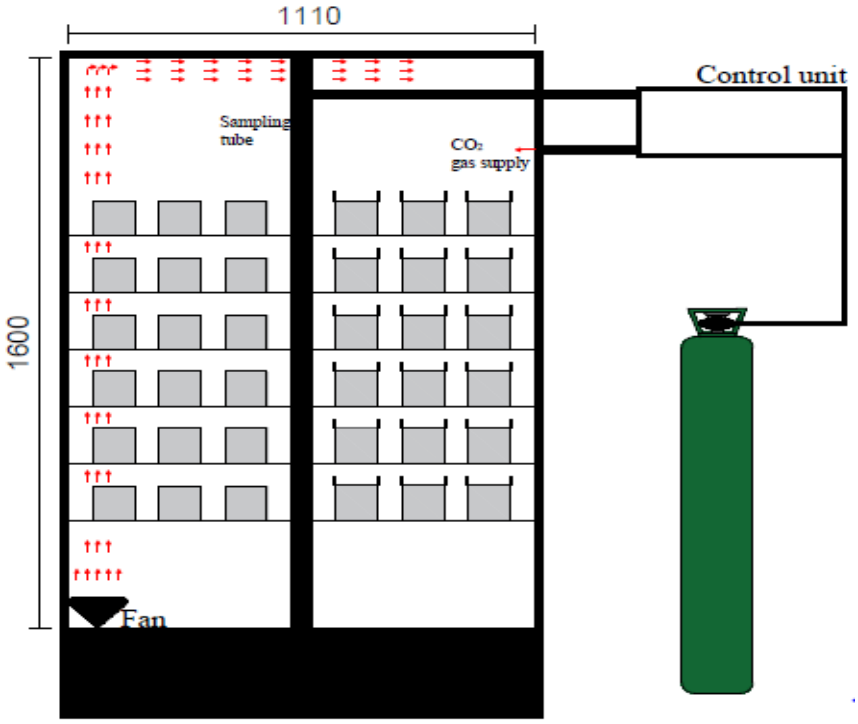

Figure 3.14: Carbonation chamber operation details

The gas was supplied from the cylinder in **Figure 3.15** (a), which was regulated at 5 kPa for a suitable pressure in the inlet pipe. The cylinder contained 31.3 kg of pressurised carbon dioxide of an instrument-grade (IG) quality which is used in laboratories. The control unit (b) was calibrated to the requirements of the South African National Accreditation System (SANAS) to maintain a constant carbon dioxide content. The values that are shown in the interface are the carbon dioxide content from a sampling tube (sampled value) and input value to be maintained in the closed system. The carbon dioxide gas was sampled using a plastic tube that had 3 mm diameter holes over its length, at a spacing of approximately 50 mm.

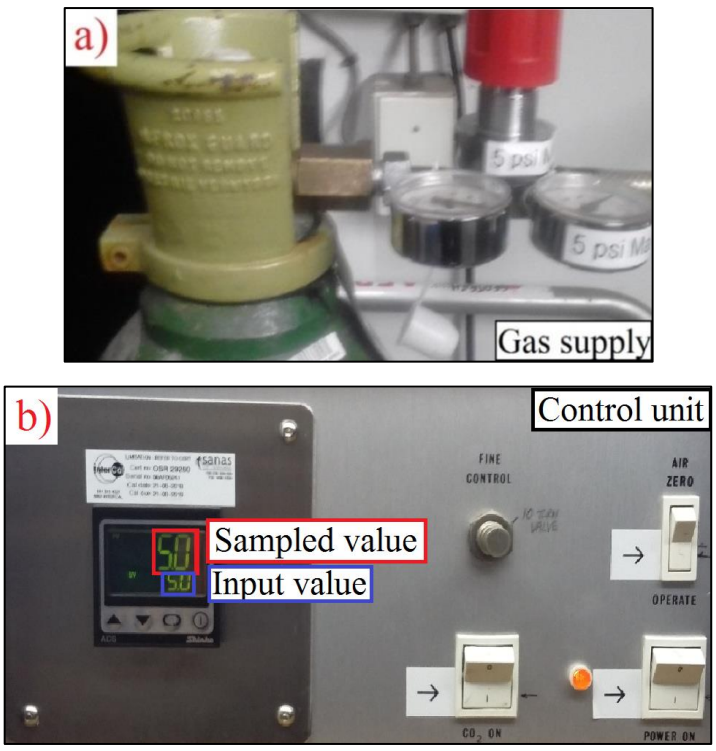

Figure 3.15: Carbonation chamber control unit and gas inlet

The control unit was calibrated to maintain a carbon dioxide content of up to 20 % at a sampling frequency of 5 minutes, to control the inlet pressure. At start-up, the carbon dioxide gas was pumped freely into the chamber until the lower bound of 4.5 % was reached, which took about 20 minutes. The control unit then decreased the pressure from the inlet, abruptly, while the carbon dioxide content stabilised at the selected value, of 5 %. The sampling frequency was adequate to prevent the carbon dioxide content from increasing too far beyond the upper limit of 5.5 % in

the start-up process. A fan was placed at the bottom corner of the chamber, facing the top, to not face the sampling tube, and to disperse the gas in a circular motion, as shown in **Figure 3.14**. The operation is illustrated simply by the movement of gas into and within the chamber (red) when the concentration had stabilised.

The relative humidity in the chamber had to be relatively constant, close to, or within the optimal range for carbonation, of 40-60 %. The chamber however had to house the concrete specimens which could expel some of the moisture of the ponding periods into the close system. The relative humidity had to be reduced to not allow the additional moisture to create a condition of saturation, at a relative humidity of 100 %. A saturated solution of magnesium chloride and potable water was used to promote a relatively constant relative humidity in the closed system. The saturated solution in Wexler & Hasegawa (1954) was used as it maintained a relative humidity within a small range of 30-35 % at temperatures up to 48 °C.

3.7.4. Application and monitoring of the exposure

3.7.4.1. Cyclic exposure regimes

The influence of carbonation on chloride penetration was based on the manner in which the exposure conditions were applied. The exposure conditions consisted of a regime of combined exposure to chloride and carbon dioxide and a reference of isolated exposure to chloride, for comparison. The sub-division of the exposure regimes in each of the exposure cycles, which lasted for 14 days, is illustrated in a timeline in **Figure 3.16**. The exposure periods of the chloride solution and carbon dioxide lasted for 3 and 9 days respectively, under an assumption that the chloride penetration was faster. The exposure cycles were thus sub-divided in a 1-to-3 ratio, with 2 days of drying in-between to open the paste pores before carbonation.

Day	1	2	3	4	5	6	7	8	9	10	11	12	13	14
Isolated chloride exposure	Chlorides			Drying										
Combined exposure	Chlorides			Drying		Carbonation								

Figure 3.16: Application of exposure regimes

Similar exposure regimes have been used to incorporate a cyclic approach instead of extended periods of chloride solution or carbonation. Studies such as Pakawat & Uomoto (2005) and Yoon (2007) made use of a 3-day wetting period for the combined exposure to chloride and carbonation. The chloride content beyond the carbonation depth was increased due to the loss of bound chloride, using exposure durations of 6 months to 1 year. Chloride penetration was regarded to be optimal in Hong & Hotoon (1999) by using a 3-day wetting period for the cyclic exposure to chloride in isolation. The duration of exposure herein was selected to be 294 days, or 21 cycles, so that the carbonation was influential to chloride penetration.

3.7.4.2. Temperature and relative humidity monitoring

The temperature and relative humidity were monitored over the course of the exposure period in the immediate vicinity of the specimens. The monitoring was performed with electronic data-loggers which were placed beside the concrete specimens and set to a recording frequency of 2 hours. The data records were used to establish time series' of the temperature and relative humidity which may be found in **Section 4.4** of the results. The behaviours of these parameters in the data records could be compared between that recorded in the laboratory and in the carbonation chamber. The influence of temperature and relative humidity on the corrosion rate was also determined from the measured values in **Section 4.5.4.7**.

3.8. Compressive strength testing

The compressive strength of the concretes was tested to assess the influence of the cement replacement on the strength development. The cube crushing test in SANS 5863 (SANS, 2006) was followed which is based on the compressive stress due to uniaxial loading, until failure. The strength was calculated as the average in sets of 3 cubes at each age with the results considered as valid if the minimum and maximum strength in the cube set did not exceed the average strength by 15 %. The loading was performed in the direction of casting with a uniform rate of 0.25 MPa/s until failure, where the failure load and appearance of the cube fracture was

recorded. The compressive strength (fc) was calculated in MPa units as the stress dispersed in the cubes under the failure load in kN units, using **Equation 3.4**.

$$f_c = \frac{F}{A_c} \qquad \text{Eqn. 3.4}$$

where:

- F (kN) denotes the failure load and
- A_c (mm^2) denotes the load-bearing (cross-section) area.

3.9. Durability testing

3.9.1. Durability index testing

The first of the sub-divisions on durability testing was focussed on the transport of gasses, moisture and chlorides in the cover concrete. The circular disc specimens were tested to assess the influence of the cement replacement and cold joint on the transport properties. The test methods of the oxygen permeability and chloride conductivity indices are specified in SANS 3001-CO3-2 (SANS, 2015) and SANS 3001-CO3-3 (SANS, 2017) respectively. The water sorptivity was not formalised at the time of the tests so the South African Durability Index manual (Alexander, 2017) was followed. The durability indices were calculated as the average in sets of 4 discs with the results considered as valid is only 1 test was not accepted.

The test procedures are discussed in this section and the minimum, maximum and average between 4 discs at each curing age are listed in **Appendix C**. The tests were performed after 28, 56 and 90 days of curing, the minimum of which was the curing duration before the start of the exposure. The oxygen permeability test is dependent on the amount and connectivity of the largest pores, the result of poor compaction and bleeding (Mackechnie, 1996). Sorptivity is dependent on the sizes of pores and their connectivity mainly in the surface region, where there is cyclic fluctuation of moisture. Chloride penetration is dependent more on the binder composition as alumina compounds can bind to the free (or diffusible) chlorides.

3.9.1.1. Oxygen permeability index

The oxygen permeability index (OPI) was tested to assess the overall macro- and micro-structure connectedness of the circular discs. The resistance to pressurised gas is sensitive to the presence of larger pores in that imperfections such as cracks short-circuit the transport paths. A purpose-built permeability cell was used in the test, which pressurised the oxygen gas through the discs in the direction of the arrows in **Figure 3.17**. The test set-up was such that the oxygen gas penetrated the outer surface of the discs, which occurs at exposed surfaces of concrete structures. A rubber collar was compressed around the discs with the intention of the oxygen gas penetrating through their thickness entirely, and not lost due to leakages.

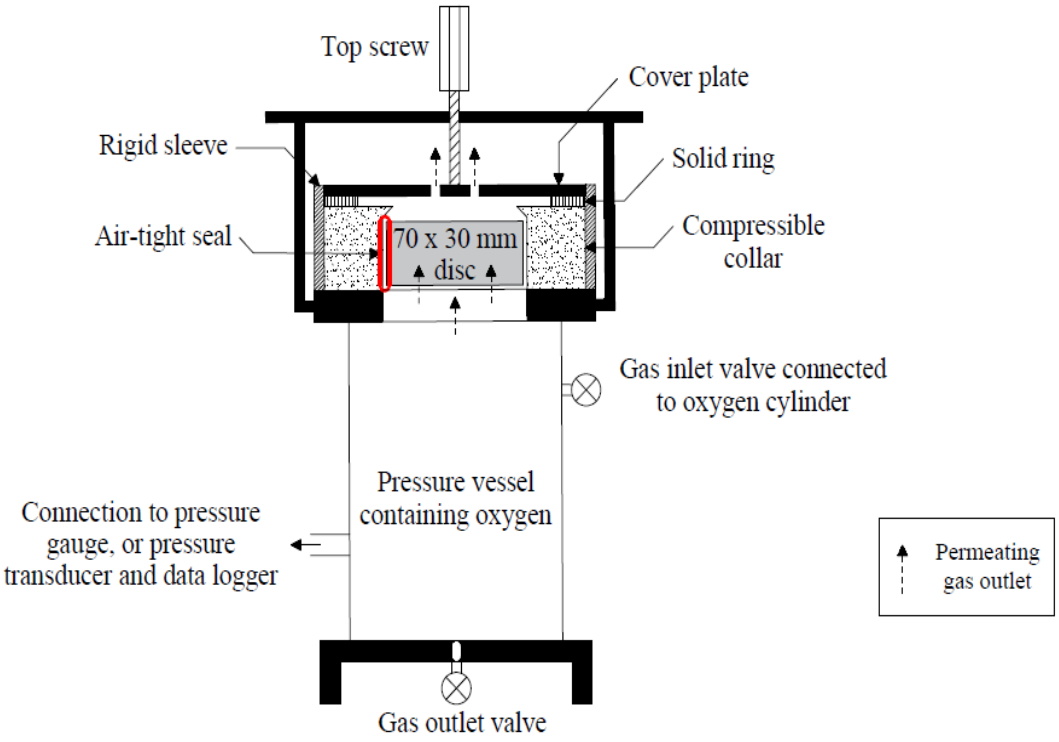

Figure 3.17: Oxygen permeability testing

The test was developed by Ballim (1993) and entails the pressure drop through the discs at regular intervals in a monitoring period of 6 hours. The pressure drop rate of the gas is described by the Darcy equation which is based on the flow through a porous medium. The monitoring started once the pressure had stabilised within a pressure range of 100 ± 5 kPa, which was dependant on the seal between the disc

and rubber collar. The pressures were recorded to the nearest 10^{-8} pA, in 5-minute intervals, using an electronic data-logger, to establish a time series of the pressure drop through the discs. The recording period was done either when the pressure of the system had reached 50 ± 5 kPa, or after a duration of 6 hours ± 15 minutes.

The pressure drop in the test was accepted based on the correlation coefficient of a linear regression between the initial pressure (P_0) and pressure over time (P_t). The regression function was forced through the time and pressure origins and the slope used to calculate the Darcy permeability coefficient (K). The regression function is required to have a correlation coefficient of larger than 0.99 for the test to be considered as valid. The K-value was calculated from the slope of the regression function (z) and permeability cell volume of 5 litres, using **Equation 3.5**. The OPI is the negative log of K, which is expressed on a logarithmic scale, within a range of 8-11 in Alexander et al., (1999), with higher values in less-permeable concrete.

$$k\,(m/s) = \frac{w\ V\ g\ d\ z}{R\ A\ T} \qquad \text{Eqn. 3.5}$$

where:

- w (kg/mol) denotes the molecular mass of oxygen, i.e. 0.0032 kg/mol,
- V (m^3) denotes the permeability cell volume,
- g (m/s^2) denotes the gravitational acceleration i.e. 9.81 m/s^2,
- R (Nm/Kmol) denotes the universal gas constant i.e. 8.313 Nm/ Kmol,
- T (Kelvin) denotes the absolute temperature,
- d (mm) denotes the thickness,
- A (mm^2) denotes the cross-section area.

3.9.1.2. Water sorptivity index

The water sorptivity index (WSI) was tested to assess the ability of the concretes to absorb the chloride solution in the wetting periods. This parameter is a suitable measure of the pore sizes and their connectivity within the surface region, in terms of the absorption resistance (Alexander et al., 1999). Of the durability indices, the

WSI was regarded as the least reliable in Beushausen & Alexander (2008), against the internationally-accepted methods. The circular discs were allowed to absorb a solution of calcium hydroxide into the exposed (outer) surface, as illustrated in the set-up in **Figure 3.18**. The outer face was placed faced down on a tray with 10 paper towels and a solution of 5 g calcium hydroxide and 1 litre of tap water.

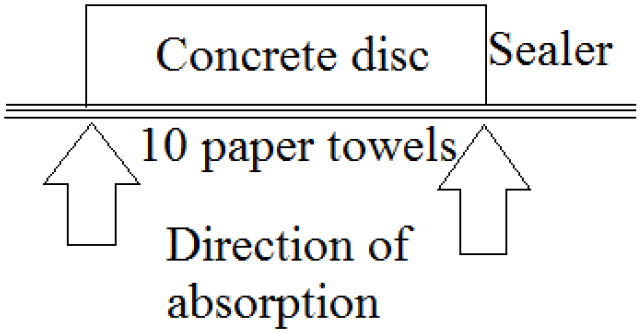

Figure 3.18: Water sorptivity testing

The test was developed by Ballim (1993) where in its modified form in Alexander (1999) involves measuring the mass gain due to absorption. The recording period was started at first contact with the solution where after the mass was measured at 3, 5, 7, 9, 12, 16 and 25 minutes, and at saturation. The curved face of the discs (perimeter) was sealed using Sellotape to promote a condition of unidirectional absorption into the test face. The saturation was performed in accelerated manner, using a vacuum-saturation system for 18 hours, starting after the masses of the 25-minute period had been measured. The discs in the chloride conductivity test were saturated with this vacuum-saturation system, as discussed in **Section 3.2.1.4**.

The sorptivity of the circular discs was determined based on the linear regression of a function between the mass gained due to absorption and square root of time. The regression function is required have a correlation coefficient of larger than 0.98 for the test to be considered as valid. The sorptivity in $mm/\sqrt{hour}$ units was calculated from the slope of the regression function (F) and disc mass before and after the vacuum saturation, using **Equation 3.6**. The WSI is expressed on a linear scale, within the range of 5-15 in Alexander et al., (1999), in a direct relationship

with the concrete permeability. The porosity (total void content) of the discs (n) was also calculated from the dry and saturated masses, using **Equation 3.7**.

$$S = \frac{Fd}{M_{sv} - M_{s0}} \quad \text{Eqn. 3.6}$$

$$n = \frac{M_{sv} - M_{s0}}{Ad\rho_w} x\,100 \quad \text{Eqn. 3.7}$$

where:

- F denotes the slope of the regression function,
- M_{sv} (g) denotes the vacuum saturated mass,
- M_{s0} (g) denotes the dry mass (at time t_0),
- ρ_w ($10^{-3}g/mm^3$) denotes the density of water and

3.9.1.3. Chloride conductivity index

The chloride conductivity index (CCI) was based on an accelerated diffusion test, to assess the resistance of the concretes to chloride penetration. Chlorides are able to penetrate through all the pores of an adequate size in the test, without favouring the larger pores, as in the OPI and WSI tests (Gous et al., 2001). The CCI test was established in Streicher & Alexander (1995) and involves measuring the current across the circular discs due to an applied voltage. The anode and cathode parts of the conduction cell, wherein the discs were housed in the test, are illustrated in **Figure 3.19**. The electrical connections to a DC power source, which applied the voltage across the discs, and ammeters, for measuring the current, are shown.

The circular discs were pre-conditioned by vacuum-saturation in the same manner as the WSI test, using a sodium-chloride solution. The chloride solution also was poured into the anode and cathode parts of the conduction cell, before the voltage was applied across the discs. The chloride solution was mixed 24 hours before the start of the saturation, in a ratio of 2.93 kg reagent-grade salt and 10 litres of tap water. The DC power source was adjusted until the voltage across the disc had stabilised at around 10 V and the current corresponding to the nearest value was

recorded. The other durability indices were tested using the same set of 4 discs at each age whereas separate sets for each concrete were prepared for the CCI test.

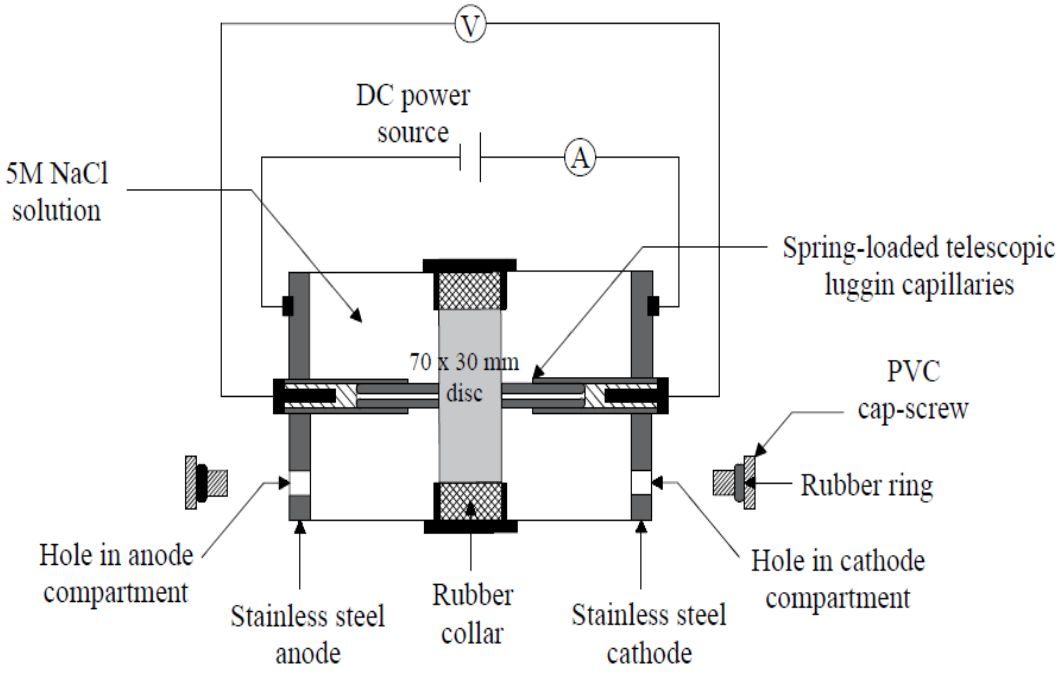

Figure 3.19: Chloride conductivity testing

The chloride conductivity in mS/cm units was calculated from the applied voltage (V) and measured current through the circular discs using **Equation 3.8**. The CCI is expressed on a linear scale, within a range of 0.75-2.5 mS/cm in Alexander et al., (1999), in a direct relationship with the concrete permeability. The porosity of the circular discs was also calculated from the measured dry and saturated masses, in the same manner as the water sorptivity test. A chloride solution density of 1.19 x 10^{-3} g/mm^3 was used to calculate the porosity, which is higher than the calcium-hydroxide solution. The porosity trends over the curing period from 28 to 90 days were compared with the other durability indices in the results in **Chapter 4**.

$$\sigma = \frac{id}{VA} \qquad \text{Eqn. 3.8}$$

where:

- i (mA) denotes the measured current and
- V (V) denotes the voltage applied.

3.9.2. Penetration state testing

3.9.2.1. Overview

The second of the durability sections was focussed on the chloride penetration and carbonation states that had accumulated due to exposure. The chloride penetration in the beams was determined using chloride profiles, which is the chloride content in depth increments spanning the cover region. The profiles were established as the total chloride content in concrete samples that were extracted after drilling into the concrete surface. The influence of the cement replacement, cold joint and carbonation in the beams was determined from the chloride contents in the surface region and at the steel level. The carbonation depths that were measured in cubes with the same section dimensions were used as an estimate of that in the beams.

The concrete sampling, chemical analysis of the chloride content and carbonation measurement are described in this section. The concrete sampling for chloride was performed after the exposure period of 21 cycles (or 294 days) as the concrete had to remain intact for the corrosion monitoring. The chloride penetration into the cover concrete of the beams after selected durations was a cumulative response to the exposure conditions. The duration of exposure prior to the sampling is greater than the minimum of 3 months which is recommended for ponding in ASTM C 1543 (ASTM, 1999). The carbonation depth in the cubes was measured after 10 and 21 cycles of exposure, as an estimate of that in the beams after the same ages.

3.9.2.2. Cover concrete sampling

The chloride profiles were established using dust samples that corresponded to constant increments in the cover depth to the steel level. Dry-drilling is considered to be the most detailed representation of chloride penetration from the methods in RILEM TC 178-TMC (RILEM, 2013). This sampling method is used due to its simplistic nature, in terms of extraction and preparation, instead of grinding layers of the cover concrete. The drill bit diameter and thickness of the depth increments

are factors to the sample size and detail that is represented in chloride profiles. The chloride content of concrete varies largely at the interface between aggregates and paste thus the smallest stone sizes at Afrisam were considered as suitable.

The beams were sampled at the mid-span with a 22 mm masonry drill bit over the centre-line of the steel, as shown in the drawing (a) in **Figure 3.20**. A photograph of the drilling set-up (b) shows that the sampling was performed using a drill press with the centre of the bit tip aligned to the mid-span. The spacings between the drill bit and edges of the Perspex dike in either direction were greater than the minimum of 25 mm in ASTM C 1543 (ASTM, 1999). The ponds were removed from the beams after the exposure along with excess salt crystals, to not influence the chloride contents. The samples were weighed and then stored in vials until the chemical analysis, to reduce the contact with the moisture in the atmosphere.

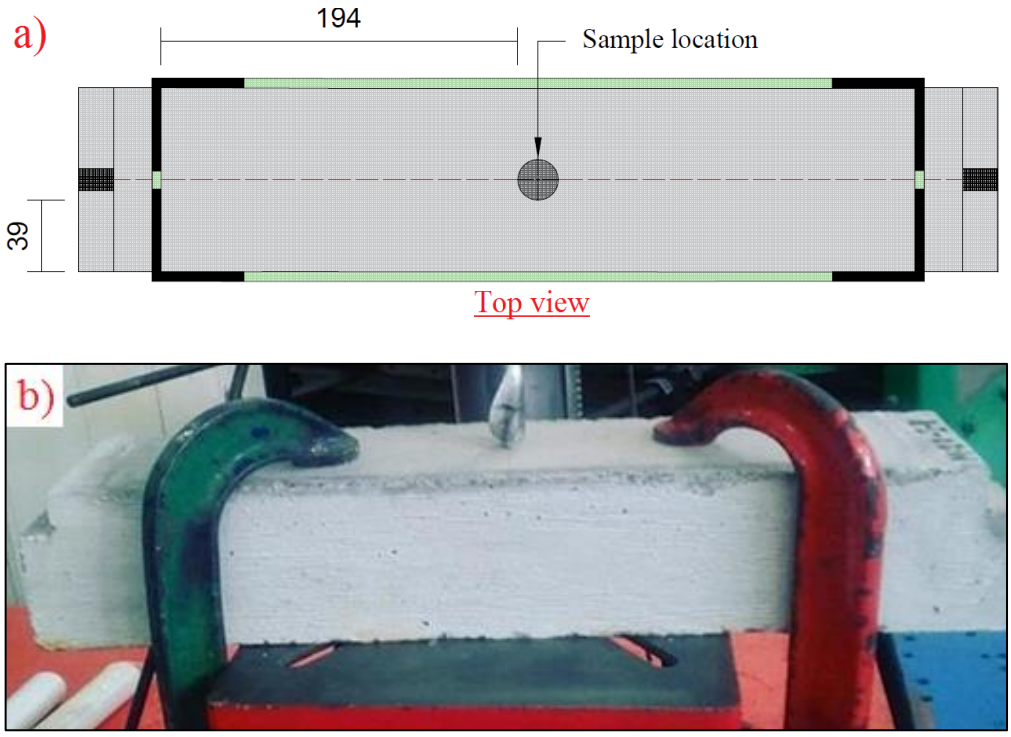

Figure 3.20: Reinforced beam sampling location and drilling set-up

The chloride profiles were established with depth increments of 5 mm and a range based on the cover depth to the steel, 10 mm or 20 mm. The chloride content in each depth increment of the profiles and corrosion behaviours were represented by

the average in sets of 3 beams. A baseline of the chloride content was determined for each concrete after 28 days of curing, to be subtracted from that after 21 cycles (or 294 days) of exposure. This took into account the impurities that were present in the dry materials and that absorbed into the concrete during the curing period of 28 days. The minimum, maximum and average of the chloride contents in each of the depth increments are listed as the % mass of the sample in **Appendix G 1**.

The baseline samples were obtained from separate un-reinforced (plain) beams with the same dimensions as the reinforced beams. The details of these beams are not discussed together with that of the reinforced beams in **Section 4.3.2.1** as they had the same dimensions. The plain beams were used as the cover concrete had to be intact at the start of exposure to not influence the transport of gasses, moisture and ions. It is worth mentioning that these plain beams were planned to be used to compare the chloride contents to that in the same cover depths in the reinforced beams. There was however too many samples together with the plain beams so the focus was placed on that in the reinforced beams, which induced the corrosion.

3.9.2.3. Chloride penetration testing

The concrete resistance to chloride penetration was determined using the chloride contents in the surface region and also at the steel level. Chloride penetration into partially-saturated concrete is dependent on the sorptivity of the surface region and chloride binding mainly in the bulk concrete. The chloride content at the steel level reflects the present extent of corrosion, although the entire profile allows the future corrosion risk to be determined (Broomfield, 2007). The chloride profiles were used to determine the transport mechanisms that either hindered or promoted the chloride penetration between the surface region and steel level. There would have been more certainty if the free chloride fraction was included in the scope of testing although all chloride is considered to be free in fully-carbonated concrete.

There are a number of methods for the chloride content in concrete; field methods are rapid but of a poor accuracy whereas laboratory methods are time-consuming. These methods usually comprise of 4 sequential steps to test the chloride content;

sampling, crushing, acid dissolution and chemical testing (Bertolini et al., 2013). The total chloride content in the samples was measured using the Dionex DX-120 Ion Chromatograph which performs isocratic ion analysis. Dionex is an American -based company that develops analytical chromatography systems for separating, isolating and identifying the components of mixtures. The main components include the guard column, analytical column, injection valve and self-regenerating suppressor (SRS). The positions of these components in the apparatus are labelled 1 to 4 to describe the operating procedure in the photograph in **Figure 3.21**.

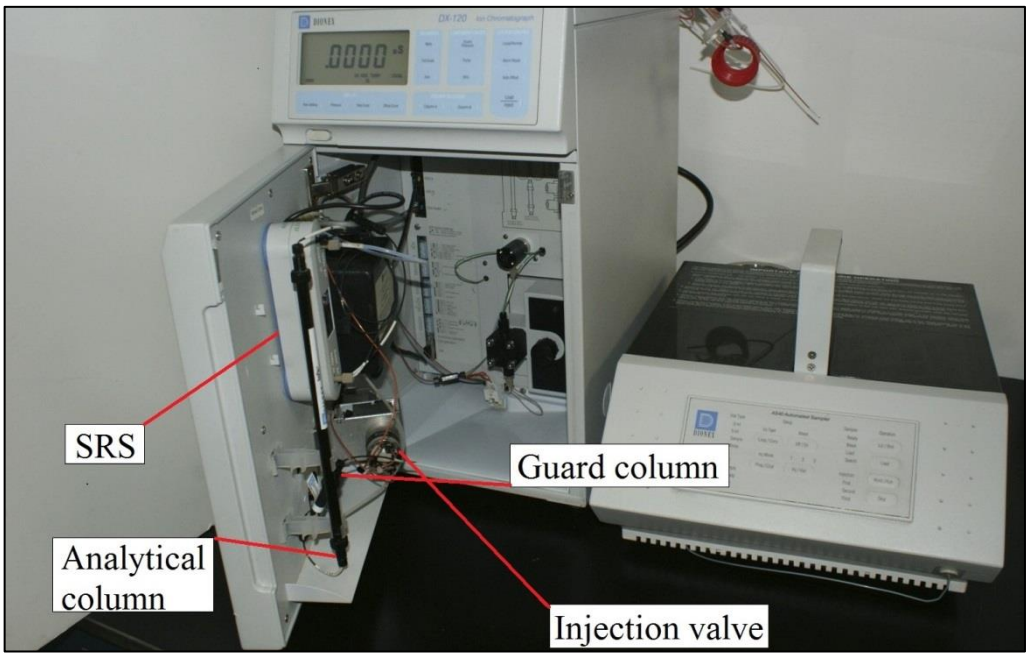

Figure 3.21: Total chloride testing

Ion-exchange chromatography is a method for separating the ionic components in mixtures based on the ionic (electrostatic) interactions. The chloride ions in the samples were separated in the analytical column (1) once they were digested to be in a liquid form. The system was pressurised with a solution of a constant chloride content and flow rate, as a reference for comparison to the sample solution, with various compounds. The apparent velocities were different between these various compounds such that the chlorides in the sample solution were separated based on the differential partitioning. The chloride content in the sample was determined in terms of the change in conductivity when the differential partitioning took place.

The sample solution was introduced to the analytical column through the injection valve (2), after it filled a loop, to be pressurised. The loop had to be filled entirely by the sample solution before the injection occurred, and the excess was diverted elsewhere, to be disposed. The guard column (3) was located before the analytical column which prevents any damage to the system due to impurities in mixtures. The self-regenerating suppressor (/s) (SRS) maintained the chloride content of the reference solution and enhanced the conductivity of the analyte solution, after the separation. The fluctuation of the solution conductivity throughout the system was reduced so that the conductivity after the separation could be clearly determined.

3.9.2.4. Carbonation depth testing

The carbonation depths in the reinforced beams were represented by the measured depths in cubes with the same section dimensions (100 x 100 mm). The cubes were loaded to result in a tensile fracture using a manual compression machine in the set-up in **Figure 3.22**. The force was applied into the cubes at the single point, as shown, so that the tensile fracture was propagated to between the plates below. The carbonation depth was measured after spraying a solution of phenolphthalein, which distinguishes the alkalinity (pH) between the surface and bulk regions of concrete. The carbonation depths were calculated as the average in sets of 2 cubes, which are listed together with the minimum and maximum in **Appendix D 2**.

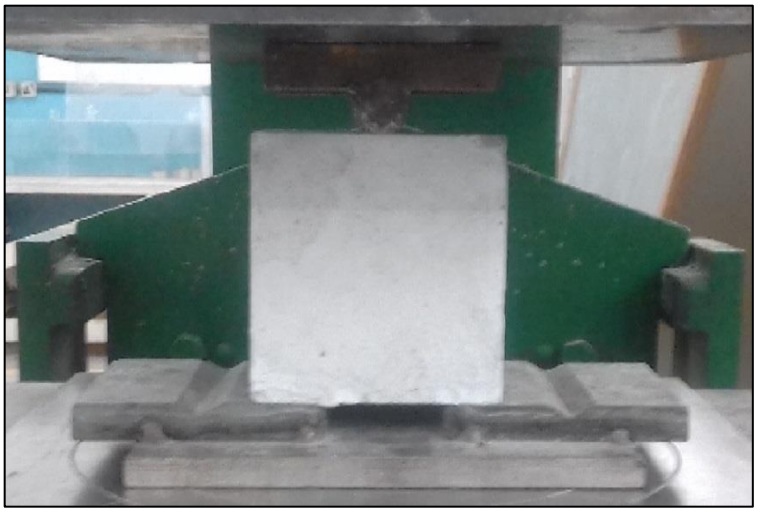

Figure 3.22: Cube fracturing set-up

Carbonation testing is discussed in **Section 2.6.4** of the literature review where the phenolphthalein solution is a simple indicator of fully-carbonated concrete. There are other tests such as X-ray diffraction (XRD) and thermal gravimetric analysis (TGA), which also identify the partially-carbonated concrete. The phenolphthalein test discerns the fully-carbonated concrete only by a rapid colour change of the sound concrete, while the surface remains colourless. The fully-carbonated region is regarded to have a pH value of around 9.5, as the alkalinity of the pore solution is neutralised. In sound concrete, beyond the fully-carbonated region, the solution turns dark purple on the fractured surface, to indicate a high pH range of 13-14.

The phenolphthalein solution was considered as suitable for the carbonation depth as all chloride in the fully-carbonated region is regarded as free. A baseline of the carbonation depths (before exposure) and that measured after 10 and 21 cycles are presented in **Section 4.5.3.5** of the results. Photographs of the fractured cubes with the phenolphthalein solution on are included to illustrate the measurement at the cube faces. The carbonation depth was measured to where there was a strong colour change to purple, using a solution of 1 % phenolphthalein powder by mass in isopropyl alcohol. The measurement was performed over 5 points at each cube face, which were equally-spaced, to then be averaged between all the faces.

3.9.3. Corrosion monitoring

3.9.3.1.Overview

The main section of the durability was focussed on the corrosion behaviour of the embedded steel as a continuous response to the exposure. The corrosion behaviour was monitored for a period of 294 days to determine the influence of the cement replacement, cold joint and carbonation on the corrosion resistance. A number of parameters were part of the corrosion monitoring scheme, viz. electric potential and corrosion rate of the embedded steel, and electrical resistivity of the concrete. The change in electric potential of the embedded steel against a reference half-cell that was placed on the concrete surface was the basis of these electrochemical

testing. The test set-ups and procedures are discussed herein and the principles of common electrochemical tests are in **Section 2.3.4.2** of the literature review.

The parameters were monitored based on the application of the exposure periods; 1 day after ponding, to dry out the surface, and on completion of the carbonation. A baseline of the parameters (before exposure) was measured after 28 days of curing for a comparison to that monitored up to 294 days of exposure. The results of the monitoring in **Section 4.5.3** are based on sets of 3 reinforced beams, which were also sampled for chloride after the exposure. The corrosion parameters were tested twice at each age and averaged to overcome electrical contact issues of the apparatus. The corrosion behaviours are plotted in the results and **Appendix E** against the increase in exposure duration, instead of listing all the readings.

3.9.3.2. Corrosion potential testing

The corrosion potential was measured as the voltage between the embedded steel and half-cell placed on the concrete surface. An electrical circuit was formed in the pore solution of the concrete which was based on the potential of the corrosion reactions. The variable potential of the steel was measured against 2 types of half-cell, of a stable potential; the copper-copper sulphate (Cu-$CuS0_4$) and silver-silver chloride (Ag-AgCl). The former was manufactured by a multinational company, Elcometer, to be compliant with that required in the ASTM C 876 (ASTM, 1999) standard. The Coulostat VIII unit was fully-integrated with an array of 3 Ag-AgCl half-cells and was manufactured to operate based on the Coulostatic method.

The concrete surface was pre-wetted using tap water before the testing and a wet cloth was used as an electrical junction under the apparatus probes. The tests were limited by an adequate circuit between the probes and pore solution thus any type of sealer creates a poor junction. The locations where the Cu-$CuS0_4$ half-cell and Ag-AgCl half-cell array were placed on the beams are shown in **Figures 3.23** and **3.24**, respectively. Photographs of the test set-ups with these apparatus are not included for the sake of brevity and instead the geometries of the probe bases are

shown. The Cu-$CuS0_4$ half-cell was placed at either end of the Perspex pond and at the mid-span, equating to a spacing of 200 mm from the cold joint to the beam ends. The Coulostat unit was restricted to being centrally-placed at the mid-span, due to its dimensions, where the half-cell array spanned a distance of 150 mm.

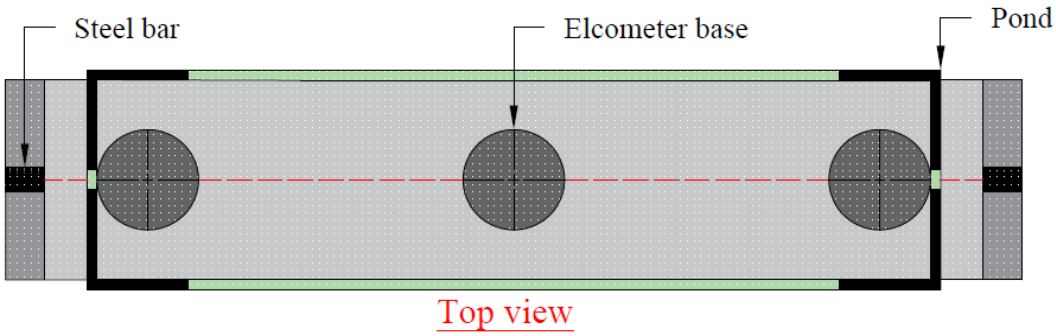

Figure 3.23: Elcometer half-cell locations

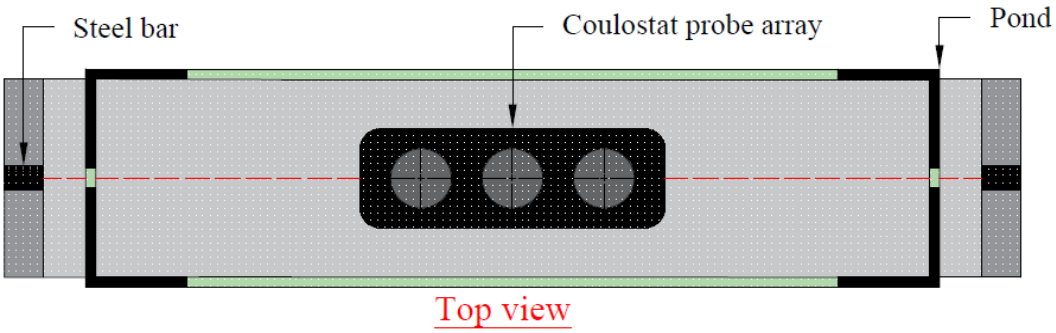

Figure 3.24: Coulostat half-cell location

The potential behaviours were classified with the ranges in ASTM C 876 (ASTM, 1999) which detects the existence of corrosion from the numerical magnitude. The relationship is limited to cover depths of less than 75 mm, so that the potential is not averaged between adjacent re-bars. The relationship between the potential and corrosion probability (in %) against the Cu-$CuS0_4$ and Ag-AgCl half-cells is listed in **Table 3.8**. The corrosion initiation of the beams was considered to occur when the potentials dropped to a value corresponding to a corrosion probability of 90 %. The conversion method in ASTM C 876 for potential readings of the common half-cells in practice may also be found in ASTM G3 (ASTM, 2014) and Ives et al., (1961). There are other sources that have recommended a conversion method between the potentials of common half-cells, such as that in Robberge (2008).

Table 3.8: Corrosion probability ranges (ASTM, 1999)

Voltage vs. Cu-$CuSO_4$ (mV)	Voltage vs. Ag-AgCl (mV)	Corrosion probability (%)
> - 200	> - 106	Low (10 %)
- 200 to - 350	- 106 to - 256	Corrosion activity uncertain
< - 350	< -256	High (90 %)
< - 500	< - 406	Severe corrosion

The relationship in **Table 3.8** is not recommended when concrete has carbonation or chloride at the steel level, is saturated, or has cyclic exposure to moisture. The limitations of potential measurement raise a requirement to use this parameter in conjunction with the corrosion rate. The temperature of the environment is also a factor to the potential due to the reactions between the metal probe and solution of its own ions, i.e. copper in copper sulphate. The equilibrium of the Cu-$CuS0_4$ half -cell is mostly influenced to a lesser degree by the temperature thus more suitable in structures (Song & Saraswathy, 2007). Both of the half-cell apparatus operated within a temperature range of 0-50 ° C, thus suitable for the laboratory setting.

Cracks, cold joints and dynamic structural activity result in localized corrosion, in that the potential may differ by up to several hundred mV over a small distance of below 300 mm (ASTM, 1999). While there is no pre-defined spacing, it is of little value to take multiple readings at the same point although a large spacing may not discern the corrosion activity (Paul, 2015). The spacing of the potential readings between the mid-span and beam ends was small compared to that available in full-scale specimens of structures. This was not anticipated to result in a large change to the potentials away from the cold joint at the mid-span, thus not identify if there was localised corrosion. The spacing between multiple locations is recommended in ASTM C 876 to be reduced if the adjacent potentials differ by over 50 mV.

3.9.3.3. Corrosion rate testing

The corrosion rate was measured as the density of the corrosion current over the steel surface using a method of polarisation resistance. Some common methods of measuring the polarisation resistance of embedded steel in concrete are discussed

in **Section 2.4.3.2** of the literature review. The Coulostat VIII apparatus was used to measure the corrosion rate and concrete resistivity, based on the Coulostatic method of polarisation. The apparatus was developed by Integrated Consulting Services in New Zealand which is a multi-disciplinary research and development organisation. The Coulostatic method is based on the change in potential about the equilibrium potential due to an applied current pulse, which increases the potential of the pore solution. The probes of the Coulostat unit that were in contact with the concrete included the 3 half-cells and electrode for applying the current pulse.

The steel bar was polarised by applying a current pulse through the stainless steel counter electrode, which was located concentrically around the central half-cell. The potential response was recorded against the 3 silver-silver chloride (Ag-AgCl) half-cells in the Coulostat after the current pulse was applied. The current was assumed to flow perpendicularly through the concrete between the counter electrode on the surface and embedded steel. The polarisation procedures were automated in terms of their pre- and post-pulse recording durations and magnitude of current imparted. Time series' of the measured voltage were established from the recording period to estimate the decay in potential after the current pulsing.

Typical time series' of the recorded voltage in the Coulostaic test between the half -cells and embedded steel are plotted in mV units in **Figure 3.25**. The principle of the Coulostatic method is illustrated by comparison of the potential decay in cases of passive (in red) and active corrosion (blue) conditions. The potential recording was performed in 0.01-second time increments against the 3 half-cells and plotted in 6-second increments. The equilibrium potential was recorded for 30 seconds (in part A) before the current pulse was applied which resulted in the potential drop, to the minimum (at B). The current pulse was applied for several milliseconds where after the potential decay (in part C) was recorded for another 30 seconds.

There are 2 aspects in the above plots to discern the corrosion state, the magnitude of the equilibrium potential (before pulsing) and potential decay. The equilibrium potential of the beams with passive corrosion remained above 0 mV whereas that

of the actively corroding beams remained at -400 mV. The minimum potential between the half-cells in the pre-pulse range (of 0-30 seconds) was compared to the Elcometer potentials at the mid-span. The potential decay of both plots started just after 30 seconds (in part C) in a curved manner until the end of the test, after 60 seconds. The majority of the potential decay occurred within 5 -10 seconds in the beams with passive corrosion and only 0.5 seconds in active conditions.

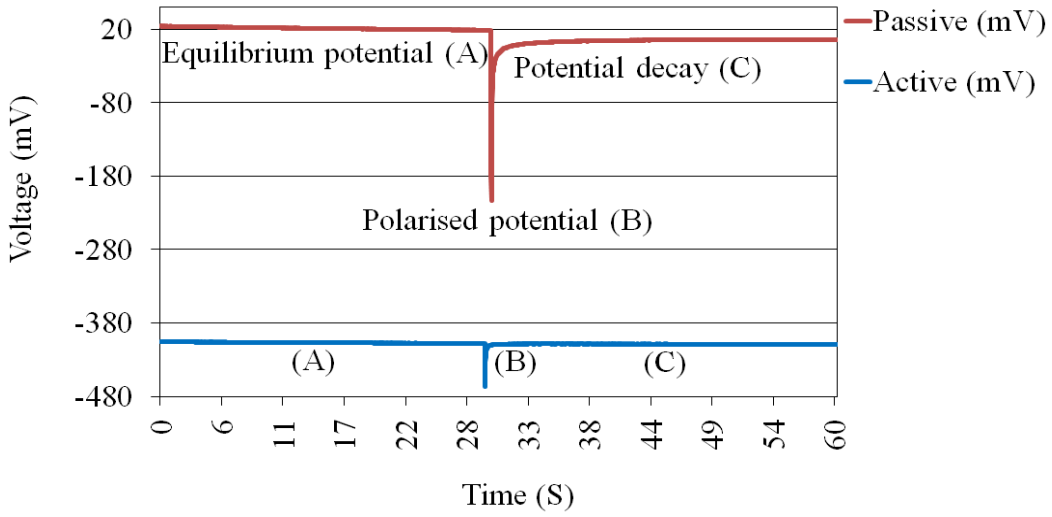

Figure 3.25: Coulostat corrosion potential transients

The polarised potential and potential decay are minimal relative to the equilibrium potential when the corrosion rate was higher (in the blue plot). This trend is due to the resistance of the corrosion current to a shift in potential from the equilibrium potential, after the current pulse. The plots were based on corrosion rate tests after ponding periods, where the additional moisture decreased the concrete resistivity and increased the corrosion rate. The polarised potential and potential decay were also decreased in Sathiyanarayanan et al., (2006) due to an increase in concrete conductivity. The addition of admixed chlorides resulted in a higher corrosion rate due to a decrease in the polarised potential and shorter duration of potential decay.

The polarisation resistance in $\Omega \cdot cm^2$ units was estimated from the potential decay, magnitude of applied current and steel area that was polarised. The polarised area was estimated using a length factor that was based on the differences in potential between the centre and outer 2 half-cells. The corrosion current density that was

dispersed over the steel bar, in µA /cm^2 units, was calculated using **Equation 2.18** in the literature review. A Stern-Geary (B) constant of 26 mV was used, which is relevant to values within the ranges of active corrosion in RILEM TC 154-EMC (RILEM, 2004). The potential of rebar's closest to the concrete surface are mainly polarised thus singly-reinforced beams were used to not average the readings.

The corrosion level of concrete structure is classified in RILEM TC 154-EMC using the corrosion current density in µA/cm^2 units and steel bar diameter in mm/ year units. The relationship between the corrosion current density and corrosion level of a structures' service life from RILEM TC 154-EMC is listed in **Table 3.9**. Corrosion current densities less than 0.1 µA/cm^2 correspond to passive corrosion whereas those in actively corroding structures reach 1 µA/cm^2. The corrosion conditions were accelerated herein in that the corrosion rates could be higher than in RILEM TC 154-EMC. There are other sources such Langford & Broomfield (1987), Bertollini et al., (2004), etc. which include such high corrosion rates.

Table 3.9: Corrosion level ranges (RILEM, 2004)

$I_{Corr.}$ (µA/cm^2)	Corrosion level
≤ 0,1	Negligible
0,1 < µA/cm^2 < 0,5	Low
0,5 < µA/cm^2 < 1	Moderate
> 1	High

3.9.3.4. Concrete resistivity testing

The electrical resistivity (conductivity) of the concretes was measured using 2 apparatus types, with different configurations of the current pulsing and half-cells probes. The first of these was the Coulostat VIII, as discussed previously, and secondly, the Resipod, which operated based on the principle of the Wenner 4-probe array. The Resipod apparatus is developed for concrete resistivity testing by Proceq which is based in Switzerland and develops apparatus for non-destructive testing. The measurement principle of the Wenner probe is discussed in **Section 2.8.2.5** of the literature review where current is applied by the outer 2 probes and

potential response measured by the inner 2 probes. The measurement is defined by the configuration of the probes where an adequate spacing is required to not be influenced by large aggregates. Wider spacings are ideal to create a homogenous current flow thus improve the accuracy of measurement (Kevern et al., 2015).

The locations where the Wenner probe was placed on the reinforced beams (a) and a photograph of the apparatus (b) are shown in **Figure 3.26**. The apparatus placed on the exposed surface of the beams, at either end of the Perspex pond and at the mid-span. The probe array was rotated to an angle of 45 º to fit within the confines of the pond and so that the probes were not placed over the steel bar. The current flows of the outer probes were thus less disturbed in the concrete in this orientation, compared to being placed over the steel bar. There was no intention to investigate the influence of probe spacing on the measurement of the Elcometer half-cell and Resipod. The Resipod readings at the mid-span were compared to that of the Coulostat, as a means of validation, in a similar manner to the potential.

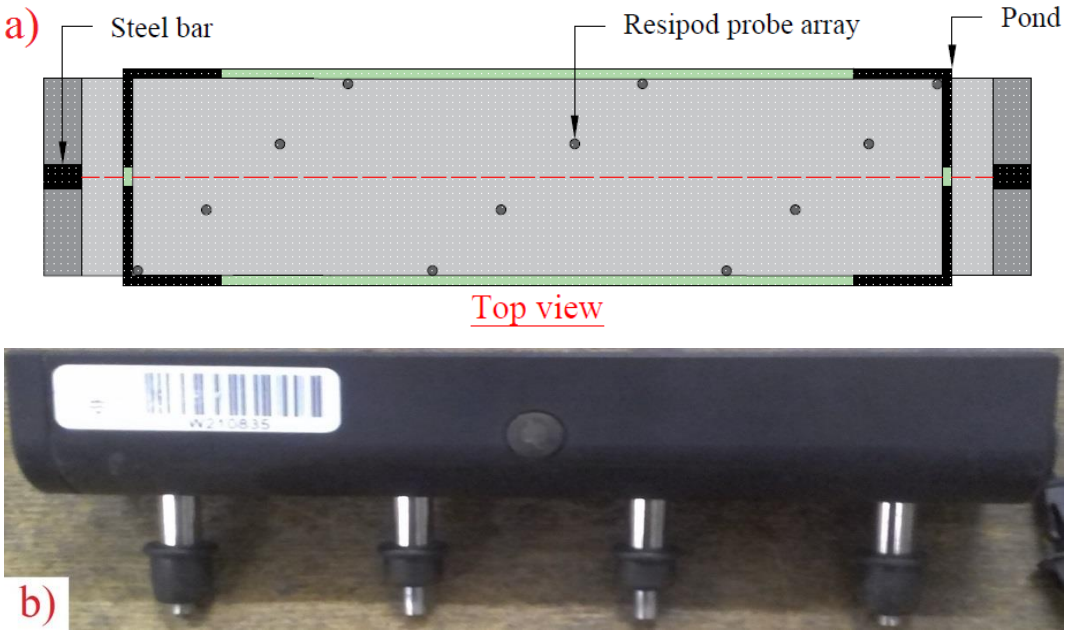

Figure 3.26: Wenner probe array test locations and probe bases

The Wenner probe spacing is dependent on the stone size where external probes are used to extend the capability of the measurement. Current flow is ideal when the probe spacing is larger than the maximum aggregate size, as these are less-

conducting. The Resipod with a spacing of 50 mm between the probes was used which conforms to industry standards whereas correction factors are applied with external probes. The Resipod with the spacing of 38 mm is compliant with the surface resistivity test in AASHTO T 358 which is based on that in AASHTO TP 95. AASHTO was the first body to define permeability classes based on the T 358 method, as an alternative to the ASTM C 1202 rapid chloride permeability test.

The half-cells in the Coulostat unit spanned the same length as the Wenner probe, of 150 mm, although had flattened bases, with the dimensions in **Figure 3.19**. The probe area in contact with the concrete surface was found to be not too influential to the resistivity of the Wenner probe in Gowers & Milliard (1999). The Coulostat unit recorded the potential over a shorter duration compared to the corrosion rate test, as the response to a current pulse. Typical time series' of the recorded voltage between the 3 half-cells in the Coulostaic test and embedded steel are plotted in mV units in **Figure 3.27**. The equilibrium potential in this test was recorded for 5 seconds (in Part A), before the current pulse (at B), and the potential decay for the same duration (part C). The beams with passive corrosion in the blue plot had a higher equilibrium potential and longer potential decay, thus a higher resistivity.

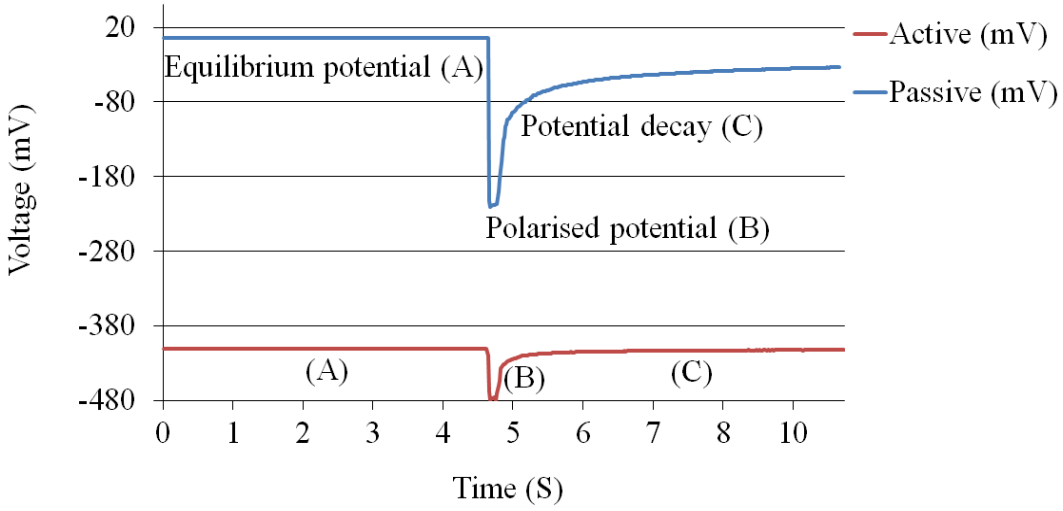

Figure 3.27: Coulostat resistivity test potential transients

The resistivity behaviour was classified with the ranges in RILEM TC 154-EMC (RILEM, 2004) which relates the corrosion risk to concrete conductivity. The

relationship between the concrete resistivity in kΩ·cm units and corrosion risk in RILEM TC 154-EMC is listed in **Table 3.10**. Concrete resistivity values of less than 10 kΩ·cm cause active corrosion due to the increased moisture and chloride contents. In Langford & Broomfield (1987) the active corrosion is sub-divided into high and very-high corrosion severity, with respective resistivity ranges of 5-10 kΩ·cm and < 5 kΩ·cm. The resistivity is similar between these sources beyond a value of 10 kΩ·cm, which corresponds to a moderate and low corrosion risk.

Table 3.10: Concrete resistivity ranges (RILEM, 2004)

Concrete resistivity (kΩ·cm)	Corrosion risk
> 100	Negligible
50-100	Low
10-50	Moderate
< 10	High

3.9.4. Corrosion damage testing

3.9.4.1. Overview

The last section of the durability was focussed on the corrosion damages that had accumulated mainly during the propagation stage of corrosion. These corrosion damages to the cover concrete and embedded steel of the reinforced beams were assessed in the **Section 4.5.5** of the results. The assessment included mapping the cracks on the exposed surface together with the uniform or pitting corrosion on the embedded steel. The cracks and corrosion maps of the beams were established after the exposure period to determine the extent of corrosion-induced damages. The exposed surface of the beams was also inspected prior to the exposure period to ensure that the cracks at the completion of exposure were induced by corrosion.

3.9.4.2. Crack width measurement

The extent of cracking on the concrete surface over the steel bars was assessed in terms of the length coverage and crack width. Crack maps were established by

mapping the measured cracks in constant increments of the uncoated length of the steel bar. The location and orientation of the cracks, at the time of measurement, indicated their origin, either due to shrinkage or corrosion. Shrinkage cracks form anywhere on a concrete surface, and with a random orientation, whereas corrosion cracks form over the steel. The corners of concrete elements crack initially, due to multi-directional exposure, and delamination occurs when corrosion spreads to adjacent steel bars (Broomfield, 2007). The imperfections from the casting stage were assumed to be less influential than the cold joint, which spanned to the steel.

The crack widths on the exposed surface were measured using the Elcometer 900 microscope, before the beams were sampled for chloride. A photograph of this apparatus is not included for the sake of brevity however the specifications of the measurement are discussed. The microscope could magnify the concrete surface by up to 50 times and measured the crack width to within a scale range of 0-1.8 mm. The crack maps were established by subdividing the exposed surface over its length in 10 mm increments, with the origin in both directions at the mid-span. The method of crack mapping on the exposed surface is illustrated together with the measured lengths of uniform and pitting corrosion damage in **Section 4.5.5.2**.

3.9.4.3. Reinforcing steel visual assessment

The corrosion damage to the steel bars after the exposure period was assessed as the coverage and corrosion type, either uniform or pitting. Corrosion maps were established in a similar manner to the crack maps, as the lengths of the steel bar that contained uniform or pitting corrosion. The steel bars were removed from the beams using a jackhammer and the pitting locations were then determined after wire-brushing the steel surface. The lengths of uniform and pitting corrosion are discussed together with photographs of the steel bars in **Section 4.5.5.2** of the results. The corrosion lengths were measured to an accuracy of 1 mm to plot the corrosion maps in 10 mm increments over the un-coated portion of the steel bars.

The crack maps of the concrete surface and corrosion maps of the steel bars could determine if the cracking had been caused due to corrosion. The corrosion maps

were also used to identify any anomalies to the corrosion behaviour not based on the concrete resistance to the transport of moisture, gasses, and ions. The drilled hole in the steel bars could corrode before the exposure period and the protruding bar ends were only protected by the epoxy coating. These bar ends were coated periodically by epoxy to close the openings where the steel was directly exposed to atmosphere. The locality of corrosion in the vicinity of the cold joint was also a means of determining the suitability of the spacing of corrosion testing locations.

3.10. Experimental summary

A summary of the salient details of the experimental programme is presented in this section as a guide to the methodology of the study. This summary is presented in the form of flow diagrams which are sub-divided broadly into the preparatory work, exposure conditions and experimental testing stages. These diagrams may be used to reference the sections of this chapter and follow the same arrangement in the results in **Chapter 4**. The parameters that were part of the preparatory work are presented together with their corresponding section numbers in a flow diagram in **Figure 3.28**. The strength and durability parameter groups are then presented together with the curing and exposure durations in the diagram in **Figure 3.29**.

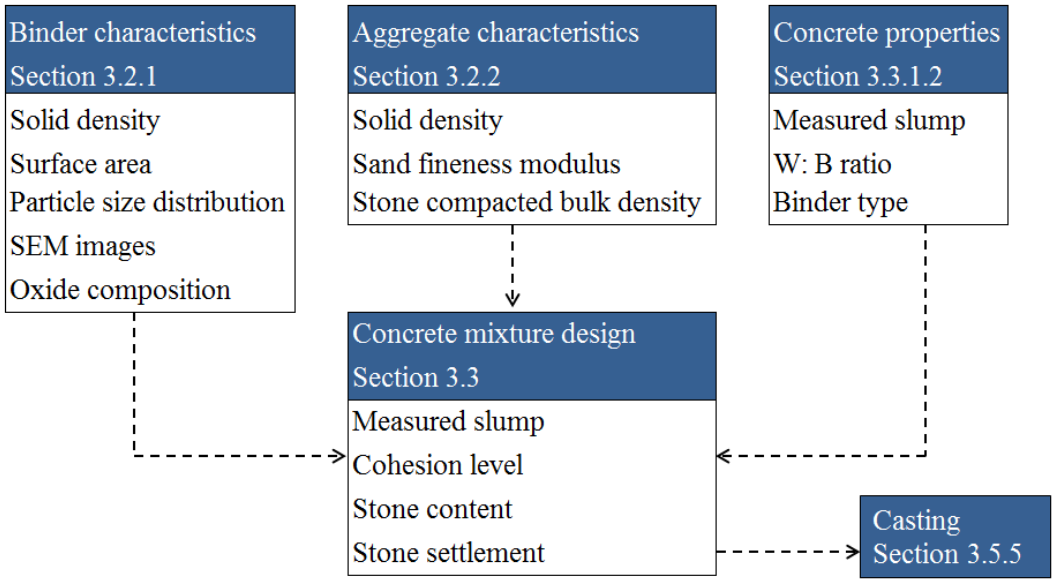

Figure 3.28: Preparatory work

The characteristics of the cementing binders are discussed in **Section 3.2.1**, which included the solid density, surface area, particle size distribution (PSD) and oxide composition. The solid density was required in the mixture design, to calculate the solid volume, whereas the other parameters were included to interpret the results. The characteristics of the crusher sand and concrete stone are discussed in **Section 3.2.2**, which included the solid density, stone compacted bulk density and crusher sand fineness modulus. The procedure of the mixture design in **Section 3.3** was based on a variation in binder type and constant values of the water: binder (W: B) ratio and slump range. One type of sand and stone were used in the concretes thus only the required characteristics were determined in the mixture design stage.

The main portion of the experimental programme involved the durations of curing and exposure before the strength and durability parameters were tested. Once the proportions of the concrete mixtures were determined in the trials the reinforced beams, cubes and circular discs could be cast. The compressive strength testing in **Section 3.7** was performed after 2, 7, 14, 28, 56 and 90 days of curing to evaluate the early-age and long-term strength development. Most of the hydration progress of rapid-hardening cement occurs within 2 days, in accordance with SANS 50197-1 (SANS, 2011). The transport properties, in terms of the Durability Indices of the South African standards, were tested after 28, 56 and 90 days of curing in **Section 3.9.2**. These parameters were tested earliest after 28 days which was the minimum duration for the specimens that were exposed to chloride and carbon dioxide.

The specimens that were exposed to chloride and carbon dioxide were initially tested before the exposure, once the 28-day curing period had been completed. This was a baseline result (at 0 days of exposure) for comparison to that measured during the exposure period. A clearer description of this preliminary testing of the experimental programme is in **Section 3.6** together with the cover depth testing details in the reinforced beams. The cover depth was measured together with the parameters that are circled in red, except the uniform and pitting corrosion on the steel bar. Once the baseline results had been obtained the chloride solution and accelerated carbonation exposure was started, to the details in **Section 3.7.2.2**.

The chloride penetration and carbonation depth were the cumulative response of the exposure conditions, as discussed in **Section 3.9.2**. The chloride profiles in the beams were established after 21 cycles of exposure and the carbonation depths measured after 10 and 21 cycles. The increase in chloride content at the cold joint was determined by comparing the profiles of the cold joint and monolithically-cast beams. The influence of carbonation on chloride penetration was determined by comparing the profiles under the combined exposure to chloride exposure in isolation. The influence of the cold joint and carbonation together on chloride penetration was determined as an extension of these in the results in **Chapter 4**.

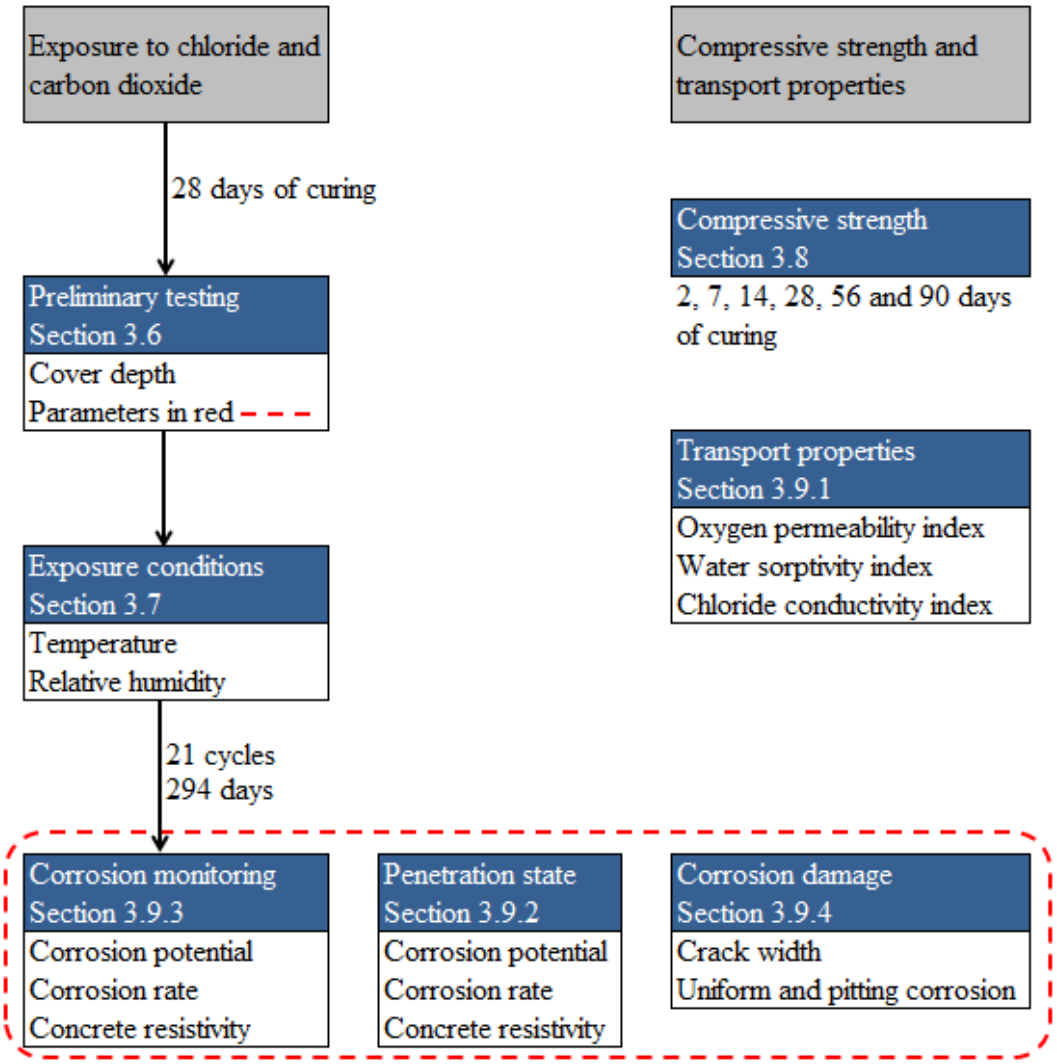

Figure 3.29: Curing, exposure and testing details

A number of assumptions were required in the assessment of the chloride profiles and carbonation depths in the results in **Chapter 4**. The first of which was that chlorides within the bound of the carbonation depth were assumed to be soluble, in that they could diffuse to the steel level. The chloride profiles were based on the total chloride fraction only thus not together with the free chloride fraction, as it is not necessary under this assumption. The second assumption of the chloride profiling was that the main factor to increasing the chloride penetration was the loss of bound chlorides in carbonated concrete. The physical factors that hinder chloride ingress due to carbonation, i.e. decrease in pore size, were thus not tested to simplify the study scope. This is due to a general finding of smaller carbonation depths in concrete with chloride thus less-influential to the chloride penetration.

The corrosion monitoring was a continuous response to the exposure conditions to determine the progress of carbonation in concrete with chloride. The parameters of the corrosion monitoring scheme are discussed in **Section 3.9.3** which included the electric potential, corrosion rate and concrete resistivity. This monitoring was intended to determine the initiation time of corrosion and maximum corrosion rate that was reached within 21 cycles. The corrosion rate was not accelerated using an approach of applying a direct current into the concrete cover over the course of the exposure period. This however raises the electrical potential in the concrete to not be representative of normal corrosion conditions (Bertolini et al., 2013).

The corrosion damage assessment was performed after the exposure had been completed, which spanned a duration of 21 cycles (or 294 days). This consisted of mapping the corrosion-induced cracks in the cover concrete together with the uniform or pitting corrosion on the steel. The occurrence of corrosion-induced cracks allowed the comparisons of the corrosion to extend to the accelerated stage of the process. The focus of the assessment was on the locality of the concrete cracking in relation to the corrosion on the steel, i.e. the widest cracks had formed over the most corroded steel. The methods whereby the maps of the cracking and corrosion on the steel surface were established are discussed in **Section 3.9.4**.

4. Experimental results and discussion

4.1. Overview

This chapter presents the results of the experimental testing to assess the influence of a cold joint and carbonation in chloride-laden concrete. Corrosion monitoring formed the bulk of the experimental programme and this was supplemented by the penetration states, transport properties and corrosion damages. These parameters were collectively used to determine the corrosion resistance of the concretes in the durability assessment. The cement replacement with fly ash and metakaolin forms the basis of the comparisons to extent the understanding on the use of pozzolanic materials in concrete. The exposure conditions, cold joint and cover depth were the secondary factors of the comparisons made, to which the study aim was based.

4.2. Fresh-state properties

The results of the fresh-state properties were based on the criteria for acceptance in the mixture design stage of the experimental programme. These properties were the consistency (as the measured slump), cohesion level and workability, which were tested with various methods. The criteria of the mixture design are intended to promote a suitable degree of homogeneity in hardened concrete, with minimal stone settlement and bleeding. The mixture proportions of the ordinary concrete were obtained in a series of 6 trials to keep constant in the fly ash and metakaolin concretes. The mixture proportions of the trial mixtures are first discussed in **Section 4.1** and the fresh-state properties that had yielded, in **Sections 4.2** to **4.5**.

4.2.1. Mixture proportions

The proportions of the trial mixtures are listed in kg/m^3 units of the mixing water (W), cementing material, 6.7 mm stone (St) and crusher sand (S) in **Table 4.1**. The ordinary concrete trials 1-6 are listed in the columns in part A and the cement

extender concrete trials to the right in part B. The water content was estimated using the C & CI procedure based on an ordinary concrete with a slump value of 75 mm. A nominal stone size of 9.5 mm was assumed in the mixture design stage which requires 235 L/m^3 of water, however the estimation started at 210 L/m^3. The water content was increased from this minimum, to 275 L/m^3 in the final (or 6th) trial wherein the measured slump fell within the selected range of 75-150 mm.

Table 4.1: Trial mixture proportions

Material proportions	A) Ordinary concrete						B) Cement extenders	
	Trial 1	Trial 2	Trial 3	Trial 4	Trial 5	Trial 6	Fly ash	Metakaolin
W (L/ m^3)	210	240	250	260	270	275	275	275
Cement	382	436	455	473	491	500	350	350
30 % Fly ash							150	
30 % Metakaolin								150
St (kg/ m^3)	677	677	577	477	477	477	477	477
S (kg/ m^3)	1280	1141	1195	1248	1202	1179	1114	1144
Superplasticiser								Note 1

1. Plasticiser 0.2-2.0 % by mass of the binder content.

The cement content in the ordinary concrete was increased from 382 kg/m^3 to 500 kg/m^3 in the final (or 6th) trial due to the increments in water content. The binder content in the final trial was close to the maximum value of 550 kg/m^3 that is specified in SANS 10100-2 (SANS, 2014). The stone content that was calculated in the first trial, of 677 g/m^3, was decreased to 477 kg/m^3 in the final trial, due to decrements of 100 kg/m^3. This value is low for concrete although is recommended in the C & CI procedure for the small sizes of the stone and coarseness of the sand. The sand content in the final trial of 1179 kg/m^3 was thus high to increase the sand-size fractions of 0.075 mm, 0.15 mm and 0.3 mm to suitable percentages.

The mixture proportions of the ordinary concrete final (or 6th trial) were then used as an initial estimation in the cement extender concrete trials. The binder content in these concretes consisted of 70 % cement and 30 % of the fly ash or metakaolin in binary blends. Though the binder content was the same the binder volume of

the cement extender concretes was increased due to the lower densities of these materials. The sand content was proportionally reduced from that in the ordinary concrete final trial, of 1179 kg/m^3, to 1114 kg/m^3 and 1144 kg/m^3 in the fly ash and metakaolin concretes respectively. The proportion of aggregate fines in these concretes was increased by up to 6 % due to their differences in the sand content.

4.2.2. Slump measurement

The measured slumps in mm units are listed together with the trial assessment and modifications of the mixture design stage in **Table 4.2**. The results of the other fresh-state properties are in the following sections, which were the cohesion level of the fresh concrete, stone settlement in the hardened concrete and stone content. The slump of ordinary concrete trials (1 to 6) is first discussed and then that of the cement extender concretes, where FA and MK denote the fly ash and metakaolin respectively. A shear collapse occurred in trial 1 of ordinary concrete as there was a lack of water, so the water content was increased by a large amount of 30 L/m^3 (or W + 30 L/m^3). The next 3 trials yielded no slump (0 mm) although the tests were valid as the concrete mass remained rigid after the slump cone was removed.

Table 4.2: Trial assessment and modifications

Trial	Slump (mm)	Cohesion level	Settlement	Stone content	Assessment	Modifications
Ordinary concrete						
1	Shear collapse	Not tested		Not tested	Not accepted	W+30 L/m^3
2	0 mm	Shear collapse		In excess	Not accepted	W+10 L/m^3 St-100 kg/m^3
3	0 mm	Shear collapse		In excess	Not accepted	W+10 L/m^3 St-100 kg/m^3
4	0 mm	Shear collapse		Workable	Not accepted	W + 10 L/m^3
5	70 mm (< 75)	Shear collapse		Workable	Not accepted	W + 5 L/m^3
6	120 mm	Uniform collapse	Minimal	Workable	Acceptable	None
Fly ash concrete						
1	140 mm	Uniform collapse	Minimal	Workable	Acceptable	None
Metakaolin concrete						
1	0 mm	Shear collapse		Workable	Not accepted	Plasticiser
2	100 mm	Uniform collapse	Minimal	Workable	Acceptable	None

The water content was incremented in small amounts of 10 L/m^3 (or W + 10 L/m^3) in trials 3 to 5, where the slump increased from 0 mm to 70 mm. There was no sensitivity to the changes below a water content of 260 L/m^3 in the 5th trial as the concrete remained rigid, without shear collapse. Once the concrete displayed sensitivity to the water content a smaller increase of 5 L/m^3 was used in the final (or 6th) trial, which increased the slump from 70 mm to 120 mm. The slump in the 5th trial, of 70 mm, was not accepted due to a persisting lack of cohesion however the 5 L/m^3 increase brought the slump to within range. The water content in the final trial, of 275 L/m^3, was accepted as the slump and other fresh-state properties were as required. The water, binder and stone contents were kept constant in the cement extender concretes, using the same water: binder (W: B) ratio, of 0.55.

It is worth mentioning that another W: B ratio of 0.65 was tested with the ordinary concrete to identify where there was sensitivity to the water content. The water content was increased in 10 L/m^3 amounts until the slump changed from 0 mm to 75 mm, at water content of 240 L/m^3. The slump of the cement extender concretes was selected to vary within a small tolerance of 20 mm from that in the ordinary concrete final (or 6th) trial. The fly ash yielded an increase in slump of 20 mm (or 17 %) in the 1st trial, to reach the upper bound of the tolerance on the ordinary concrete final trial, of 140 mm. At the same replacement level of 30 % and water content of 275 L/m^3 the metakaolin yielded no slump, thus a plasticiser was used.

The plasticiser increased the metakaolin concrete slump to reach the lower bound of the tolerance on the ordinary concrete final trial, of 100 mm. The decrease in slump of the metakaolin concrete without the plasticiser indicated that the surface characteristics of the binders were the main factor to the water requirement. The particle sizes were similar between the binders thus the differences in the surface area were important to their reactivity with the addition of the mixing water. The surface area of the metakaolin particles was 400 % and 426 % larger than the cement and fly ash respectively, due to the flaky shape and rough texture. The fly ash particles took on a smooth shape and round texture which yielded a decrease in the water requirement (or increase in slump) compared to the ordinary concrete.

The measured slumps of the concretes that were used to cast the test specimens are listed together with the other sampling details in **Table 4.3**. The casting details include the mixture volumes, fresh-state properties (for the comparison to the final trials) and plastic density. Cast 1 denotes the concrete for the monolithically-cast specimens and half of the cold joint specimens and cast 2 refers to concrete on the other side of the cold joint. The test specimen details are as described in **Section 3.5** of the experimental programme and the trial specimens were used to assess the suitability of the carbonation. The trial specimens were fabricated from ordinary concrete and the results of which are found in the relevant sections of this chapter.

Table 4.3: Concrete casting and sampling details

Cast description	Volume (L)	Slump (mm)	Cohesion	Stone content	Density (kg/m^3)
Ordinary concrete					
Trial sets cast 1	149	120	Acceptable	Acceptable	2428
Trial sets cast 2	52	120	Acceptable	Acceptable	2441
Standard sets cast 1	129	120	Acceptable	Acceptable	2411
Standard sets cast 2	52	100-105	Acceptable	Acceptable	2442
Fly ash concrete					
Standard sets cast 1	149	135-140	Acceptable	Acceptable	2337
Standard sets cast 2	52	140	Acceptable	Acceptable	2329
Metakaolin concrete					
Standard sets cast 1	149	100	Acceptable	Acceptable	2399
Standard sets cast 2	52	100	Acceptable	Acceptable	2386

The slump of the concretes that were to cast the test specimens are discussed here and the other fresh-state properties of the casting are in the following sections. The slump of the ordinary concretes fell within a range of 100-125 mm which was a maximum difference of 15 % from that in the final (or 6th) trial. The slump of the fly ash concretes fell within a range of 135-140 mm which was a maximum difference of only 5 % from the final trial. The slump of the metakaolin concretes were increased with plasticiser to within a negligible difference of 2 % from that in the final trial, of 100 mm. The volume of plasticiser was much larger in the concretes that were used for the specimens, of up to 5 litres for the largest of casts.

4.2.3. Cohesion level

The concrete behaviour and appearance that is representative of the cohesion level is listed together with the trial assessment and modifications earlier in **Table 4.2**. The cohesion level of the fresh concretes was based on the collapsing behaviour of the concrete mass while tapping the plate below of the slump cone. The stone settlement test was performed with the concrete mixtures of the final trials only, by casting 3 cubes with 100 mm sides for each concrete. These were cut open to view the dispersion of the large stones in the mortar, to represent the resistance to settlement. The cohesion level of the fresh concrete in the trial mixtures is first discussed and then the stone settlement in the hardened concrete of the final trials.

The cohesion level of the ordinary concrete trial mixtures was increased from the poor behaviour initially to an acceptable level in the final (6th) trial. There was a lack of cohesion in the 1st trial as there was a shear collapse of the concrete mass in the slump test, before the slump was measured. The cohesion level was then increased by a minor degree in trials 2-4 as the concrete mass was intact for the slump to be measured. There was a large change in the cohesion level when the slump increased from 0 to 70 mm in the 5th trial, although this cohesion level was still too low. The water content in the final trial brought the cohesion to a suitable level as the concrete mass fell uniformly in the cohesion test, without breaking.

The fly ash yielded a lower cohesion level in comparison to the ordinary concrete although these differences in concrete behaviour were minor. There was a faster collapse of the concrete mass than the ordinary concrete in the same duration of the cohesion test due to the increase in the consistency, as measured by the slump. The cohesion level of the metakaolin concrete without plasticiser was minimal, similar to that of the ordinary concrete in the 1st trial, at the lowest water content of 210 kg/m^3. With incremental dosage of plasticiser the cohesion increased to a suitable level, which was when the slump had fallen within the selected range, of 120 ± 20 mm. The cohesion level of concretes was thus dependent mainly on the consistency as it was suitable when the slump had reached the selected range.

The stone settlement was tested on the proportions of the final trial mixtures, after the other fresh-state properties had been accepted. Sets of 3 cubes were prepared from the final trial mixtures of each concrete to view the dispersion of the largest stones over the cross-section. The largest stones were uniformly dispersed in the mortar over the entire section which is indicative of minimal stone settlement. The cohesion level was thus acceptable given the compaction method and settlement depth of 100 mm. There was however air voids in the concrete which cannot be avoided although their extent was minor thus mostly freed up by the compaction. Both the capillary pores and entrapped air voids are relevant to the durability as these determine the transport of gasses, moisture and ions (Bertolini et al., 2013).

4.2.4. Stone content

The concrete behaviour and appearance that indicated the stone content is listed together with the trial assessment and modifications earlier in **Table 4.2**. The stone content was assessed qualitatively in 3 tests, according to that described in **Section 3.3.1.5** of the experimental programme. The ordinary concrete in the 1st trial reflected an excess of the stone even through the stone content of 677 kg/m^3 was low for concretes with the standard stone sizes. The increase in water content by 30 L/m^3 (or W + 30 L/m^3 in Table 4.1) was the only modification in the 1st trial, to increase the slump. The fresh concrete however remained in a harsh state in the 2nd trial even through the water content was increased by a large amount.

The stone content was decreased from 677 kg/m^3 to 477 kg/m^3, using 100 kg/m^3 decrements (or St - 100 kg/m^3), after the 2nd and 3rd trials. These modifications were made based the C & CI procedure in the case where a concrete mixture is too harsh (or unworkable). The stone content was suitable in the 4th trial however the slump and cohesion level were found to be unsuitable, as discussed in the previous sections. The stone content of 477 kg/m^3 was thus kept constant until the final (or 6th) trial while the water content was increased until the slump fell within range. There were no changes to the fly ash concrete compared to the ordinary concrete final trial whereas plasticiser had to be used in the metakaolin concrete.

4.2.5. Plastic density

The plastic densities of the concretes that were used to cast the test specimens are listed in kg/m^3 units together with the other fresh-state properties, previously in **Table 4.3**. The density was calculated as the average between 3 tests, as the mass of fresh concrete that was floated flush in plastic cube moulds, with a volume of 1 litre. This is compared to the theoretical density, which was calculated from the densities of the concrete materials and proportions of the final trial mixtures. The theoretical density of the ordinary concrete final (or 6th) trial mixture, of 2430 kg/m^3, which was used in the casting, falls within the range of ordinary concrete (Neville, 2011). The theoretical density of the fly ash and metakaolin concretes were 2366 kg/m^3 and 2378 kg/m^3 respectively, due to the larger particle volumes.

The plastic densities of the ordinary concrete mixtures that were used to cast the test specimens fell within a range of 2419-2453 kg/m^3. These measured values vary by a maximum of 1 % from the theoretical density of the proportions of the final trial mixture, of 2430 kg/m^3. The fly ash and metakaolin concrete plastic densities fell within respective ranges of 2329-2348 kg/m^3 and 2386-2409 kg/m^3, a variation of up to 1.6 %. There was also a similarity in the measured slump and other fresh-state properties between the final trial mixtures and that used to cast the test specimens. Factors such as the material characteristics, type of concrete mixer, mixture volume, etc. were thus not influential to the fresh-state properties.

4.3. Mechanical properties

4.3.1. Overview

The results of the compressive strength according to the crushing test in SANS 5863 (SANS, 2006) are presented and discussed in this section. The uniaxial loading procedure was followed according to that discussed in **Section 3.8** of the experimental programme. The compressive strength of the concretes was tested over a period of 90 days to assess the influence of cement replacement on strength

development. The cube failures were acceptable according to SANS 5863 in that the damage was on the faces that were perpendicular to the loading faces. The minimum, maximum and average strengths in the cube sets after each curing age are listed in **Appendix B**. The variation of the strength in the sets of 3 cubes was acceptable in that the range limits did not exceed the average strength by 15 %.

4.3.2. Early-age compressive strength

The compressive strength (fc) in the early-age is plotted in MPa units against the curing age in a curing period of 2 to 28 days in **Figure 4.1**. The error bars (I) represent a confidence interval of 95 % which is based on the variation of strength in the sets of cubes after each curing age, assuming a normal distribution. The ordinary concrete strength after 2 days, of 38.5 MPa, exceeded that under the 52.5 R strength class in SANS 50197-1 (SANS, 2011), of 30 MPa, and the typical performance at Afrisam, of 33 MPa. The strength of the metakaolin concrete after 2 days exceeded that of the ordinary and fly ash concretes by 12 % and 29 % respectively. Most of the strength after 28 days had yielded after 2 days; 67 %, 63 % and 62 % by the ordinary, fly ash and metakaolin concretes respectively.

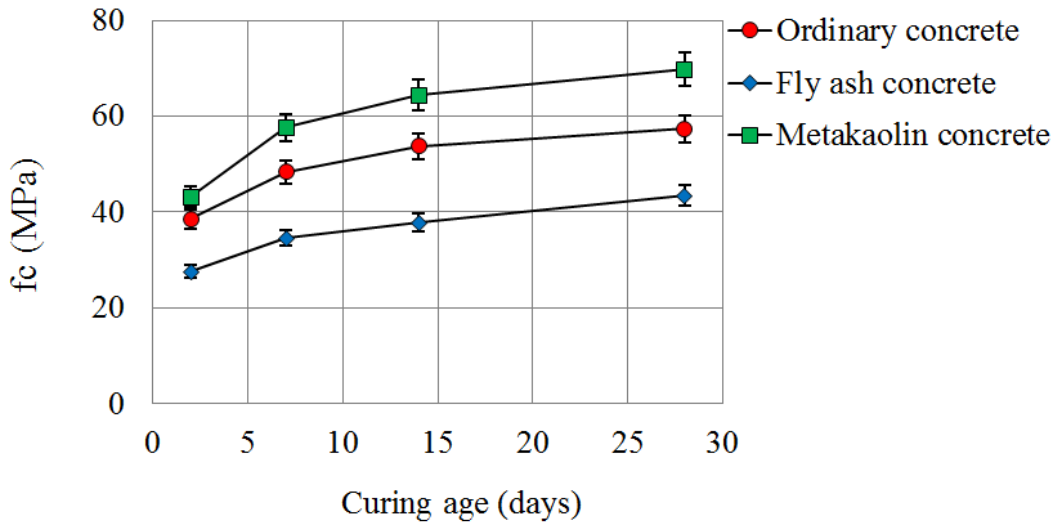

Figure 4.1: Compressive strength from 2 to 28 days

The strength that was gained within the intervals of 2-7, 7-14 and 14-28 days, is plotted as the percentage (%) of the 28-day strength in **Figure 4.2**. The reactivity

of the fly ash and metakaolin, relative to the ordinary concrete, is clearer from these intervals. The ordinary concrete gained the largest % of its 28-day strength within 2 days as the cement extenders required the calcium hydroxide from the cement hydration. The metakaolin concrete then gained the largest % of its 28-day strength within the period of 2-7 days, with 21 % of the early-age strength. The reactivity of the cement and metakaolin to contribute to the strength development was thus mostly within 7 days. The reactivity of the fly ash is evident from 14 to 28 days, wherein the fly ash concrete gained the largest % of its 28-day strength.

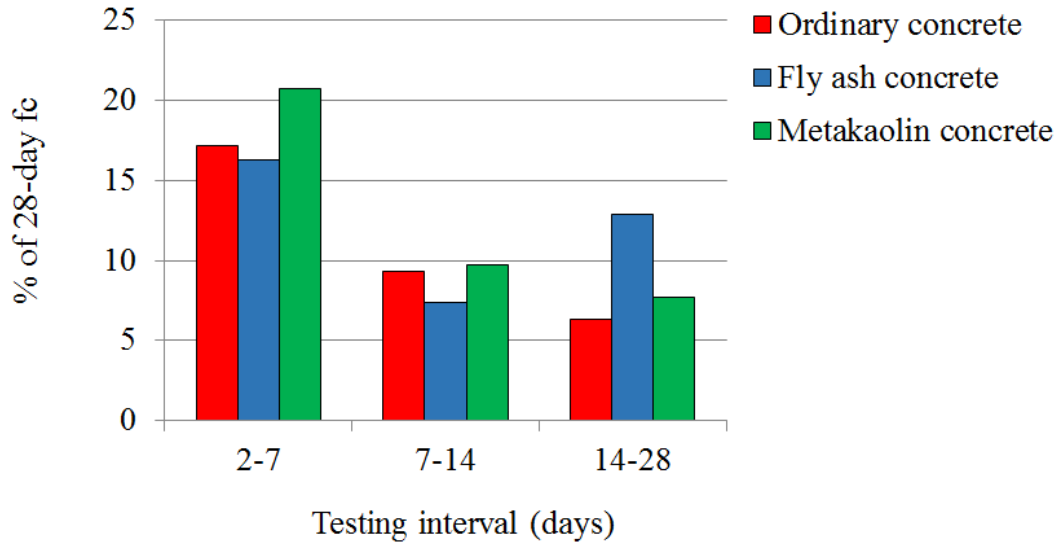

Figure 4.2: Compressive strength gained in intervals up to 28 days

The 28-day strength of the ordinary concrete, of 57.4 MPa, exceeded that under the 52.5 R strength class (of 52.5 MPa) and was similar to the typical performance at Afrisam, of 59 MPa. The 28-day strength of the metakaolin concrete, of 69.8 MPa, exceeded the ordinary concrete strength by 18 % after 28 days, whereas that of the fly ash concrete was 38 % lower. This trend of an increase in strength due to cement replacement using metakaolin has been found in a number of studies. The concretes with metakaolin in Bakera & Alexander (2017) and Ferreira et al., (2015) also yielded an increase in strength compared to ordinary concrete. The strength was increased at curing ages of within 28 days at certain water: binder (W: B) ratios and replacement levels. The increase in strength due to metakaolin herein at a curing age of 7 days thus may be attributed to the high cement grade.

4.3.3. Long-term compressive strength

The long-term compressive strength (fc) is plotted in MPa units against the curing age in a curing period of 2 to 90 days in **Figure 4.3**. This plot is an extension of the early-age to determine the long-term contributions to strength of the cement extenders, with maintained curing. The fly ash concrete breached the gap in strength after 28 days, which was 32 % lower than the ordinary concrete, to be 18 % lower after 90 days. From 28 to 90 days the fly ash concrete yielded 17 % of its 90-day strength whereas the other concretes yielded less than 10 % of the 90-day strength in the same period. The ordinary concrete and metakaolin concretes only yielded respective proportions of 8 % and 4 % of their 90-day strength from 28 to 90 days. The lack of strength development in these concretes is evident in the flatter lines between the plot points whereas that of the fly ash concrete is steeper.

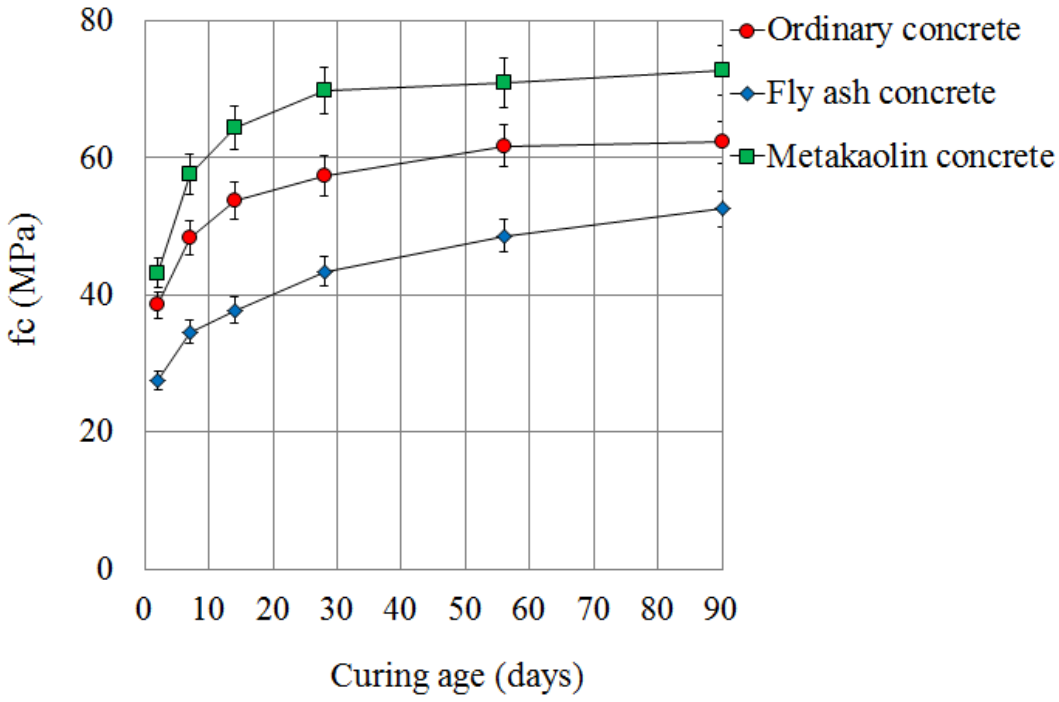

Figure 4.3: Compressive strength from 2 to 90 days

The trend of a delayed (or slower) reactivity of fly ash to contribute to strength development has been found in a number of studies. The characteristics of the fly ash herein were synonymous of a slower reactivity, as determined by the lower

surface area compared to the other binders. Though the fly ash did not result in an increase in strength within the 90-day curing period compared to the ordinary concrete, it may have bridged this gap with a longer curing duration. There was a similar trend of an increase in strength development in Paul (2015) due to cement replacement with fly ash. The strength of mortar with cement only was higher after 28 days although the fly ash mortar yielded a higher strength after 120 days.

The strength of fly ash concrete after 90 days of curing in Islam & Islam (2010) was increased by the replacement level of fly ash. The strength of the ordinary concrete up to 28 days was higher than that of all the fly ash concretes, which had a replacement level of up to 60 %. After 60 days the strength was increased with replacement levels of up to 40 % only thus a longer curing duration was required. After 90 days the strength of the fly ash concrete was higher than the ordinary concrete at all replacement levels, of up to 60 %. Contrary to this, Balakrishna & Nataraja (2013) found a decrease in strength in a period of 90 days with fly ash replacement levels of up to 30 %. This trend of lower strength in fly ash concrete over 90 days is similar to herein which may be attributed to a high cement grade.

4.4. Exposure conditions

4.4.1 Overview

The temperature and relative humidity were monitored over the course of the exposure to identify any discrepancies against the other results. The temperature in the carbonation chamber was sensitive to the ambient conditions whereas the humidity was influenced by the moisture of test specimens. The specimens were stored in a sheltered laboratory during the exposure which was anticipated to decrease the magnitude of the temperature extremes and prevented contact with rain. The temperature and relative humidity were monitored for comparisons between the ambient conditions and the closed system that was formed in the carbonation chamber. A timeline of the entire exposure period for each concrete type is also discussed as a background to the durability results in **Section 4.5**.

4.4.2. Timeline of exposure conditions

The exposure conditions in the experimental programme spanned from 17 June 2018 to 8 December 2019 for all the test specimens. The exposure conditions were started on 17 June 2018 in a trial period of 8 weeks, wherein the carbonation depth, electric potential and concrete resistivity were tested. The reinforced beam and cube specimens that were used in the trial period of exposure were fabricated from the ordinary concrete. The trial period of exposure spanned from 17 June to 5 August 2018 which consisted of 4 cycles of the isolated chloride and combined exposure, each lasting 2 weeks. The results of the trial period of exposure are discussed together with the carbonation depth and corrosion results in **Section 4.5**.

The first specimens that were used in the longer exposure periods of 294 days were fabricated from the fly ash concrete. These were exposed in a period from 27 August 2018 to 17 June 2019 which spanned the summer and winter months. The next specimens that were exposed for 294 days were fabricated from the ordinary concrete, in a period from 5 November 2018 to 26 August 2019. The relative humidity in the carbonation chamber was influenced by the number of specimens that was being housed at any time. The relative humidity in the chamber was thus further increased when the metakaolin concrete specimens were exposed, on top of that due to the other concretes. The metakolin concrete specimens were the last to be exposed in the experimental programme, in a period from 18 February to 8 December 2019. The differences in relative humidity in the chamber due to the addition of specimens during the exposure are discussed in the following section.

4.4.3. Temperature behaviour

The temperature behaviour is plotted in °C units under both the exposure regimes with a monitoring frequency of 2 hours in **Figure 4.4**. The temperature of the laboratory (in blue) and carbonation chamber (red) was similar over the course of the exposure period. The temperature extremes such as cold fronts and warm spells lasted for up to 1 week, as shown in the examples at A and B respectively.

The corrosion risk was theoretically highest in the summer periods on record wherein temperatures were closer to 30 °C. The corrosion risk was lowest in the coldest periods on record which were the winter months of July 2018 and June 2019. The monthly averages differed by up to 11 % between the records thus there was a high sensitivity of the temperature in the chamber to the environment.

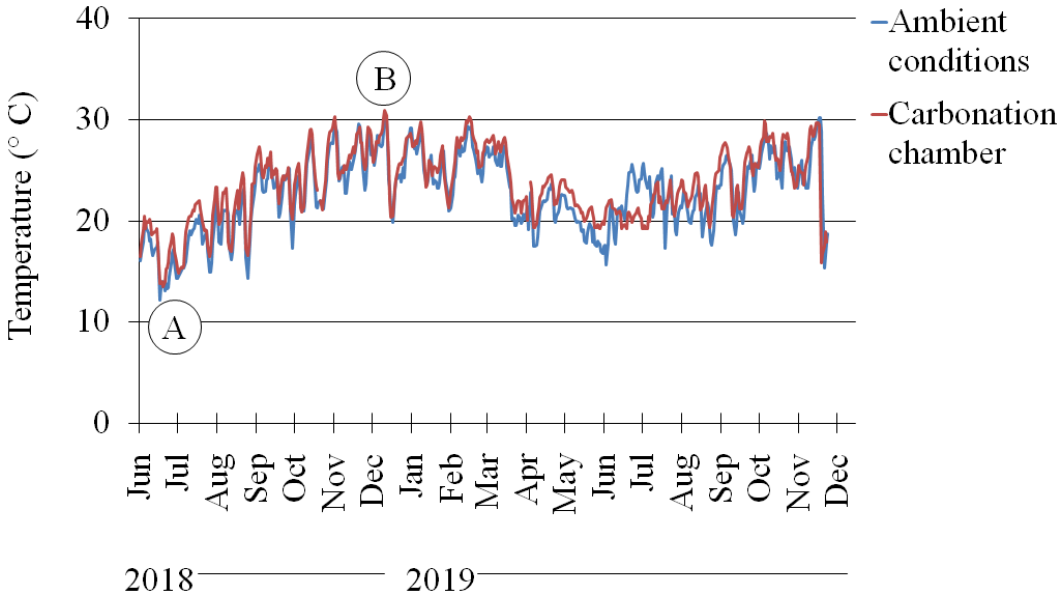

Figure 4.4: Temperature behaviour records

4.4.4. Relative humidity behaviour

The relative humidity behaviour is plotted in % under both the exposure regimes with a monitoring frequency of 2 hours in **Figure 4.5**. The relative humidity in the carbonation chamber (in red) was independent of that in the laboratory (blue) as the chamber was closed off to atmosphere. The relative humidity in the sheltered laboratory was based on the temperature and moisture in the atmosphere which varied based on seasonal and local changes. The monthly averages of the ambient exposure (blue) were higher in the summer months, close to 60 %, and lowest in September of both years, close to 20 %. The relative humidity in the chamber was increased due to moisture of the test specimens thus was required to be decreased for the carbonation to take place. The intention was to increase the duration in which the relative humidity fell within the ideal range for carbonation of 40-60 %.

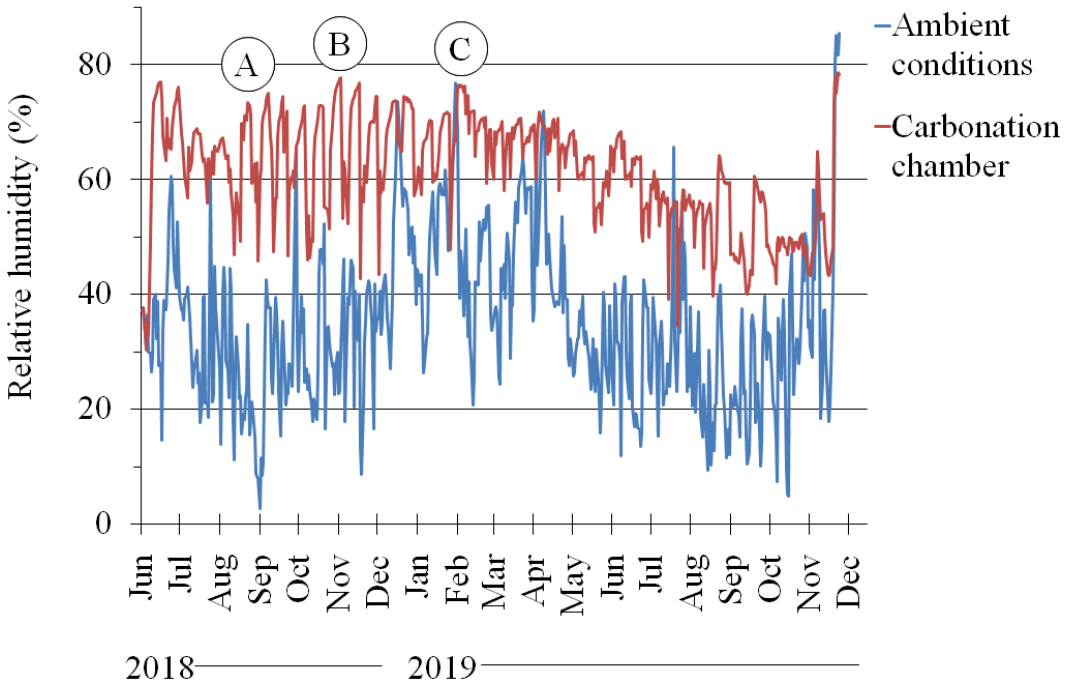

Figure 4.5: Relative humidity behaviour records

The relative humidity in the carbonation chamber took on a cyclic behaviour, as shown by the relatively constant peaks throughout the exposure. This occurred due to a release of moisture from the test specimens in the carbon dioxide periods and opening the chamber to the atmosphere. The saturated solution of magnesium chloride was used as it maintained a relative humidity within a small range of 30-35 % in Wexler & Hasegawa (1954) at temperatures up to 48 °C. This however was a closed system, without any presence of moisture within, which was not the case while the specimens were housed. At the start of the carbonation periods the relative humidity increased to a range of 60-75 %, as shown in the peak that is enclosed in black. Without the specimens present the relative humidity reverted back to that of the closed system with the solution, within a range of 40-50 %.

The other aspect of the relativity humidity in the chamber was that its magnitude reduced over time as there as was less moisture from the test specimens. At the end of the trial period the peaks in relative humidity increased due to the addition of the fly ash concrete specimens, as shown at A. After this the magnitude of the peaks in relative humidity decreased until the addition of the ordinary concrete

specimens, at B. There were specimens made of 2 concrete types beyond this time although the magnitude of the relative humidity continued to decrease with each cycle. The addition of the metakaolin concrete specimens at C increased the magnitude of the peaks in relative humidity, on top of that of the other concretes. There was a steady decrease in the magnitude of the peaks in relative humidity until the end of the exposure period, as the specimens were taken out the chamber.

The relative humidity of the ambient conditions (blue) indicated that there were changes to the moisture content in the atmosphere over the record. This may be attributed to maintained periods of an excess or lack of moisture that is suspended in the atmosphere. The relative humidity fluctuated within a range of 20-40 % throughout the majority of the data record, both in the summer and winter months. The relative humidity reached closer to or just above 80 % in the summer months of November to February in both years and below 20 % in the winter months. These periods of extremities in the relative humidity lasted for only up to several days thus could not present the same degree of influence as that in the chamber.

4.5. Durability

4.5.1. Overview

The results of the durability testing form the main contribution of the study and are presented and discussed in this section. The transport properties in terms the concrete resistance to gasses, moisture and chloride ions are discussed in **Section 4.5.2**. The chloride penetration into the cover concrete of the reinforced beams and carbonation depths in the cubes are then discussed in **Section 4.5.3**. The focus of the concrete durability in the results is on monitoring the corrosion behaviour of the embedded steel in **Section 4.5.4**. The corrosion damages in terms of the corrosion on the embedded steel and resulting concrete cracking and are discussed in **Section 4.5.3**. The parameters of the durability are illustrated in a flow diagram to reference their test methods in **Section 3.10** in the experimental programme.

4.5.2. Transport properties

4.5.2.1. Overview

The results of the transport properties in terms of the South African durability indices are presented and discussed in this section. These durability indices were tested to assess the influence of the cement replacement and cold joint on the transport of gasses, moisture and chloride ions. The concrete quality is graded in this section using the ranges that were established in Alexander et al., (1999), which are listed in **Table 4.1**. The durability indices are sensitive to the nature and extent of curing thus provide information to predict the performance of concrete in a particular environment. The procedures of the oxygen permeability, water sorptivity and chloride conductivity tests are discussed in **Section 3.9.2** of the experimental programme. The minimum, maximum and average of the durability indices in sets of 4 circular discs after each curing age are listed in **Appendix C**.

Table 4.1: Concrete quality grading (Alexander et al., 1999)

Concrete quality	OPI	WSI	CCI
Excellent	> 10	< 6	< 0.75
Good	9.5-10	6-10	0.75-1.5
Poor	9-9.5	10-15	1.5-2.5
Very poor	< 9	> 15	> 2.5

The susceptibility of the concretes to the transport of gasses, moisture and ions at the introduction of exposure is determined using the results after 28 days of curing. The results after the curing ages of 56 and 90 days are used to identify the changes to the transport properties by maintaining the curing of the cement extender concretes. Broadly the strength of concrete may indicate the durability however common cement extenders tend to decrease the transport of gasses, moisture and chlorides. It was unknown when the changes due to the pozzolanic reaction of the cement extenders would occur within the curing period of 90 days. The strength development trends over the 90-day curing period in **Section 4.3** showed that the majority of the hydration had occurred within a period of 28 days.

4.5.2.2. Oxygen permeability

The oxygen permeability indices (OPI) of the concretes were determined as the negative log of the Darcy coefficient (k) in m/s units. The average OPI values between the sets of circular discs after curing ages of 28, 56 and 90 days are presented in the bar chart in **Figure 4.6**. Note that the concrete permeability was lower with an increase in the OPI value, so that the general trend was an increase in the OPI values with the curing age. The OPI values of the monolithically-cast discs (M) are presented for the curing ages of 28, 56 and 90 days and that of the cold joint (CJ) discs, after 28 days only. The curing age axis in days increases from 28 to 90 days (left to right) with the disc notations of M and CJ just beside.

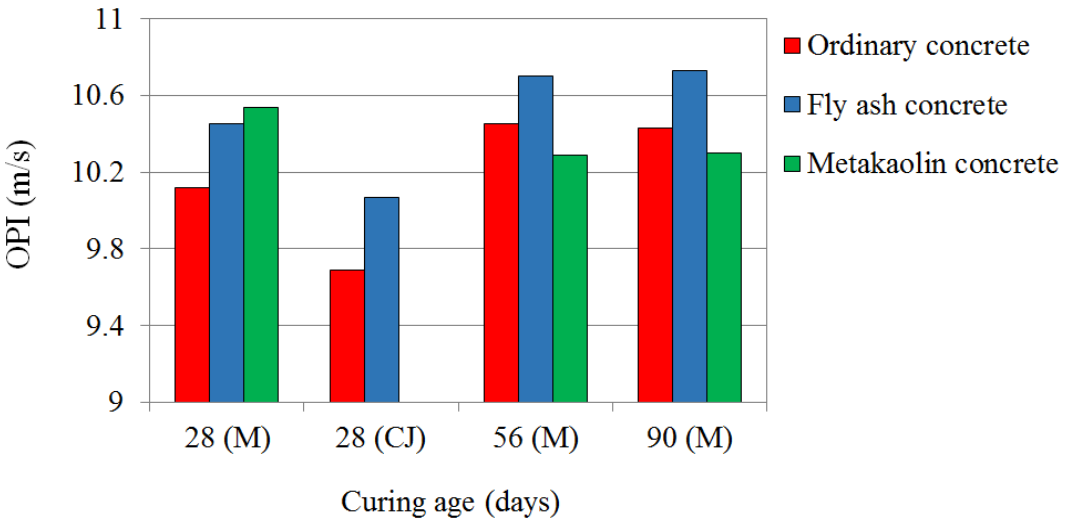

Figure 4.6: Oxygen permeability indices from 28 to 90 days

Greater than 95 % of the magnitude of the OPI values after 90 days of curing had yielded after 28 days by the monolithically-cast disc sets. Without the circular discs with a cold joint the OPI values fell within the concrete quality range that is regarded as excellent (OPI > 10) in Alexander et al., (1999) after 28 days. The OPI values of the discs with a cold joint were up to 4 % lower than that of the monolithically-cast after 28 days. The cold joint discs were tested in the case of the ordinary and fly ash concretes only due to complications of the test apparatus with that of the metakaolin concrete. The increase in oxygen permeability may be attributed to additional voids and an increase in their connectivity along the joint

plane. The total porosity (void volume) of the cold joint discs was found to be higher than that of the monolithically-cast discs, as discussed in **Section 4.5.2.5**.

The OPI values of the cement extender concretes after 28 days of curing were up to 5 % higher than that of the ordinary concrete, of 10.1. The change in OPI was negligible thereafter where 3 % of the 90-day OPI had yielded from 28 to 90 days by the ordinary and fly ash concretes. The metakaolin concrete had the largest OPI value after 28 days, of 10.5, however the fly ash concrete had the largest OPI after 90 days, of 10.7. The OPI values of the metakaolin concrete from 28 to 90 days are an anomaly against the trend of the other concretes, as their OPI values increased over the same period. The anomaly in the OPI values of the metakaolin concrete occurred after the 70 mm diameter head of the coring drill was changed.

The increase in OPI of the cement extender concretes, of up to 5 %, indicates that the fly ash and metakaolin decreased the oxygen permeability. The decrease in permeability of gasses is typical of materials with smaller particle sizes as these superimpose the pores of cement paste. The connectivity of the pores in paste may be reduced which closes the transport paths of gasses, even with a higher total porosity. The small differences in the OPI (of within 5 %) between the concretes may be attributed to a similarity in the particle sizes between the binders. The binders had similar proportions of particles in the size ranges wherein the majority of the particles were contained. There would likely be larger differences in the OPI between the concretes if coarser (or lower grade) cements were used instead.

Cement extenders have been found to increase in resistance to gas permeation in concrete for a given water: binder (W: B) ratio. The curing age however was required to be sufficient so that the pozzolanic reactions of these materials may close the pores in the cement paste. The OPI values of the concretes with fly ash and slag in Mackechnie (1996) were higher than the ordinary concrete after a curing age of 28 days. There were similarly small differences in the OPI between the concretes such that the test was regarded to be less-sensitive to the particle sizes of the binders. The OPI values of the concretes with fly ash and silica fume

in Ikotun et al., (2017) were higher than the ordinary concrete after 28 days of curing. The OPI values of the concretes with up to 20 % metakaolin in Bakera & Alexander (2017) higher than the ordinary concrete after the same curing age.

4.5.2.3. Water sorptivity

The water sorptivity indices (WSI) of the concretes were determined from the increase in mass due to absorption into the circular discs. The average WSI values in mm/√hour units between the sets of circular discs after curing ages of 28, 56 and 90 days are presented in the bar chart in **Figure 4.7**. The nomenclatures of the previous chart are used for the discs which include the monolithically-cast (M) and cold joint (CJ) discs. The error bars (I) represent a confidence interval of 95 % which is based on the variation of WSI values after each curing age, assuming a normal distribution. Note that the water permeability was increased with the WSI value, so that the general trend was a decrease in WSI value with the curing age.

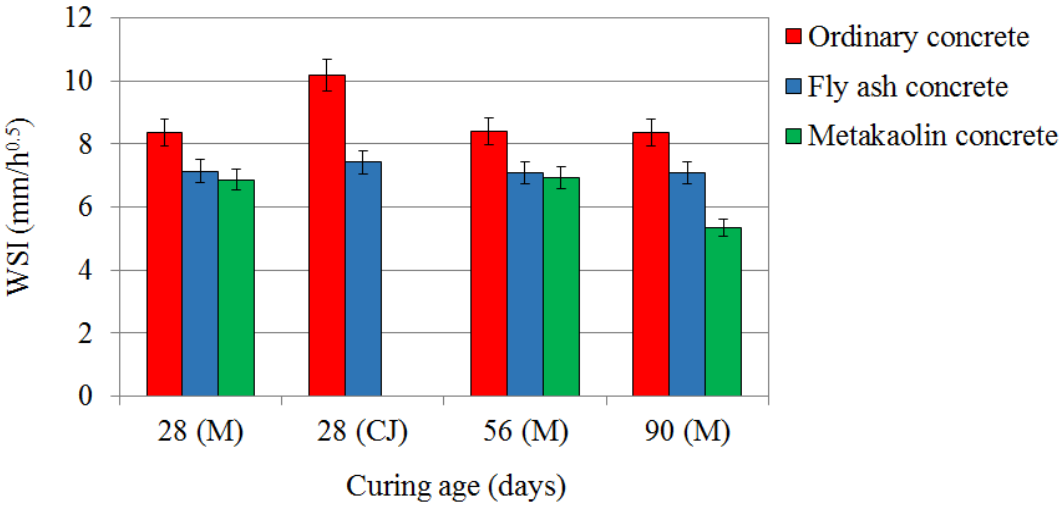

Figure 4.7: Water sorptivity indices from 28 to 90 days

The WSI values of the discs with a cold joint were increased by 22 % and 4 % in the ordinary and fly ash concretes respectively after 28 days. The WSI of the cold joint discs that were made of the ordinary concrete reached the concrete quality range that is regarded as poor (WSI > 10). The magnitude of these changes in the WSI were lower than the increase in chloride content in the reinforced beams

(with a cold joint), as discussed in **Section 4.5.3**. This may be attributed to cutting off the surface layer of the discs which did not contain the defects that occur in the casting stage. The sorptivity test is particularly sensitive to the concrete properties at the surface instead of the properties through the entire volume (Ballim, 1993).

Greater than 99 % of the magnitude of the WSI values after 90 days of curing had yielded after 28 days by the monolithically-cast disc sets that were made of the ordinary and fly ash concretes. The WSI of the metakaolin concrete decreased by 22 % of the 90-day WSI from 28 to 90 days which reflects that there was a further progress of the pozzolanic reaction. The WSI values of the monolithically-cast discs fell within the concrete quality range that is regarded as good ($6 < WSI < 10$) in Alexander et al., (1999) after 28 days. The WSI values of the fly ash and metakaolin concretes were up to 15 % and 36 % lower than that of the ordinary concrete respectively over 90 days. After 90 days the metakaolin was the only binder that yielded a concrete quality that is regarded as excellent (with $WSI < 6$).

The high resistance to sorptivity has been found in a number of studies due to cement extenders, for a given water: binder (W: B) ratio. The sorptivity of the fly ash concrete was similar to that in Mackechnie (1996) where the WSI values were lower than the ordinary concrete after 28 days of curing. The water permeability of the concretes with fly ash in Liu et al., (2014) was lower than the ordinary concrete only after 90 days. The WSI values of the concretes with metakaolin in Bakera & Alexander (2017) were significantly lower than the ordinary concrete after 28 days. The sorptivity of the metakaolin concrete herein related strongly to the total porosity in the curing period of 90 days, as discussed in **Section 4.5.2.5**.

4.5.2.4. Chloride conductivity

The chloride conductivity indices (CCI) of the concretes were determined from the diffusion test in the South African standards. The CCI has been related to the corrosion rate under chloride exposure in isolation in a number of studies such as Mackechnie (1996) and Scott (2004). The average CCI values in mS/cm units between the sets of circular discs after curing ages of 28, 56 and 90 days are

presented in the bar chart in **Figure 4.8**. The nomenclatures of the monolithically-cast and cold joint discs and error bars (I) of the plot points are the same as in the previous sections. Note that the chloride conductivity was decreased with the CCI value, so that the general trend was a decrease in CCI value with the curing age.

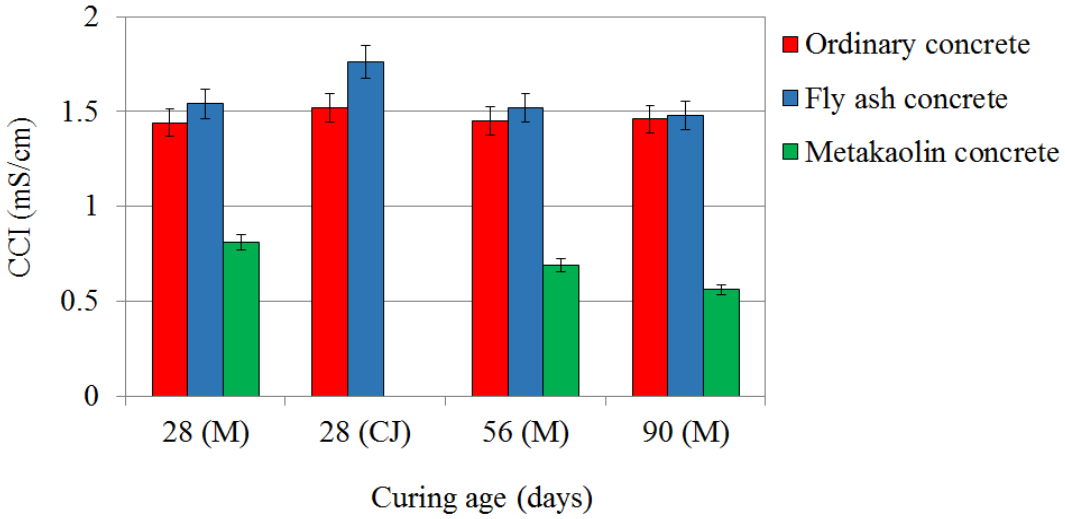

Figure 4.8: Chloride conductivity indices from 28 to 90 days

Greater than 95 % of the magnitude of the CCI values after 90 days of curing had yielded after 28 days in the monolithically-cast disc sets that were made of the ordinary and fly ash concretes. The CCI of the metakaolin concrete decreased by 45 % of the 90-day CCI from 28 to 90 days, the largest change of the durability indices. The CCI values of the monolithically-cast discs fell within the concrete quality range that is regarded as good (CCI < 1.5) in Alexander et al., (1999) after 28 days. The CCI of the monolithically-cast discs that were made of the ordinary concrete was relatively constant from 28 to 90 days, with CCI values of 1.44 and 1.46 respectively. This negligible change in the CCI from 28 to 90 days was the same as the OPI and WSI trends thus as a curing duration of 28 days was suitable.

The CCI values of the discs with a cold joint were increased by 6 % and 14 % in the ordinary and fly ash concretes respectively after 28 days. The CCI of the cold joint discs that were made of both these concretes entered the concrete quality range that is regarded as poor (CCI > 1.5). The chloride diffusion coefficient of the concrete with a cold joint in Sung-Won & Seung-Jun (2016) was increased by

a similar magnitude, by up to around 20 %. The diffusion coefficient was further increased by cracks, on top of that due to the cold joint, which reflects the corrosion risk if both defects are present. Some of the reinforced beams herein contained both defects due to a lower cover depth, as discussed in **Section 4.5.3**.

The CCI of the fly ash concrete decreased by 4 % between the curing ages of 28 and 90 days, from 1.54 to 1.48 respectively. This corresponds to a shift of the CCI from the concrete quality ranges of poor (CCI > 1.5) to good (< 1.5) in this curing period. The CCI values of the metakaolin concrete shifted into the excellent quality range (< 0.75) where the CCI after 28 days of 0.82 decreased by 31 %, to 0.56 after 90 days. These CCI values were within a range of 44-62 % lower than the other concretes due to the high chloride resistance of metakaolin. Though this material had smaller particle sizes than the cement, the alumina content is also influential to chloride resistance. The alumina compounds comprised of 43.5 %, 28.5-30.5 % and less than 5 % in the metakaolin, fly ash and cement respectively.

The increase in chloride resistance due to metakaolin has been found in a number of studies due to its high reactivity and alumina content. The CCI values of the concretes with metakaolin in Bakera & Alexander (2017) were much lower than the ordinary concrete after 28 days of curing. The chloride diffusion rates of the pastes with metakaolin in Cabrera & Nwaubani (1998) were much lower than that with fly ash after 60 days. The low resistance of fly ash concrete after 28 days herein has also been found due to its delayed reactivity to resist the diffusion of chlorides. The CCI values of the concretes with fly ash in Mackechnie (1996) were lower than the ordinary concrete after 28 days due to the slower reactivity.

4.5.2.5. Total porosity

The total porosities (n) of the concretes were determined as the void percentage (%) in the circular discs after they were vacuum-saturated. This parameter is compared in this section between the discs that were saturated with the solutions of calcium-hydroxide and sodium-chloride. The average of the total porosity

values in percentage (%) between the sets of circular discs after curing ages of 28, 56 and 90 days are presented in the bar chart in **Figure 4.9**. The nomenclatures of the monolithically- cast and cold joint discs and error bars (I) of the plot points are the same as in the previous sections. There is a general trend of a decrease in the porosity with the curing age as the binder particles were being hydrated.

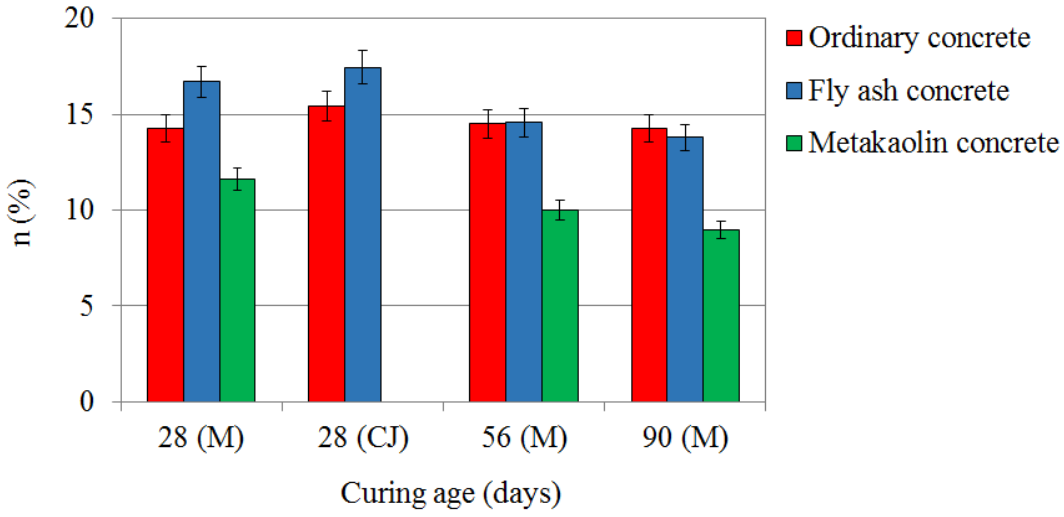

Figure 4.9: Total porosities from 28 to 90 days

Greater than 99 % of the magnitude of the porosity values after 90 days of curing had yielded after 28 days in the monolithically-cast disc sets that were made of the ordinary concrete. The porosity of the fly ash and metakaolin concrete reduced by 21 % and 30 % of their 90-day porosity respectively in the period from 28 to 90 days. The porosity was largest in the fly ash concrete after 28 days, 17.4 % larger than the ordinary concrete, reducing to 3.5 % lower after 90 days. The porosity was lowest in the metakaolin concrete at all curing ages, within a range of 18.6-37.1 % lower than the ordinary concrete. Curing up to 90 days was thus important to reduce the volume of un-hydrated fly ash and metakolin and fill the paste pores.

The pore sizes and total porosity of concretes with fly ash has been found to be lower than ordinary concrete after a cuing age of 28 days. The total porosity of the pastes with fly ash in Zeng et al. (2012) was higher than the plain paste up to 28 days with an increase in replacement level, up to 60 %. After 90 days there were minor differences in the porosity between these pastes as there was a smaller

volume of un-hydrated material. The pore sizes of the concrete with fly ash in the pore size distributions (PSD) in Liu et al., (2014) were lower than the ordinary concrete after 90 days. The porosity trend of the fly ash concrete herein was such that curing ages of longer than 90 days would continue to reduce the porosity.

A rapid reduction of the pore sizes and total porosity of concrete with metakaolin after 28 days of curing has not invariably been found in the literature. The pore sizes in the PSD of the concretes with metakaolin in Khatib & Wild (1996) were lower than the ordinary concrete after 14 days. Though PSDs were not established herein the low porosities of the metakaolin concrete at 28 days suggest that the pore sizes were smaller than that of the ordinary concrete. The PSDs in Ferreira et al., (2015) after a later age of 90 days also found smaller pore sizes although the total porosities were larger. The total porosity is thus not a controlling factor of the concrete penetrability as the pore sizes may be reduced to close the transport paths. It is clear from the oxygen permeability results that the cement extenders both superimposed the pores and capillaries, to decrease the oxygen permeability.

The average of the total porosity in the circular disc sets that were saturated with the sodium-chloride solution are omitted for the sake of brevity. The trends of the porosity from 28 to 90 days in these disc sets were the same as that which were saturated with the calcium-hydroxide solution (in the sorptivity test). The porosity values after the curing ages of 28, 56 and 90 days were however 56-62 % lower than that of the calcium-hydroxide solution. This trend of a lower porosity in the discs with chloride is a general finding, due to the difference in the density of the solutions (Bakera & Alexander, 2017). The similarity in the trends of the porosity between the saturating solutions indicates the strength of the porosity results.

4.5.3. Penetration state

4.5.3.1. Overview

The results of the chloride profiling and carbonation depth are presented and discussed in this section as a cumulative assessment of the exposure. These were

tested to assess the influence of the cement replacement, carbonation, cover depth and cold joint on the chloride penetration. The chloride profiles in the reinforced beams were based on the total chloride content by mass in the concrete samples in the cover concrete. Each sample was extracted from a 5 mm depth increment of the concrete over the steel bar, to the top level of the bar surface. The carbonation depth in the cover region of the beams was estimated from that in the plain cubes, which did not have a cold joint or cracks. The results of the chloride penetration and carbonation depth are sub-divided into chloride penetration in the reinforced beams after 21 cycles of exposure, carbonation depth in the plain cubes after 10 and 21 cycles of exposure and carbonation depth in the trial period of exposure.

4.5.3.2. Chloride penetration

The chloride profiles in the 20 mm cover reinforced beams that were made of the ordinary concrete (denoted CEM) are plotted in **Figure 4.10**. The profiles were established from the samples in sets of 3 beams with a cover depth of 20 mm after 21 cycles of exposure. The error bars (I) represent a confidence interval of 95 % that is based on the variation of the chloride content in the beam sets, assuming a normal distribution. The nomenclatures include the monolithically-cast (M) beams and the beams with a cold joint (CJ) under the isolated (I) and combined (C) exposure regimes. The red line is the average of the carbonation depths which were measured in the sets of 2 cubes after 21 cycles (or 294 days) of exposure.

The minimum, maximum and average of the chloride contents in the sets of 3 reinforced beams in each depth increment are listed in **Appendix C**. The sampling was performed at the mid-span using a 25 mm drill bit and the data points that are plotted were at the centre of the 5 mm depth increments. The chloride contents in each concrete sample of the reinforced beams took into account the baseline chloride contents which were sampled before the exposure. The chloride contents in each of the 5 mm increments were subtracted from that obtained before the exposure for each concrete type. The baseline samples were obtained from the un-reinforced beams after a curing period of 28-day, as discussed in **Section 3.9.3.3**.

The minimum, maximum and average of the chloride contents in the sets of 3 un-reinforced beams before the exposure period are also listed in **Appendix C**.

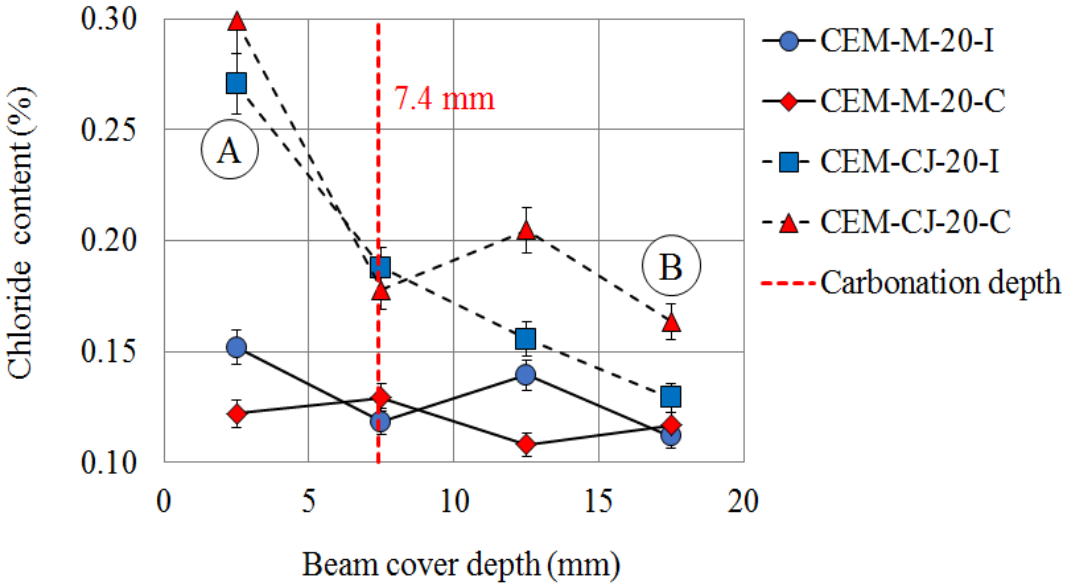

Figure 4.10: Chloride profiles in the ordinary concrete 20 mm cover beams

As shown there is a reduction in the chloride content of the cold joint beams (CJ) towards the end of the profiles, at a depth of 20 mm. The chloride penetration is assessed herein as the chloride contents in the surface region (A) and at the steel surface (B). The chloride contents in the 10 mm cover beams (presented later) could be considered to be within the surface region where the steel bar was in a closer proximity to the surface. The chloride content in the depth increment of 5-10 mm in the (20 mm cover) cold joint beams (CJ) was up to 245 % larger than the monolithically-cast beams. The durability indices of the circular discs with a cold joint differed by up to only 22 % as the surface concrete layer was removed.

The carbonation depth in the plain cubes under the combined exposure (red line) reached 7.4 mm after 21 cycles of exposure. This equates to 37 % of the cover depth in the reinforced beams without considering the presence of a cold joint or cracks in the cubes. There was an increase in the chloride content beyond the carbonation depth of 7.4 mm mainly in the beams with a cold joint, as shown at point B. The chloride content in the monolithically-cast beams in the depth

increment of 15-20 mm was only up to 4.4 % higher than that under the isolated chloride exposure. The chloride content in the cold joint beams in the same depth increment was up to 27 % larger than that under the isolated chloride exposure. This increase in chloride content at the steel surface (at a depth of 20 mm) due to the cold joint and carbonation formed part of the hypothesis of the study.

The trend of an increase in the chloride content beyond the carbonation depth is similar to a number of studies in the literature. An increase in the chloride content beyond the carbonation depth is part of the hypothesis of this study to determine the corrosion risk of chloride at a cold joint. The main part of the hypothesis was whether the corrosion rate was increased due to an increase in the chloride content beyond the carbonation depth at cold joints, which is addressed in **Section 4.5.3**. There is a general consensus in the literature that chloride penetration is increased in carbonated concrete which was attributed to a loss of chloride binding ability in concrete of a lower alkalinity (pH). The duration of exposure was required to be sufficient so that the carbonation depth was influential to the chloride penetration

The chloride content beyond the carbonation depth was also increased in ordinary concrete over a range of water: binder ratios in Yoon (2007). This was evident after 1 year of exposure which was applied in cyclic regimes or to concretes with add-mixed chloride. The pre-carbonation of ordinary concrete in Malheiro et al., (2016) before the chloride exposure also increased the chloride content beyond the carbonation depth. The carbonation resistance tends to be lower in concrete with cement extenders thus more of the chloride at the surface is shifted to the greater depths. The chloride content beyond the carbonation depth in Pakawat & Uomoto (2005) was larger in the concrete with slag than that in the ordinary concrete. This was also found in the concrete with fly ash and silica fume in Wang et al., (2016) due to an increase in the carbonation depth compared to the ordinary concrete.

The chloride profiles in the 10 mm cover reinforced beams that were made of the ordinary concrete (denoted CEM) are plotted in **Figure 4.11**. The nomenclatures of the reinforced beams and error bars (I) of the plot points are the same as in the

previous sets of chloride profiles. The chloride content up to a depth of 10 mm was 7-75 % larger than in the corresponding depth increments of the 20 mm cover beams. This increase in chloride content may be attributed to corrosion-induced cracking over the steel, as discussed in **Section 4.5.5**. The chloride content at the steel, from 5-10 mm, was increased due to the carbonation compared to that under the isolated chloride exposure. The chloride content at the steel was respectfully 4 % and 29 % larger in the carbonated monolithically-cast and cold joint beams.

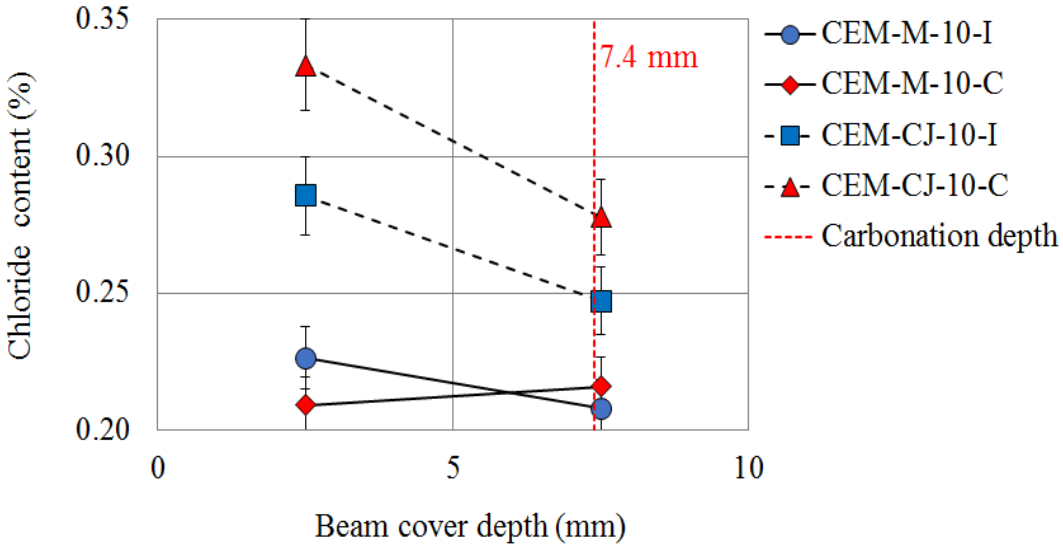

Figure 4.11: Chloride profiles in the ordinary concrete 10 mm cover beams

The chloride profiles in the 20 mm cover reinforced beams that were made of the fly ash concrete (denoted FA) are plotted in **Figure 4.12**. The nomenclatures of the reinforced beams and error bars (I) of the plot points are the same as in the previous sets of chloride profiles. The fly ash concrete yielded the lowest resistance of the concretes to chloride penetration as the chloride content was the highest in most depth increments. The chloride contents up to a depth of 15 mm were 5-243 % larger than in the corresponding depth increments in the ordinary concrete beams. The increase in chloride content in the surface region (A) caused the largest shift of chloride in the carbonated cold joint beams to the steel, at B.

The carbonation depth in the plain cubes under the combined exposure (red line) reached 10.9 mm after 21 cycles, equating to 55 % of the cover depth in the 20

mm cover beams. There was an increase in the chloride content beyond the carbonation depth of 10.9 mm, with a larger magnitude in the beams with a cold joint, as shown at B. The chloride content in the monolithically-cast beams in the depth increment of 15-20 mm was only up to 4 % higher than that under the isolated chloride exposure. The chloride content in the cold joint beams in the same depth increment was up to 44 % larger than that under the isolated chloride exposure. The increase in chloride content at the steel (at a depth of 20 mm) due to the cold joint and carbonation was greatest which is shown by a large gap at B.

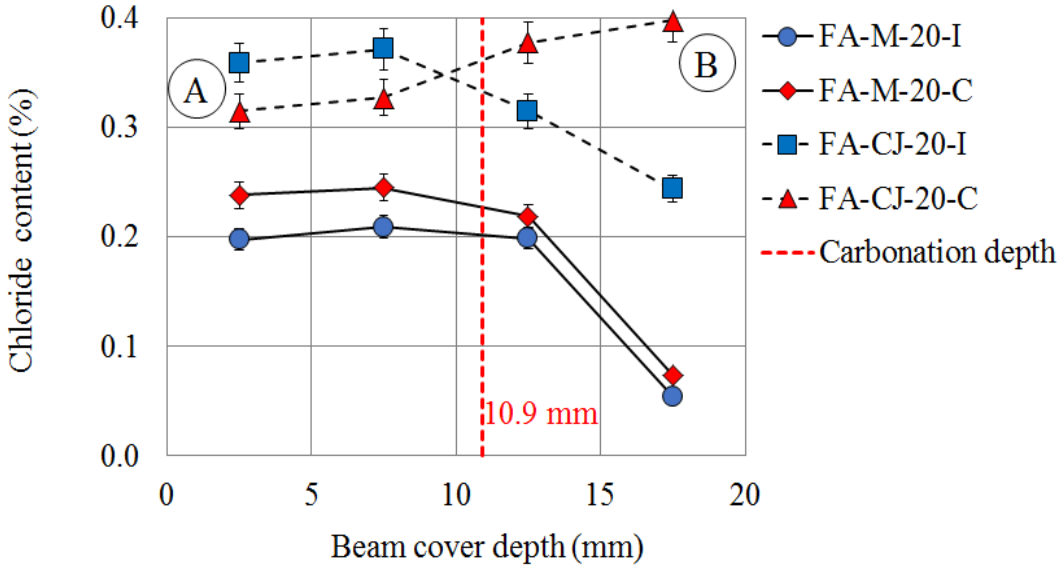

Figure 4.12: Chloride profiles in the fly ash concrete 20 mm cover beams

The increase in chloride content in the fly ash concrete has been found in a number of studies due to the relatively slow reactivity. The fly ash concrete was the most susceptible of the concretes to chloride penetration as the chloride conductivity index was the highest after 28 days of curing. The chloride content in the concretes with fly ash in Liu et al., (2014) in a single depth increment of 3 mm was higher than the ordinary concrete. This was found after sampling ages of up to 150 days however the exposure to a chloride solution started after the concrete had hardened for 24 hours. The exposure to chloride in Liu et al., (2020) was started after 90 days curing so that the pore sizes were reduced to a larger extent due to the fly ash. The free (or diffusible) chloride content was lower than that in the ordinary concrete in the depth increments up to a cover depth of 40 mm.

The chloride profiles in the 10 mm cover reinforced beams that were made of the fly ash concrete (denoted FA) are plotted in **Figure 4.13**. The nomenclatures of the reinforced beams and error bars (I) of the plot points are the same as in the previous sets of chloride profiles. The chloride contents in this beam set were the largest of all beams, up to 18 % larger than in the corresponding depth increments of the 10 mm cover ordinary concrete beams. The extent of corrosion-induced cracking was the largest of all the 10 mm cover beam sets due to the high chloride contents at the steel surface, as discussed in **Section 4.5.5**. The chloride content at the steel, from 5-10 mm, differed by up to 1 % between the exposure regimes for both beam types. The sampling range of 10 mm was not sufficient to determine if the chloride content was increased beyond the carbonation depth of 10.9 mm.

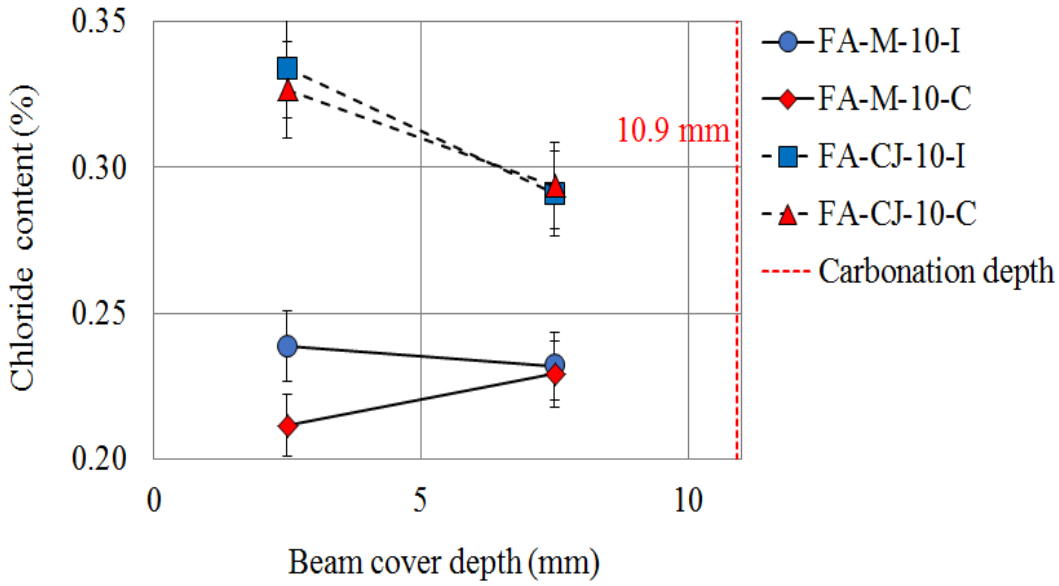

Figure 4.13: Chloride profiles in the fly ash concrete 10 mm cover beams

The chloride profiles in the 20 mm cover reinforced beams that were made of the metakaolin concrete (denoted MK) are plotted in **Figure 4.14**. The nomenclatures of the reinforced beams and error bars (I) of the plot points are the same as in the previous sets of chloride profiles. The metakaolin yielded the highest resistance to chloride penetration of the cementing binders as the chloride contents were the lowest of the concretes in most of the depth increments. The chloride contents up to a depth of 15 mm were 2-72 % lower than the corresponding depth increments

in the ordinary concrete beams. The exception to this was that the chloride content in the carbonated monolithically-cast beams was larger up to a depth of 10 mm. Nevertheless, the increase in chloride content in the surface region (A) caused the largest shift of chloride in the carbonated cold joint beams to the steel, at B.

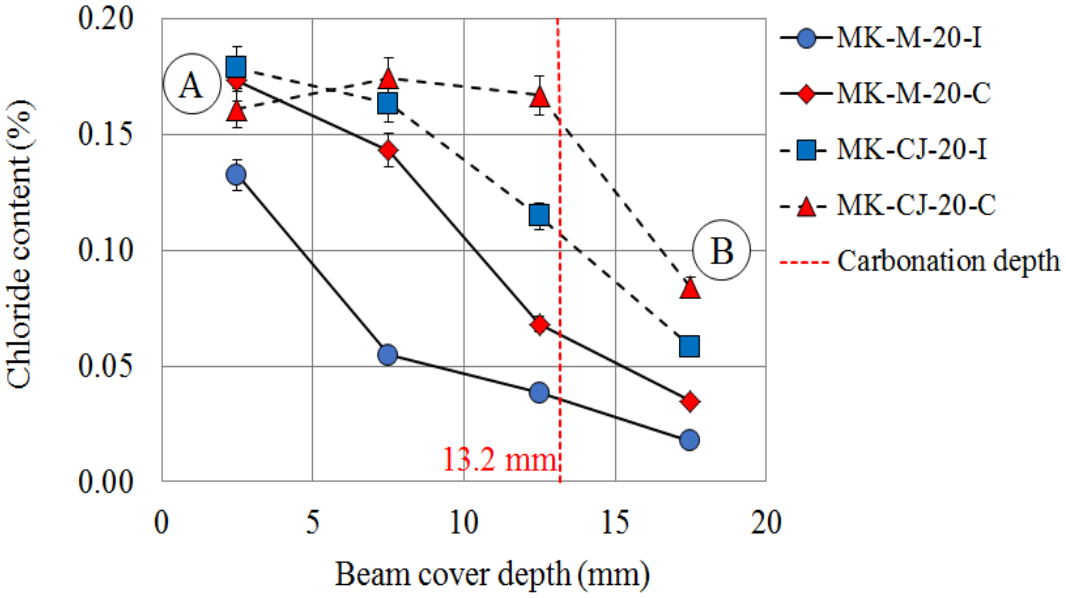

Figure 4.14: Chloride profiles in the metakaolin concrete 20 mm cover beams

The carbonation depth in the plain cubes under the combined exposure (red line) reached 13.2 mm after 21 cycles, equating to 66 % of the cover region in the 20 mm cover beams. There was an increase in the chloride content beyond the carbonation depth of 13.2 mm, with a larger magnitude in the beams with a cold joint, as shown at B. The chloride content in the monolithically-cast beams in the depth increment of 15-20 mm was up to 98 % larger than that under the isolated chloride exposure. The chloride content in the cold joint beams in the same depth increment was up to 44 % larger than that under the isolated chloride exposure. The increase in chloride content at the steel (at a depth of 20 mm) due to the cold joint and carbonation was greatest in magnitude which is shown by a gap at B.

The decrease in chloride content in the metakaolin concrete has been found in a number studies due to its high reactivity and alumina content. The metakaolin concrete was the least susceptible of the concretes to chloride penetration as the

chloride conductivity index was the lowest after 28 days of curing. The chloride contents in the concretes with up to 20 % metakaolin in Ferreira et al., (2015) were higher than the ordinary concrete after 90 days of exposure. There was also a reduction in the chloride content in the concretes with up to 20 % metakaolin in Bakera & Alexander (2019) after 90 days of exposure. The replacement level of the metakaolin herein (of 30 %) was sufficient to decrease the chloride content compared to the ordinary concrete. It is uncertain whether lower replacement levels (under 30 %) would have decreased the chloride content to the same extent.

The chloride profiles in the 10 mm cover reinforced beams that were made of the metakaolin concrete (denoted MK) are plotted in **Figure 4.15**. The nomenclatures of the reinforced beams and error bars (I) of the plot points are the same as in the previous sets of chloride profiles. The chloride contents in this beam set were the lowest of the 10 mm cover beams, 10-45 % lower than in the corresponding depth increments in the 10 mm cover ordinary concrete beams. The extent of corrosion-induced cracking was the lowest of all the 10 mm cover beams due to the low chloride contents, as discussed in **Section 4.5.5**. The chloride content at the steel, from 5-10 mm, was increased due to the carbonation compared to that under the isolated chloride exposure. The chloride content at the steel was respectfully 37 % and 38 % larger in the carbonated monolithically-cast and cold joint beams.

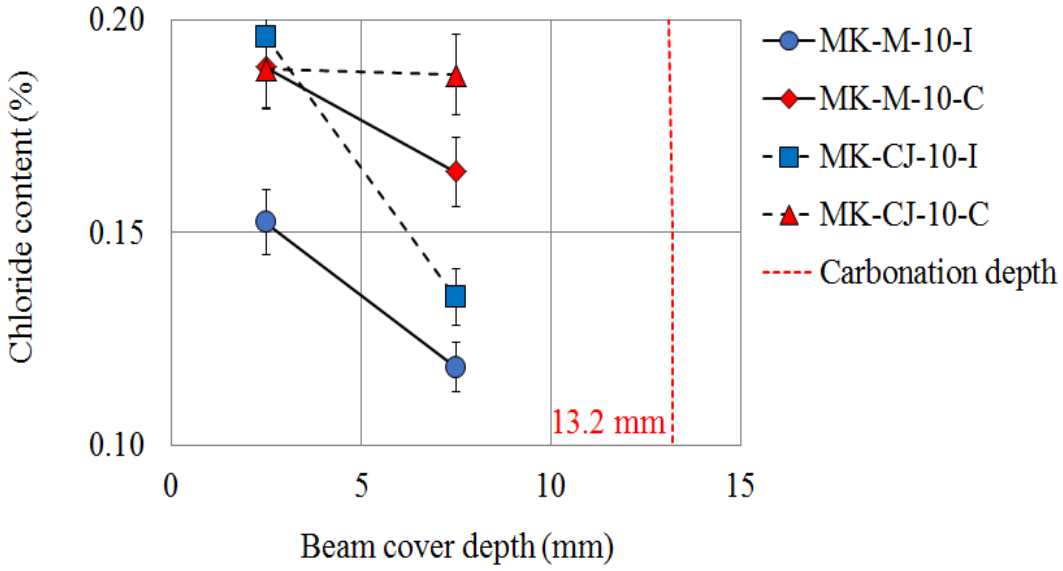

Figure 4.15: Chloride profiles in the metakaolin concrete 10 mm cover beams

4.5.3.3. Carbonation depth

The carbonation depth in mm in the plain concrete cubes in the test intervals of 1-10 and 11-21 cycles are plotted in **Figure 4.16**. The error bars (I) represent a confidence interval of 95 % that is based on the variation of the carbonation depth in the cube sets, assuming a normal distribution. The carbonation depths in the ordinary (denoted CEM), fly ash (FA) and metakaolin (MK) concretes are plotted under the isolated (I) and combined (C) regimes. The data points are the average of the carbonation depths that were measured in sets of 2 cubes after 10 and 21 cycles of exposure. The measurement method of the carbonation depth at each of the cube faces is illustrated with the aid of photographs together with the results. The exposure regimes in this case include isolated exposure to carbon dioxide (solid lines), which excluded the wetting periods, and the combined exposure (C).

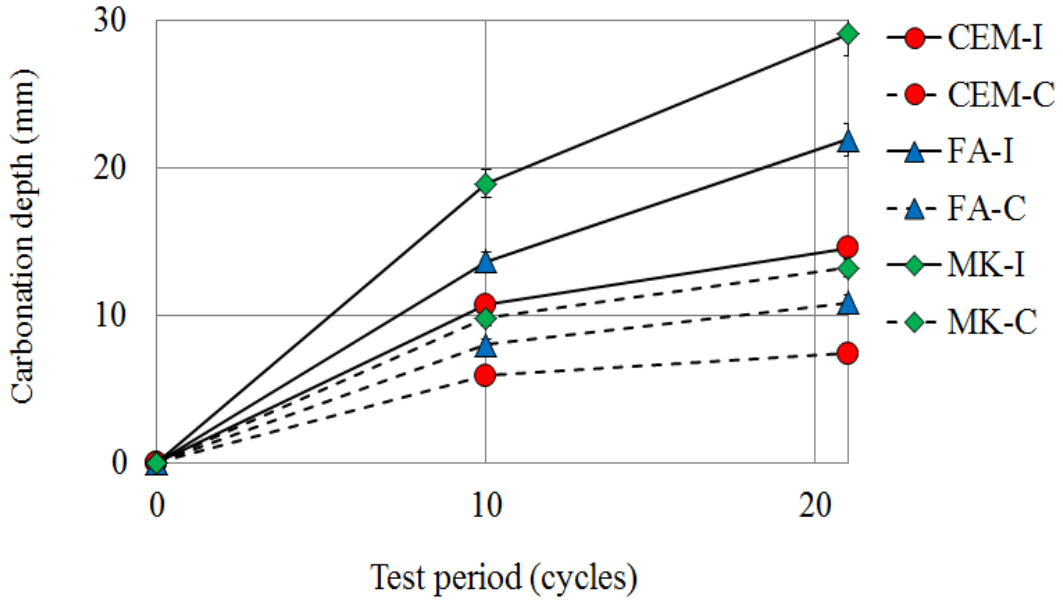

Figure 4.16: Carbonation depths after 10 and 21 cycles

The chloride penetration in the reinforced beams was not tested after 10 cycles of exposure as the concrete had to be intact for the corrosion testing. The carbonation depths were a means of determining the resistance of the concretes in the intervals of 1-10 and 10-21 exposure cycles. The minimum, maximum and average of the

carbonation depths in the cube sets after 10 and 21 cycles of exposure are listed in **Appendix D 2**. The details of the carbonation testing using the phenolphthalein indicator solution may be found in **Section 3.9.3** of the experimental programme. The baseline values of the carbonation depths before the exposure are also listed in **Appendix D 2** together with that obtained during the exposure period.

The carbonation rate in Figure 4.20 was higher up to 10 cycles of exposure and lower in the cubes that were exposed to the chloride solution. The carbonation state before the exposure in the ordinary concrete cube set after 28 days of curing is shown in the photographs in **Figure 4.17**. The measurement method in each cube is shown later in the cube sets that had carbonated after 10 and 21 cycles of exposure. The entire section of the cubes below in the baseline tests turned a dark purple instantly after the applying the phenolphthalein solution. Photographs of the cubes that were made of the cement extender concretes are not included for the sake of brevity as these had the same appearance. A rapid colour change to dark purple resembles a sound concrete, with a pH value of greater than 9.5.

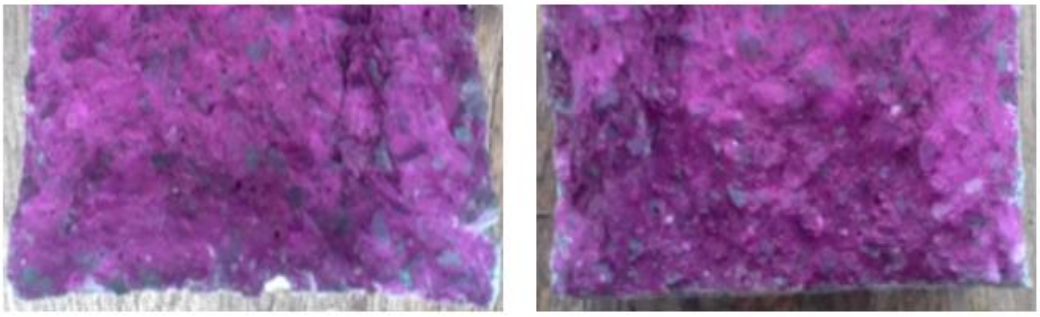

Figure 4.17: Baseline of the carbonation depths

The phenolphthalein test is regarded as an underestimate of the pH of the pore solution as the pH of ordinary concrete falls within a range of 13-14. In concretes that have been exposed to chloride or carbon dioxide, the pH decreases to within a range of 10-12 although still results in a strong colour change. Photographs of cubes that were made of the ordinary (CEM), fly ash (FA) and metakaolin (MK) concretes are shown from left to right after 10 cycles of exposure in **Figure 4.18**. Only 1 of the cubes from each set is shown under the isolated carbon dioxide

exposure (part A) and combined exposure (B) regimes. A scale distance of 20 mm is included in the central cube together with the measurement points at 1 of its faces, to illustrate the measurement. The representative depth of each cube was based on the average between its faces, with 5 points that were equally-spaced.

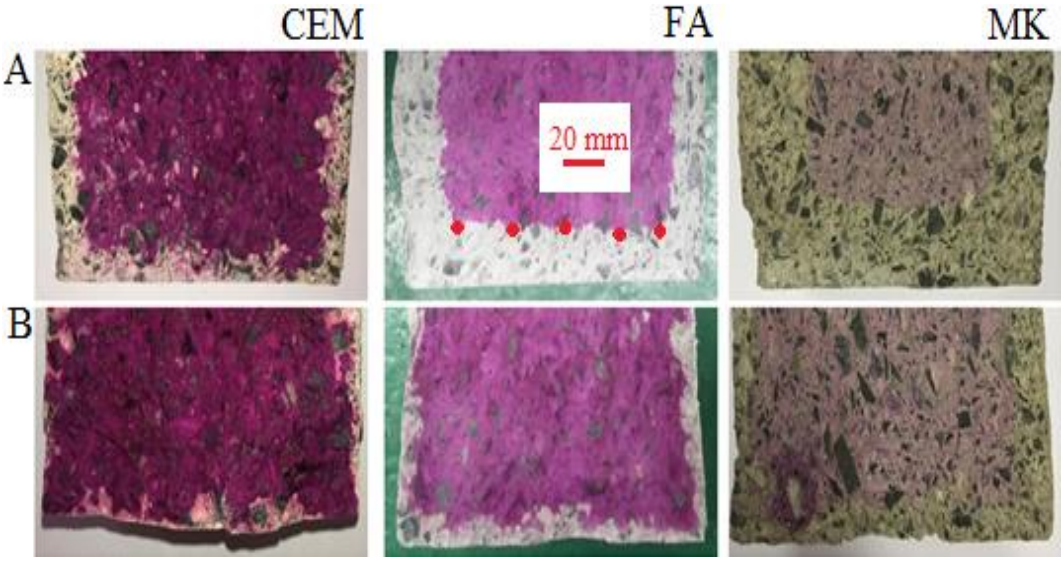

Figure 4.18: Carbonation depths after 10 cycles

The carbonation depths in the cubes that were also exposed to the chloride solution (B) were 41-55 % lower than that in the cubes that were exposed to the carbon dioxide gas only (A). The chloride solution thus blocked the paste pores at the cube surfaces to an extent which reduced the penetration of carbon dioxide. The carbonation depths of the cubes in the test period of 1-10 cycles were within a range of 59-82 % of that measured after 21 cycles. This decrease in carbonation rate after 10 cycles may be attributed to the reduction of the pore sizes and total porosity of the paste. Though these parameters were not measured in the exposure period this reduction in the carbonation rate with time reflects this phenomenon.

The carbonation depth in the ordinary concrete fell within respective ranges of 66 -78 % and 50-60 % less than in the fly ash and metakaolin concretes after 10 cycles. The carbonation depth in the ordinary concrete reached 5.9 mm after 10 cycles which was exceeded by the fly ash and metakaolin concretes with 8 mm and 9.8 mm respectively. The un-carbonated portion of the cement extender

concrete cubes in Figure 4.21 took on a lighter shade of purple during the test. This indicates that the pH of the pore solution beyond the carbonation depth in the cement extender concretes had reduced from a range of 13-14 to below a pH of 9.5. The bulk portion of the metakaolin concrete cubes took on the lightest shade of purple whereas that of the other concretes was closer to that baseline tests.

Photographs of cubes that were made of the ordinary and fly ash concretes are shown from left to right after 21 cycles of exposure in **Figure 4.19**. Only 1 of the cubes from each set is shown for the cubes under the isolated carbon dioxide exposure (part A) and combined exposure (B). The cubes that were made of the metakaolin concrete were not photographed at the end of the exposure period however their carbonation depths were measured. The carbonation depth in the ordinary concrete cubes fell within respective ranges of 28-51 % and 69-100 % larger than the fly ash and metakaolin concretes. The carbonation depth of the ordinary concrete cubes reached 7.4 mm after 21 cycles which was exceeded by the fly ash and metakaolin concretes with 10.9 mm and 13.2 mm respectively.

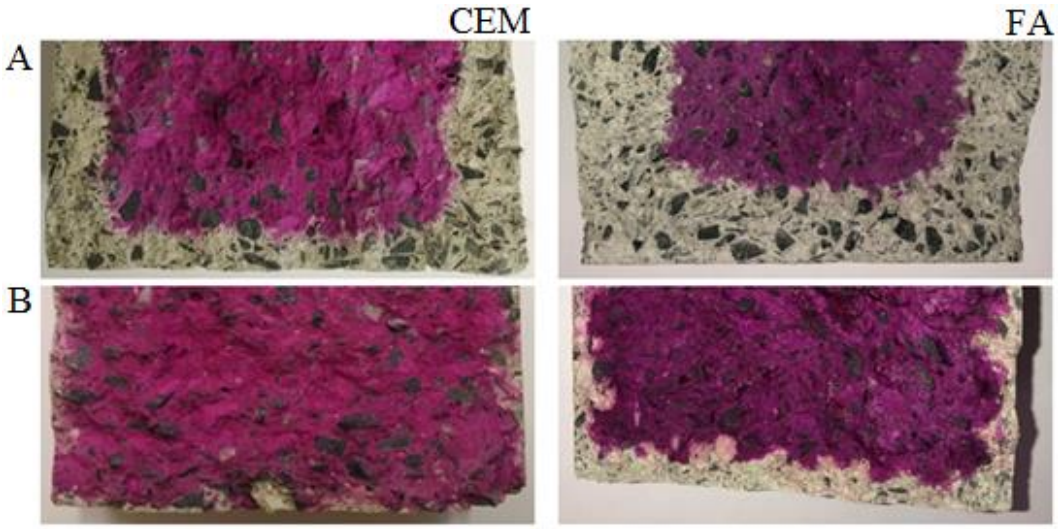

Figure 4.19: Carbonation depths after 21 cycles

The alkalinity (or pH) of the pore solution in the paste fraction was the main factor to the carbonation resistance of the concretes. The cement extenders yielded a reduction in the oxygen permeability from this index value (in **Section 4.5.1.2**)

due to the smaller particle sizes. The carbonation was slower in the pores of the ordinary concrete as there was more calcium oxide for the carbonation reactions to occur. The calcium oxide content both cement extenders were negligible in comparison to the rapid-hardening cement as these materials comprised of silica and alumina. The rapid-hardening cement contained 65 % calcium oxide by mass, whereas the fly ash and metakaolin contained 6-9.5 % and 0 % respectively.

The carbonation resistance of the concretes is comparable to studies that include cement extenders with lower calcium oxide contents. The concretes with fly ash, slag and silica fume in Ikotun et al., (2017) had larger carbonation depths in a period of exposure to atmospheric carbon dioxide for 2 years. At the same W: B ratio the carbonation depths in the concretes with fly ash, slag or silica fume were larger than the ordinary concrete. The oxygen permeability indices of these concretes were however lower as these materials have smaller particle sizes thus could reduce the gas transport paths. The carbonation depths were increased in the concretes with fly ash in Moreno & Sagues (1998), more so with an increase in the replacement level. The calcium oxide content in the concrete was lower with an increase in the replacement level thus resulting in a lower carbonation depth.

The trend of lower carbonation depths in concrete with chloride has also been found as the concrete pores are blocked by moisture. The carbonation depth of the concretes in Yoon (2007) that were exposed to a chloride solution was within 25 % of that exposed to carbon dioxide only after 1 year. A shorter period of 210 days in Pakawat & Uomoto (2005) revealed a similar trend where the carbonation depths were reduced by 33 % in the concrete with chloride. The carbonation depths in Ghahari et al., (2016) were reduced by similar magnitudes in concrete with chloride after 28 and 90 days. These studies were based on cyclic exposure with a varying duration of the chloride solution periods and found the same trend.

The other factor to the carbonation depth was the relative humidity of the carbonation chamber which was most favourable for the metakaolin concrete specimens. The monthly average of the relative humidity (in **Section 4.4.3**) fell

within the optimum range for carbonation, of 40-60 %, when the metakaolin concrete specimens were housed. The relative humidity of the chamber was the highest prior to this period, when the ordinary and fly ash concrete specimens were housed. The relative humidity decreased from a maximum of above 75 % as these other specimens sets were being removed thus could release less of their moisture into the system. The metakaolin concrete specimens were the last sets in the chamber where the relative humidity reached a maximum of closer to 60 %.

4.5.3.4. Carbonation of trial specimens

The carbonation progress in the plain concrete cubes in the trial period was based on 4 test ages after the baseline (before the exposure). The carbonation depth in sets of 2 cubes was measured at each age of this trial period of exposure which lasted for 2 months (or 4 exposure cycles). Only the ordinary concrete was used in this trial period as it was anticipated to be the most resistant of the concretes due to its calcium oxide content. These cube sets were exposed to an exposure regime of carbon dioxide gas only which excluded the wetting periods under the regime of combined exposure. The progress of carbonation under this exposure condition was regarded as suitable to assess the effectiveness of the carbonation chamber.

The carbonation depth after 2 weeks (or 1 cycle) of exposure to carbon dioxide reached 1 mm according to the aforementioned test method. The bulk of the cubes (beyond the carbonation depth) took on a dark shade of purple as the pH of the pore solution had not decreased. After 1 month (or 2 cycles) there was not much difference where the carbonation depth had progressed to 2.1 mm in the set of 2 cubes. The change in carbonation depth was relatively larger after these cycles where the average in the cube sets after 3 and 4 cycles increased to 4.1 mm and 5.3 mm respectively. The trial period was just less than $1/5^{th}$ of the duration of the 21-cycle period thus the carbonation depth would have reached around 25 mm under the same conditions. Though the trial period did not include the chloride exposure the conditions of the carbonation chamber were regarded to be suitable.

4.5.4. Corrosion behaviour

4.5.4.1. Overview

The results of the corrosion behaviour are presented and discussed in this section as a continuous assessment of the exposure. The various corrosion parameters were tested to assess the influence of the cement replacement, carbonation, cover depth and cold joint on chloride-induced corrosion. The corrosion potential and corrosion rate over 21 cycles (or 294 days) of exposure is assessed in **Sections 4.5.4.2** and **4.5.4.3**, respectively. The corrosion resistance is determined to rank the factors that were influential to these corrosion parameters, i.e. cold joint, cover depth, etc. in **Section 4.5.4.4**. The corrosion resistance was based on the corrosion initiation time of the corrosion potential and maximum corrosion rate that was reached in the exposure period. The relationship between the corrosion potential and corrosion rate is established from all the corrosion readings in **Section 4.5.4.4**.

The concrete resistivity over 294 days is presented to assess the conductivity that sustained the corrosion rate in **Section 4.5.4.5**. Cyclic exposure to moisture causes a fluctuation of the concrete conductivity which tends to occur in a marine zone. The temperature and relative humidity in the laboratory and carbonation chamber are related to the corrosion rate in **Section 4.5.4.6**. The cover depth between the exposed surface and embedded steel is related to the corrosion rate in **Section 4.5.4.6**. Any discrepancies in the corrosion resistance of the corrosion monitoring were thus found in terms of the temperature extremes or variation in cover depth. Lastly, the differences in the corrosion potential and concrete resistivity at the beam ends are discussed regarding the spacing from the cold joint to the bar ends.

4.5.4.2. Corrosion potential

The potential behaviour at the mid-span of the 20 mm cover ordinary concrete (denoted CEM) beams is plotted in mV units in **Figure 4.20**. The potential was monitored for 294 days using the Elcometer apparatus according to that discussed in **Section 3.2.2.1** of the experimental programme. The Elcometer is based on the

copper-copper sulphate (Cu-$CuSO_4$) half-cell which is the most common probe for structures and laboratories. The nomenclatures include the monolithically-cast (M) beams and the beams with a cold joint (CJ) under the regimes of isolated (I) and combined (C) exposure. The plotted points are based on the average in sets of 3 reinforced beams as the corrosion activity may vary due to the heterogeneity of concrete. Note that a decrease in the corrosion potential throughout this section corresponds to a higher probability of corrosion activity of the embedded steel.

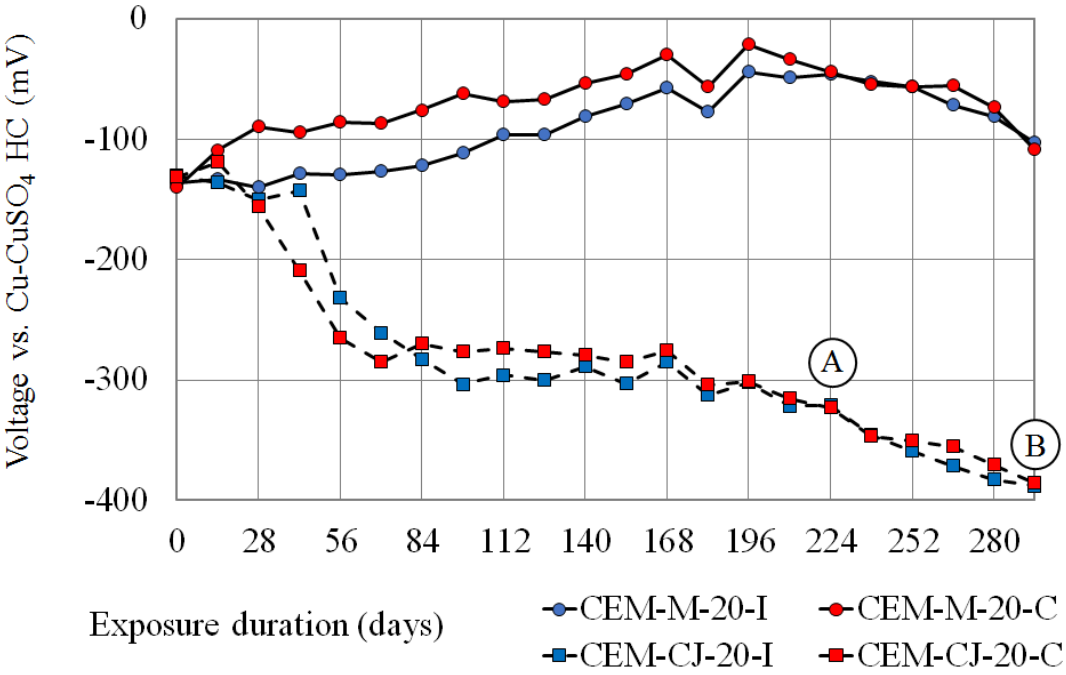

Figure 4.20: Corrosion potential in the ordinary concrete 20 mm cover beams

The corrosion parameters were monitored at a frequency of twice per exposure cycle; 1 day after the ponding and on completion of the carbonation. The readings from each beam are not listed for the sake of brevity and instead the averages between the sets are plotted. A moving average of the readings was calculated on a cyclic basis between the potentials after the chloride solution and carbonation. This was performed in the plots of all the corrosion parameters herein to decrease the magnitude of fluctuation (or "noise"). The corrosion potential, corrosion rate and concrete resistivity plots are thus the average of 2 readings per cycle in sets of 3 beams. Note that the carbonation depths that are referenced in these corrosion sections are based on the carbonation depth in the chloride-contaminated concrete.

The cold joint was the main factor due to a rapid change in corrosion potential after 28 days until the completion of exposure, after 294 days. The potential of the monolithically-cast beams fell within the range of passive corrosion in ASTM C 876 (ASTM, 1999), of > -200 mV, throughout the exposure period. The cold joint resulted in the potential to decrease into the range of active corrosion, of < -350 mV, which corresponds to a corrosion probability of 90 %. The beams with a cold joint reached the range of active corrosion after 224 days of exposure, as shown at point A. The potential then continued to decrease until the completion of exposure period, to reach a minimum potential of closer to -400 mV, as shown at point B.

There was a decrease in the potential in the monolithically-cast beams after 196 days even though these values fell within the range of passive corrosion. The potential of these beams may have reached the range of active corrosion within a relatively short duration. Likewise the cold joint beams may have cracked which generally decreases the potential to the range of severe corrosion, of < -500 mV. The corrosion initiation time is not compared between these beam types as the monolithically-cast beams had not actively corroded. The differences in potential between the exposure regimes were within 10 % in the monolithically-cast and cold joint beams. The carbonation depth of 7.4 mm under the combined exposure was thus not too influential to the potential at the larger cover depth of 20 mm.

The potential drops into the range of active corrosion, relative to that remaining passive over 294 days, are typical of factors such as the water: binder (W: B) ratio, defects, etc. The potential monitoring in Islam & Sugiyama (2010) found that the potential dropped into the range of active corrosion in concrete with a higher W: B ratio. The potential of the specimens with a lower W: B ratio in the concrete remained within the passive range of corrosion throughout the exposure period. The potential monitoring in Paul (2015) found that the potential dropped into the range of active corrosion in specimens that were exposure to chloride solution. The specimens that were exposed to the regime of drying exposure fell mostly within the passive range of corrosion throughout the exposure period.

The potential behaviour at the mid-span of the 10 mm cover ordinary concrete (denoted CEM) beams in mV units is plotted in **Figure 4.21**. The plots are based on the copper-copper sulphate (Cu-CuSO4) half-cell of the Elcometer apparatus with the same nomenclatures of the reinforced beams. The differences in the potential between the monolithically-cast and cold joint beam sets were smaller than that at a cover depth of 20 mm. The monolithically-cast beams were corroded at a cover depth of 10 mm as there was a smaller distance between the embedded steel and concrete (or exposed) surface. The potential of the cold joint beams reached the range of active corrosion in ASTM C 876, of < -350 mV, after 56 days, as shown at point A. The potential of the monolithically-cast beams then decreased close to or within the same potential range after 98 days, as shown at B.

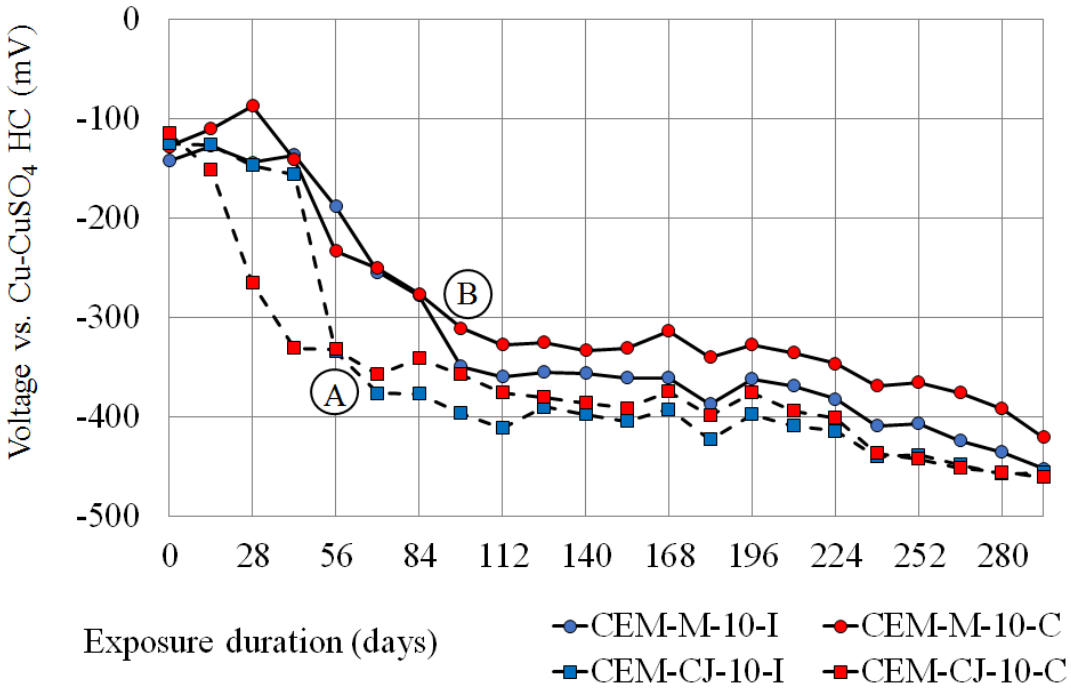

Figure 4.21: Corrosion potential in the ordinary concrete 10 mm cover beams

The differences in potential between the 10 mm cover beams were reduced after 98 days, to reach a minimum difference of 10 % after 294 days. The minimum potentials were obtained in the final (or 21st) exposure cycle, which were closer to the range of severe corrosion, of -500 mV. These potentials were due to cracking in the cover concrete when the corrosion rate had become accelerated, which is discussed later in **Section 4.5.5.3**. Though the potentials did not enter the range of

severe corrosion the formation of these cracks indicated that the corrosion rate had become accelerated in the propagation stage. The differences in potential between the exposure regimes were again within 10 % in the monolithically-cast and cold joint beams. The carbonation depth of 7.4 mm under the combined exposure was thus not too influential to the potential even at a lower cover depth of 10 mm.

The potential behaviour at the mid-span of the 20 mm cover fly ash concrete (denoted FA) beams in mV units is plotted in **Figure 4.22**. The plots are based on the copper-copper sulphate (Cu-CuSO4) half-cell of the Elcometer apparatus with the same nomenclatures of the reinforced beams. The potential of the monolithically-cast beams fell within the range of passive corrosion in ASTM C 876, of > -200 mV, throughout the exposure period. The potential of the cold joint beams decreased close to or within the range of active corrosion in ASTM C 876, of < -350 mV, after 140 days, as shown at point A. The potential did not continue to decrease thereafter, in that these readings (after 140 days) were the lowest of the exposure period. The potential of the cold joint beams stabilised closer to -300 mV whereas that of the beams monolithically-cast increased closer to 0 mV.

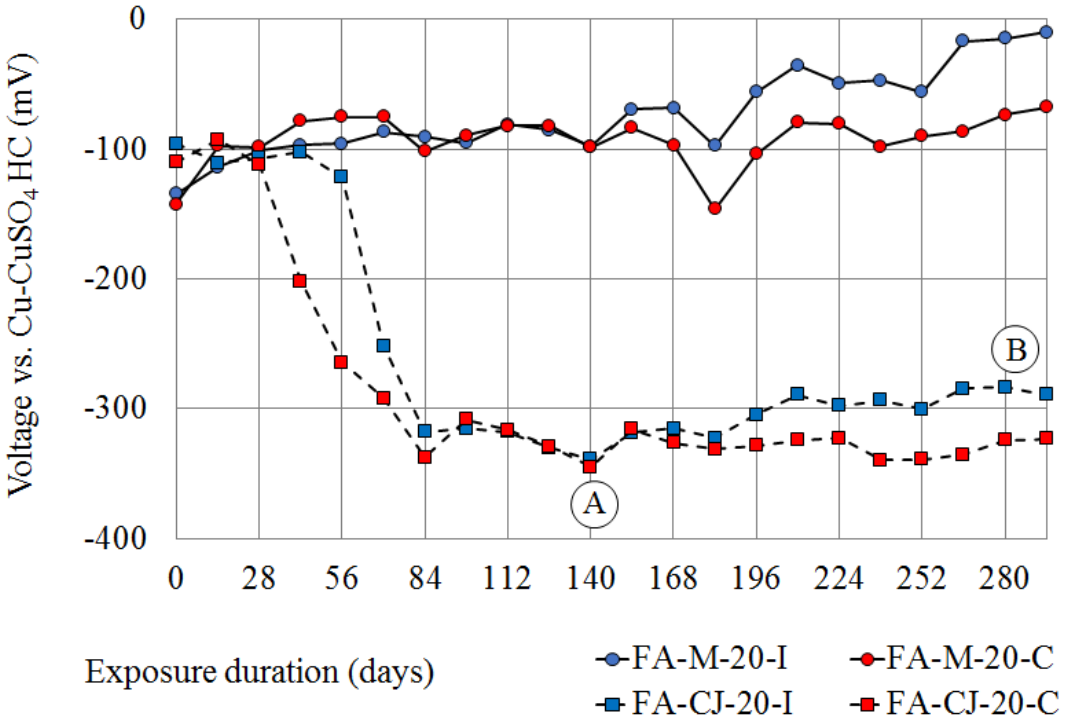

Figure 4.22: Corrosion potential in the fly ash concrete 20 mm cover beams

The potential of the cold joint beams was relatively constant once it had dropped near to or within the range of active corrosion. This indicates that there was a restriction to the corrosion rate in the fly ash concrete at this cover depth, which is shown in the next section. The potential of the cold joint beams reverted to the transition range of corrosion, -200 mV to -350 mV, where the readings were closer to that after 56 days, as shown at B. The differences in potential between the exposure regimes were within 15 % in the monolithically-cast and cold joint beams. The carbonation depth of 10.9 mm under the combined exposure was thus more influential to the potential than in the ordinary concrete at this cover depth.

The potential behaviour at the mid-span of the 10 mm cover fly ash concrete (denoted FA) beams in mV units is plotted in **Figure 4.23**. The plots are based on the copper-copper sulphate (Cu-CuSO4) half-cell of the Elcometer apparatus with the same nomenclatures of the reinforced beams. The potential of the cold joint beam sets reached the range of active corrosion in ASTM C 876, of < -350 mV from 32 to 56 days of exposure, as shown at point A. The potential of the monolithically-cast beams decreased close to or within the same range after 140 days, at shown at B. The potential of the cold joint beams stabilised closer to -400 mV while that of the monolithically-cast beams stabilised closer to -300 mV.

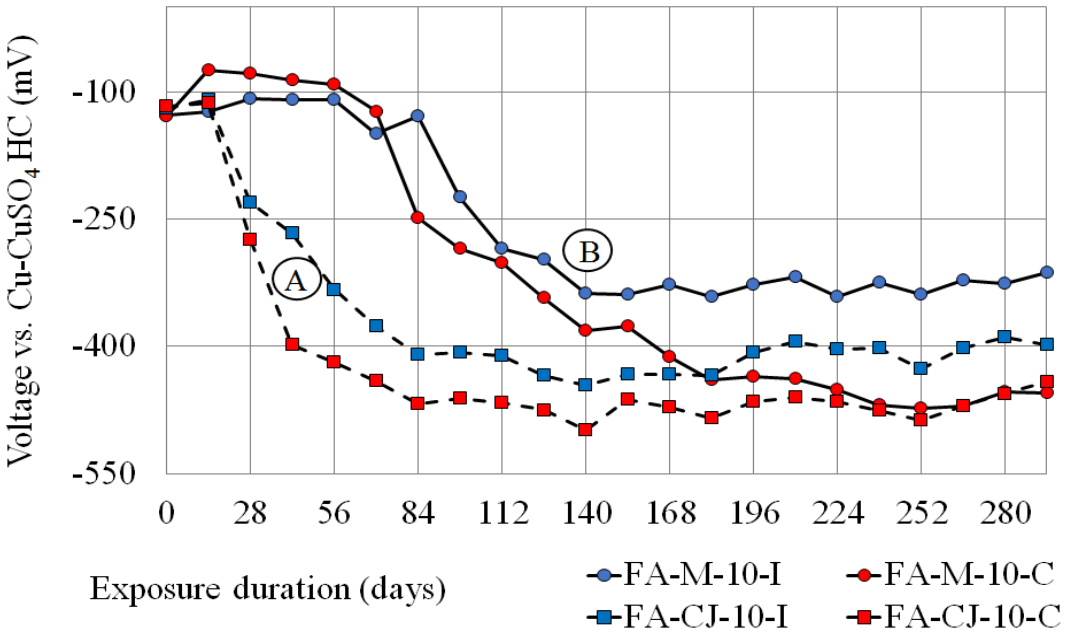

Figure 4.23: Corrosion potential in the fly ash concrete 10 mm cover beams

The differences in potential between the carbonated beams and that under the isolated chloride exposure were larger than the ordinary concrete within the range of active corrosion. The potential of the carbonated beams was up to 46 % lower than that under the isolated exposure once these beams had reached the range of active corrosion. The carbonation depth of 10.9 mm under the combined exposure was thus more influential to the potential in comparison to that of the ordinary concrete beams. This was due to the carbonation depth reaching the steel surface in the 10 mm cover concrete beams thus could also take part in increasing the corrosion activity. The potential of the carbonated beams of both types stabilised at the range of severe corrosion, of < -500 mV, until the completion of exposure.

The potential behaviour at the mid-span of the 20 mm cover metakaolin concrete (denoted MK) beams in mV units is plotted in **Figure 4.24**. The plots are based on the copper-copper sulphate ($Cu\text{-}CuSO_4$) half-cell of the Elcometer apparatus with the same nomenclatures of the reinforced beams. The corrosion parameters of the metakaolin concrete were not tested on 8 of the 43 scheduled days in the exposure period, which are shown after 252 days. The potential of the monolithically-cast beams fell within the range of passive corrosion in ASTM C 876, of > -200 mV, throughout the exposure period. The potential of the cold joint beams did not enter the range of active corrosion in ASTM C 876 at any stage in the exposure period.

Note that the actual readings were used, in that a moving average is higher as it was also based on that after the carbonation and drying periods. The potential of the cold joint beams under the isolated chloride exposure decreased to a minimum of -348 mV after 158 days, as shown at point A. The potential of the carbonated beams with a cold joint decreased to a minimum of -340 mV after 214 days, as shown at B. The potential of the cold joint beams was relatively constant once it had decreased near to the range of active corrosion, as with the fly ash concrete. The differences in potential between the exposure regimes were within 25 % in the monolithically-cast and cold joint beam sets, the largest at a cover depth of 20 mm. The carbonation depth of 13.2 mm under the combined exposure was thus more influential to the potential than in the ordinary concrete at this cover depth.

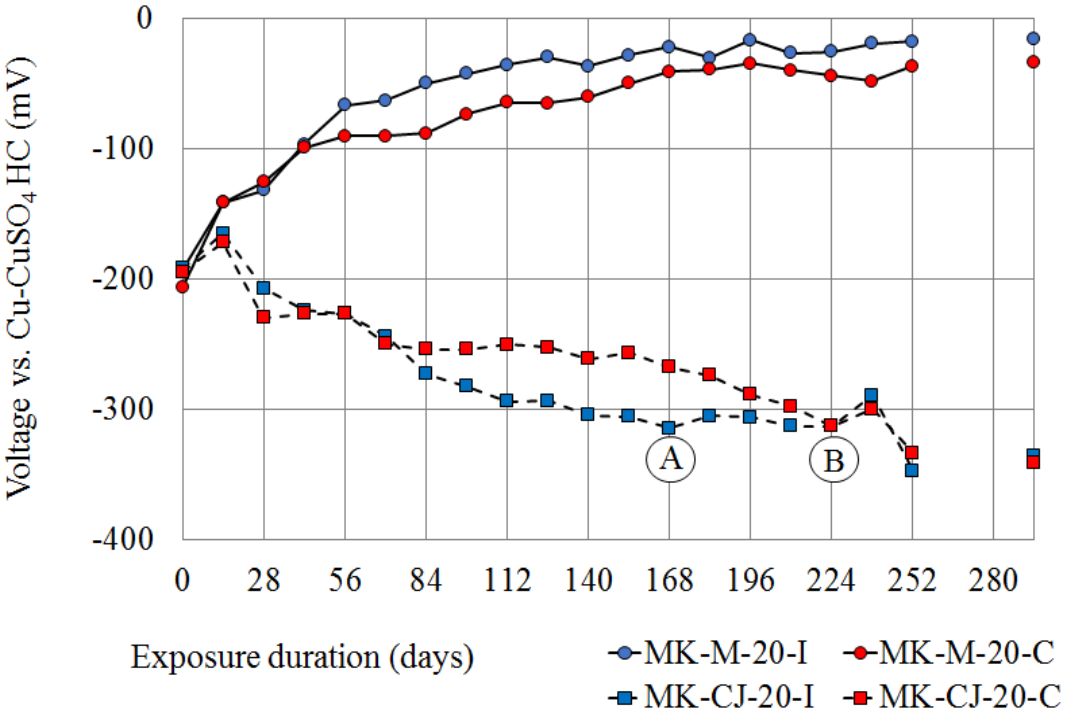

Figure 4.24: Corrosion potential in the metakaolin concrete 20 mm cover beams

The potential behaviour at the mid-span of the 10 mm cover metakaolin concrete (denoted MK) beams in mV units is plotted in **Figure 4.25**. The plots are based on the copper-copper sulphate ($Cu\text{-}CuSO_4$) half-cell of the Elcometer apparatus with the same nomenclatures of the reinforced beams. The gap in the readings at the latter of the exposure period is the same as in the plot of the 20 mm cover beams (after 252 days). The potential was decreased by the largest magnitude between the concretes even through this trend was not apparent at a cover depth of 20 mm. The carbonation depth of 13.2 mm in the cubes under the combined exposure was most influential to the potential as it reached 3.2 mm beyond the steel surface.

The potential of the carbonated cold joint beams reached the range of active corrosion in ASTM C 876 after 46 days of exposure, as shown at point A. The other beam sets reached the range of active corrosion later in the exposure period, from 172 to 214 days. The presence of the carbonation front at the steel surface is evident by the drop in potential towards the latter of the exposure. The potential of the carbonated cold joint beams reached a minimum of -507 mV which was the only beam set to reach the range of severe corrosion, as shown at B. The potential

of both types of beams under the isolated chloride exposure reached -343 mV at the completion of exposure. The potential of both types of carbonated beams was up to 56 % less than that under isolated chloride exposure, mainly after 196 days.

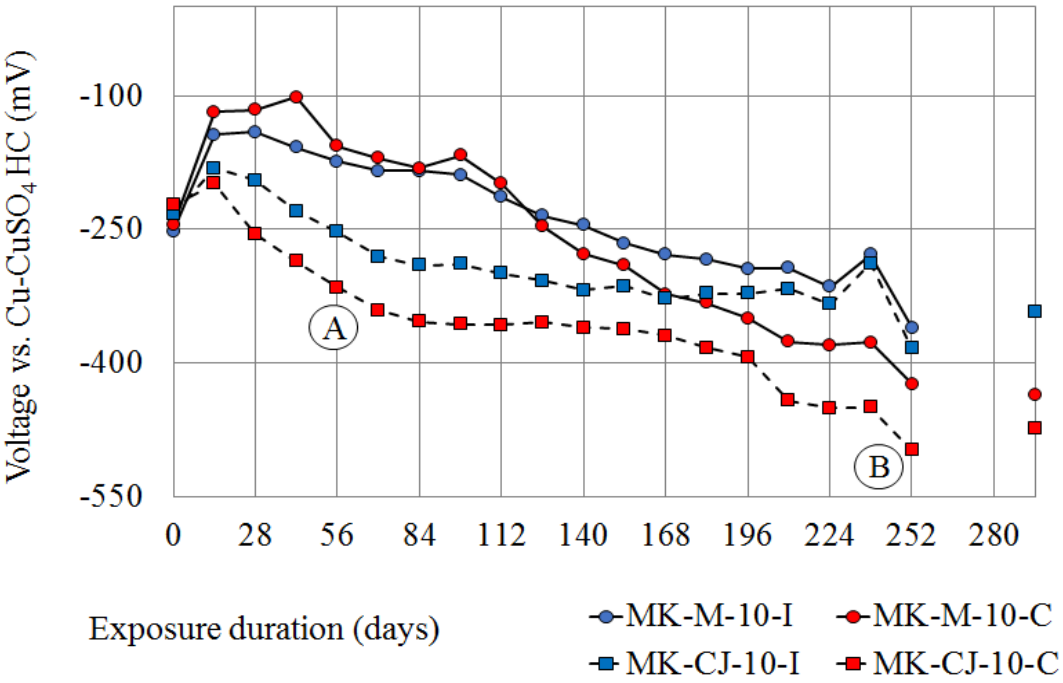

Figure 4.25: Corrosion potential in the metakaolin concrete 10 mm cover beams

The potential behaviour at the mid-span of all reinforced beam sets from the Coulostat unit is plotted in mV units in **Figures E.1** to **E.6** (in Appendix E). The Coulostat is based on the silver-silver chloride (Ag-AgCl) half-cell and was used for comparing the potential to the copper-copper sulphate (Cu-$CuSO_4$) half-cell. The potential behaviour is plotted in the same manner although the Coulostat unit was not available at the introduction of the exposure. The potential behaviour in mV units in the ordinary concrete beams is plotted in **Figures E.1** and **E.2** in a period from 18 days until 294 days. The potential behaviour in mV units in the fly ash concrete beams is plotted in **Figures H.3** and **H.4** in a period from 88 days 294 days. The potential behaviour in mV units in the metakaolin concrete beams is plotted in **Figures H.3** and **H.4** over the entire duration of the exposure.

There was similarity in potential behaviour between the half-cells although the Ag-AgCl half-cell indicated that there was a higher corrosion activity. This does

not reflect negatively on the Cu-$CuSO_4$ half-cell as these potential behaviours related well to the corrosion rate, as discussed later. The potential of the Ag-AgCl half-cell was 17-21 mV more positive than the Cu-$CuSO_4$ half-cell in all beam sets. This is similar to the conversion ranges such as in Roberge (2008) and ASTM C 876 (ASTM, 1999) where the potentials of the Cu-$CuSO_4$ half-cell were increased by 94 mV. The potential of the 20 mm cover beams decreased to the range of active corrosion at an earlier age and the 10 mm beams reached the range of severe corrosion. The Ag-AgCl half-cell was the more conservative of the apparatus however both were a suitable means of determining the initiation time.

4.5.4.3. Corrosion rate

The corrosion rate behaviour at the mid-span of the 20 mm cover ordinary concrete (denoted CEM) beams is plotted in $\mu A/cm^2$ units in **Figure 4.26**. The parameter was measured using the Coulostat apparatus which is based on the Coulostatic method of polarisation, as discussed in **Section 3.2.2.1**. The corrosion rate in this study is the corrosion current density that was dispersed on the steel surface during the polarisation. The plot points for each beam type, exposure regime and cover depth are the average of 2 readings per exposure cycle in sets of 3 beams. The nomenclatures include the monolithically-cast (M) beams and the beams with a cold joint (CJ) under the regimes of isolated (I) and combined (C) exposure. The monitoring period of the ordinary concrete beams spanned from 18 days in the 2nd cycle to the completion of the exposure period, after 294 days.

The corrosion rates of the monolithically-cast beams were less than 1 $\mu A/cm^2$ throughout the recording period, from 18 to 294 days. These fall within the ranges that are promulgated in the RILEM TC 154-EMC (RILEM, 2004) standard for polarisation methods. The cold joint resulted in an increase in the corrosion rate to beyond that in RILEM TC 154-EMC at the low cover depths of 20 mm and 10 mm in this study. The corrosion rate of the beams with a cold joint increased from that of the monolithically-cast beams from 56 days of exposure, as shown at point A. The potential of the cold joint beams reached the range of active corrosion in

ASTM C 876 (ASTM, 1999) after 224 days, as shown in the previous section. Once the potential dropped into the range of active corrosion there was an abrupt increase in corrosion rate to a maximum value of 7.6 µA /cm^2, as shown at B.

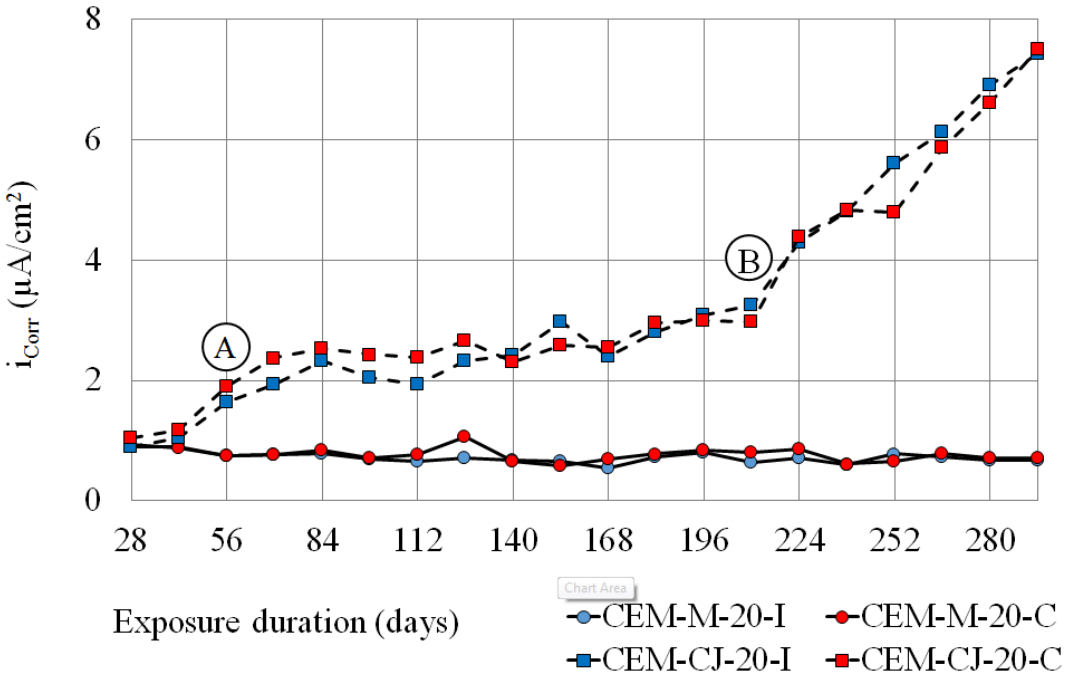

Figure 4.26: Corrosion rate in the ordinary concrete 20 mm cover beams

The cold joint resulted in an increase in the corrosion rate to reach higher ranges such as in Langford & Broomfield (1987) which classify the corrosion severity. The corrosion rate of both cold joint beam sets, of up to 7.6 µA/cm^2, spanned the corrosion severity range of low-moderate and moderate-high in this source. The corrosion rate of the monolithically-cast beam sets was lower than 1 µA/cm^2 throughout the exposure which falls within the range of a low corrosion severity in a number of sources. The maximum corrosion rate was respectively only 8 % and 1 % larger in the monolithically-cast and cold joint beams due to carbonation. The carbonation depth of 7.4 mm within the exposure period thus did not result in an increase in the corrosion rate in both beam types at a cover depth of 20 mm.

The corrosion rate behaviour at the mid-span of the 10 mm cover ordinary concrete (denoted CEM) beams is plotted in µA/cm^2 units in **Figure 4.27**. The corrosion rate is plotted over a monitoring period from 18 days of exposure until

294 days with the same nomenclatures of the reinforced beams. The corrosion rates of all beams increased in a steady manner until 112 days within a corrosion rate range of 8.5 µA /cm^2. The entry to active corrosion was not certain in the 10 mm cover beams as the corrosion rates generally increased in a rapid manner throughout the testing period of 276 days. The corrosion rate of the carbonated beams with a cold joint diverted from that of the other beam sets after 112 days, as shown at point A. The corrosion rate of this beam set then increased to reach a maximum value of 36.3 µA /cm^2, in the final (or 21st) cycle, as shown at B.

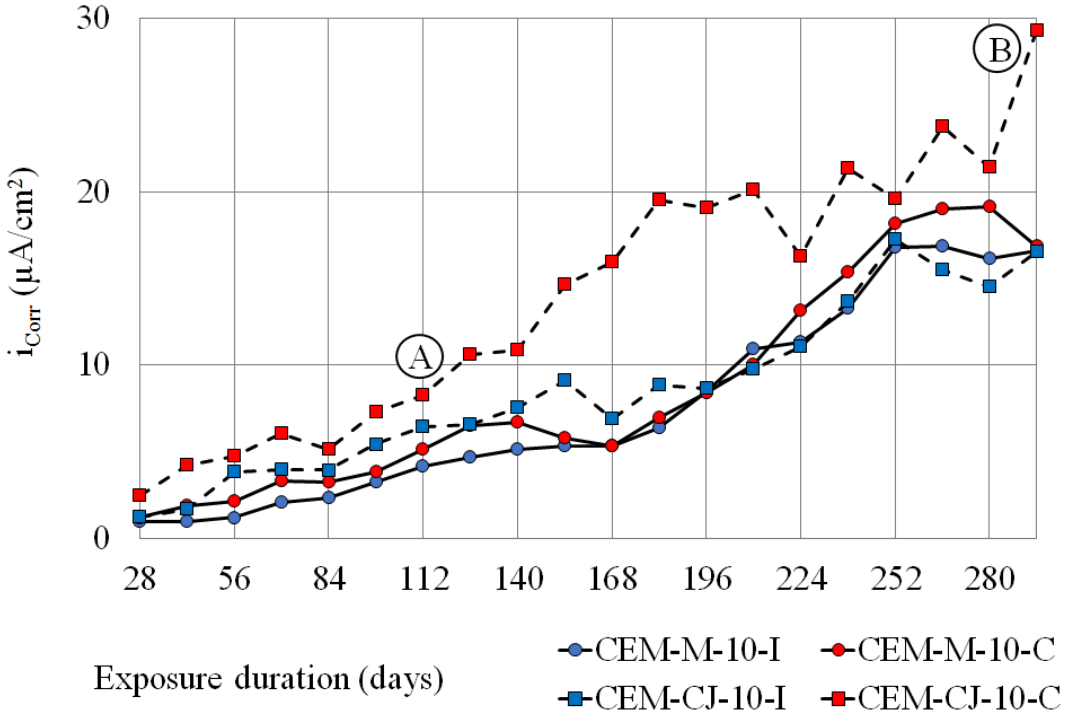

Figure 4.27: Corrosion rate in the ordinary concrete 10 mm cover beams

The extent of cracking in the carbonated beams with a cold joint was the largest of the ordinary concrete 10 mm cover beams, as discussed in **Section 4.5.3.2**. The corrosion rate of the remaining beam sets did not bridge this gap as these were not cracked to the same extent as this carbonated beam set. The corrosion rate of the carbonated monolithically-cast beams reached 25.1 µA /cm^2, which was followed by the beam sets under the isolated chloride exposure, with 21 µA /cm^2. These corrosion rates fall within the ranges of sources such as Bertollini et al., (2004), which classify such accelerated corrosion rates. The maximum corrosion rate was

18 % and 68 % larger due to carbonation in the monolithically-cast and cold joint beams respectively. The carbonation depth of 7.4 mm thus caused the largest increase in the corrosion rate in the cold joint beams at a cover depth of 10 mm.

The corrosion rate behaviour at the mid-span of the 20 mm cover fly ash concrete (denoted FA) beams is plotted in µA /cm^2 units in **Figure 4.28**. The corrosion rate is plotted over a monitoring period from 98 days of exposure until 294 days with the same nomenclatures of the reinforced beams. The corrosion rates of the monolithically-cast beams were under 1 µA/cm^2 throughout the recording period of 294 days. The corrosion rates of the cold joint beams were larger than the monolithically-cast beams at the start of the exposure, as shown by the gap after 98 days. The corrosion rate of the carbonated beams with a cold joint diverted from that under the isolated chloride exposure after 140 days, as shown at point A.

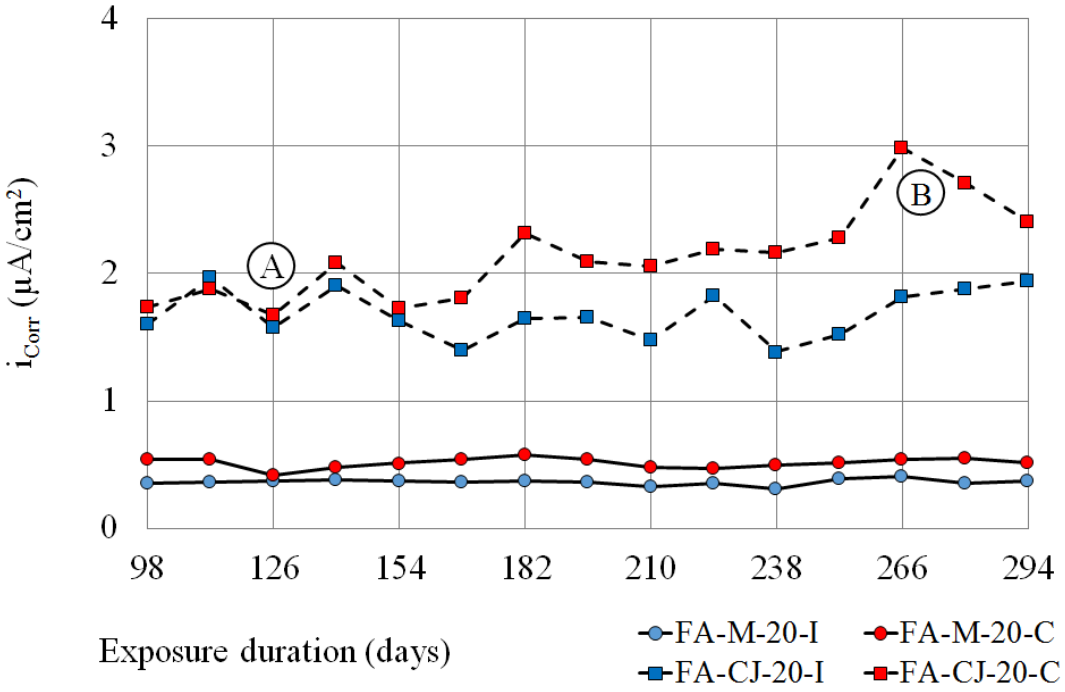

Figure 4.28: Corrosion rate in the fly ash concrete 20 mm cover beams

The potential of the cold joint beams reached close to or within the range of active corrosion in ASTM C 876 (ASTM, 1999) after 140 days, as shown in the previous section. The increase in corrosion rate in the cold joint beams under both exposure regimes after 140 days could thus be regarded to be within the range of active

corrosion. The corrosion rate of the carbonated beams with a cold joint increased after 140 days and then reached a maximum value of 3.2 µA /cm^2 after 266 days, as shown at B. The maximum corrosion rate of the carbonated beams with a cold joint was 29 % larger than that under the isolated chloride exposure, of 2.5 µA /cm^2. The carbonation depth of 10.9 mm thus caused a larger increase in corrosion rate at the cold joint compared to the ordinary concrete at a cover depth of 20 mm.

The corrosion rate behaviour at the mid-span of the 10 mm cover fly ash concrete (denoted FA) beams is plotted in µA/cm^2 units in **Figure 4.29**. The corrosion rate is plotted over a monitoring period from 98 days of exposure until 294 days with the same nomenclatures of the reinforced beams. The entry to active corrosion was again not certain in the 10 mm cover beams as the corrosion rates increased more rapidly compared to that of the 20 mm cover beams. The corrosion rate of the carbonated beams with a cold joint had diverted from that of the other beam sets before 98 days of exposure, as shown at point A. The corrosion rate of this beam set increased to reach the highest value of the 10 mm cover beams, of 62.1 µA /cm^2, as shown at B. The extent of cracking in this beam set was the largest of the 10 mm cover beams due to these conditions, as discussed in **Section 4.5.3.2**.

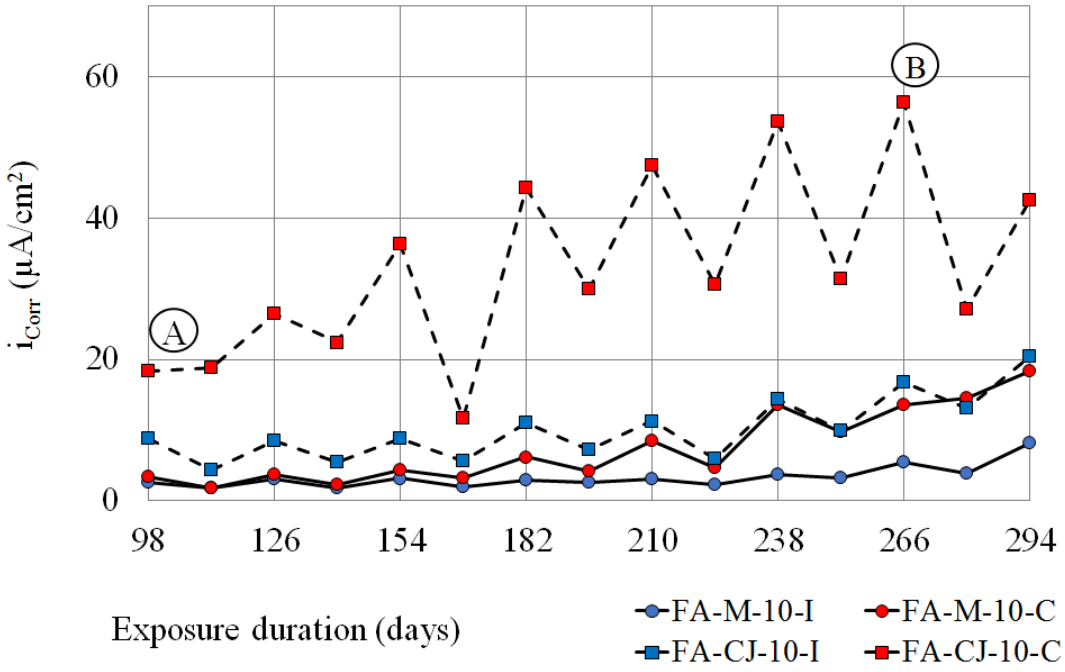

Figure 4.29: Corrosion rate in the fly ash concrete 10 mm cover beams

The corrosion rates of the other beam sets were much lower than that of the carbonated beams with a cold joint, as with the ordinary concrete. The maximum corrosion rate of the carbonated monolithically-cast beams equalled that of the cold joint beams under the isolated chloride exposure, of 20 µA /cm^2. The extent of cracking in these beam sets was thus lower than the carbonated beams with a cold joint after the exposure. The monolithically-cast beam set under the isolated chloride exposure had negligible to no cracking as the corrosion rate remained below 10 µA /cm^2. The maximum corrosion rate was 347 % and 54 % larger due to the carbonation in the monolithically-cast and cold joint beams respectively. The carbonation depth of 10.9 mm thus caused a larger increase in corrosion rate in both beam types compared to the ordinary concrete at a cover depth of 10 mm.

The corrosion rate behaviour at the mid-span of the 20 mm cover metakaolin concrete (denoted MK) beams is plotted in µA/cm^2 units in **Figure 4.30**. The corrosion rate is plotted over the full exposure duration of 294 days with the same nomenclatures of the reinforced beams. The gap in the plot towards the latter of the exposure period is the same as in the potential plots of the previous section. The corrosion rates of the monolithically-cast beams averaged less than 1 µA/cm^2 beyond 28 days until the completion of exposure, after 294 days. The baseline values of these beam sets were the highest of the concretes which is an anomaly in the results, although not significant. This anomaly of the baseline corrosion rates in the metakaolin concrete beams was the only instance throughout the study.

The corrosion rate of the beams with a cold joint increased from that of the monolithically-cast beams from 56 days of exposure, as shown at point A. The potential of these beam sets decreased close to the range of active corrosion in ASTM C 876 after 112 days, as shown in the previous section. The increase in corrosion rate in the cold joint beams under both exposure regimes after 112 days could thus be regarded to be within the range of active corrosion. The corrosion rate of the cold joint beams increased after 140 days and then reached a maximum value of 4.2 µA /cm^2, as shown at B. The corrosion rate was on average 19 % and 10 % larger due to carbonation in the monolithically-cast and cold joint beams

respectively. The carbonation depth of 13.2 mm also caused a larger increase in the corrosion rate compared to the ordinary concrete at a cover depth of 20 mm.

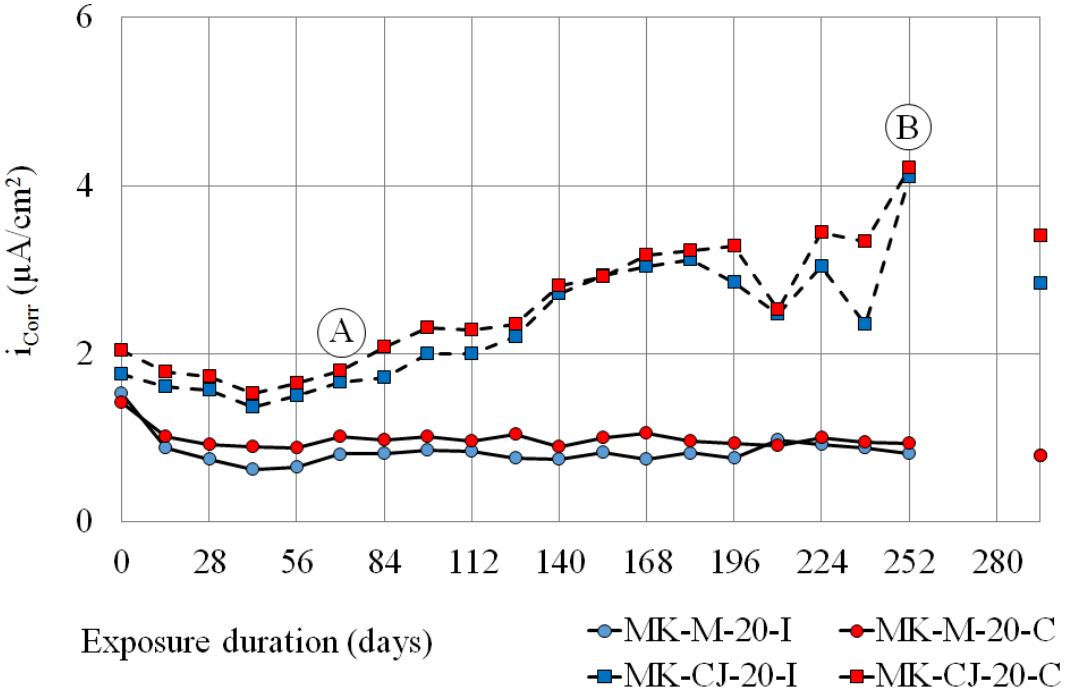

Figure 4.30: Corrosion rate in the metakaolin concrete 20 mm cover beams

The corrosion rate behaviour at the mid-span of the 10 mm cover metakaolin concrete (denoted MK) beams is plotted in µA/cm^2 units in **Figure 4.31**. The corrosion rate is plotted over the full exposure duration of 294 days with the same nomenclatures of the reinforced beams. The gap in the readings at the latter of the exposure period is the same as in the plot of the 20 mm cover beams (after 252 days). The entry to active corrosion was again not certain in the 10 mm cover beams as the corrosion rates generally increased in a rapid manner compared to the beams with a cover depth of 20 mm. The corrosion rate of the carbonated beams with a cold joint diverted from that of the remaining beam sets after 56 days, as shown at point A. The corrosion rate of this beam set increased to reach the highest value of these 10 mm cover beams, of 34.7 µA /cm^2, as shown at B.

The corrosion rates of the other beam sets were much lower than that of the carbonated beams with a cold joint, as with the other concretes. The corrosion rate of the carbonated monolithically-cast beams increased significantly at the latter of

the exposure, to reach a maximum value of 16.7 µA /cm^2. The corrosion rate of both types of beams under the isolated chloride exposure remained below 8 µA /cm^2 throughout the exposure. The corrosion rate was respectively 326 % and 141 % larger in the monolithically-cast and cold joint beams due to carbonation. The carbonation depth of 10.9 mm caused the largest increase in corrosion rate in both beam types at a cover depth of 10 mm. The extent of cracking in the metakaolin concrete was the lowest at this cover depth, as discussed in **Section 4.5.3.2**.

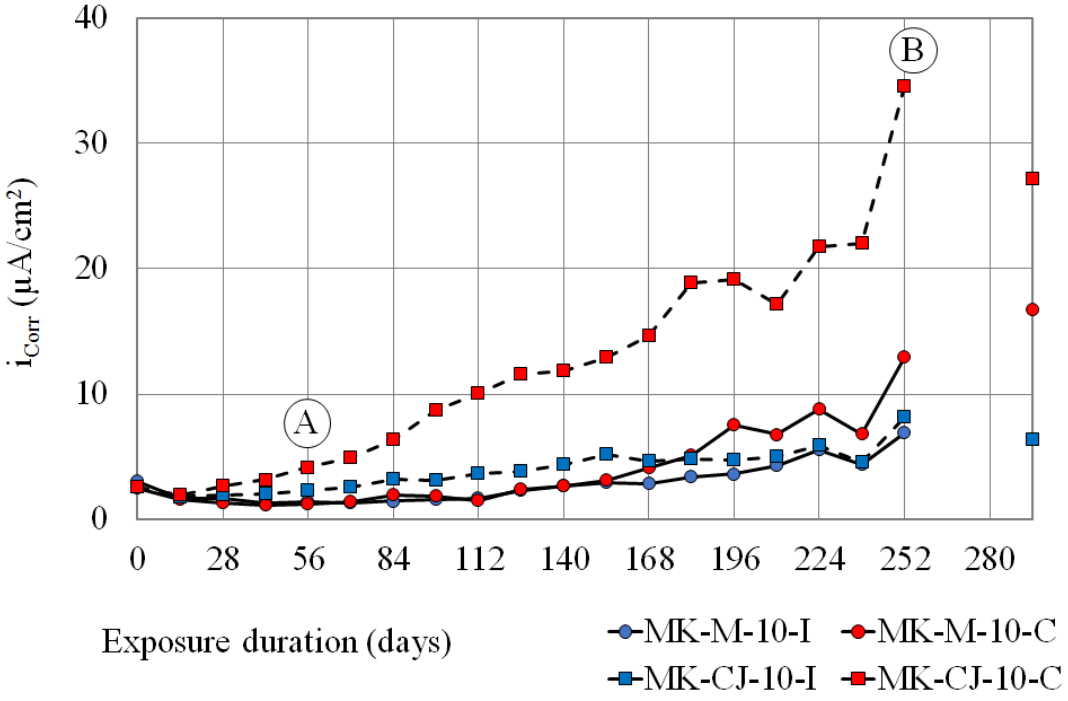

Figure 4.31: Corrosion rate in the metakaolin concrete 10 mm cover beams

4.5.4.4. Corrosion resistance

The concrete resistance of the concretes is more informed with the inclusion of the corrosion rate as there are limitations to the potential. The potential behaviour was such that were minor changes in the range of active corrosion whereas the corrosion rate continued to increase in some cases. The corrosion resistance of the beams is determined from the initiation time and maximum corrosion rate that was sustained within the timeframe of exposure. The duration (in exposure cycles) in the range of active and severe corrosion and maximum corrosion rate of all

beam sets are listed in **Table 4.5**. The copper-copper sulphate (Cu-$CuSO_4$) half-cell was preferable as the potential records spanned the entire exposure period.

Table 4.5: Corrosion resistance summary

Concrete type	20 mm cover beams				10 mm cover beams			
Ordinary concrete	M-20-I	M-20-C	CJ-20-I	CJ-20-C	M-10-I	M-10-C	CJ-10-I	CJ-10-C
Active corrosion	0	0	4	4	15	15	18	19
Severe corrosion	0	0	0	0	0	0	0	0
Max ($\mu A/cm^2$)	1.0	1.1	7.5	7.6	21.2	25.1	21.5	36.3
Fly ash concrete	M-20-I	M-20-C	CJ-20-I	CJ-20-C	M-10-I	M-10-C	CJ-10-I	CJ-10-C
Active corrosion	0	0	0	1	10	12	19	7
Severe corrosion	0	0	0	0	0	0	0	12
Max ($\mu A/cm^2$)	0.4	0.6	2.5	3.2	9.0	40.4	40.3	62.1
Metakaolin concrete	M-20-I	M-20-C	CJ-20-I	CJ-20-C	M-10-I	M-10-C	CJ-10-I	CJ-10-C
Active corrosion	0	0	0	0	6	9	9	18
Severe corrosion	0	0	0	0	0	0	0	5
Max ($\mu A/cm^2$)	1.5	1.4	4.1	4.2	6.9	16.7	8.1	34.6

The factors that were influential to the corrosion progress in chloride-laden concrete were the 1) cold joint, 2) cover depth, 3) carbonation and 4) cement replacement. These 4 factors are discussed sequentially in this section in terms of the magnitude of influence on the corrosion rate and potential throughout the exposure period. The cold joint was the main factor to the corrosion initiation time and maximum corrosion rate at both cover depths, of 20 mm and 10 mm. The corrosion rates of the cold joint beams with a cover depth of 20 mm were 2.7-7.5 times larger than the corresponding monolithically-cast beams. The potential dropped near to or within the range of active corrosion in these beams while the monolithically-cast beams remained within the range of passive corrosion.

The corrosion stages were based on the concrete quality and cracking of the concrete, which accelerates the corrosion rate. A reduction of the cover depth from 20 mm to 10 mm was a means to include the accelerated stage of corrosion, in addition to that influenced by the concrete quality only. The corrosion rates

were around 10 times larger in the 10 mm beams due to corrosion-induced cracks that formed at the latter of the exposure. Cracks that were formed before exposure have been found to increase the corrosion rate that was sustained at a given cover depth. An increase in the crack width resulted in an increase in the corrosion rate by up to 75 % over an exposure period of 90 weeks in Scott & Alexander (2007). An increase in the crack width and spacing of loading-induced cracks resulted in an increase in the corrosion rate in periods of up to 108 weeks in Paul (2015).

A cold joint that was formed before exposure has also been found to increase the corrosion rate that was sustained for a given cover depth. The corrosion rates of the specimens were several orders of magnitude larger at the cold joint than in the surrounding concrete in Miyazato & Otsuki (2010). Away from the joint the corrosion rates were much lower under all exposure regimes; constant wet or dry, and cyclic exposure. The corrosion rates herein were measured at the mid-span only, where a cold joint was formed to compare to that of separate monolithically-cast beams. This was also performed in the specimens in Roxas & Lejano (2018) to compare the corrosion resistance to under exposure to either fresh or sea water. The corrosion rates of the specimens with a cold joint were higher after 2 weeks out of an 8-week period which is similar to that of the cold joint specimens herein.

The influence of carbonation was based on the corrosion rate that was reached at the latter of the exposure at both cover depths, 10 mm and 20 mm. The corrosion rate of the carbonated beams was up to 29 % larger than that of the corresponding beam sets under the isolated chloride exposure at a cover depth of 20 mm. There were no significant changes in the corrosion rate of the monolithically-cast beams due to carbonation as the potential remained within the range of passive corrosion. The carbonation depth in the 20 mm cover beams had not reached the steel thus there was an un-carbonated portion of concrete to resist the chloride penetration. There was little to no un-carbonated concrete in the 10 mm cover beams hence the increased influence of the carbonation depth on the corrosion. The corrosion rate of the carbonated beams with a cover depth of 10 mm was up to 3.47 times larger than that of the corresponding beam sets under the isolated chloride exposure.

The synergy of chloride built-up at defects and carbonation resulted in a significant increase in the chloride penetration and corrosion rate. The chloride content at the steel was up to 7.3 times larger in the carbonated beams with a cold joint compared to the monolithically-beams under the isolated chloride exposure. The corrosion rate of the carbonated beams with a cold joint was up to 7.2 times larger than the monolithcally-cast beam sets under the isolated chloride exposure. This increase in the corrosion rate was the main part of the hypothesis of this study and was consistent with the finding of an increase in the chloride content beyond the carbonation depth. The potential alone would not have identified the corrosion risk of chloride at a cold joint thus not support the study hypothesis.

An increase in the corrosion rate due to carbonation in concrete with chloride is similar to a number of studies in a laboratory setting. The carbonation progress in concrete with chloride was determined more clearly by the corrosion rate instead of the corrosion potential alone. The corrosion rates were higher in the carbonated concretes with admixed chloride compared to that exposed to carbon dixoide only in Moreno & Sagues (1998). The potential was decreased in the concretes with chloride which indicated that the corrosion severity was higher under combined exposure. The corrosion rates were higher in the concretes with slag compared to the ordinary concrete under the exposure to carbonation and chloride solution in Chaparro et al., (2010). The potential found that the corrosion initiation time was decreased in the slag concretes which was due to their larger carbonation depths.

The benefit of the fly ash and metakaolin was limited to a cover depth of 20 mm where the corrosion rate was lower than the ordinary concrete. The maximum corrosion rate of the fly ash and metakaolin concrete beams with a cold joint was respectfully 2.4 and 1.8 times lower than the ordinary concrete. These beams also had higher potentials throughout the exposure period which indicates a lower corrosion activity. A decrease in the corrosion rate in the fly ash and metakaolin concretes may be attributed to the concrete resistivity and oxygen permeability. The oxygen permeability indices (or OPI) were lower than the ordinary concrete (in **Section 4.5.2.2**) which is the main factor of corrosion in partially-saturated

concrete. The concrete resistivity was higher than the ordinary concrete, in that there was a lower conductivity for corrosion current, as shown in **Section 4.5.4.6**.

4.5.4.5. Corrosion rate-potential relationship

The potential measurement was a means of determining the corrosion initiation time however it is influenced by various factors, i.e. oxygen availability, etc. The influence of a cold joint, cover reduction, carbonation and cement replacement were better represented using the corrosion rate. There is no general correlation between the potential and corrosion rate as the parameters respond differently to the same factors (RILEM, 2004).The corrosion rate was the main parameter of the corrosion state thus aided the assessment of the potential and concrete resistivity. The potentials in the range of active corrosion were within a relatively constant range whereas the corrosion rate continued to increase, as discussed in **Section 4.5.4.3**. The other discrepancy was that some of the carbonated beams had higher potentials, or a lower corrosion activity, while the corrosion rate was higher.

The readings of the beams at all testing ages are used to assess the relationship between the potential and corrosion rate. This relationship is presented from the potentials of the silver-silver chloride (or Ag-AgCl) half-cell for the ordinary concrete (CEM) beams in a scatter plot in **Figure 4.32**. The Ag-AgCl half-cell potentials of the Coulostat unit were used as these were measured using the same apparatus and at the same time. The readings at the mid-span are in the negative direction on the potential (or horizontal) axis with a randomised legend for the beam sets. The corrosion rates remained below 5 μA /cm^2 in a potential range of up to -300 mV and then increased rapidly within the range of active corrosion.

The entry to the range of active corrosion in the plot below is at a potential of approximately -300 mV, as shown at point A. The corrosion rates are much higher thereafter, until the maximum values at B, as these beams had been within the range active corrosion for a longer duration. The relationship between the copper-copper sulphate (Cu-$CuSO_4$) half-cell potential and corrosion rate are omitted for

the sake of brevity. The entry of the Cu-$CuSO_4$ half-cell to the range of active corrosion was evident within a similar potential range of -300 mV to -350 mV. The active corrosion was better-represented by the corrosion rate, particularly when there were cracks in the concrete. The corrosion rate of both half-cell types fell within a range of up to 5 µA /cm^2 during the initiation stage of corrosion.

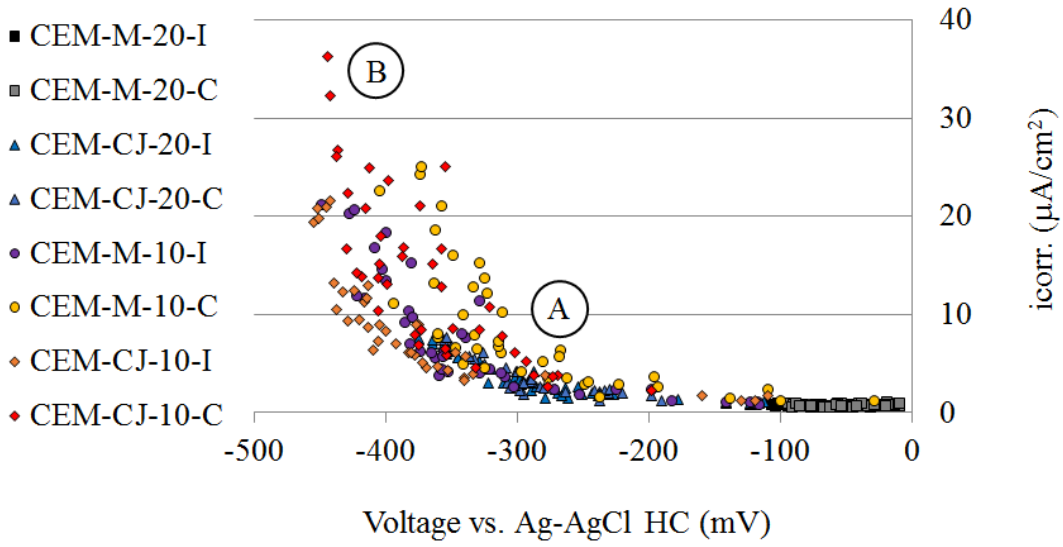

Figure 4.32: Potential-corrosion rate relationship

The relationship between the potential and corrosion rate for the fly ash and metakaolin concretes is omitted for the sake of brevity. This found the same trend of the corrosion rates remaining below around 5 µA /cm^2 in the initiation period and then increasing rapidly in the propagation phase. This maximum corrosion rate between the concretes in the initiation period thus provides more certainty to the potential bound to the range of active corrosion. The potential of the ordinary concrete beams indicated that there was a decrease in the corrosion activity due to carbonation. The potential in the fly ash and metakaolin concrete beams mostly indicated that there was an increase in the corrosion activity due to carbonation. The corrosion rate was invariably higher in the carbonated beams thus related better to the potential when it indicated that there was a higher corrosion severity.

The trend of a decrease in the potential (or higher corrosion activity) due to carbonation has been found in a number of studies such as Pakawat & Uomoto

(2005) and Moreno & Sagues (1998). The carbonation depth was greater in the concretes with the cement extenders which resulted in a decrease in potential after some time of exposure. The influence of carbonation on the potential and concrete resistivity herein was determined in the trial period of 4 cycles of exposure. The plots of the behaviours are not included for the sake of brevity as the changes due to the carbonation were minimal. The potentials were increased in the carbonated beams from the end of the 1st cycle, which reflects a lower corrosion activity. The resistivity was increased in the carbonated beams, which indicates that there was a lower concrete conductivity. The corrosion rate was thus considered to be used to aid the potential and clearly represent the carbonation progress in the concretes.

4.5.4.6. Concrete resistivity

The concrete resistivity behaviour at the mid-span of the 20 mm cover ordinary concrete (denoted CEM) beams is plotted in kΩ·cm units in **Figure 4.33**. The resistivity was monitored for 294 days using the Resipod apparatus according to that discussed in **Section 3.9.3.4** of the experimental programme. The Resipod is based on the Wenner 4-probe array which is most common for structures and laboratories. The nomenclatures include the monolithically-cast (M) beams and the beams with a cold joint (CJ) under the regimes of isolated (I) and combined (C) exposure. The plot points for each beam type, exposure regime and cover depth are the average of 2 readings per exposure cycle in sets of 3 beams.

The resistivity of the 20 mm cover beams fell within the range of a high corrosion risk in RILEM TC-154 EMC (RILEM, 2004), of under 10 kΩ·cm, until 168 days, as shown at point A. The resistivity of these beams then increased to within the range of a moderate corrosion risk, of over 10 kΩ·cm, and reached a maximum value of around 15 kΩ·cm, at point B. The trend of an increase in the resistivity was due to the decrease of the pore sizes of paste with continued hydration (Hope et al., 1985). The cold joint resulted in an average decrease in the resistivity of 20 % and 15 % under the isolated chloride and combined exposure respectively. The corrosion rate was up to 7.5 times larger than that of the monolithically-cast

beams at a cover depth of 20 mm. The resistivity was thus not suitable in the cold joint beams to determine the corrosion risk compared to the monolithic concrete.

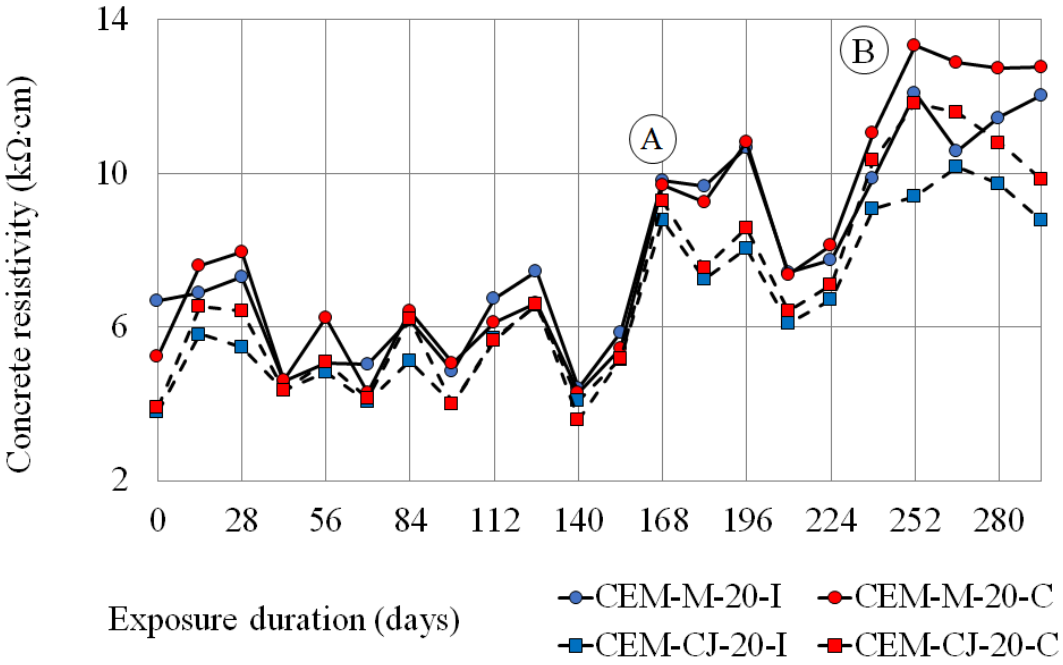

Figure 4.33: Concrete resistivity in the ordinary concrete 20 mm cover beams

The carbonation resulted in an average change in resistivity by 8 % and 3 % in the monolithically-cast and cold joint beams respectively. The corrosion rate of the carbonated beams was up to 29 % larger than that of the beams under the isolated chloride exposure at a cover depth of 20 mm. Carbonation increases the contact resistance between the base of measurement probes and concrete surface however only when it has reached a depth that is similar to the probe spacing (Kevern et al., 2015). The carbonation depth in the plain cubes under combined exposure was within a quarter of the probe spacing of the Resipod and Coulostat probe arrays, of 50 mm. The chloride exposure over the monitoring period may have improved the electrical contact between the bases of these probes and concrete surface.

The concrete resistivity behaviour of the 10 mm cover beams is omitted for the sake of brevity as it is identical to that of the 20 mm cover beams. The resistivity readings fell within smaller ranges, on average 18-44 % lower than that of the 20 mm beams. This lower resistivity was due to a closer proximity of the steel bar,

which is more conductive than concrete, thus causes a disturbance of the current in the measurement. Similar cover depths of 20 mm, 10 mm and 1 mm in Weydert & Gehlen (1999) caused the resistivity to reduce to complete disturbance (or no resistivity) at a cover depth of 1 mm. The cracking herein could have decreased the resistivity due to the increased moisture and chloride contents in the vicinity of the steel. The cracks were however formed at the latter of the exposure and the resistivity was decreased by a constant magnitude throughout the exposure period.

The concrete resistivity behaviour at the mid-span of the 20 mm cover fly ash concrete (denoted FA) beams is plotted in kΩ·cm units in **Figure 4.34**. The resistivity is plotted over the full exposure duration of 294 days with the same nomenclatures of the reinforced beams. The resistivity of the 20 mm cover beams fell within the range of a high corrosion risk in RILEM TC-154 EMC (RILEM, 2004), of less than 10 kΩ·cm, until 28 days, as shown at point A. The resistivity of these beams then increased to within the range of a moderate corrosion risk, of over 10 kΩ·cm, and reached a maximum value of around 19 kΩ·cm, at point B. The influence of a cold joint and carbonation on the resistivity was minimal, as the differences between the beam sets were up to 22 % and 3 % respectively.

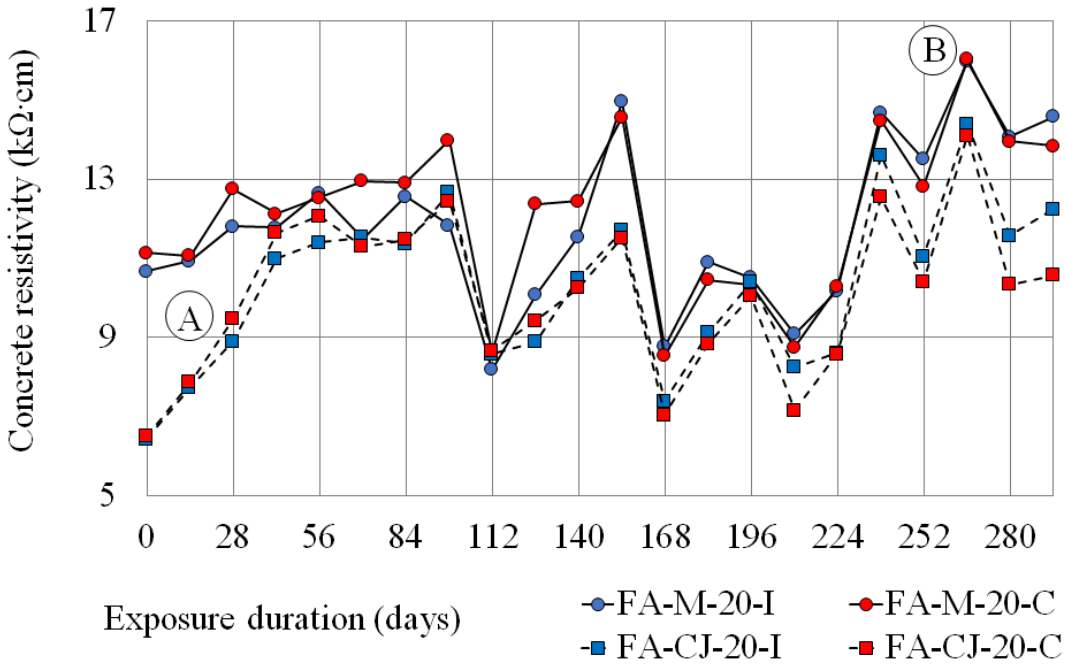

Figure 4.34: Concrete resistivity in the fly ash concrete 20 mm cover beams

The resistivity behaviour at the mid-span of the 20 mm cover metakaolin concrete (denoted MK) beams is plotted in kΩ·cm units in **Figure 4.35**. The resistivity is plotted over the full exposure duration of 294 days with the same nomenclatures of the reinforced beams. The resistivity was the highest of the concretes as only the baseline readings (before exposure) fell within the range of high corrosion risk in RILEM TC-154 EMC, of below 10 kΩ·cm, as shown at point A. The resistivity of all the beams then increased to within the range of moderate corrosion risk, of 10-50 kΩ·cm, and reached a maximum value of around 45 kΩ·cm, at point B. The influence of a cold joint and carbonation on the resistivity was thus negligible, as the differences between the beam sets were up to 1 % throughout the exposure.

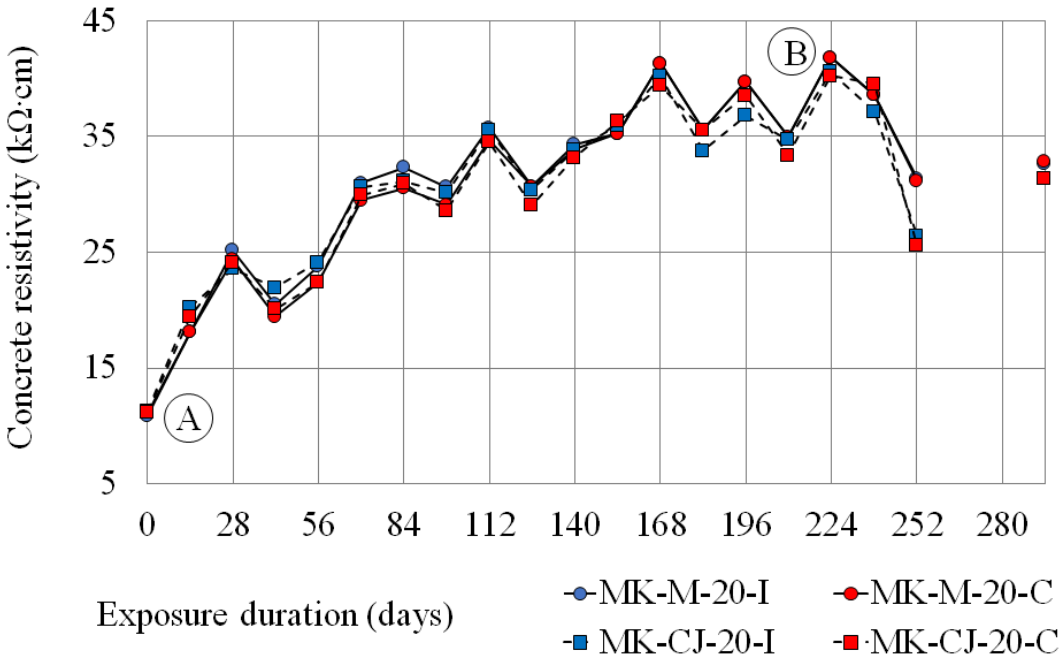

Figure 4.35: Concrete resistivity in the metakaolin concrete 20 mm cover beams

The high resistivity of the metakaolin concrete relates strongly to the chloride conductivity indices (CCI) over the 90-day curing period. The CCI values were in a range of 38-56 % lower than the other concretes thus suitable to represent the control of corrosion due to resistivity. The fly ash may be considered to be based more on cathodic control as the resistivity ranges were half that of the metkaolin concrete. This may be yielded by decreasing the oxygen paths in concrete by superimposing the paste pores with cementing materials that have smaller particle

sizes. The fly ash had the smallest particle sizes of the binders thus could decrease the connectivity of the transport paths after an adequate curing age. The maximum corrosion rate was decreased by a larger magnitude in the fly ash concrete at a cover depth of 20 mm thus placing an importance of the oxygen permeability.

The concrete resistivity could be regarded to determine the corrosion risk of the concretes instead of the chloride conductivity index. The large increase in the resistivity of the metakaolin concrete could replace the lowest of CCI values after 28 days of curing. Though the CCI of the fly ash concrete did not decrease to below that of the ordinary concrete after 90 days it may have done so with further curing. This would have related better to the increase in resistivity of the fly ash concrete beams into the moderate range of corrosion risk sooner than the ordinary concrete. There was a strong relationship between the resistivity and chloride diffusion coefficient in Kevern et al., (2015) with the same type of Wenner probe (Resipod). This relationship was also found in Safehiana & Ramezanianpour (2015) from the cores that were extracted from a concrete jetty in a marine zone.

The increase in resistivity due to cement extenders has been found in a number of studies due to their smaller particle sizes and composition. The fly ash, slag and silica fume in Scott & Alexander (2007) yielded an increase in the resistivity compared to the ordinary concrete over 90 weeks of exposure. This increase in the resistivity was a factor that decreased the corrosion rate at cover depths of up to 40 mm. The fly ash and metakaolin herein increase in the resistivity at cover depths of 10 mm and 20 mm regardless of the chloride penetration or carbonation depth. Metakaolin has also been found to increase the concrete resistivity due to the reactivity to decrease the pore sizes of the paste and the alumina content. The resistivity of concretes with binary and ternary blends of metakaolin in Ferreira et al., (2015) was up to 69 % larger compared to ordinary concrete over 180 days.

The resistivity behaviour at the mid-span of the 20 mm cover reinforced beams from the Coulostat is plotted in kΩ·cm units in **Figures E.7** to **E.9** (in Appendix **E**). The Coulostat is based on the Coulostatic method of polarisation and was used

to compare to the resistivity behaviour of the Wenner probe array. The resistivity behaviour in kΩ·cm units in the 20 mm cover ordinary concrete beams is plotted in **Figure E.7** in a period from 18 days until 294 days. The resistivity behaviour in kΩ·cm units in the fly ash concrete beams is then plotted in **Figure E.8** in a period from 88 days until 294 days. The resistivity behaviour in kΩ·cm units of the metakaolin concrete beams is plotted in **Figure E.9** over the full exposure period, of 294 days. The gaps in the resistivity behaviour are the same as in the potential and corrosion rate behaviours, as the Coulostat was used later into the exposure.

The resistivity behaviour of the 10 mm cover beams are omitted in **Appendix E** for the sake of brevity as the behaviours were the same as the 20 mm beams. The resistivity behaviours were identical to that of the Wenner probe with a difference of up to 5 % in the magnitude between the apparatus. The Wenner probe was more susceptible to electrical contact issues when it was placed on the concrete as the Coulostat bases were flattened. The Coulostat readings were mostly less than that of the Wenner probe which indicated that the corrosion risk had increased. The Coulostat readings were however taken last, after the exposed surface of the beams was saturated for the longest time which increases the electrical contact.

4.5.4.7. Temperature, relative humidity and cover depth

The relationship between the corrosion rate and temperature for the ordinary concrete beams is presented in a scatter plot in **Figure 4.36**. The temperature plot points in º C are the averages of the 2-hour monitoring intervals on days that the corrosion readings were obtained. This was done instead of averaging the readings in each of the exposure periods, i.e. the previous 3 days of ponding or 9 days of carbonation. The representative values take into account the local maximums in temperature which lasted for several days and could influence the corrosion. The corrosion rates under the isolated chloride (in blue) and combined (red) exposure fell within a temperature range of 16-29 °C throughout the exposure period of 294 days. The data points are clustered within this temperature range however the main aspect was a minor increase in temperature in the carbonation chamber.

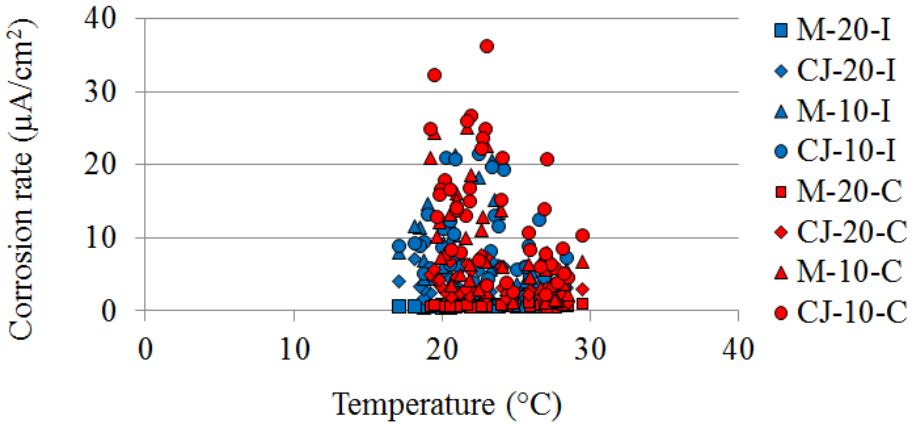

Figure 4.36: Corrosion rate-temperature relationship

The temperature of the carbonation chamber (red) was higher than that in the laboratory (blue) throughout the exposure period. The differences in temperature between the exposure regimes were minor compared to the differences in the corrosion rate. There is a horizontal shift right of the temperature readings under the combined exposure (red), within a small temperature range of 2-4 °C. The corrosion rates in the vertical axis of the beams with a cover depth of 10 mm were much larger than that under the isolated chloride exposure. The temperature was not too influential to the corrosion rate in comparison to the chloride penetration and carbonation at the steel. The temperature-corrosion rate relationship of the other concretes is omitted for the sake of brevity as there was a similar trend.

The relationship between the corrosion rate and relative humidity for the ordinary concrete beams is presented in a scatter plot in **Figure 4.37**. The relative humidity plot points in % are the averages of the 2-hour monitoring intervals on days that the corrosion readings were obtained. The relative humidity of the carbonation chamber was much higher throughout the exposure as shown by a horizontal shift of the readings by 19-26 %. The relative humidity may be regarded as a larger factor to the increase in corrosion rate in the carbonated beams however the main contribution to the moisture was due to the ponding. The presence of carbonation at the steel thus was the main factor to the increase in corrosion rate, as shown in the **Section 4.5.4.3**. The relative humidity-corrosion rate relationship of the other concretes was had similar differences thus were omitted for the sake of brevity.

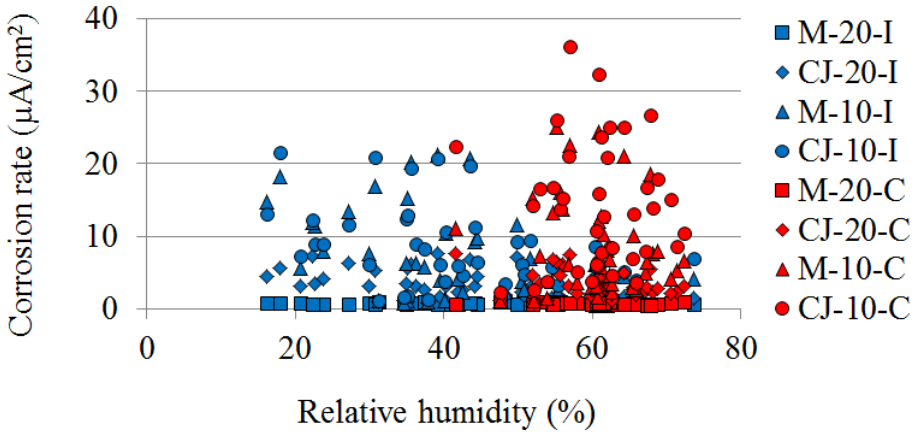

Figure 4.37: Corrosion rate-relative humidity relationship

The average of the measured (or actual) cover depths in the 20 mm cover beam sets is presented in a scatter plot in **Figure 4.38**. The ID codes of the beams are on the horizontal axis which is sub-divided as the ordinary concrete (denoted CEM), fly ash concrete (FA) and metakaolin concrete (MK). The beam nomenclatures include the monolithically-cast (M) beams and the beams with a cold joint (CJ) under the regimes of isolated (I) and combined (C) exposure. The cover depths of the 10 mm cover beams were not measured with the Elcometer apparatus as the search field was interfered due to the closer proximity of the steel, thus out of the measurement range. The cover depths of the 20 mm cover beams at the mid-span of the beams and at either end of the exposed surface are listed in **Appendix A**.

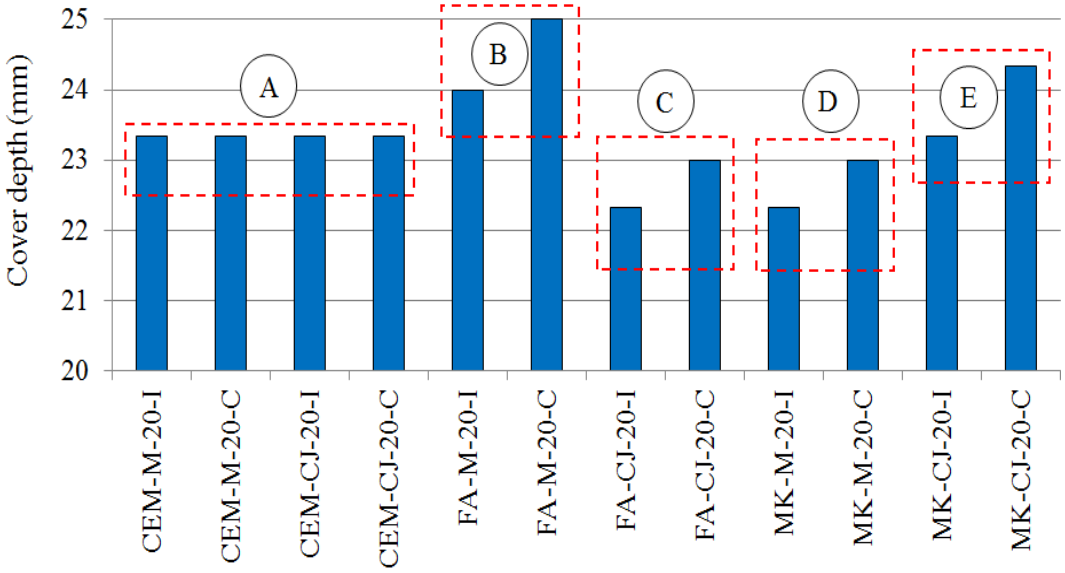

Figure 4.38: Measured cover depths

The cover depths at the mid-span of the 20 mm beams were within a range of 22.4-25 mm thus differed from the planned cover depth of 20 mm. At the ends of the Perspex pond, the cover depths differed by a maximum of only 1 mm from that measured at the mid-span location. The cover depths at the ends of the pond are not presented here for the sake of brevity although could have been used in the comparisons. The cover depths in the ordinary concrete monolithically-cast and cold joint beams under both exposure regimes averaged at 23.3 mm, as shown in section A. The average of the cover depths in the fly ash (B) and metakaolin concrete (C) beams differed by up to 2 mm from that of the ordinary concrete.

The actual cover depth in the fly ash and metakaolin concrete beams varied by up to 8.5 % from that in the ordinary concrete beams. This variation of the cover depth could influence the corrosion rate as the planned cover depths of 20 mm and 10 mm were low given the exposure conditions. There was however no trend indicating that this variation of the cover depth in both cement extender concretes directly influenced the corrosion rate. The corrosion rate in the fly ash concrete beams with a cold joint was the lowest between the concretes even through the cover depth was decreased by up to 1 mm. The metakaolin concrete beams with a cold joint had a lower corrosion rate than that of the ordinary concrete with an increase in cover depth by up to 1 mm. The corrosion rates of the monolithically-cast beams were minor although followed the same trend between the concretes.

4.5.4.8. Beam end readings

The potential and concrete resistivity was also measured at either end of the Perspex pond to assess the changes in these parameters away from the cold joint. These changes could be compared to that in the monolithically-cast beams, using the same spacing of apparatus probes within the confines of the pond. The spacing of the test locations was dependent on the geometry of the copper-copper sulphate ($Cu\text{-}CuSO_4$) half-cell Wenner probe array, as discussed in **Section 3.9.4.4** of the experimental programme. A larger spacing would have been available in full-scale specimens, to assess the corrosion activity with a larger spacing away from the

cold joint. The main testing location however was at the mid-span as the cold joint was placed in separate specimens, rather than using larger beam dimensions.

The behaviours of the potential and resistivity at the bar ends are omitted for the sake of brevity as these were the same as that at the mid-span. The spacing of the copper-copper sulphate half-cell test location between the mid-span and beam ends, of 200 mm, resulted in a potential difference of up to 20 %. The differences in the potential were larger in the 10 mm cover beams, i.e. end readings were up to 50 mV larger than a mid-span reading, of -400 mV. The spacing between the test locations of the Wenner probe was negligible and resulted in differences in the resistivity of up to 30 %. The prevailing trends of the potential and resistivity between the mid-span and bar ends throughout the exposure period are as follows:

- The electrical potential was lower at the cold joint to reflect a higher corrosion activity, already from the start of exposure.
- The concrete resistivity was lower at the cold joint from the start of exposure as there was more chlorides and moisture present.
- After the wetting periods the differences of both the parameters was decreased as there was more moisture and chlorides away from the joint.
- The readings in the monolithically-cast beams were in a random arrangement of the order of magnitude over the bar length, i.e. not highest at the mid-span.
- There were smaller differences in the potential over the bar length of the actively corroding beams, as there was more corrosion away from the joint.

Potential mapping is used to identify where the corrosion rate is highest, to lower the amount of corrosion rate readings that are required. This approach has been used in a number of studies to determine the location of corrosion that has been induced by defects such as cracks and cold joint. The potentials were significantly lower at the cracks that were formed in the casting in Paul (2015) with a spacing of 50 mm between the test locations. The reduction of the potential was constant over an exposure period of 25 weeks which is similar to that induced by the cold joint herein. The corrosion rate in Miyazato & Otsuki (2010) was decreased to

approximately nothing away from a cold joint using a spacing of 20 mm in a grid-like manner. The spacing of the test locations herein may be regarded as sufficient to identify the influence of a cold joint on the corrosion and concrete resistivity.

4.5.5. Corrosion damages

4.5.5.1. Overview

The results of the corrosion damages which had accumulated in the propagation stage are presented and discussed in this section. The damages to the embedded steel bars in terms of the distribution of uniform and pitting corrosion forms are presented in **Section 4.5.4.2**.The extent of cracking in the cover concrete after the exposure, in terms of the coverage and crack width, is presented in **Section 4.5.4.3**. The methods of establishing the maps of the cover concrete cracking and steel corrosion are discussed in **Section 3.9.5** of the experimental programme. Parameters such as the steel mass loss were not tested as the focus herein was on the locality of corrosion damage, instead of a relationship with the corrosion rate.

4.5.5.2. Corrosion formations

The averages of the corroded lengths in the ordinary concrete monolithically-cast beam sets with a cover depth of 20 mm are listed in **Table 4.6**. There was no corrosion on the steel in this beam type in the cement extender concretes thus the values are all 0 mm. The corroded lengths that are discussed throughout this section are from the individual steel bars in each set unless otherwise mentioned. The steel bars in the ordinary concrete had uniform corrosion in the direction of exposure as this was the smallest depth to the steel. The corrosion differences between the concretes in the 20 mm cover monolithically-cast beams are shown in the photographs in **Figure 4.39**. There was 110 mm of uniform corrosion in the of exposure direction the ordinary concrete beam with the ID of CEM-M-20-I-1, as shown at A. The fly ash concrete beam with the ID of FA-M-20-I-1 had no damage as the corrosion rate was passive throughout the exposure, as shown at B.

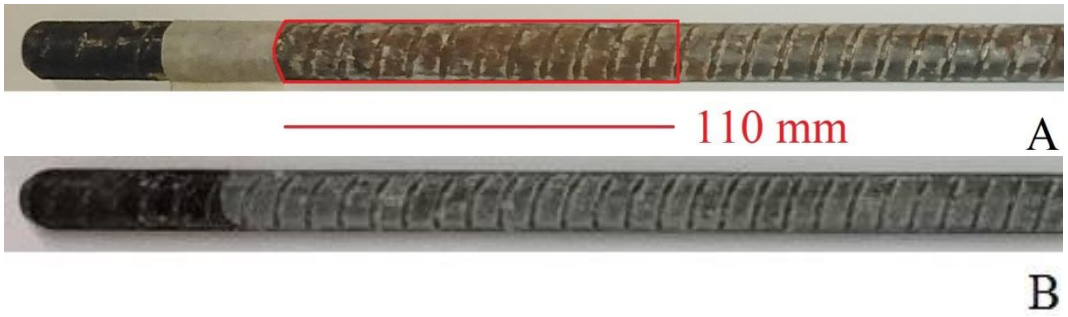

Figure 4.39: Corrosion in the 20 mm cover monolithic beams

The corrosion on the steel bars in the ordinary concrete monolithically-cast beams reflects the dependence on the oxygen availability (or cover depth). The cement extender concretes yielded a higher resistivity and lower oxygen permeability (as the OPI) thus resisted the corrosion at this cover depth. The decrease in potential in the ordinary concrete beams at the latter of the exposure thus was due to the corrosion, as discussed in **Section 4.5.4.4**. The corroded length in the ordinary concrete was an average of 27 % larger in the set of 3 carbonated beams, from the values in Table 4.5. This minor increase in the corrosion length in these beams was not discerning of the corrosion risk however the differences would have been larger with further exposure. There were no damages to the epoxy coating in any of the beams and the visible scratches occurred when removing the steel bars.

Table 4.6: Corroded lengths in the 20 mm cover monolithic beams

Reinforced beam	Uniform (mm)		Pitting (mm)	
	Exposed	Opposite	Exposed	Opposite
CEM-M-20-I	157	62	0	0
CEM-M-20-C	192	82	0	0
FA-M-20-I	0	0	0	0
FA-M-20-C	0	0	0	0
MK-M-20-I	0	0	0	0
MK-M-20-C	0	0	0	0

1. Exposed: Surface of steel facing the concrete surface.
2. Opposite: Opposite surface of steel to the concrete surface.

The averages of the corroded lengths in the cold joint beam sets with a cover depth of 20 mm are listed in mm units for all the concretes in **Table 4.7**. The cold

joint induced the corrosion in all beams at this cover depth on both sides of the steel, i.e. not only at the surface. The corrosion differences between the concretes in the 20 mm cover cold joint beams are shown in the photographs in **Figure 4.40**. There was 230 mm of uniform corrosion on the steel bar of the ordinary concrete beam with the ID of CEM-CJ-20-I-1, as shown at A. The corroded lengths in both the cement extender concretes were less than that of the ordinary concrete and in a closer proximity to the cold joint. The fly ash concrete beam with the ID of FA-CJ-20-I-1 had a smaller corroded length of 65 mm at the cold joint, as shown at B.

Table 4.7: Corroded lengths in the 20 mm cover cold joint beams

Reinforced beam	Uniform (mm)		Pitting (mm)	
	Exposed	Opposite	Exposed	Opposite
CEM-CJ-20-I-1	210	72	0	0
CEM-CJ-20-C-1	220	77	0	0
FA-CJ-20-I-1	50	25	0	0
FA-CJ-20-C-1	62	33	0	0
MK-CJ-20-I-1	62	40	0	0
MK-CJ-20-C-1	73	42	0	0



Figure 4.40: Corrosion in the 20 mm cover cold joint beams

The corroded lengths of the ordinary concrete cold joint beams fell within a range of 60-270 mm under both the exposure regimes. These measured lengths were within respective ranges of 25-215 mm and 10-190 mm larger than that in the fly

ash and metakaolin concrete beams. The corroded length in the ordinary concrete was on average 7 % larger in the set of carbonated beams on both sides of the steel bars. The influence of the carbonation on the corroded length of the steel was on average larger in the beams that were made of the cement extender concretes. The corroded length in the fly ash and metakaolin concretes was 33 % and 19 % larger in the set of carbonated beams on both sides of the steel bars respectively.

The potential readings at the bar ends in **Section 4.5.4.8** were thus influenced by the corrosion reactions on other areas of the steel, i.e. at the mid-span. Where the corrosion cells had formed in a close proximity to the cold joint the potential at the bar ends was based on that at the mid-span location. This disturbance of the potential was more prominent in the cement extender concretes as the corroded lengths were lower and in a closer to the cold joint. There would have been larger differences in the potential between the mid-span and beam ends if specimens with larger dimensions were used. The spacing of the test locations was however not important as the cold joint was fabricated in separate beams for comparison.

The averages of the corroded lengths in the monolithically-cast beam sets with a cover depth of 10 mm are listed for all concretes in **Table 4.8**. The decrease in cover depth resulted in significantly larger coverage of corrosion on both sides of the steel surface, with pitting corrosion. Photographs of the monolithically-cast beams are not shown as these corrosion damages may be seen in the 10 mm cover cold joint beams in **Figure 4.41**. The corroded lengths of uniform corrosion in all of the monolithically-cast beams were up to 400 mm, which was un-coated length between the steel bar ends. The pitting corrosion was formed on the uniformly-corroded areas of the steel and covered a length of up to 150 mm in all the beams.

The influence of carbonation on the corroded lengths in the cement extender concretes was larger than that in the ordinary concrete. The uniform and pitting corroded lengths in the ordinary concrete were on average 27 % larger in the carbonated beams on both sides of the steel bars. In the fly ash and metakaolin concretes the corroded lengths were respectively up to 12 and 20 times larger due

to carbonation on both sides of the steel. The pitting length in these concretes was up to 60 mm under the isolated chloride exposure whereas that in the carbonated beams was up to 150 mm. The carbonation depth was close to the steel in the ordinary concrete and beyond the steel surface in both cement extender concretes.

Table 4.8: Corroded lengths in the 10 mm cover monolithic beams

Reinforced beam	Uniform (mm)		Pitting (mm)	
	Exposed	Opposite	Exposed	Opposite
CEM-M-10-I-1	320	49	62	23
CEM-M-10-C-1	360	62	65	27
FA-M-10-I-1	205	27	35	3
FA-M-10-C-1	373	47	122	40
MK-M-10-I-1	52	25	5	0
MK-M-10-C-1	245	50	98	8

The averages of the corroded lengths in the cold joint beam sets with a cover depth of 10 mm are listed for all concretes in **Table 4.9**. The cold joint resulted in the most severe corrosion at the cover depth of 10 mm in terms of the coverage of pitting over the length of the steel bars. The corrosion damage that was typically found in the 10 mm cover beams with a cold joint is shown in the photograph in **Figure 4.41**. There was 305 mm of uniform corrosion on the steel of the ordinary concrete beam with the ID of CEM-CJ-10-I-1 with 130 mm of small pits closer to the mid-span. The pitting corrosion is difficult to view with an overlay of the rust products although the affected bar length was determined after wire-brushing away the corrosion. The pits were not continuous in the affected area of the steel however the pitting length was simplified as the locality was more important.



Figure 4.41: Corrosion in the 10 mm cover cold joint beams

The corroded lengths of the uniform and pitting corrosion in the cold joint beams were up to 400 mm and 195 mm respectively. The influence of the carbonation on the uniform and pitting corrosion lengths was again the largest in the fly ash and metakaolin concretes. The uniform and pitting corroded length in the ordinary concrete was on average 57 % larger in the carbonated beams on both sides of the steel bars. In the fly ash and metakaolin concretes the uniform and pitting lengths were respectively up to 1.5 and 8.8 times larger as the carbonation depth had reached the steel. The differences in corrosion length in the cold joint beams that were made of the cement extender concretes were however lower than that in the monolithically-cast beams. This may be attributed to the significant increase in the corrosion rate due to the joint at this cover depth under both exposure regimes.

Table 4.9: Corroded lengths in the 10 mm cover cold joint beams

Reinforced beam	Uniform (mm)		Pitting (mm)	
	Exposed	Opposite	Exposed	Opposite
CEM-CJ-10-I-1	400	258	102	47
CEM-CJ-10-C-1	400	265	120	73
FA-CJ-10-I-1	333	28	103	28
FA-CJ-10-C-1	343	40	160	23
MK-CJ-10-I-1	63	25	15	3
MK-CJ-10-C-1	282	53	100	27

4.5.5.3. Crack formations

Corrosion-induced cracks were formed in the beams with a cover depth of 10 mm as the corrosion rate had accelerated during the propagation stage. A typical monolithically-cast beam with the ID of CEM-M-10-C-1 is shown in an Autocad drawing in **Figure 4.42**. The cracks were sub-divided into 10 mm segments over the exposed surface with the representative crack in each as the average of the minimums and maximum crack widths. The colour-schemed legend of the beam is related to the crack width, from black, in the un-cracked cover concrete, to red, the widest cracks. Where the steel had corroded more distinctly, i.e. pitting, the concrete had cracked due to the expansion pressures which originated at the steel

surface. The known characteristics of these cracks were their orientation, in line with the steel bar, width, and connectivity which was visible at the surface.

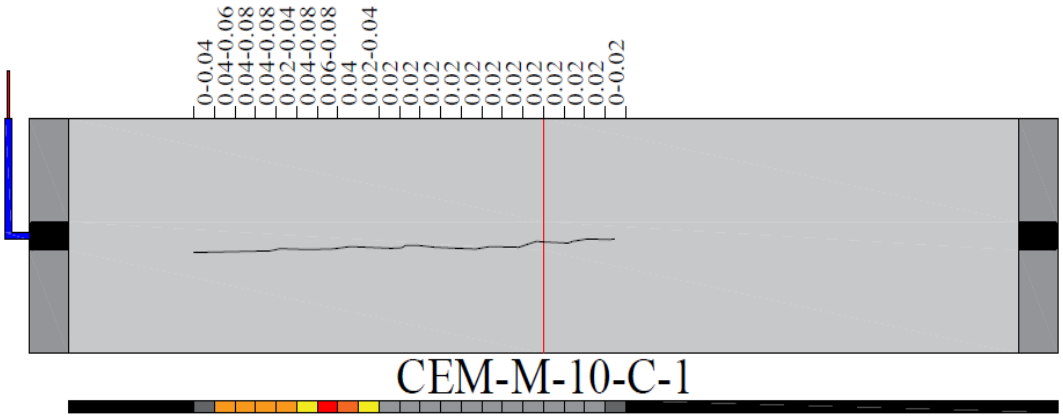

Figure 4.42: Cracking in the 10 mm cover monolithic beams

A typical cold joint beam with the ID of CEM-M-10-C-1 is presented in the same manner as the previous Autocad drawing in **Figure 4.43**. The extent of cracking in the cold joint beams was larger than in the monolithically-cast beams due to a reduction of the corrosion initiation time. The cracks were invariably widest in a closer proximity to the joint and decreased towards the beam ends, where there was no cracking. The cold joint created a definitive point for the corrosion to be established in a shorter time whereas the monolithically-cast beams cracked later at over any part of the bar. The corrosion products were also transported through the cold joint which was apparent when sampling at the mid-span for chloride.

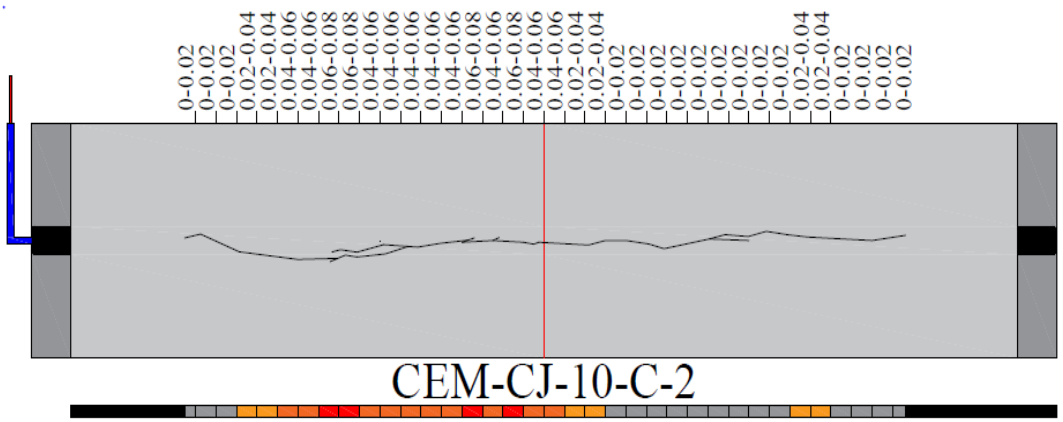

Figure 4.43: Cracking in the 10 mm cover cold joint beams

The maximum crack widths and average of the crack lengths in mm units in the monolithically-cast beams with a cover depth of 10 mm are listed in **Table 4.10**. The crack length (or extent of cracking) was more representative of the corrosion as the crack width was relatively constant between the beams. The crack length in the monolithically-cast beams was up to 244 mm over the un-coated length of the steel, of 400 mm. The crack length in the ordinary concrete beams was on average 54 % larger due to carbonation compared to that under the isolated chloride exposure. The crack length in the fly ash concrete beams was 3.5 times larger due to carbonation as 2 beams were un-cracked under the isolated chloride exposure. The metakaolin concrete beams under the isolated chloride exposure were all un-cracked whereas the carbonated beams had an average crack length of 55 mm.

Table 4.10: Crack formation in the 10 mm cover monolithic beams

Reinforced beam	Max crack width (mm)	Crack length (mm)
CEM-M-10-I	0.10	158
CEM-M-10-C	0.08	244
FA-M-10-I	0.06	45
FA-M-10-C	0.08	158
MK-M-10-I	No cracking	No cracking
MK-M-10-C	0.04	55

The maximum crack widths and average of the crack lengths in mm units in the cold joint beam with a cover depth of 10 mm are listed in **Table 4.11**. The crack length in the monolithically-cast beams was up to 345 mm over the un-coated length of the steel bars, of 400 mm. The crack length in the ordinary concrete beams was on average 1.16 times larger due to carbonation compared to that under the isolated chloride exposure. The crack length in the fly ash concrete beams was 4 % larger due to carbonation compared to that under the isolated chloride exposure. The metakaolin concrete beams under the isolated chloride exposure were all un-cracked whereas the carbonated beams had an average crack length of 100 mm. The small differences in the crack length in the fly ash concrete beams may be attributed to an increase in the corrosion rate due to the cold joint.

Table 4.11: Crack formation in the 10 mm cover cold joint beams

Reinforced beam	Max crack width (mm)	Crack length (mm)
CEM-CJ-10-I	0.10	159
CEM-CJ-10-C	0.08	345
FA-CJ-10-I	0.06	305
FA-CJ-10-C	0.08	318
MK-CJ-10-I	No cracking	No cracking
MK-CJ-10-C	0.04	100

The cracking in the beams with a cold joint was the largest in terms of the length coverage, 1-6.7 times larger than the corresponding monolithically-cast beams. The carbonation caused an increase in the crack length in both beam types which occurred when the carbonation depth had reached close to or at the steel surface. The carbonated cold joint beams were thus most cracked where the crack lengths were 2.2-7.1 times larger than the reference beams, which were monolithically-cast under the isolate chloride exposure. There was no cracking in the reference beams that were made the metakaolin concrete whereas there was up to 100 mm cracking in the carbonated beams. The influence of the cold joint and carbonation was thus accentuated in the extent of cracking, together with the steel corrosion.

The chloride contents in the 10 mm cover beams were increased in due to the cracking although not to the extent of the cold joint. In the cracked 10 mm cover beams the chloride content was increased by up to 75 % compared to that of the corresponding 20 mm cover beams. The exception to this was that some of the fly ash concrete beams however had chloride contents of up to 22 % lower than that of the corresponding 20 mm cover beams. The cold joint increased the chloride content by up to 5.4 times compared to that of the corresponding monolithically-cast beams at both cover depths (10 mm and 20 mm). The cold joint was thus the main factor to the chloride content as it was present from the introduction of the exposure whereas the cracks developed in the propagation phase of corrosion.

4.6. Final discussion

This chapter has covered a multitude of concepts which need to be tied up to relate these with the stated aim of the study. The cement replacement with fly ash and metakaolin was a means of comparing the concrete properties and to assess the durability performance. The physical characteristics and compositions of these materials were tested as this aspect of concrete quality and extent of curing was important to the concrete properties. The fly ash was less-reactive of the cement extenders as the surface area of the smooth and round particles was lower than the rapid-hardening cement. The metakaolin was the most reactive of the 3 binders as the surface area of the rougher and angular particles was larger than that of the cement. The particle sizes of the cement extenders were smaller than the cement thus could decrease the pore sizes and total porosity with an adequate curing.

The fresh-state properties were the first indication of the reactivity of the binders when they were combined with the cement in concrete. The slump of the fly ash concrete was higher than the ordinary concrete whereas metakaolin concrete required plasticiser to yield a slump closer to the other concretes. The other fresh-state properties, cohesion level and stone content were dependent mainly on the consistency (or slump) as these were acceptable once the slump fell within range. The changes in the fresh-state properties may be attributed to the differences in surface area of the binders as there was a similarity in the particle sizes. The small changes in the particle sizes between the binders were due to the fineness of the cement, which could yield changes in the concrete properties with further curing.

The compressive strength was the only concrete property in hardened-state that was tested within the early-age period of 28 days. The reactivity of the cementing binders after the fresh-state was apparent in the trends of strength development within curing periods of up to 90 days. The majority of the 90-day strength had yielded after 2 days due to the use of rapid-hardening cement with a high grade in the concretes. The high reactivity of the metakaolin, to contribute to strength, was apparent mainly up 7 days whereas the fly ash maintained an increase in strength

up to 90 days. The strength of the metakaolin concrete was up to 25 % larger than the ordinary concrete whereas the strength of the fly ash concrete reached 18 % lower after 90 days. Broadly the strength relates to the durability however the transport properties were tested to assess the influence of the cement extenders.

The transport properties were tested to assess the susceptibility of the concretes to chloride penetration, carbonation and corrosion. The fineness (or particle sizes) and composition of the binders was discerned more clearly by the resistance of the concretes to gasses, moisture and chloride ions. The oxygen permeability and water sorptivity were dependent on the physical properties of the microstructure, namely the pore sizes and their connectivity. The chloride conductivity was also dependent on the composition of the binders as chloride may be chemically-bound to alumina compounds of paste. The oxygen permeability and water sorptivity were lower in the cement extender concretes than the ordinary concrete after 28 days of curing. This decrease in permeability occurred due to their smaller particle sizes which may superimpose the pores of cement paste with sufficient curing.

The chloride conductivity was reduced by a larger magnitude in the metakaolin concrete due to its increase in alumina content compared to the other binders. The fly ash concrete yielded a chloride conductivity index that differed by only 1 % compared to the ordinary concrete after 90 days of curing. Greater than 95 % of the magnitudes of the transport properties after 90 days of curing had yielded after 28 days by the ordinary and fly ash concretes. The curing duration of 28 days may thus be regarded to be suitable in these concretes before the exposure to chloride and carbon dioxide. Though the metakaolin concrete yielded larger changes from 28 to 90 days, the permeability was lower than the other concretes after 28 days.

The chloride penetration and carbonation depth was tested after the exposure to chloride in isolation and in a combination with carbon dioxide. An increase in the chloride content beyond the carbonation depth at the cold joint was part of the hypothesis which may increase the corrosion risk of embedded steel. The cold joint resulted in the largest increase in chloride content at both cover depths of 20

mm and 10 mm compared to the monolithically-cast beams. The cracks in the 10 mm cover beams also increased the chloride content although not to the extent of that caused by the cold joint. The cold joint increased in transport rates of the circular discs although not to the extent of the beams as the surface layer was cut off in the disc preparation. The increase in chloride content in the beams could be shifted to beyond the carbonation depth to increase the corrosion rate at the steel.

There was a consistent trend of an increase in the chloride content beyond the carbonation depth due to the loss of the chloride binding capacity. The increase in chloride content beyond the carbonation depth was greater in the cement extender concretes due to their low resistance to carbonation. The carbonation depth was larger in these concretes due to the lower calcium oxide contents compared to that of the rapid-hardening cement. There was thus a larger chloride content that could be shifted beyond the carbonation depth in the fly ash and metakaolin concretes to the embedded steel. The increase in chloride content beyond the carbonation was mainly found in the beams with a cold joint within the timeframe of the exposure. A longer duration of exposure would have resulted in a larger increase in chloride content beyond the carbonation depth also in the monolithically-cast beams.

The corrosion behaviour was monitored in the exposure period as the corrosion potential, corrosion rate and concrete resistivity. The corrosion initiation time and maximum corrosion rate that was reached were a means to assess the corrosion resistance. The cold joint was the main factor to the initiation time and maximum corrosion rate at both cover depths, of 20 mm and 10 mm. The corrosion rates of the cold joint beams with a cover depth of 20 mm were 2.7-7.5 times larger than the corresponding monolithically-cast beams. The potential indicated that these cold joint beams were actively corroding whereas the monolithically-cast beams remained under passive corrosion. A reduction in the cover depth was a means to include the accelerated stage of corrosion, due to corrosion-induced cracks on the exposed surface. The corrosion rate in the cracked beams reached values of up to 10 times larger than in the corresponding beams with a cover depth of 20 mm.

The influence of carbonation was based on the corrosion rate that was reached within the exposure period at both of the cover depths, 10 mm and 20 mm. The corrosion rate of the carbonated beams was up to 29 % larger than the beams under the isolated chloride exposure at a cover depth of 20 mm. The corrosion rate of the carbonated beams was up to 3.47 times larger the beams under isolated chloride exposure at a cover depth of 20 mm. The corrosion rate of the carbonated beams with a cold joint was up to 7.2 times larger than the reference beams, the monolithcally-cast beams under the isolated chloride exposure. An increase in the corrosion rate was the main part of the hypothesis which was consistent with an increase in the chloride content beyond the carboantion depth. Further exposure would have increased the corrosion rate of the beams under passive corrosion, however, these served as a reference for the comparisons to the corroded beams.

The benefit of the fly ash and metakaolin was limited to a cover depth of 20 mm where the corrosion rate was lower than the ordinary concrete. The maximum corrosion rate of the cement extender concrete beams with a cold joint was up to 2.4 times lower than that of the ordinary concrete. The decrease in corrosion rate in these concretes at a cover depth of 20 mm may be attributed to the concrete resistivity and oxygen permeability. The oxygen permeability was lower than the ordinary concrete which is the main factor of corrosion in partially-saturated concrete. The concrete resistivity was higher than the ordinary concrete, in that there was a lower conductivity of the current of the corrosion reactions on the steel. At the lower cover depth of 10 mm the fly ash and metakaolin concretes were susceptible to the carbonation as this was intended to result in the cracking.

The extent of cracking in the cover concrete and corrosion on the steel were a means to validate the corrosion monitoring. The beams with a cover depth of 20 mm only contained corrosion damage to the steel surface, and not the cracking in the cover concrete. The corrosion in the monolithically-cast beams was only present in the ordinary concrete whereas the cement extender concretes had no apparent corrosion. This minor corrosion validates the potential falling within the range of passive corrosion throughout the exposure, with no increase in corrosion

rate. The cold joint induced corrosion in all beams at a cover depth of 20 mm on both sides of the steel, i.e. not only at the exposed surface. The corroded lengths were lower in the cement extender concretes beams and in the vicinity of the cold joint at the mid-span. This validates the decrease in the corrosion rate in in these concretes once the potential had dropped to within the range of active corrosion.

The decrease in cover depth from 20 mm to 10 mm resulted in significantly larger coverage of corrosion on both sides of the steel surface, with pitting corrosion. The lengths of pitting corrosion were increased due to the cold joint in the 10 mm cover beams compared to that in the monolithically-cast beams. Where the steel had corroded more distinctly, i.e. pitting, the concrete had cracked due to the expansion pressures which originated at the steel surface. The carbonated beams contained the largest crack lengths and corrosion damage as the carbonation depth had reached the steel. In the 20 mm cover beams, the differences in the corrosion lengths due to carbonation were smaller as the carbonation depth was further from the steel. The crack length related to the maximum corrosion rate where the carbonated beams with a cold joint contained the largest crack lengths of all sets.

5. Conclusions and recommendations

5.1. Summary

This study was set out to investigate a practical case of corrosion which may be regarded as the worst problem to the durability of concrete structures worldwide. Chloride penetration is increased at the locations of defects which imposes a significant change in the corrosion activity of embedded steel. An increase in the chloride content beyond the carbonation depth may be increased at cold joints thus increase the corrosion rate of embedded steel. This corrosion case stems from the knowledge on corrosion at cold joints and that under combined exposure to chloride and carbon dioxide. The multitude of factors in the environment may be encapsulated in a laboratory setting which is a means of extrapolating that in a service life of structures. This study was based on an experimental investigation by testing a number of parameters which may be grouped under the following:

1. Corrosion monitoring of the embedded steel,
2. Chloride penetration and carbonation depths in the concrete,
3. Transport properties of oxygen, water and chloride ions and,
4. Corrosion damage as concrete cracking and steel corrosion.

The studies that were discussed in the Literature Review in **Chapter 2** of this study identified a number of trends that were important to the study. These were the influence of defects on chloride penetration and corrosion, the influence of carbonation in concrete with chloride, and the properties of concrete with cement extenders. The corrosion case of chloride at cold joints in carbonated concrete provided a means of assessing the durability with less-known cementing materials in concrete. The benefits to the durability of adding such materials to concrete were of interest to the study to determine their applicability in service conditions. The interaction of chloride in carbonated concrete was found in the experimental programme over an exposure period for a number of comparisons in the results.

The results found an agreement between the experimental parameters which validated the hypothesis of this study. The increase in chloride content beyond the carbonation depth at the cold joint was found within the timeframe of the exposure period. This increase in chloride content resulted in an increase in the corrosion rate at the embedded steel which would pose a risk to the service life of concrete structures. This trend was found by comparisons of the carbonated specimens with a cold joint to the monolithically-cast specimens and under the isolated chloride exposure. The carbonation depth that was reached within the timeframe of the exposure was sufficiently influential to the chloride penetration and corrosion rate. This was apparent by the carbonation reaching a depth that could influence the majority of the chlorides in the surface region of concrete.

The corrosion damage in terms of the length of corrosion on the steel and cracking in the cover concrete were consisted with the corrosion results. The influence of the material characteristics on the concrete properties was also consistent with a number of studies in the literature. The benefit of fly ash and metakaolin under the combined exposure resided in a reduction of the corrosion rate with a sufficient cover depth. These materials were more susceptible to carbonation thus the cover depth is important to the corrosion rate if there is an increase in chloride content beyond the carbonation depth. The cover depths were however significantly low thus these materials would decrease the corrosion rate with the cover depths in standards. The aim of this study was achieved in that the benefit of these materials under the corrosion case in question was found and consistent with the literature.

5.2. Conclusions

The conclusions that follow form the main contribution of this study and pertain to the parameters that determined the response to the exposure conditions:

- The binder characteristics; surface area, particle sizes and composition, were sufficient to relate to the strength and durability properties.

- The fly ash and metakaolin yielded a reduction in the transport of gasses, moisture and chloride ions after a sufficient curing age.
- The amount of voids and their connectivity at the cold joint increased the chloride content in the beams and decreased the corrosion initiation time.
- The cold joint in the beams resulted in an increase in the chloride content beyond the carbonation depth, at the steel surface.
- The cement extenders decreased the corrosion rate at a sufficient cover depth, due to the increase in concrete resistivity and decrease in oxygen permeability.
- The extent of concrete cracking and corrosion damage to the steel were consistent with the corrosion monitoring.
- The carbonation depth in all concretes was sufficient as it progressed beyond the majority of the chlorides in the surface region.
- An increase in the chloride content beyond the carbonation depth at the cold joint resulted in the highest corrosion rate in all concretes. Cold joints (or any defects) thus may be problematic to the service life in marine environments if the carbonation depth is sufficient.

5.3. Recommendations

The corrosion mechanism was replicated under a number of cases in this study however there were gaps in knowledge which may be expanded on. It is typical to assume an ideal condition of certain factors in an experimental setting to simplify the scope of an investigation. Though the scope of this study was reduced to a specific set of parameter groups there was an agreement between these parameters to achieve the stated aim. The general approach of this study was thus considered to be suitable given the timeframe of the experimental programme and constraints of resources. A number of recommendations in line with this scope which would improve the accuracy and interpretation of the experimental results as follows:

- The concrete mixture designs could include a range of water: binder (W: B) ratios or cement grades to assess the performance of the cement extenders.

Tertiary blends would also increase the applicability of the cement extenders to provide resistance to the transport of gasses, moisture and ions.

- A pore size distribution of the concretes would have aided the results in terms of the influence of the cement extenders on the pore sizes.
- The exposure conditions could be improved by regulating the chloride content in the wetting cycles and relative humidity in the carbonation chamber.
- The chloride penetration and carbonation depths in the cover concrete could be validated with other methods of chemical analysis. The free chloride content would determine the influence of the carbonation on the chloride binding however most chloride is diffusible in carbonated concrete. A method of pH testing could determine the decrease in the alkalinity in the zones of carbonated concrete, fully- and partially-carbonated.
- The corrosion potential and concrete resistivity were measured using 2 types of apparatus as a means of validation. The corrosion rate could also have been measured with another method, i.e. linear polarisation resistance, which would validate that measured using the Coulostatic method.
- The corrosion damage assessment was simplified, in that the corrosion rate was not related to the concrete cracking or steel corrosion. Other parameters such as the steel mass loss and crack width in the concrete could be measured to aid more certainty to the results.

References

1. AASHTO, 2006. *AASHTO T259: Standard Method of Test for Resistance of Concrete to Chloride Ion Penetration,* s.l.: The American Association of State Highway and Transportation Officials.
2. AASHTO, 2007. *AASHTO T 277-07: Electrical indication of concrete's ability to resist chloride ion penetration,* s.l.: The American Association of State Highway and Transportation Officials.
3. AASHTO, 2011. *AASHTO TP 95-11: Standard Method of Test for Surface Resistivity Indication of Concrete's Ability to Resist Chloride Ion Penetration,* s.l.: The American Association of State Highway and Transportation Officials.
4. AASHTO, 2015. *AASHTO T 358-15,* s.l.: The American Association of State Highway and Transportation Officials.
5. ACI, 1991. *ACI 211.1-91: Standard practice for selecting proportions for normal, heavyweight, and mass concrete,* Farmington Hills, Michigan: American Concrete Institute.
6. ACI-Committee-365, 2005. *Service life prediction. Report No. ACI 365.1R,* Farmington Hills, Michigan, U. S.: ACI-Committee-365.
7. Alexander, M. et al., 2009. *Fultons concrete technology*. 9 ed. Midrand, South Africa: Cement & Concrete Institute (C & CI).
8. Alexander, M. G., 2017. *Durability Index Testing Procedure Manual,* Cape Town: University of Cape Town.
9. Alexander, M. G., Ballim, Y. & Stanish, K., 2008. A Framework for use of Durability Indexes in Performance-Based Design and Specifications for Reinforced Concrete Structures. *Materials and Structures,* Volume 41, p. 921–936.
10. Alexander, M. G., Mackechnie, J. R. & Ballim, Y., 1999. *Guide to the use of Durability Indexes for Achieving Durability in Concrete Structures.* s.l.:Research monograph. p. 36.
11. Alexander, M. & Mindess, S., 2005. *Aggregates in Concrete.* 1st ed. New York: Taylor & Francis.

12. Alonso, C., Andrade, C. & González, J. A., 1988. Relation between concrete resistivity and corrosion rate of the reinforcements in concrete resistivity and corrosion rate of the reinforcements in carbonated mortar made with several cement types. *Cement and Concrete Research,* 18(5), pp. 687-698.
13. Andrade, C. & Alonso, C., 1996. Corrosion rate monitoring in the laboratory and on-site.. *Corrosion and Building Materials,* 10(5), pp. 315-328.
14. Andrade, C. & González, J. A., 1978. Quantitative measurements of corrosion rate of reinforcing steels embedded in concrete using polarization resistance measurements. *Werkstoffe und Korrosion,* Volume 29, pp. 515-519.
15. Ann, K. Y. & Song, H. W., 2007. Chloride threshold level for corrosion of steel in concrete. *Corrosion Science,* 49(1), pp. 4113-4133.
16. Antoni, M., Rossen, J., Martirena, F. & Scrivener, K., 2012. Cement substitution by a combination of metakaolin and limestone. *Cemement and Concrete Research,* Volume 42, p. 1579–1589.
17. ASTM, 1999. *ASTM C 1543 – 19 Standard Test Method for Determining the Penetration of Chloride Ion into Concrete by Ponding,* West Conshohocken, United States: ASTM International.
18. ASTM, 1999. *ASTM C876 - 99: Standard Test Method for Corrosion Potentials of Un-coated Reinforcing Steel in Concrete,* West Conshohocken, United States: ASTM International.
19. ASTM, 2007. *ASTM C1202 - 07 Standard Test Method for Electrical Indication of Concrete's Ability to Resist Chloride Ion Penetration,* s.l.: ASTM International.
20. ASTM, 2008. *ASTM C 618-08a Standard specification for coal fly ash and raw or calcined natural pozzolan for use in concrete,* West Conshohocken, United States: American Society for Testing and Materials.
21. ASTM, 2009. *ASTM G 57 - 20: Standard test method for Measurement of Soil Resistivity Using the Wenner Four-Electrode Method,* West Conshohocken, United States: ASTM International.

22. ASTM, 2014. *ASTM G3-14: Standard Practice for Convensions Applicable to Electrochemical Measurements in Corrosion Testing,* s.l.: ASTM International.

23. Bai, J., Wild, S. & Sabir, B. B., 2003. Chloride ingress and strength loss in concrete with different PC–PFA–MK binder compositions exposed to synthetic seawater. *Cement and Concrete Research,* Volume 33, p. 353–362.

24. Bakera, A. & Alexander, M. G., 2017. *Properties of Western Cape Concretes with Metakaolin.* Cape Town, South Africa, Department of Civil Engineering, University of Cape Town.

25. Bakera, A. & Alexander, M. G., n.d. *Properties of Western Cape Concretes with Metakaolin.* Cape Town, South Africa, Department of Civil Engineering, University of Cape Town.

26. Bakera, A. T. & Alexander, M. G., 2019. Use of metakaolin as a supplementary cementitious material in concrete, with a focus on durability properties. *RILEM Technical Letters,* Volume 4, p. 89-102.

27. Balakrishna, M. N. & Nataraja, M. C., 2013. Proportioning of Fly Ash Concrete Mixes A Compresensive Approach. *International Journal of Emerging Science and Engineering (IJESE),* 1(8).

28. Ballim, Y., 1993. Towards an early age index for the durability of concrete. Proceedings of International Conference: Concrete 2000. In: R. Dhir & M. R. Jones, eds. *Economic and Durable Construction through Excellence.* London: E & FN Spon, pp. R.K. and Jones, M.R. (Eds.), E & FN Spon, pp. 1003-1012..

29. Barnes, R. & Zheng, T., 2008. *Research on factors affecting concrete cover measurement,* NSW, Australia: The e-Journal of Nondestructive Testing.

30. Bentur, A., Diamond, S. & Berke, N., 1997. *Steel corrosion in concrete, Fundamentals and Civil Engineering Practice.* 1 ed. London: E & FN Spon.

31. Bertolini, L., Elsener, B., Pedeferri, P. & Polder, R. P., 2004. *Corrosion of Steel in Concrete.* Weinheim: WILEY-VCH Verlag GmbH & Co. KGaA.

32. Bertolini, L., Elsener, B., Pedeferri, P. & Polder, R. P., 2013. *Corrosion of Steel in Concrete: Prevention, Diagnosis, Repair.* 2nd ed. Weinheim, Germany: WILEY-VHC Verlag GmbH & Co. KGaA.

33. Bertolini, L. et al., 2013. *Corrosion of Steel in Concrete: Prevention, Diagnosis, Repair.* 2nd ed. Weinheim, Germany: WILEY-VHC Verlag GmbH & Co. KGaA.

34. Beushausen, H. & Alexander, M. G., 2008. Paper 671: The South African durability index tests in an international comparison. *Journal of the South African Institution of Civil Engineering,* 50(1), p. 25–31.

35. Broomfield, J. P., 2007. *Corrosion of Steel in Concrete: Understanding, Investigation and Repair.* 2nd ed. Milton, England & New York, U. S. A: Taylor & Francis.

36. BS-EN, 2000. *BS EN 206-1: Concrete, Specification, performance, production and conformity,* s.l.: Standard by British-Adopted European Standard.

37. BS-EN, 2001. *BS EN 934-2: Admixtures for concrete, mortar and grout,* s.l.: Standard by British-Adopted European Standard.

38. Bucher, R., Cyr, M. & Escadeillas, G., 2015. Carbonation of Blended Binders Containing Metakaolin. *Calcined Clays for Sustainable Concrete, RILEM Bookseries,* Volume 10.

39. BUILD, N., 1999. *NT BUILD 492: Chloride Migration Coefficient from nonsteady state migration experiments,* s.l.: NORTEST.

40. Cabrera, J. G. & Nwaubani, S. O., 1998. The microstructure and chloride ion diffusion characteristics of cements containing metakaolin and fly ash. *Preceedings of the 6th CANMET/ACI International Conference on Fly Ash, Silica Fume and Natural Pozzolans in Concrete,* Volume 1, pp. 493-506.

41. CEB, 1989. *CEB Design Guide Bulletin d'information 182: Durable Concrete Structures,* s.l.: Committee Euro-International du Beton (CEB).

42. Chang, C. & Chen, J., 2004. The experimental investigation of concrete carbonation depth. *Cement and Concrete Research,* Volume 36, p. 1760–1767.

43. Chaparro, W. A., Lopez, E. V. & Gutierrez, R. M. D., 2012. Corrosion behaviour of steel bar embedded in alkali-activated slag concrete subjected to carbonation and chloride attack. *Dyna,* 79(171), pp. 80-87.

44. Chi, J. M., Huang, R. & Yang, C. C., 2002. Effects of Carbonation on Mechanical Properties and Durability of Concrete using Accelerated Testing Method. *Journal of Marine Science and Technology,* 10(1), pp. 14-20.
45. Clément, A., Laurens, S., Arliguie, G. & Deby, F., 2012. Numerical study of the linear polarization resistance technique applied to reinforced concrete for corrosion assessment. *European Journal of Environmental and Civil Engineering,* p. 17.
46. Domone, J. & Illston, P., 2010. *Construction Materaials: Their nature and behaviour.* 4th ed. London: Spon Press.
47. DuraCrete, 1998. *Probabilistic performance-based durability design: modelling of degradation. Document, D. P. No. BE95-1347/R4-5,* The Netherlands: s.n.
48. DuraCrete, 2000. *DuraCrete Final Technical Report, "The European Union – Brite EuRam III, DuraCrete – Probabilistic performance based durability design of concrete structures, Document BE95-1347/ R17, CUR ,* Gouda, The Netherlands: s.n.
49. Farzad, M., Fancy, S. F., Lau, K. & Azizinamini, A., 2019. Chloride Penetration at Cold Joints of Structural Members with Dissimilar Concrete Incorporating UHPC. *Infrastructures,* 4(18).
50. Feliu, S., Gonzalez, S., Andrade, J. & Feliu, C., 1987. On-site determination of the Polarization Resistance in a reinforced beam. *Corrosion (USA),* Volume 43, pp. 1-9.
51. Ferreira, R. M., Castro-Gomes, J. P., Costa, P. & Malheiro, R., 2015. Effect of Metakaolin on the Chloride Ingress Properties of Concrete. *KSCE Journal of Civil Engineering (0000) 00(0):1-10,* pp. 1-10.
52. Gehlen, C., 2000. *PHd Thesis: Probabilistische lebensdauerbemessung von stahlbetonbauwerken- zuver-lassigkeitsbetrachtung zur wirksamen vermeidung von bewehrungskorrosion,* Aachen, Germany: RWTH Aachen.
53. Ghahari, S. A., Ramezanianpour, A. M., Ramezanianpour, A. A. & Esmaeili, M., 2016. An accelerated test method of simultaneous carbonation and

chloride ion ingress: Durability of silica fume concrete in severe environments. *Advances in Materials Science and Engineering.*

54. Glass, G. K. & Buenfeld, N. R., 1997. Presentation of the chloride threshold for corrosion of steel. *Corrosion Science,* 39(5), pp. 1001-1013.
55. Glass, G. K. & Buenfeld, N. R., 2000. The influence of chloride binding on the chlroide induced corrosion risk in reinforced concrete. *Corrosion Science,* 42(1), pp. 329-344.
56. Glass, G. K. & Buenfeld, N. R., 2000. The inhibitive effects of electrochemical treatment applied to steel in concrete. *Corrosion Science,* 42(1), pp. 923-927.
57. Glass, G. K., Hassanein, N. M. & Buenfeld, N. R., 1997. Neural network modelling of chloride binding. *Magazine of Concrete Research,* 49(181), p. 323–335.
58. Glass, G. K., Reddy, B. & Buenfeld, N. R., 2000. The participation of bound chloride in passive film breakdown on steel in concrete. *Corrosion Science,* 42(11), pp. 2013-2021.
59. González, J. & Andrade, C., 1982. Effect of carbonation, chlorides an relative ambient humidity on the corrosion ofgalvanized rebars embeded in concrete. *British Corrosion Journal,* 17(1), pp. 21-28.
60. Gous, S. M., Alexander, M. G. & Maritz, G., 2001. Use of Durability Index Tests for the Assessment and Control of Concrete Quality on Site. *Concrete Beton,* Volume 98, pp. 5-16.
61. Gowers, K. & Milliard, S., 1999. Electrochemical technology for corrosion assessment of reinforced concrete structures. *Civ. Engrs. Structs. and Bldgs,* pp. 129-134.
62. Hausmann, D. A., 1967. Steel corrosion in concrete'. *Materials Protection,* Volume 6, pp. 19-23.
63. Heckroodt, R. O., 2002. *Guide to deterioration and failure of building materials.* London: Thomas Telford Ltd.

64. Hong, K. & Hooton, R., 1999. Effects of cyclic chloride exposure on penetration of concrete cover. *Cement and Concrete Research,* 29(9), pp. 1379-1386.

65. Hope, B. B., Ip, A. K. & Manning, D. G., 1985. Corrosion and electrical impedance in concrete. *Cement and Concrete Research,* 15(3), pp. 525-534.

66. Horiguchi, K., Yamaguchi, T., Maruya, T. & Takewaka, K., 2020. Study on the method of measuring the chloride threshold value of corrosion and estimation of the values in durbality design of concrete structures. *Journal of Advanced Concrete Technology,* Volume 18, pp. 571-587.

67. Hunkeler, F., 2005. *Corrosion in reinforced concrete structures.* Cambridge: Woodmead Publishing.

68. Ikotun, J. O., Otieno, M. B. & Ballim, Y., 2017. *Prediction of Carbonation-Induced Corrosion Initiation of Steel in RC Structures Exposed to Natural Inland Environment of South Africa.* Chennai, India, 71st RILEM Annual Week & ICACMS 2017.

69. Islam, G. M. S. & Sugiyama, T., 2010. Determination of Corrosion Initiation of Rebar in Concrete by Monitoring Half-Cell Potential. *Malaysian Journal of Civil Engineering,* 22(2), pp. 186-201.

70. Islam, M. & Islam, S., 2010. Strength Behaviour of Mortat Using Fly Ash as Partial Replacement of Cement. *Concrete Research Letters,* 1(3).

71. Ives, D. J. G., Janz, G. J. & King, C. V., 1961. Reference Electrodes Theory and Practice. *Journal of the Electrochemical Society,* 108(11).

72. Kevern, J. T., Halmen, C. & Hudson, D., 2015. *Evaluation of Resistivity Meters for Concrete Quality Assurance,* s.l.: Missouri Department of Transportation.

73. Khatib, J. M. & Wild, S., 1996. Pore size distribution of metakaolin paste. *Cement and Concrete Research,* 26(10), pp. 1545-1553.

74. Kim, H. S., Lee, S. H. & Moon, H. Y., 2007. Strength properties and durability aspects of high strength concrete using Korean metakaolin. *Construction and Building Materials,* Volume 21, pp. 1229-1237.

75. Kunowsky, M., Marco-Lozar, J. P. & Linares-Solano, A., 2013. Material Demands for Storage Technologies in a Hydrogen Economy. *Journal of Renewable Energy,* Volume 2013.

76. Langford, P. & Broomfield, J., 1987. Monitoring the corrosion of reinforcing steel. *Construction Repair,* 1(2), pp. 32-36.

77. Laverriere, R. & Pachova, T., 2012. *Ion Chromatography*, Geneve: Universite de Geneve.

78. Li, C. Q., 2002. Initiation of Chloride-Induced Reinforcement Corrosion in Concrete Structural Members-Prediction. *ACI Structural Journal.*

79. LIFE-365, 2005. *Service life prediction model, Computer program for predicting the service life and life-cycle costs of reinforced concrete exposed to chlorides,* s.l.: ACI Commitee 365.

80. Liu, J. et al., 2020. Effect of fly ash as cement replacement on chloride diffusion, chloride binding capacity, and micro-properties of concrete in a water soaking environment. *Applied Sciences.*

81. Liu, J., Xing, Q. Q. F. & Pan, D., 2014. Permeation properties and pore structure of surface layer of fly ash concrete. *Materials,* Volume 7, pp. 4282-4296.

82. Liu, W. et al., 2016. Carbonation of concrete made with dredged marine sand and its effect on chloride binding. *Construction and Building Materials,* Volume 120, pp. 1-9.

83. Lowell, S., Shields, J. E., Thomas, M. A. & Thommes, M., 2004. *Characterization of Porous Solids and Powders: Surface Area, Pore Size and Density.* 1 ed. s.l.:Springer.

84. Mackechnie, J. R., 1996. *PHd Thesis: Predictions of Reinforced Concrete Durability in the Marine Environment,* Cape Town: University of Cape Town.

85. Mackechnie, J. R., 1997. *Predictions of reinforced concrete durability in the marine environment: Research Monograph No. 1,* s.l.: University of Cape Town and the University of Witwatersrand, Johannesburg.

86. Malheiro, R. et al., 2016. *Proceedings of the 7th International Conference on Safety and Durability of Structures: Chloride penetration into carbonated concrete.* Portugal, s.n.

87. Mangat, P. S., El-Khatib, J. M. & Molloy, B. T., 1994. Microstructure, chloride diffusion and reinforcement corrosion in blended cement paste and concrete. *Cement and Concrete Composites,* 16(2), pp. 73-81.

88. Mangat, P. S. & Molloy, B. T., 1994. Prediction of long-term chloride concentration in concrete. *Materials and Structures,* Volume 27, p. 338–346.

89. Mansfield, 1981. *Corrosion,* 37(5), pp. 301-307.

90. Meddah, M. S. & Tagnit-Hamou, A., 2009. Pore Strucutre of Concrete with Mineral Admixtures and its Effect on Self-desication Shrinkage. *ACI Materials Journal,* 3(May-June).

91. Miyazato, S.-i. & Otsuki, N., 2010. Steel Corrosion Induced by Chloride or Carbonation in Mortar with Bending Cracks or Joints. *Journal of Advanced Concrete Technology,* 8(2), pp. 135-144.

92. Montemor, M. F., Simoes, A. M. P. & Ferreira, M. G. S., 2003. Chloride-induced corrosion on reinforcing steel: from the fundamental to the monitoring techniques. *Cement & Concrete Composite,* Volume 25, pp. 491-502.

93. Moreno, E. I. & Sagues, A. A., 1998. Carbonation-induced corrosion of blended-cement concrete mix designs for highway structures. *NACE International.*

94. Nakamura, E. et al., 2008. *Half-cell potential measurements to assess corrosion risk of reinforcement steels in a pc bridge.* Como Lake, Italy, International RILEM Conference.

95. Neville, A., 2011. *Properties of Concrete.* 5th ed. Harlow, England: Pearson Education Limited.

96. NT-BUILD, 1999. Chloride migration coefficient from non-steady-state migration experiments. *NT BUILD 492: Concrete, mortar and cement-based repair materials,* 1(8).

97. Nwaubani, S. O., Shiathas, C. & Muntasser, T. Z., 2003. A comparitive study of the properties and durability of binary and ternary cementitious systems. *ACI Symposium Publication,* Volume 212, pp. 459-474.

98. Otieno, M. B., 2014. *The Development of Empirical Chloride-induced Corrosion Rate Prediction Models for Cracked and Uncracked Steel Reinforced Concrete Structures in the Marine Tidal Zone,* Cape Town: University of Cape Town.

99. Owens, G., 2009. *Fulton's concrete technology.* 9th ed. Midrand, South Africa: Cement & Concrete Institute.

100. Pakawat, S. & Uomoto, T., 2005. Effect of Cyclic Exposure of Carbonation and Chloride on Corrosion of Reinforcing Steel in Concrete. *Seisan-Kenkyu,* 57(2), pp. 29-32.

101. Paul, S., 2015. *The Role of Cracks and Chlorides in Corrosion of Reinforced Strain Hardening Cement-Based Composite (R/SHCC),* Stellenbosch, South Africa: Stellenbosch University.

102. Polder, R. et al., 2000. Test methods for on-site measurement of resistivity of concrete. *Materials and Structures,* Volume 33, pp. 603-611.

103. Quraishi, M. A., Nayak, D. K., Kumar, R. & Kumar, V., 2017. Corrosion of reinforcing steel in concrete and its control: An overview. *Journal of Steel Structures and Construction,* 3(1).

104. Ramezanianpour, A. A., Ghahari, S. A. & Esmaeili, M., 2014. Effect of combined carbonation and chloride ion ingress by an accelerated test method on microscopic and mechanical properties of concrete. *Construction and Building Materials,* Volume 58, p. 138–146.

105. RILEM, 2004. RILEM TC 154-EMC: 'Electrochemical Techniques for Measuring Metallic Corrosion': Recommendations: Test methods for on-site corrosion rate measurement of steel reinforcement in concrete by means of the polarization resistance method. *Materials and Structures,* Volume 37, pp. 623-643.

106. RILEM, 2004. RILEM TC 154-EMC: Electrochemical Techniques for Measuring Metallic Corrosion: Recommendations: Test methods for on-site

corrosion rate measurement of steel reinforcement in concrete by means of the polarization resistance method. *Materials and Structures,* Volume 37, pp. 623-643.

107. RILEM, 2013. Recommendation of RILEM TC 178-TMC: Testing and modelling chloride penetration in concrete - Methods for obtaining dust samples by means of grinding concrete in order to determine the chloride concentration profile. *Materials and Structures,* Volume 46, p. 337–344.

108. Roberge, P. R., 2008. *Corrosion Engineering: Principles and Practice.* 1st ed. New York: The McGraw-Hill Companies.

109. Roxas, C. L. & Lejano, B. A., 2018. Macrocell corrosion assessment of steel in cold-jointed concrete mixed and cured in seawater. *International Journal of Geomate,* 14(42), pp. 83-89.

110. Safehiana, M. & Ramezanianpour, A. A., 2015. Prediction of RC structure service life from field long term chloride diffusion. *Computers and Concrete,* 15(4), pp. 589-606.

111. SANS, 2006. *Concrete tests — Dimensions, tolerances and uses of cast test specimens,* Pretoria: South African National Standard.

112. SANS, 2006. *SANS 5845: Bulk densities and void contents of aggregates,* Pretoria: South African National Standard.

113. SANS, 2006. *SANS 5860: Concrete tests - Dimensions, tolerances and uses of cast test specimens,* Pretoria: South African National Standard.

114. SANS, 2006. *SANS 5861-1 Part 1: Mixing fresh concrete in the laboratory,* Pretoria: South African National Standard.

115. SANS, 2006. *SANS 5861-3 Concrete tests Part 3: Making and curing of test specimens,* Pretoria: South African National Standard.

116. SANS, 2006. *SANS 5862-1 Concrete tests - Consistence of freshly mixed concrete - Slump test,* Pretoria: South African National Standard.

117. SANS, 2006. *SANS 5863:2006 Concrete tests - Compressive strength of hardened concrete,* Pretoria: South African National Standard.

118. SANS, 2008. *SANS 201: Sieve analysis, fines content and dust content of aggregates,* Pretoria: South African National Standard.

119. SANS, 2008. *SANS 5847: Flakiness index of course aggregates,* Pretoria: South African National Standard.

120. SANS, 2011. *SANS 50197-1 Cement Part 1: Composition, specifications and conformity criteria for common cements,* Pretoria: South African National Standard.

121. SANS, 2014. *SANS 10100-2 The structural use of concrete Part 2: Materials and execution of work,* Pretoria: South African National Standard.

122. SANS, 2014. *SANS 1083 Aggregates from natural sources - Aggregates for concrete,* Pretoria: South African National Standard.

123. SANS, 2014. *SANS 50450-1 Fly ash for concrete Part 1: Definition, specifications and conformity criteria,* Pretoria: South African National Standard.

124. SANS, 2014. *SANS 51008:2 Mixing water for concrete - Specificantion for sampling, testing and assessing the suitabity of water, including water recovered from processes in the concrete industry as mixing water for concrete,* Pretoria: South African National Standard.

125. SANS, 2014. *SANS 920: Steel bars for concrete reinforcement,* Pretoria: South African National Standard.

126. SANS, 2015. *SANS 3001-CO3-1:2015 Civil engineering test methods Part CO3-1: Concrete durability index testing — Preparation of test specimens,* Pretoria: South African National Standard.

127. SANS, 2015. *SANS 3001-CO3-2:2015 Civil engineering test methods Part CO3-2: Concrete durability index testing — Oxygen permeability test,* Pretoria: South African National Standard.

128. SANS, 2017. *SANS 3001-CO3-3 Civil engineering test methods Part CO3-3: Concrete durability index testing — Chloride conductivity test,* Pretoria: South African National Standard.

129. Sathiyanarayanan, S. et al., 2006. Corrosion monitoring of steel in concrete by galvanostatic pulse technique. *Cement & Concrete Composites,* Volume 28, p. 630–637.

130. Scott, A. N., 2004. *PHd Thesis: The influence of binder type and cracking on reinforcing steel corrosion in concrete,* Cape Town: Department of civil engineering, University of Cape Town.

131. Scott, A. N. & Alexander, M. G., 2007. The influence of binder type, cracking and cover on corrosion rates of steel in chloride-contaminated concrete. *Magazine of Concrete Research,* 59(7), pp. 495-505.

132. Siddique, R., 2008. *Waste Materials and By-Products in Concrete.* s.l.:Springer.

133. Song, H. & Saraswathy, V., 2007. Corrosion monitoring of concrete structures. *International Journal of Electrochemical Science,* Volume 2, pp. 1-28.

134. Stern, M. & Geary, A. L., 1957. Electrochemical Polarization: I.A. theoretical analysis of the shape of polarization curves. *Journal of Electrochemical Society,* 104(1), pp. 56-63.

135. Streicher, P. & Alexander, M. G., 1995. A chloride conduction test for concrete. *Cement and Concrete Research,* 25(6), pp. 1284-1294.

136. Sung-Won, Y. & Seung-Jun, K., 2016. Effects of cold joint and loading conditions on chloride diffusion in concrete containing GGBFS. *Construction and Building Materials,* Volume 115, p. 247–255.

137. Thommes, M. et al., 2015. IUPAC Technical Report: Physisorption of gases, with reference to the evaluation of surface area and pore size distribution. *Pure and Applied Chemistry*, 87(9-10).

138. Tuutti, K., 1982. *Corrosion of Steel in Concrete,* Stockholm: Lund University.

139. Wang, Y., Basheer, P. A. M., Nanukuttan, S. & Bai, Y., 2016. *Influence of Chloride Ions on the Process of Carbonation in Concretes.* London, University College London, U.K..

140. Wesche, K., 2004. *Fly Ash in Concrete: Properties and Performance.* s.l.:Spon.

141. Wexler, A. & Hasegawa, S., 1954. Relative Humidity-Temperature Relationships of Some Saturated Salt Solutions in the Temperature Range of

0-50 Degrees Celcius. *Journa tof Research of the National Bureau of Standards,* Issue 2512.

142. Weydert, R. & Gehlen, C., 1999. Electrolytic resistivity of cover concrete: Relevance, measurement and interpretation. *Durability of Building Materials and Componenets,* Volume 8, pp. 409-419.

143. Yoon, I., 2007. Deterioration of Concrete Due to Combined Reaction of Carbonation and Chloride Penetration: Experimental Study. *Key Engineering Materials,* Volume 348-349, pp. 729-732.

144. Zeng, Q., Li, K., Fen-Chong, T. & Dangla, P., 2012. Pore structure characterization of cement pastes blended with high-volume fly ash. *Cement and Concrete Research,* 42(1), pp. 194-204.

145. Zhiguon, N. & Ri, Y., 2013. Experimental investigation of concrete carbonation under different conditions. *Study of Civil Engineering and Architecture (SCEA),* 2(4).

146. Zivica, V., 2002. Significance and influence of the ambient temperature as a rate factor of steel reinforcement corrosion. *Bull. Mater. Sci.,* 25(5), pp. 375-379.

Appendix A: Cover depth testing

Table A.1: Cover depth in the ordinary concrete beams

Beams	Type	Beam set	Depth (mm)	Wire end	Midspan	Label end
Ordinary concrete trial beams	Monolithic	CEM-M-25-I	Range	{23; 24}	{22; 24}	{22; 24}
			μ (mm)	23	23	23
		CEM-M-25-C	Range	{22; 23}	{21; 23}	{20; 23}
			μ (mm)	23	22	21
	Cold joint	CEM-CJ-25-I	Range	{22; 25}	{23; 25}	{22; 24}
			μ (mm)	24	24	23
		CEM-CJ-25-C	Range	{23; 25}	{24; 25}	{24; 25}
			μ (mm)	24	24	24
Ordinary concrete beams	Monolithic	CEM-M-20-I	Range	{23; 24}	{23; 24}	{23; 24}
			μ (mm)	23	23	24
		CEM-M-20-C	Range	{23; 24}	{24; 25}	{23; 24}
			μ (mm)	24	24	24
	Cold joint	CEM-CJ-20-I	Range	{24; 24}	{24; 24}	{24; 24}
			μ (mm)	24	24	24
		CEM-CJ-20-C	Range	{23; 25}	{23; 24}	{23; 24}
			μ (mm)	24	24	23

Table A.2: Cover depth in the cement extender concrete beams

Beams	Type	Beam set	Depth (mm)	Wire end	Midspan	Label end
Fly ash concrete beams	Monolithic	FA-M-25-I	Range	{23; 25}	{23; 25}	{23; 24}
			μ (mm)	24	24	24
		FA-M-25-C	Range	{24; 25}	{25; 25}	{25; 25}
			μ (mm)	25	25	25
	Cold joint	FA-CJ-25-I	Range	{22; 23}	{22; 23}	{22; 23}
			μ (mm)	22	22	22
		FA-CJ-25-C	Range	{23; 24}	{21; 24}	{22; 25}
			μ (mm)	23	23	23
Metakaolin concrete beams	Monolithic	MK-M-20-I	Range	{20; 24}	{21; 24}	{21; 23}
			μ (mm)	22	22	22
		MK-M-20-C	Range	{23; 23}	{23; 23}	{23; 23}
			μ (mm)	23	23	23
	Cold joint	MK-CJ-20-I	Range	{23; 24}	{23; 24}	{23; 23}
			μ (mm)	23	23	23
		MK-CJ-20-C	Range	{22; 28}	{22; 26}	{22; 24}
			μ (mm)	25	24	23

1. Range: {Minimum; Maximum}.
2. μ: Average.

Appendix B: Compressive strength testing

Table B.1: Details of the compressive strength testing

Age (d)	f_c (MPa)	Ordinary concrete	Fly ash concrete	Metakaolin concrete
2	Range	{37.1; 39.5}	{26.7; 28.4}	{42.4; 44.2}
	μ (of f_c)	38.50	27.60	43.20
	σ (of f_c)	1.30	0.90	0.90
7	Range	{47.5; 49.2}	{32.9; 34.6}	{57.3; 58.2}
	μ (of f_c)	48.40	33.60	57.60
	σ (of f_c)	0.90	0.90	0.50
14	Range	{52.9; 54.7}	{36.0; 38.9}	{63.7; 65.3}
	μ (of f_c)	53.70	37.50	64.40
	σ (of f_c)	0.90	1.50	0.80
28	Range	{56.4; 58.6}	{42.2; 44.3}	{69.2; 70.4}
	μ (of f_c)	57.40	43.50	69.80
	σ (of f_c)	1.10	1.10	0.60
56	Range	{61.4; 62}	{46.3; 48.4}	{70.2; 72.0}
	μ (of f_c)	61.80	47.30	71.00
	σ (of f_c)	0.30	1.10	0.90
90	Range	{62.1; 62.4}	{51.8; 53.4}	{71.6; 73.9}
	μ (of f_c)	62.30	52.60	72.80
	σ (of f_c)	0.20	0.80	1.10

1. f_C: Compressive strength (in MPa).
2. Range: {Minimum; Maximum}.
3. μ: Average.
4. σ: Standard deviation.

Appendix C: Durability indices

Table C.1: Details of the oxygen permeability testing

Age (d)	Disc type	OPI	Ordinary concrete	Fly ash concrete	Metakaolin concrete
28	Monolithic	Range	{10.01; 10.29}	{10.39; 10.50}	{10.36; 10.72}
		μ (of OPI)	10.12	10.45	10.54
		σ (of OPI)	0.13	0.05	0.18
28	Cold joint	Range	{9.39; 9.97}	{9.98; 10.18}	
		μ (of OPI)	9.69	10.07	
		σ (of OPI)	0.25	0.09	
56	Monolithic	Range	{10.42; 10.49}	{10.63; 10.74}	{10.03; 10.67}
		μ (of OPI)	10.45	10.70	10.29
		σ (of OPI)	0.04	0.06	0.34
90	Monolithic	Range	{10.39; 10.48}	{10.70; 10.77}	{10.21; 10.40}
		μ (of OPI)	10.43	10.73	10.30
		σ (of OPI)	0.05	0.03	0.08

Table C.2: Darcy coefficients of permeability

Age (d)	Disc type	k (m/s)x10^{-11}	Ordinary concrete	Fly ash concrete	Metakaolin concrete
28	Monolithic	Range	{5.12; 9.84}	{3.18; 4.04}	{1.91; 4.33}
		μ (of k)	7.88	3.55	3.03
		σ (of k)	2.11	0.38	1.22
28	Cold joint	Range	{0.11; 0.41}	{1.04; 9.41}	
		μ (of k)	0.23	6.28	
		σ (of k)	0.13	3.67	
56	Monolithic	Range	{3.25; 3.81}	{1.82; 2.34}	{2.12; 9.31}
		μ (of k)	3.58	2.02	6.07
		σ (of k)	0.29	0.28	3.65
90	Monolithic	Range	{3.29; 4.09}	{1.71; 1.98}	{3.97; 6.20}
		μ (of k)	3.70	1.86	5.07
		σ (of k)	0.40	0.13	0.93

1. OPI: Oxygen Permeability Index.
2. k: Darcy permeability coefficient in m/s x 10^{-11}.
3. Range: {Minimum; Maximum}.
4. μ: Average.
5. σ: Standard deviation.

Table C.3: Details of the water sorptivity testing

Age (d)	Disc type	WSI	Ordinary concrete	Fly ash concrete	Metakaolin concrete
28	Monolithic	Range	{8.25; 8.61}	{6.93; 7.33}	{6.67; 7.04}
		μ (of WSI)	8.37	7.14	6.87
		σ (of WSI)	0.17	0.18	0.19
28	Cold joint	Range	{9.66; 11.17}	{6.96; 7.68}	
		μ (of WSI)	10.17	7.42	
		σ (of WSI)	0.70	0.31	
56	Monolithic	Range	{8.29; 8.51}	{6.94; 7.24}	{6.85; 7.02}
		μ (of WSI)	8.39	7.09	6.94
		σ (of WSI)	0.11	0.12	0.07
90	Monolithic	Range	{8.13; 8.64}	{7.02; 7.14}	{4.86; 5.72}
		μ (of WSI)	8.37	7.08	5.34
		σ (of WSI)	0.26	0.06	0.36

Table C.4: Details of the total porosity testing

Age (d)	Disc type	n (%)	Ordinary concrete	Fly ash concrete	Metakaolin concrete
28	Monolithic	Range	{14.05; 14.55}	{15.86; 17.26}	{11.29; 11.87}
		μ (of n)	14.27	16.68	11.62
		σ (of n)	0.21	0.63	0.30
28	Cold joint	Range	{15.01; 16.30}	{16.73; 17.78}	
		μ (of n)	15.44	17.45	
		σ (of n)	0.59	0.49	
56	Monolithic	Range	{14.18; 14.79}	{14.03; 14.94}	{9.47; 10.26}
		μ (of n)	14.49	14.55	9.99
		σ (of n)	0.30	0.42	0.36
90	Monolithic	Range	{14.12; 14.49}	{13.50; 14.10}	{8.11; 9.73}
		μ (of n)	14.28	13.78	8.97
		σ (of n)	0.19	0.30	0.85

1. S: Water sorptivity index in $mm/hr^{0.5}$.
2. n: Porosity (or % void volume) with the calcium hydroxide solution.
3. Range: {Minimum; Maximum}.
4. μ: Average.
5. σ: Standard deviation.

Table C.5: Details of the chloride conductivity testing

Age (d)	Disc type	CCI	Ordinary concrete	Fly ash concrete	Metakaolin concrete
28	Monolithic	Range	{1.31; 1.63}	{1.41; 1.63}	{0.71; 0.93}
		μ (of CCI)	1.44	1.54	0.81
		σ (of CCI)	0.14	0.09	0.11
28	Cold joint	Range	{1.39; 1.66}	{1.70; 1.81}	
		μ (of CCI)	1.52	1.76	
		σ (of CCI)	0.12	0.05	
56	Monolithic	Range	{1.29; 1.68}	{1.41; 1.62}	{0.59; 0.81}
		μ (of CCI)	1.45	1.52	0.69
		σ (of CCI)	0.17	0.10	0.10
90	Monolithic	Range	{1.41; 1.52}	{1.33; 1.62}	{0.41; 0.67}
		μ (of CCI)	1.46	1.48	0.56
		σ (of CCI)	0.05	0.13	0.12

Table C.6: Details of the chloride solution porosity testing

Age (d)	Disc type	n (%)	Ordinary concrete	Fly ash concrete	Metakaolin concrete
28	Monolithic	Range	{5.54; 5.99}	{6.22; 7.32}	{4.36; 4.69}
		μ (of n)	5.79	6.70	4.51
		σ (of n)	0.22	0.46	0.17
28	Cold joint	Range	{5.30; 6.39}	{7.02; 7.49}	
		μ (of n)	5.91	7.26	
		σ (of n)	0.49	0.20	
56	Monolithic	Range	{5.17; 5.78}	{6.10; 6.52}	{3.99; 4.35}
		μ (of n)	5.47	6.26	4.12
		σ (of n)	0.31	0.18	0.16
90	Monolithic	Range	{5.72; 6.01}	{5.36; 6.62}	{3.58; 4.20}
		μ (of n)	5.82	6.08	3.92
		σ (of n)	0.13	0.59	0.27

1. C: Chloride conductivity in mS/cm.
2. n: Porosity (or % void volume) with the chloride solution.
3. Range: {Minimum; Maximum}.
4. μ: Average.
5. σ: Standard deviation.

Appendix D: Penetration state

Appendix D 1: Chloride profiles in reinforced beams

Table D.1: Chloride profiles in the ordinary concrete 20 mm cover beams

Beam set	Chl (% mass)	0-5 mm	5-10 mm	10-15 mm	15-20 mm
CEM-M-20-I	Range	{0.12; 0.19}	{0.1; 0.14}	{0.11; 0.18}	{0.1; 0.14}
	μ (of Chl)	0.15	0.12	0.14	0.11
CEM-M-20-C	Range	{0.11; 0.14}	{0.11; 0.15}	{0.1; 0.12}	{0.1; 0.13}
	μ (of Chl)	0.12	0.13	0.11	0.12
CEM-CJ-20-I	Range	{0.25; 0.3}	{0.15; 0.24}	{0.13; 0.18}	{0.12; 0.14}
	μ (of Chl)	0.27	0.19	0.16	0.13
CEM-CJ-20-C	Range	{0.25; 0.33}	{0.15; 0.16}	{0.2; 0.21}	{0.14; 0.18}
	μ (of Chl)	0.30	0.15	0.21	0.16

Table D.2: Chloride profiles in the fly ash concrete 20 mm cover beams

Beam set	Chl (% mass)	0-5 mm	5-10 mm	10-15 mm	15-20 mm
FA-M-20-I	Range	{0.18; 0.21}	{0.16; 0.26}	{0.17; 0.23}	{0.04; 0.08}
	μ (of Chl)	0.20	0.21	0.20	0.05
FA-M-20-C	Range	{0.18; 0.29}	{0.22; 0.27}	{0.13; 0.28}	{0.1; 0.11}
	μ (of Chl)	0.24	0.24	0.22	0.07
FA-CJ-20-I	Range	{0.35; 0.37}	{0.33; 0.4}	{0.26; 0.4}	{0.21; 0.27}
	μ (of Chl)	0.36	0.37	0.31	0.24
FA-CJ-20-C	Range	{0.28; 0.36}	{0.28; 0.37}	{0.31; 0.44}	{0.35; 0.44}
	μ (of Chl)	0.32	0.33	0.38	0.40

Table D.3: Chloride profiles in the metakaolin concrete 20 mm cover beams

Beam set	Chl (% mass)	0-5 mm	5-10 mm	10-15 mm	15-20 mm
MK-M-20-I	Range	{0.11; 0.16}	{0.04; 0.07}	{0.02; 0.05}	{0.01; 0.03}
	μ (of Chl)	0.13	0.05	0.04	0.02
MK-M-20-C	Range	{0.17; 0.18}	{0.13; 0.15}	{0.05; 0.08}	{0.02; 0.05}
	μ (of Chl)	0.17	0.14	0.07	0.03
MK-CJ-20-I	Range	{0.16; 0.19}	{0.15; 0.18}	{0.1; 0.13}	{0.05; 0.07}
	μ (of Chl)	0.18	0.16	0.11	0.06
MK-CJ-20-C	Range	{0.15; 0.17}	{0.17; 0.18}	{0.13; 0.21}	{0.08; 0.09}
	μ (of Chl)	0.16	0.17	0.17	0.08

Table D.4: Chloride profiles in the ordinary concrete 10 mm cover beams

Beam set	Chl (% mass)	0-5 mm	5-10 mm
CEM-M-10-I	Range	{0.19; 0.27}	{0.18; 0.24}
	μ (of Chl)	0.23	0.21
CEM-M-10-C	Range	{0.2; 0.23}	{0.19; 0.24}
	μ (of Chl)	0.21	0.22
CEM-CJ-10-I	Range	{0.26; 0.31}	{0.21; 0.29}
	μ (of Chl)	0.29	0.25
CEM-CJ-10-C	Range	{0.32; 0.35}	{0.25; 0.31}
	μ (of Chl)	0.33	0.28

Table D.5: Chloride profiles in the fly ash concrete 10 mm cover beams

Beam set	Chl (% mass)	0-5 mm	5-10 mm
FA-M-10-I	Range	{0.2; 0.27}	{0.2; 0.26}
	μ (of Chl)	0.24	0.23
FA-M-10-C	Range	{0.18; 0.26}	{0.2; 0.25}
	μ (of Chl)	0.21	0.23
FA-CJ-10-I	Range	{0.32; 0.35}	{0.26; 0.31}
	μ (of Chl)	0.33	0.29
FA-CJ-10-C	Range	{0.27; 0.37}	{0.27; 0.32}
	μ (of Chl)	0.33	0.29

Table D.6: Chloride profiles in the metakaolin concrete 10 mm cover beams

Beam set	Chl (% mass)	0-5 mm	5-10 mm
MK-M-10-I	Range	{0.14; 0.17}	{0.12; 0.14}
	μ (of Chl)	0.15	0.12
MK-M-10-C	Range	{0.17; 0.21}	{0.14; 0.18}
	μ (of Chl)	0.19	0.16
MK-CJ-10-I	Range	{0.17; 0.21}	{0.13; 0.15}
	μ (of Chl)	0.20	0.13
MK-CJ-10-C	Range	{0.18; 0.2}	{0.18; 0.2}
	μ (of Chl)	0.19	0.19

1. Chl: Chloride content in % mass of the concrete sample.
2. n: Porosity (or % void volume) with the chloride solution.
3. μ: Average.

Appendix D 2: Carbonation depth testing details

Table D.7: Carbonation depths under isolated carbon dioxide exposure

Exposure info.		D_C (mm)	Concrete type		
Cycles	Duration		Ordinary concrete	Fly ash concrete	Metakaolin concrete
Baseline	0 days	Range	{0; 0}	{0; 0}	{0; 0}
		μ (of D_C)	0.0	0.0	0.0
		σ (of D_C)	0.0	0.0	0.0
10 cycles	140 days	Range	{9.6; 11.8}	{12.9; 14.4}	{18.3; 19.6}
		μ (of D_C)	10.7	13.7	18.9
		σ (of D_C)	1.1	0.8	0.7
21 cycles	294 days	Range	{14.4; 14.7}	{21.8; 22.0}	{28.8; 29.5}
		μ (of D_C)	14.6	21.9	29.1
		σ (of D_C)	0.1	0.1	0.4

Table D.8: Carbonation depths under combined exposure

Exposure info.		D_C (mm)	Concrete type		
Cycles	Duration		Ordinary concrete	Fly ash concrete	Metakaolin concrete
Baseline	0 days	Range	{0; 0}	{0; 0}	{0; 0}
		μ (of D_C)	0.0	0.0	0.0
		σ (of D_C)	0.0	0.0	0.0
10 cycles	140 days	Range	{4.9; 6.8}	{7.9; 8.1}	{9.4; 10.3}
		μ (of D_C)	5.9	8.0	9.8
		σ (of D_C)	1.1	0.1	0.4
21 cycles	294 days	Range	{6.5; 8.3}	{10.4; 11.3}	{12.9; 13.5}
		μ (of D_C)	7.4	10.9	13.2
		σ (of D_C)	0.9	0.5	0.3

1. dc: Carbonation depth.
2. Isolated exposure: Carbon dioxide in isolation.
3. Combined exposure: Carbon dioxide and chloride.
4. Range: {Minimum; Maximum}.
5. μ: Average.
6. σ: Standard deviation.

Appendix E: Corrosion behaviour

Appendix E 1: Coulostat apparatus potential behaviour

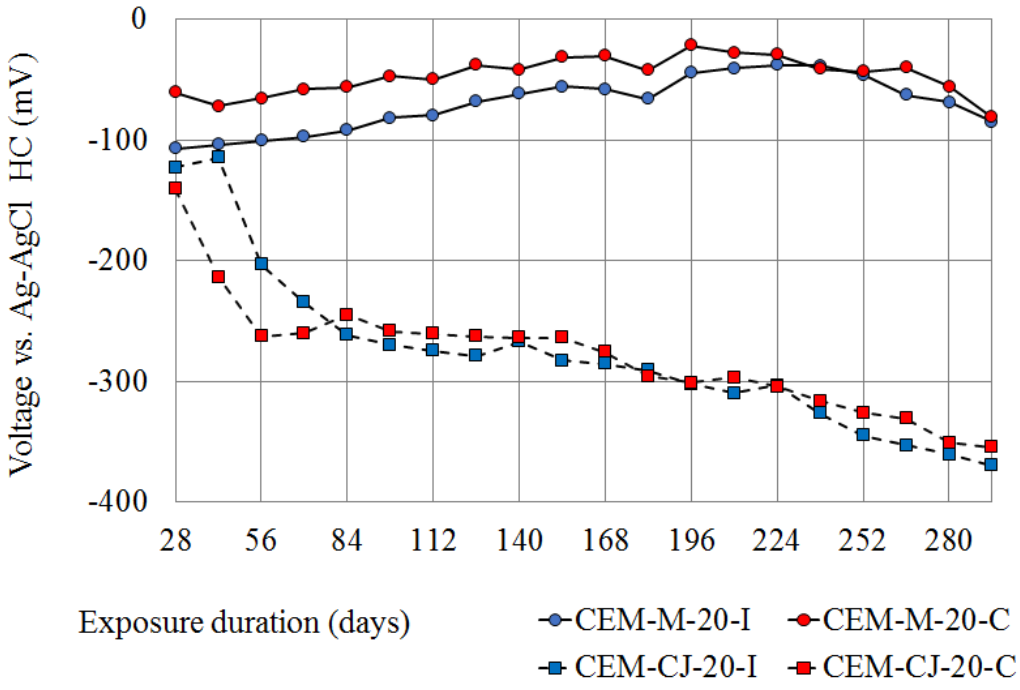

Figure E.1: Corrosion potential in the ordinary concrete 20 mm cover beams

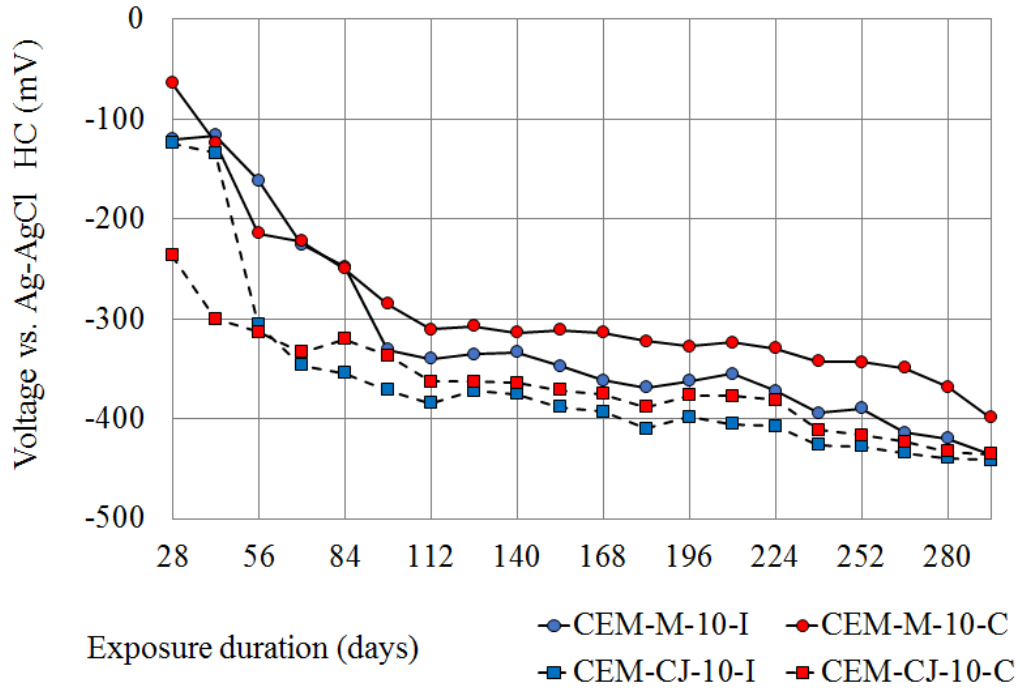

Figure E.2: Corrosion potential in the ordinary concrete 10 mm cover beams

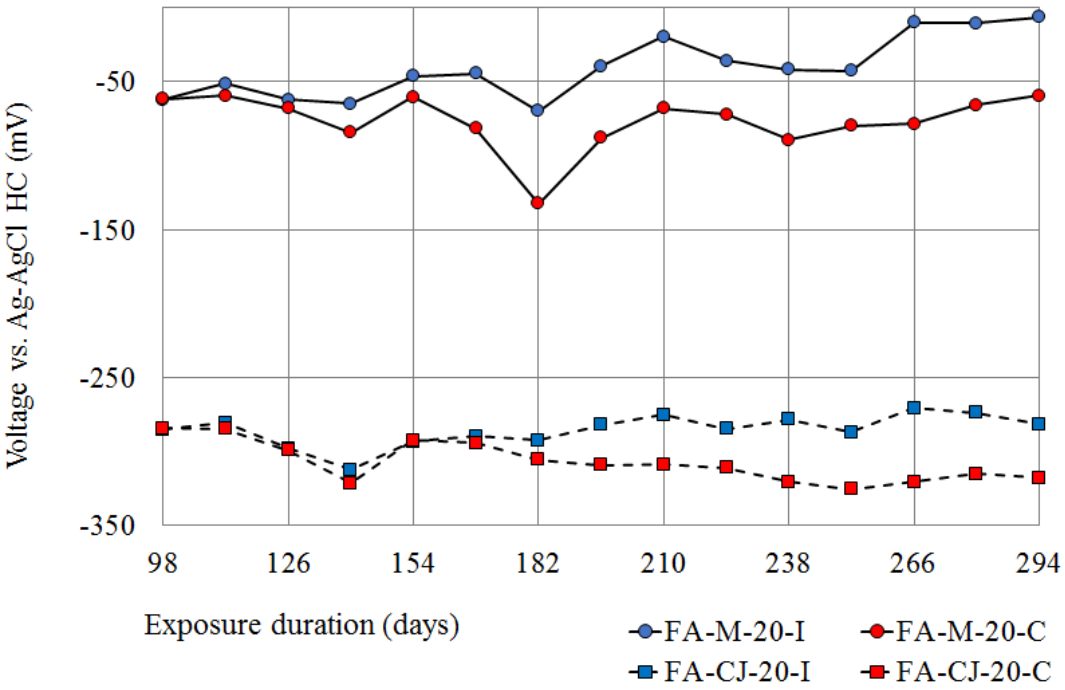

Figure E.3: Corrosion potential in the fly ash concrete 20 mm cover beams

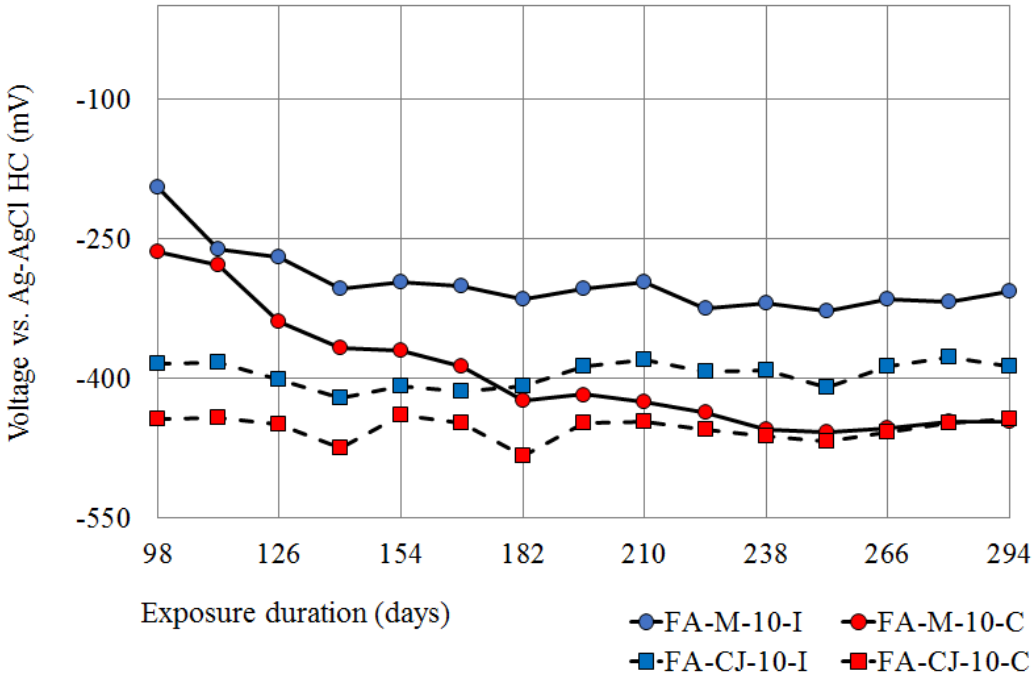

Figure E.4: Corrosion potential in the fly ash concrete 10 mm cover beams

1. Minimum potential against the Ag-AgCl half-cell array.
2. Average of 2 readings at each testing age.

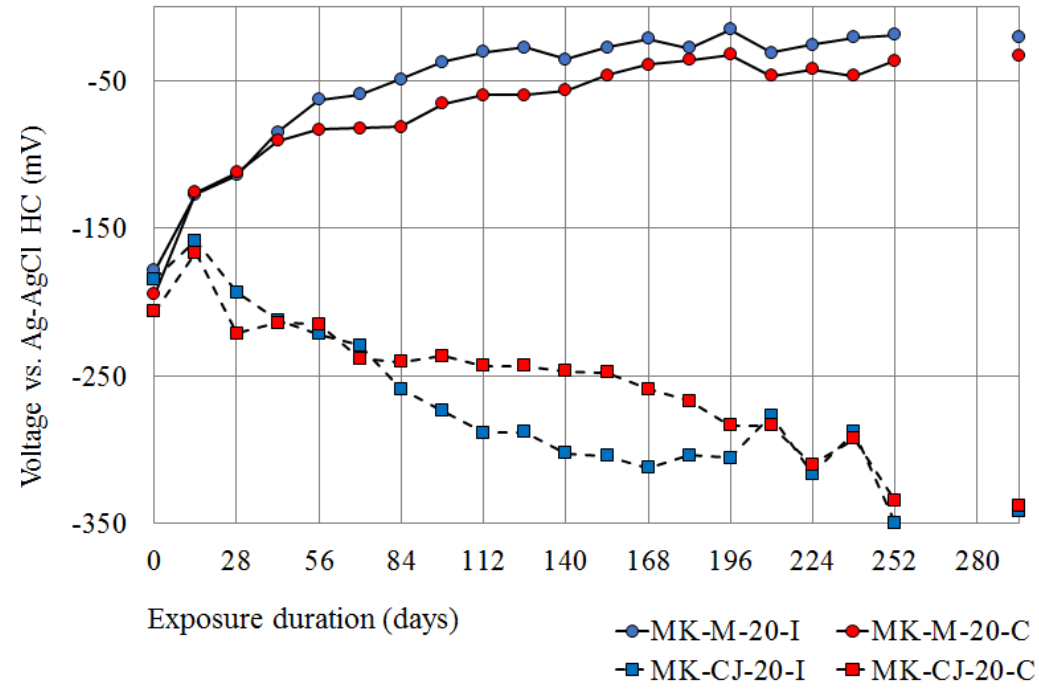

Figure E.5: Corrosion potential in the metakaolin concrete 20 mm cover beams

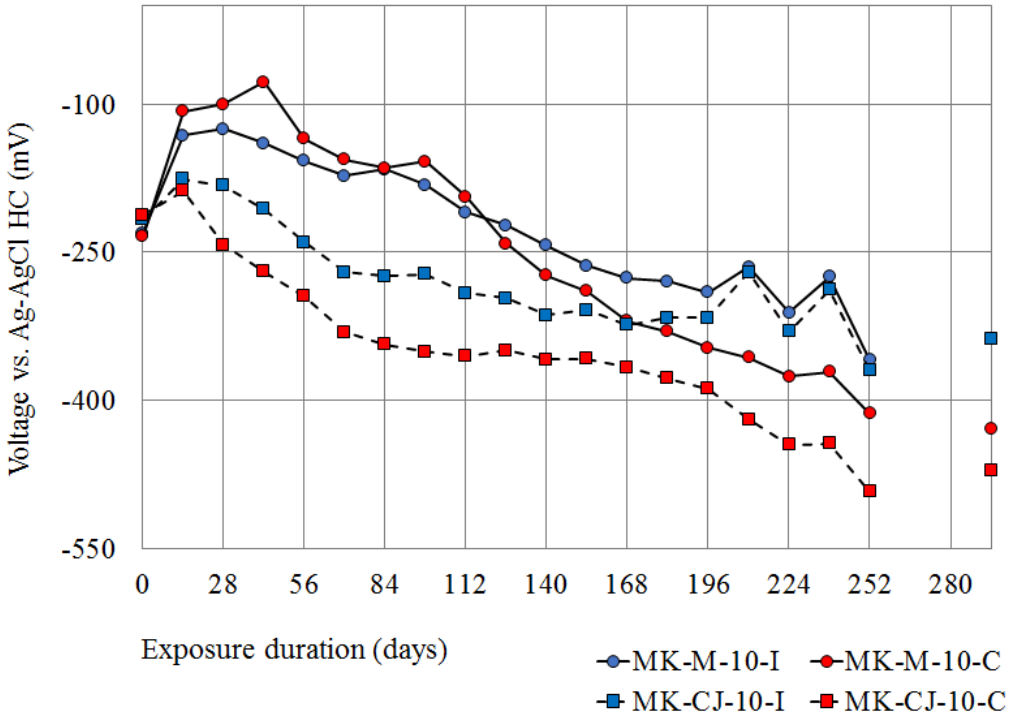

Figure E.6: Corrosion potential in the metakaolin concrete 10 mm cover beams

1. Minimum potential against the Ag-AgCl half-cell array.
2. Average of 2 readings at each testing age.

Appendix E 2: Coulostat apparatus resistivity behaviour

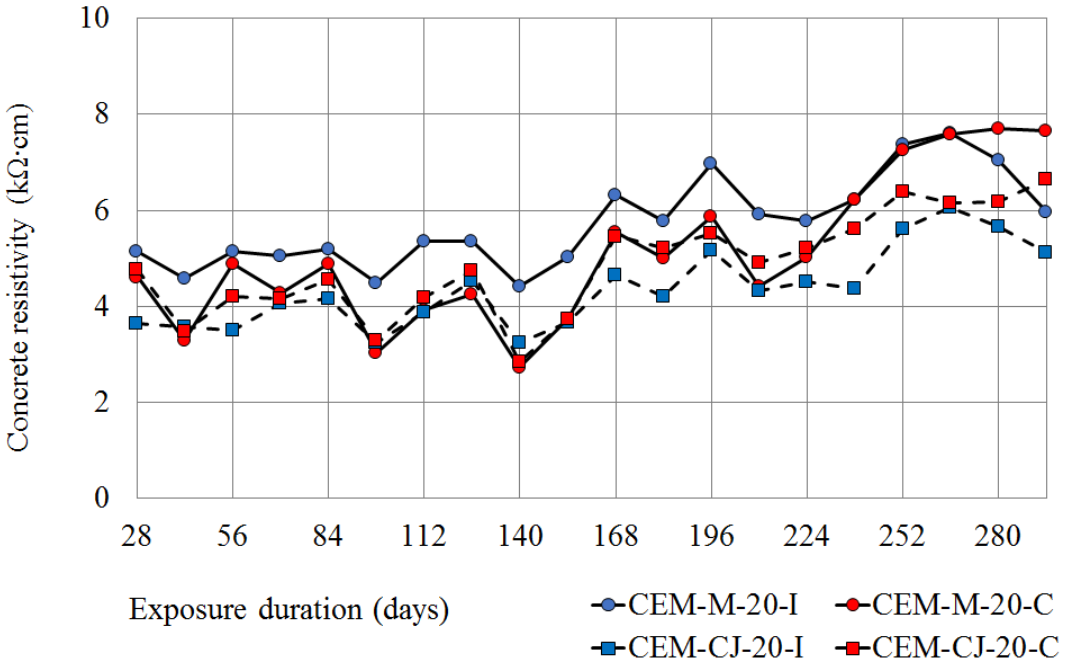

Figure E.7: Concrete resistivity in the ordinary concrete 20 mm cover beams

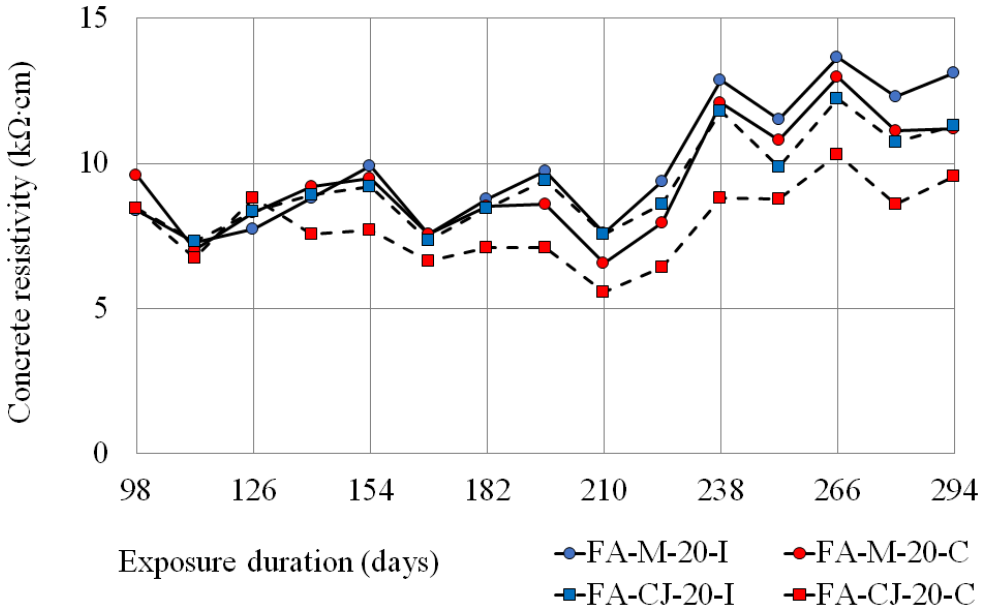

Figure E.8: Concrete resistivity in the fly ash concrete 20 mm cover beams

1. Minimum resistivity against the Ag-AgCl half-cell array.
2. Average of 2 readings at each testing age.

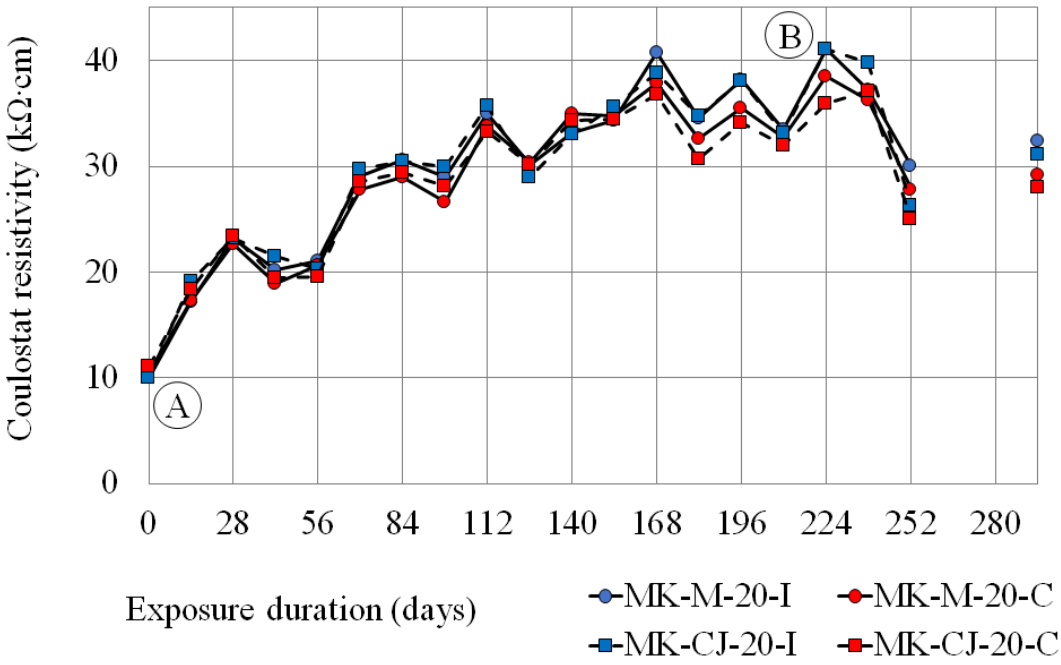

Figure E.9: Concrete resistivity in the metakaolin concrete 20 mm cover beams

1. Minimum resistivity against the Ag-AgCl half-cell array.
2. Average of 2 readings at each testing age.